UNIVERSITY OF COPENHAGEN

Magnetic Frustration under Pressure

Written by Lise Ørduk Sandberg
Handed in 15 March 2022

Supervisors: Kim Lefmann and
Pascale P. Deen

This thesis has been submitted to the
PhD School of the Faculty of Science,
University of Copenhagen
Niels Bohr Institute
University of Copenhagen

Preface

The work presented in this thesis is the result of my work at the Niels Bohr Institute at the University of Copenhagen and the European Spallation Source from July 2017 to December 2021. The project has been a collaboration between 3 different PhD students. We have all had different backgrounds and focus, but we have worked closely together on all parts of the projects. Ingrid Marie Bakke Fj´allvåg has worked at the University of Oslo with sample preparation and characterization as her main focus. The single crystals were made in a mirror furnace at the University of Lund, and I have been very involved in that process. Richard Edberg has been based at KTH in Stockholm, and he has mainly focused on Monte Carlo simulations of the magnetic systems based on the neutron scattering measurements and magnetization measurements that have been performed within the project. I did not take part in the simulation code, but we met (online or physically) several times a week to discuss assumptions, expectations and results, except during the months where I was on parental leave.

As such, this has been a truly collaborative project which is also reflected in the list of publications which contain publications/manuscripts within sample preparation, theoretical simulation as well as experimental neutron scattering and pressure cell, which has been my main focus.

This thesis assumes prior knowledge within the field of physics taught at B.Sc. level including quantum mechanics and electrodynamics.

Abstract

This thesis has two main topics, it describes the development, testing and calibration of a uniaxial pressure cell and it describes a neutron scattering and magnetic susceptibility study of the magnetically frustrated compound $Yb_3Ga_5O_{12}$ at ambient pressure.

We have designed, constructed and tested a uniaxial pressure cell which is able to apply a uniaxial pressure up to 2 GPa to a polished cylindrical crystalline sample. The pressure cell targets the study of magnetically frustrated compounds which have weak and diffuse scattering features. The cell therefore provides a highly uniform and low background signal to enable extraction of these weak signals. Furthermore, it accommodates polarisation analysis which allows separation of the weak magnetic scattering signal from the nuclear contribution to the scattering signal.

We have shown that the pressure cell is indeed able to apply a uniaxial pressure to the magnetically frustrated spin ice compound $Ho_2Ti_2O_7$ and we have detected the pressure induced changes in the diffuse scattering patterns at two different neutron scattering experiments. In addition, these changes match well the theoretically predicted changes based on Monte Carlo simulations.

The spin-spin interactions in $Yb_3Ga_5O_{12}$ are very weak, and crystal field considerations, neglecting magnetic exchange, are able to correctly describe magnetic susceptibility measurements except at the lowest temperatures. Crystal field calculations also correctly predict the crystal field excitations which we have measured with thermal neutron scattering. Cold neutron scattering studies at temperatures near 100 mK at two different neutron scattering instruments revealed distinct diffuse scattering pattern with 6-fold symmetry following the crystal symmetry. Reverse Monte Carlo simulations showed that spins correlate antiferromagnetically across the 10-ion loops while nearest neighbour spins correlate ferromagnetically. All spins have an easy axis connecting the centres of the triangles which lead us to propose a 1.5-in-1.5-out ground state manifold in analogy with the 2-in-2-out ground state manifold for spin ice compounds. In contrast to the spin ice ground state, the 1.5-in-1.5-out state allows for spin fluctuations within a single triangle, and it is thereby related to the magnetic monopoles which describe the dynamics of spin ice compounds.

Cold inelastic neutron scattering of $Yb_3Ga_5O_{12}$ shows three dispersionless soft mode excitations which are not single ion effects. We do not yet have a physical interpretation of these excitations, but they are magnetic in origin The isostructural compound $Gd_3Ga_5O_{12}$

also has three dispersionless soft mode excitations which are linked to the dynamics on the 10-ion loops. Although the ground state of $Yb_3Ga_5O_{12}$ is very different to that of $Gd_3Ga_5O_{12}$, it is likely that the dynamics of $Yb_3Ga_5O_{12}$ is also linked to the collective behaviour of all spins on a triangle or a 10-ion loops.

Sammenfatning

Der er to hovedemner i denne afhandling: den beskriver udvikling, test og kalibrering af en uniaksiel trykcelle, og så beskriver den studiet af materialet $Yb_3Ga_5O_{12}$, der er magnetisk frustreret.

Vi har designet, konstrueret og testet en uniaksiel trykcelle, der kan påføre et uniaksielt tryk op til 2 GPa til en poleret, cylinderformet enkeltkrystalsprøve. Trykcellen har en ensartet neutronspredningsbaggrund, hvilket gør det muligt at studere magnetisk frustrerede prøver, der giver anledning til diffuse spredning. Ydermere understøtter den brugen af polarisationsanalyse, hvilket gør det muligt at adskille det magnetisk of nukleare spredningssignal.

Vi har vist, at cellen kan påføre et uniaxielt tryk til det magnetisk frustrerede materiale $Ho_2Ti_2O_7$, og vi har været i stand til at måle de trykforårsagede ændringer i det diffuse spredningssignal ved to forskellige eksperimenter. De målte ændringer stemmer endvidere godt overens med de teoretisk forudsagte ændringer, der er baseret på Monte Carlo simulationer.

Spin-spin-vekselvirkningerne i $Yb_3Ga_5O_{12}$ er meget svage, og det er muligt at beskrive målingerne af magnetisk suscpetibilitet med krystalfeltsbetragtninger, hvor vi helt negligerer exchange, pånær ved de allerlaveste temperaturer. Krystalfeltsberegningerne er også i stand til at forudsige placeringen af krystalfeltseksitationerne, som vi har målt med termisk neutronspredning. Neutronspredningsstudier omkring 100 mK ved to forskellige neutronspredningsinstrumenter indeholder tydelig diffus spredning med 6-foldssymmetri, der følger krystalsymmetrien. Revers Monte Carlo simulationer har vist, at spinene korrelerer antiferromagnetisk på tværs af 10-spin-ringene og ferromagnetisk mellem nærmeste nabo spin. Alle spin har en let akse, der forbinder centrene af trekanterne, hvilket gør, at vi foreslår en 1.5-ind-1.5-ud grundtilstand med en stærk analogi til den 2-ind-2-ud tilstand, der beskriver spinis. Modsat spinisgrundtilstanden, er der spinfluktuationer i 1.5-in-1.5-ud tilstanden i hver enkelt trekant, og dermed er der også analogier til de magnetiske monopoler, der bruges til at beskrive dynamikken i spinismaterialer.

Uelastisk neutronspredning med kolde neutroner af $Yb_3Ga_5O_{12}$ viser tre dispersionsløse soft mode eksitationer, der ikke er enkeltionseffekter. Vi har endnu ikke en fysisk fortolkning af disse eksitationer, men det isostrukturelle materiale $Gd_3Ga_5O_{12}$ har også tre dispersionsløse soft-mode eksitationer, der er styret af dynamikken af spinnene på en 10-

ions-ring. Selvom grundtilstanden af $Yb_3Ga_5O_{12}$ er meget forskellig fra grundtilstanden af $Gd_3Ga_5O_{12}$, er det sandsynligt, at dynamikken i $Yb_3Ga_5O_{12}$ også indebærer alle spins i en trekant eller en 10-ions-ring.

Populærvidenskabelig sammenfatning

Denne afhandling har to dele. Den ene del beskriver studiet af den magnetisk frustrerede krystal $Yb_3Ga_5O_{12}$. Figur 1 beskriver ideen bag magnetisk frustration. Systemet med tre spin (markeret med pile) på hvert hjørne af en trekant har lavest energi, hvis alle spin peger i modsat retning af deres nabo. Spinnene kan kun pege enten op eller ned, så det kan kun lade sig gøre for 2 af spinnene at pege modsat deres nabo. Det sidst spin vil pege samme vej som et af nabospinnene uanset hvilken vej, det peger. En elektrons spin er et lille magnetfelt, og det er en af de fundamentale egenskaber ved en elektron, ligesom dens ladning er det. En enkelt trekant som den i figur 1 har 6 mulige spinkonfiguration med samme energi, og for en ægte krystal, der indeholder 10^{23} spin (det er 100.000.000.000.000.000.000.000 spin), vil der i praksis være uendeligt mange muligheder. Derfor vil systemet ikke ordne i en af de mange grundtilstande, men fluktuere mellem dem, og man siger, at systemet er magnetisk frustreret. Det magnetiske signal fra et frustreret system, som vi kan måle med neutronspredning, giver anledning til nogle brede, diffuse signaler, der minder om det, man måler strukturelt fra en væske, og man kalder derfor også disse systemer for spinvæsker. I denne afhandling har vi undersøgt de diffuse neutronspredningssignaler fra $Yb_3Ga_5O_{12}$, hvor trekanterne er sat sammen i ringe med 10 spins i hver ring. Det viser sig, at spinnene i $Yb_3Ga_5O_{12}$ korrelerer på tværs af både trekanterne og ringene hvilket giver anledning til nogle tydelige diffuse neutronspredningssignaler.

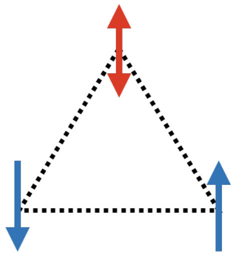

Figure 1: En trekant med et spin på hvert hjørne. Spinnene er markeret med pile, der kun kan pege op eller ned. Systemet har lavest energi, hvis alle spin peger modsat af deres nabospin, men dette kan kun lade sig gøre for 2 ud af 3 spins. Det sidste spin vil nødvendigvis pege samme vej som det ene nabospin og modsat vej af det andet nabospin.

Den anden halvdel af afhandlingen beskriver udviklingen af en trykcelle, der kan påføre uniaxielt tryk til magnetisk frustrerede materialer. Fordi krystalgeometrien er så vigtig i disse materialer, er det forventningen, at man kan ændre både struktur og dynamik ganske betragteligt ved at påføre et uniaksielt tryk, hvor man ændrer krystalsymmetrien. Vores trykcelle kan påføre 2.5 tonnes, eller hvad der svarer til vægten af 2 Citroën Berlingo, til et areal på få mm^2. Trykcellen opfylder en række krav, for eksempel må der ikke være skarpe signaturer i baggrundssignalet fra cellen, hvis vi skal kunne studere ændringerne i de svage, diffuse neutronspredningssignaler. Derudover må der ikke være noget magnetisk i trykcellen, fordi dette ødelægger polariseringen af neutronerne, som vi bruger til at adskille det magnetiske neutronspredningssignal. Til sidst, er fysikken af magnetisk frustrerede materialer oftest mest interessant ved meget lave temperaturer langt under 1 K (-272°), og materialerne i trykcellen skal derfor have rigtigt god termisk ledeevne, så vi kan køle cellen inden for en rimelig tidsramme. Vi har lavet flere forsøg, hvor vi har kunne måle trykinducerede ændringer i det magnetisk frustrerede materiale $Ho_2Ti_2O_7$, hvilket viser, at cellen opfylder alle disse krav.

Acknowledgements

First of all, I would like to thank my two supervisors, Kim Lefmann and Pascale P. Deen for many enjoyable years. You have both opened your homes and families to me and it has been an honour and a lot of fun to get to know you at home and on travels. Your patience is admirable when you have explained science, both magnetism and neutron scattering as well as politics when working in science, and I greatly value our many discussions.

I would also like to thank the technicians in the workshop at the Niels Bohr Institute, including Jan Oechsle and Dennis Wistisen for a very inspiring collaboration when developing the pressure cell and load gauge. Your enthusiasm and innovative approach has been a great motivation and it has been a lot of fun working with you. I would also like to thank our collaborators at the European Spallation Source for their inputs and help with the development of the pressure cell, especially Alexander Holmes and Malcolm Guthrie for many fruitful discussions.

The people in the magnetism group at the Niels Bohr Institute has been a key motivation for me throughout the last decade. Thank you all for creating a warm and enjoyable social climate and for many scientific discussions. I would especially like to thank Sofie Holm-Janas, Jakob Lass and Morten Haubro. I have also enjoyed the teamwork within the NNSP collaboration with Richard Edberg, Ingrid Marie Bakke Fjellvåg and Patrik Henelius. It has been highly interesting to learn from you and to get to know you on our many meetings and also on travels for beamtimes and conferences.

Finally and most importantly, I would like to thank my family for their patience and support. It had not been possible for me to write this thesis without you and I am very proud to be your wife, mother, sister and daughter.

All of these people and many more have made the last years a lot of fun, and I will keep many good memories from my PhD studies. Thank you.

Contents

List of Figures

List of Abbreviations

AFM: Antiferromagnetic
CCR: closed-cycle refrigerator
CuBe: Copper berryllium
DAC: Diamond anvil cell
DM: Dzyaloshinsky-Moriya
DTO: $Dy_2Ti_2O_7$
FEA: Finite Element Analysis
FM: Ferromagnetic
GGG: $Gd_3Ga_5O_{12}$
HTO: $Ho_2Ti_2O_7$
ω: sample rotation during TOF experiment.
LN2: liquid nitrogen
PA: Polarisation analysis
RMC: reverse Monte Carlo
TOF: Time of flight
WC10: Tungsten Carbide MT10MG
YbGG: $Yb_3Ga_5O_{12}$
2θ: Scattering angle defined in eq 3.3

List of Publications

Publications:

- R. Edberg, **L. Ø. Sandberg**, I. M. B. Bakke, M. L. Haubro, L. C Folkers, A. Wildes, O. Zaharko, M. Guthrie, A. T. Holmes, M. H. Sørby, K. Lefmann, P. P. Deen and P. Henelius. "Dipolar spin ice under uniaxial pressure", *Physical Review B* 14, 100 (2019)

- K. Kunnus, M. Vacher, T. C. B. Harlang, K. S. Kjær, K. Haldrup, E. Biasin, T. B. van Driel, M. Pápai, P. Chabera, Y. Liu, H. Tatsuno, C. Timm, E. K´allman, M. Delcey, R. W. Hartsock, M. E. Reinhard, S. Koroidov, M. G. Laursen, F. B. Hansen, P. Vester, M. Christensen, **L. Ø. Sandberg**, Z. Németh, D. S. Szemes, Éva Bajnóczi, R. Alonso-Mori, J. M. Glownia, S. Nelson, M. Sikorski, D. Sokaras, H. T. Lemke, S. E. Canton, K. B. Møller, M. M. Nielsen, G. Vankó, K. W´arnmark, V. Sundstr´om, P. Persson, M. Lundberg, J. Uhlig and K. J. Gaffney, " Vibrational wavepacket dynamics in Fe carbene photosensitizer determined with femtosecond X-ray emission and scattering ", *Nature Communications* 11, 634 (2020)

- R. Edberg, I. M. B. Bakke, H. Kondo, **L. Ø. Sandberg**, M. L. Haubro, M. Guthrie, A. T. Holmes, J. Engqvist, A. Wildes, K. Matsuhira, K. Lefmann, P. P. Deen, M. Mito and P. Henelius, "Effects of uniaxial pressure on the spin ice $Ho_2Ti_2O_7$", *Physical Review B* 18, 102 (2020).

- **L. Ø. Sandberg**, R. Edberg, I. M. B. Bakke, K. S. Pedersen, M. C. Hatnean, G. Balakrishnan, L. Mangin-Thro, A. Wildes, B. Fåk, G. Ehlers, G. Sala, P. Henelius, K. Lefmann and P. P. Deen. "Emergent magnetic behavior in the frustrated $Yb_3Ga_5O_{12}$ garnet", *Physical Review B* 6, 104 (2021)

Manuscripts:

- **L. Ø. Sandberg**, M. L. Haubro, M. E. Kamminga, K. M. L. Krighaar, R. Edberg, I. M. B. Fjellvåg, M. Guthrie, A. T. Holmes, L. Mangin-Thro, A. Wildes, M. Boehm, J. Oechsle, K.-E. Nielsen, D. W. Wistisen, K. Theodor, P. Henelius, K. Lefmann, and P. P. Deen. "Design, calibration, and performance of a uniaxial pressure cell for neutron scattering studies of quantum magnetism." Manuscript to be submitted to Rev. Sci. Instr

- R. Edberg, I. M. Fjellvåg, **L. Ø. Sandberg**, P. P. Deen, K. Lefmann, P. Henelius, and A. Rydh, "Magnetic monopole relaxation effects probed by modulation calorimetry in small spin-ice samples". Submitted to *Physical Review B.*
- I. M. B. Fjellvåg, M. L. Haubro, **L. Ø. Sandberg**, R. Edberg, K. Lefmann, P. Henelius, T. Hansen, O. R. F. Rosa, B. C. Hauback and P. P. Deen. "Single crystal growth of pyrochlore titanate oxides (RE2Ti2O7) by optical zone melting for neutron and magnetic property studies".
- M. E. Kamminga, K. M. L. Krighaar, A. T. Rømer, **L. Ø. Sandberg**, P. P. Deen, M. Boehm, G. D. Gu, J. M. Tranquada, and K. Lefmann. "Evolution of magnetic stripes under uniaxial stress in La1.885Ba0.115CuO4 studied by neutron scattering". Submitted to *Physical Review B.*

Chapter 1

Introduction

Magnetically frustrated compounds have shown to display novel and emergent behaviour due to the correlated, but disordered, ground state manifold which is macroscopically degenerate. In 3 dimensional systems with rare earth ions, the interplay between spin-spin interactions and anisotropy has been shown to govern the physics in classical spin ice compounds such as $Ho_2Ti_2O_7$ and $Dy_2Ti_2O_7$, where the rare earth ion occupy the tetrahedra in the pyrochlore lattice. The excitations from the spin ice ground state manifold is described by an emergent gauge field and is modelled as magnetic monopole excitations [15, 23, 28]. More recently, the study of $Gd_3Ga_5O_{12}$ revealed a hidden long range order of the collective spin of each 10-ion loop of Gd^{3+} spins, called the director, despite absence of long range correlations between the individual Gd^{3+} spins [56]. Here, we have studied $Yb_3Ga_5O_{12}$, which is isostructural to $Gd_3Ga_5O_{12}$, but has an effective spin $S = 1/2$ with a highly isolated Kramer's doublet ground state due to a strong crystal field thereby enabling quantum effects.

The crystal structure is highly important in magnetic frustration, and hydrostatic pressure is a standard external pertubation at many neutron scattering facilities. Unlike hydrostatic pressure, uniaxial pressure breaks the crystal symmetry and it is thereby possible to directly tune the strength of competing spin-spin interactions along different crystallographic directions. This could lead to novel phases of matter and a better understanding of the nature of the spin interactions in the materials which is especially relevant for magnetically frustrated compounds. However, until now, uniaxial pressure cells have not been widely used in neutron scattering, particularly for the case of neutron diffuse magnetic scattering, primarily as a result of the many technical challenges when applying uniaxial pressure. We have developed a uniaxial pressure cell which has overcome the previous challenges and it is now ready to be used at many different neutron scattering instruments. The physics of the classical spin ice compound $Ho_2Ti_2O_7$ at ambient pressure has been well studied during the last two decades, and we have therefore used this compound to test the effect of the pressure whereby we have shown clear pressure induced changes in the diffuse scattering signals measured with polarisation analysis.

Chapter 2

Magnetism

This chapter describes the basic concepts in magnetism and magnetic interactions in addition to a brief introduction to the field of frustrated magnetism. The most frequently studied systems in magnetism involve *transition metals* where 3d orbitals carry the magnetic moment and *rare earth ions* where the more localised 4f orbitals carry the magnetic moment. This project has focused on rare earth ion compounds with Yb^{3+} and Ho^{3+} and this chapter therefore focuses on the magnetism in rare earth ions and magnetic frustration in these compounds.

2.1 Basic Concepts in Magnetism

The description of the basic concepts in magnetism in this section is largely based on ref. [9]. Magnetism as used in this thesis describes the properties and interactions of the electron magnetic moment

$$\boldsymbol{\mu} = \mu_B(g_L\mathbf{L} + g_S\mathbf{S}), \tag{2.1}$$

where $\mathbf{L}$ and $\mathbf{S}$ are the orbital and spin angular momenta of the electron respectively while $g_L \approx 1$ and $g_S \approx 2$ are the g-factors of the orbital and spin angular momentum respectively and μ_B is the Bohr magneton. Rare earth ions generally have a strong spin-orbit coupling, and as a result $\mathbf{L}$ and $\mathbf{S}$ are not separately conserved, but the total angular momentum, $\mathbf{J} = \mathbf{L} + \mathbf{S}$ is conserved. A better description of the magnetic moment is therefore often

$$\boldsymbol{\mu} = \mu_B g_J \mathbf{J}, \tag{2.2}$$

where g_J is the projection of $\mathbf{L} + 2\mathbf{S}$ onto $\mathbf{J}$, termed the Landé g-factor,

$$g_J = \frac{3}{2} + \frac{S(S+1) - L(L+1)}{2J(J+1)}. \tag{2.3}$$

Hund's Rules

The ground state spin configuration of a partially filled orbital is described empirically by *Hund's rules*:

1. Maximize the total spin angular moment, S.
2. Maximise the total orbital angular moment, L,
3. The total magnetic moment, J, is found as J $= |L + S|$, if the shell is more than half full and J $= |L - S|$ if the shell is less than half full.

Hund's first and second rule both minimize the Coulomb interaction between the electrons. The first rule separates the electrons in space because identical fermions cannot occupy the same quantum state according to the Pauli exclusion principle, and electrons with equal spin states therefore cannot occupy the same spatial state. The second rule is more subtle, and it is here described with a classical analogy. When L is maximised, the electrons rotate the same way around the nucleus, and the average distance between the electrons is therefore minimized resulting in a reduced Coulomb interaction. The third rule minimises the spin-orbit interaction. Hund's rules only apply to systems where the spin-orbit interaction is a small pertubation to the electrostatic repulsion between the electrons. This is not generally true for rare earth ion compounds, but Hund's rules often provide a good estimate of the ground state spin configuration despite a strong spin-orbit coupling.

The ground state spin configuration obtained from Hund's rules is typically denoted with the term symbol, $^{2S+1}L_J$, where S and J are written as numerical values while L is denoted by the corresponding letter, S, P, D, F for $L = 0, 1, 2, 3$ respectively. As an example, table 2.1 shows the ground state configuration of Yb^{3+} based on Hund's rule. Yb^{3+} has an outer shell $4\mathrm{f}^{13}$ meaning that there are 13 electrons in the 4f orbital. The table shows that the ground state configuration of Yb^{3+} is $^2\mathrm{F}_{7/2}$ where S = 1/2, L = 3 and since the orbital is more than half filled, J $= |L + S| = 7/2$.

m_l	↑	↓
3	x	x
2	x	x
1	x	x
0	x	x
-1	x	x
-2	x	x
-3	x	

Table 2.1: Ground state configuration of Yb^{3+} which has outer shell $4\mathrm{f}^{13}$ based on Hund's rules. Crosses mark occupied states.

Paramagnetism

The spins in a true *paramagnetic* system are uncorrelated and do not interact and they will therefore align perfectly with an external magnetic field according to the Zeeman interaction described in section 2.2.4. In most real systems, the interactions are not zero, and the paramagnetic regime of a system is used to describe the high temperature limit where thermal fluctuations are much stronger than the spin-spin interactions.

For low magnetic fields, the magnetic susceptibility of a paramagnet follows the *Curie law*,

$$\chi \approx \frac{n\mu_0\mu_{\text{eff}}^2}{3k_BT}, \tag{2.4}$$

where n is the amount of magnetic moments per unit volume, μ_0 is the vacuum permeability and k_B is the Boltzmann's constant. μ_{eff} is the effective magnetic moment defined by

$$\mu_{\text{eff}} = g_J\mu_B\sqrt{J(J+1)}. \tag{2.5}$$

The susceptiblity of paramagnetic ions offer a method to test the validity of the Hund's rules as an estimate of the ground state configuration based on a comparison of the measured μ_{eff} and the calculated μ_{eff} based on the obtained values from S, L and J. For most rare earth ions including Yb^{3+} and Ho^{3+} which are studied in this thesis, the ground state spin configuration obtained from Hund's rules provide a good estimate of the experimentally determined μ_{eff} and thereby the actual ground state spin configuration [9].

2.2 Magnetic Interactions

There are four contributions to the energy of magnetic systems described in this thesis: the exchange interaction, $\mathcal{H}_{\text{ex}}$, the dipole interaction, $\mathcal{H}_{\text{dip}}$, the Zeeman interaction, $\mathcal{H}_{\text{zee}}$ and the crystal field interaction, $\mathcal{H}_{\text{cf}}$, resulting in a total Hamiltonian,

$$\mathcal{H} = \mathcal{H}_{\text{ex}} + \mathcal{H}_{\text{dip}} + \mathcal{H}_{\text{cf}} + \mathcal{H}_{\text{zee}}. \tag{2.6}$$

The exchange interaction and the dipole interaction couple the magnetic states of different sites, and they are therefore referred to as spin-spin interactions. The crystal field and Zeeman interactions are single ion effects where each ion responds to an effective field. This section contains a description of each of the four terms in equation 2.6.

2.2.1 Exchange interaction

Exchange interaction provides an indirect description of the Coulomb interaction between electrons and the *Pauli exclusion principle* which states that two fermions cannot occupy the same quantum state. This is the dominant contributions to the magnetic structure in most materials and it is therefore described here despite its weakness in $Ho_2Ti_2O_7$ and $Yb_3Ga_5O_{12}$ which are studied in this thesis.

Exchange interaction can be derived from the *symmetrization requirement* stating that the total wave function must be symmetric under exchange of bosons with integer spins and anti-symmetric under exchange of fermions with half integer spins [30].

In the following, we will derive the exchange interaction between two electrons with $\mathbf{L} = 0$ for simplicity so $\mathbf{J} = \mathbf{S}$ based on the symmetrization requirement. In this section, the symbol $\mathbf{S}$ is used to avoid confusion with the exchange integral, J.

The spin state of two electrons can combine into three symmetric triplet states,

$$\chi_T = \left|\uparrow\downarrow\right\rangle, \frac{\left|\uparrow\downarrow\right\rangle + \left|\downarrow\uparrow\right\rangle}{\sqrt{2}}, \left|\downarrow\downarrow\right\rangle \tag{2.7}$$

which have total spin S = 1, and an anti-symmetric singlet state,

$$\chi_S = \frac{\left|\uparrow\downarrow\right\rangle - \left|\downarrow\uparrow\right\rangle}{\sqrt{2}}, \tag{2.8}$$

which has total spin S = 0. The spatial states $\psi_a(\mathbf{r_1})$ and $\psi_b(\mathbf{r_2})$ respectively for the two electrons at positions $\mathbf{r_1}$ and $\mathbf{r_2}$ respectively can combine into a symmetric or antisymmetric state because identical fermions cannot be in the same place,

$$\Psi_\pm = \frac{1}{\sqrt{2}}[\psi_a(\mathbf{r_1})\psi_b(\mathbf{r_2}) \pm \psi_a(\mathbf{r_2})\psi_b(\mathbf{r_1})], \tag{2.9}$$

resulting in the total asymmetric wave functions

$$\Psi_S = \Psi_+\chi_S \tag{2.10}$$
$$\Psi_T = \Psi_-\chi_T. \tag{2.11}$$

The singlet and triplet spin states are eigenstates to the Hamiltonian

$$\mathcal{H}_{\text{ex}} = -2J\mathbf{S_1}\cdot\mathbf{S_2}, \tag{2.12}$$

where J is the exchange integral which can be positive or negative. The eigenvalues are found by rewriting $\mathcal{H}_{\text{ex}}$ into

$$\mathcal{H}_{\text{ex}} = -J[\mathbf{S}_{\text{tot}}{}^2 - \mathbf{S_1}{}^2 - \mathbf{S_2}{}^2]. \tag{2.13}$$

The eigenvalue of $\mathbf{S^2}$ is S(S+1), and

$$E_T = -\frac{J}{2}, \tag{2.14}$$
$$E_S = +\frac{3J}{2}. \tag{2.15}$$

Equations 2.14 and 2.15 show that systems with $J > 0$ have triplet ground states and systems with $J < 0$ have singlet ground states. From the difference between the two equations,

$$J = \frac{E_S - E_T}{2}, \tag{2.16}$$

and the exchange integral thereby represents the difference in electrostatic energy between the symmetric and anti-symmetric spatial states which reflects the orbital overlap of the two sites.

The spin Hamiltonian in equation 2.12 is generalized to,

$$\mathcal{H}_{\text{ex}} = -\sum_{ij} J_{ij}\mathbf{S_i} \cdot \mathbf{S_j}, \tag{2.17}$$

which is termed the *Heisenberg Hamiltonian*. The summation is performed over all ion sites in the sytem, and the factor of 2 in equation 2.12 is therefore omitted because each spin pair is summed twice in equation 2.17. J_{ij} is the exchange integral between spins i and j. In equation 2.17, all spins are *Heisenberg spins* which are free to point in all directions.

Direct Exchange

The exchange integral, J, represents the overlap of the spatial wave functions of the two interacting electrons and exchange interaction as derived above only occurs in systems with direct orbital overlap, direct exchange. Direct exchange can describe formation of diatomic molecules such as H_2 where two hydrogen atoms form a bonding symmetric total spatial wave function. This reduces the kinetic energy of the electrons compared to an anti-bonding anti-symmetric total spatial wave function where the electrons cannot occupy the space between the atoms. Consequently, two hydrogen atoms will form the molecule H_2 with a triplet spin state.

In rare earth compounds the magnetic moment is carried by the 4f electrons which are highly localised, and the orbital overlap between neighbouring sites is therefore very small. The 3d orbitals in transition metal compounds are less localized than 4f electrons, but even in transition metal compounds, the exchange interaction is often mediated by other electrons in *indirect exchange*.

Indirect Exchange

Superexchange is the most important type of indirect exchange for ionic solids with transition metals. In superexchange, the magnetic interaction between two magnetic ions is mediated by a non-magnetic ion, typically oxygen. Here, the electrons are delocalized across the non-magnetic and magnetic ions, which lowers the kinetic energy similarly to the singlet state in a diatomic molecule. Superexchange therefore generally favours an antiferromagnetic (AFM) ground state where spins on the magnetic ions anti-align, but it can also result in a ferromagnetic (FM) ground state, where the spins align depending on the crystal symmetry and on the orbitals of the interacting electrons. Rare earth ions are too localized to interact directly with neighbouring oxygen atoms, but they can interact with the 5s, 5p and 5d electrons and which extent further in space and can mediate the indirect exchange between the rare earth ions. Despite variations in the physical interpretation, indirect exchange is typically well described by the Heisenberg Hamiltonian in equation 2.17.

Another type of indirect exchange interaction is the *itenerant exchange* or Ruderman-Kittel-Kasuya-Yosida (*RKKY interaction*) where the exchange interaction is mediated by conduction electrons. In the RKKY interaction, the exchange integral oscillates in space between FM and AFM interactions and the periodicity depends only on the Fermi wavevector, k_F,

$$J_{\mathrm{RKKY}} \propto \frac{\cos(2k_F r)}{r^3} \tag{2.18}$$

The oscillations are a result of the sharpness of the density of state distribution which results in ripples when Fourier transformed to real space. The interaction is long range because the conduction electrons which mediate the RKKY interaction are non-localised, but the interaction decays with r as a result of a finite mean free path of the conduction electrons. No metals are studied in this thesis, and the RKKY interaction is thus unable to describe the magnetic interactions in these systems.

Anisotropic Exchange

The *anisotropic exchange* or Dzyaloshinsky-Moriya (*DM interaction*) is a relativistic effect caused by the spin-orbit coupling. It leads to a term in the Hamiltonian,

$$\mathcal{H}_{\mathrm{DM}} = \mathbf{D} \cdot \mathbf{S_1} \times \mathbf{S_2}, \tag{2.19}$$

when acting between the two spins $\mathbf{S_1}$ and $\mathbf{S_2}$, and it therefore typically results in a canting of the spins or to the formation of magnetic skyrmions [72]. Furthermore, it is important to describe the magnetism in the quantum spin liquid candidate, $\mathrm{Na_4Ir_3O_8}$ [64], where Ir^{4+} occupy a hyperkagome lattice as described in chapter 6.

$\mathbf{D}$ is either parallel or perpendicular to the line connecting the spins $\mathbf{S_1}$ and $\mathbf{S_2}$ depending on the crystal symmetry, unless the crystal field has inversion symmetry with respect to the centre of the two spins in which case $\mathbf{D} = 0$.

2.2.2 Dipole-Dipole Interaction

A magnetic moment creates a long-range dipole field, and two magnetic moments, $\boldsymbol{\mu_1}$ and $\boldsymbol{\mu_2}$ separated by a distance, $\boldsymbol{r}$, has the internal dipolar interaction energy

$$\mathcal{H}_{\text{dip}} = \frac{\mu_0}{4\pi r^3}[\boldsymbol{\mu_1} \cdot \boldsymbol{\mu_2} - 3(\boldsymbol{\mu_1} \cdot \hat{\boldsymbol{r}})(\boldsymbol{\mu_2} \cdot \hat{\boldsymbol{r}})]. \tag{2.20}$$

The energy of the dipolar interaction is on the order 10-100 μeV which is less than 1 K, and exchange interactions, which are typically on of the order eV, will therefore typically completely dominate the magnetic structure and dynamics. However, in systems with very weak exchange interaction such as $\mathrm{Ho_2Ti_2O_7}$ and $\mathrm{Yb_3Ga_5O_{12}}$ which are studied in this thesis, dipolar interactions are very important and it is the dominant spin-spin interaction at least in the case of $\mathrm{Ho_2Ti_2O_7}$

2.2.3 Crystal field effects in rare earth crystals

This section contains a description of the *crystal field* interactions which is largely based on chapter 1.4 of ref. [39]. Crystal field interactions describe the interactions between a single ion and the electric field which is a result of the charge distribution of the surrounding ions. It is thereby a single ion effect that is independent of the magnetic state of neighbouring ions, and the resulting Hamiltonian is the sum of the crystal field contribution to the Hamiltonian of a single ion:

$$\mathcal{H}_{\text{CF}} = \sum_i \mathcal{H}_{\text{CF}}(i). \tag{2.21}$$

This is different from exchange interactions and dipole interactions that couple the magnetic states of two different sites.

The crystal field is typically described by the *Racah operators*, $\tilde{O}_l^m(J)$, which transform like spherical harmonics or *Stevens Operators*, $O_l^m(J)$, which transform like tesseral harmonics, according to:

$$\begin{aligned}\mathcal{H}_{\text{CF}} &= \sum_i \sum_{lm} A_{lm}\langle r^l\rangle \alpha_l \left(\frac{2l+1}{4\pi}\right)^{1/2} \tilde{O}_l^m(J) &(2.22)\\ &= \sum_i \sum_{lm} B_l^m O_l^m(J). &(2.23)\end{aligned}$$

Because the crystal field must be symmetric in the spatial coordinates x, y and z, it can only depend on even l. A_{lm} is the effective charge distribution of the surrounding ions projected into the Y_l^m-basis, and B_l^m are the Stevens parameters. α_l is the Stevens factor describing the form of the electronic charge cloud of the single ion and its sign describes planar or Ising anisotropy. The Stevens factors of $\mathrm{Dy^{3+}}$, $\mathrm{Ho^3}$ and $\mathrm{Yb^{3+}}$ are presented in table 2.2. The Stevens factors of $\mathrm{Yb^{3+}}$ are 1-2 orders of magnitude larger than the Stevens

Ion^{3+}	$\alpha_2 \cdot 10^2$	$\alpha_4 \cdot 10^4$	$\alpha_6 \cdot 10^6$
Dy	-0.6349	-0.5920	1.035
Ho	-0.2222	-0.3330	-1.294
Yb	3.175	- 17.32	148.0

Table 2.2: Stevens factors of rare earth ions which are most relevant to this project from ref. [39]. A complete list is found in chapter 1.4 of ref. [39].

factors for Ho^3 and Dy^{3+} showing the importance of crystal field effects in compounds with Yb^{3+}.

In equations 2.22 and 2.23, the electrons are assumed to be sufficiently localized that there is no orbital overlap between the 4f orbitals and orbitals of other ions, which is typically a good approximation for rare earth ions. The crystal field is described with Stevens operators as defined in equation 2.23 in the rest of the thesis due to its compact formulation.

The challenge in crystal field calculations is to determine the Stevens parameters, B_l^m, because the complete charge distribution of all electrons and nuclei surrounding the ion is rarely known. One approach is to use the point-charge model, where an adjustable point charge is placed on each site or the parameters are fitted to experimental data. Very often, the result is obtained from a combined method where an initial suggestion is calculated which is adjusted based on a fit to experimental data.

The crystal field will often result in a *spin anisotropy* which creates easy axes or easy planes where the spins have reduced energy. Systems with very strong easy axes are referred to as *Ising systems*, where spins are restricted to point along a single quantization axis. In some systems, the crystal field results in a global easy axis where a single axis is defined for the entire crystal. However, in many systems, including those studied in this thesis, a local easy axis is defined based on the local crystal environment. This is further discussed in chapters 6 and 5.

2.2.4 Zeeman Interaction

The Zeeman Interaction, $\mathcal{H}_{\text{zee}}$, describes the interaction between a magnetic moment $\boldsymbol{\mu}$ and an externally applied magnetic field, $\mathbf{B}$,

$$\mathcal{H}_{\text{zee}} = -\sum_i \boldsymbol{\mu_i} \cdot \mathbf{B}. \tag{2.24}$$

The Zeeman interaction gives rise to a splitting of the states based on their m quantum number which is the projection of the angular momentum onto the quantization axis along the applied field. For the triplet and singlet states which were described previously in the section, the triplet state is split into three states with m_S = -1, 0 and 1 respectively, and the non-degenerate singlet state is not affected by the external field because $S = 0$.

2.2.5 Curie-Weiss Temperature

In a system with interacting spins, the low field susceptibility does not follow the Curie law like a paramagnet, but the *Curie-Weiss law*,

$$\chi \propto \frac{1}{T - \theta_{\mathrm{CW}}}, \tag{2.25}$$

where the *Curie-Weiss temperature*, θ_{CW}, represents the total magnetic interactions. Equation 2.25 shows that θ_{CW} can be found from a linear fit to the inverse susceptibility. The magnitude of θ_{CW} describes the strength of the interactions, and non-frustrated systems will therefore have long-range magnetic order at temperatures $T < \theta_{\mathrm{CW}}$ as further discussed in the next section. The sign of θ_{CW} describes the type of interaction, where $\theta_{\mathrm{CW}} < 0K$ indicating FM interactions and $\theta_{\mathrm{CW}} > 0K$ indicate AFM interactions.

In most systems, NN interactions are much stronger than interactions between ions which are further apart, and θ_{CW} is therefore often assigned to directly to represent the NN interactions. However, in systems with very weak NN interactions such as $\mathrm{Yb_3Ga_5O_{12}}$, it does not necessarily represent directly the NN interactions as is it discussed in chapter 6.

2.3 Frustrated Magnetism

Generally, systems order when the temperature is decreased below an energy which corresponds to the interactions in the system, but in a frustrated system a macroscopically large amount of degenerate ground states form a ground state manifold and thereby prevents order at this temperature. Instead, the system enters a phase of correlated disorder where the system is correlated on short length scales, but disordered on long length scales [40].

This thesis involves frustration within the field of magnetism, but frustrated systems are found within scientific fields as different as stellar nuclear matter [58], social dynamics [2] and protein folding [1]. Magnetic systems are often used as model systems because the interactions are easily tuned with external parameters such as temperature, field and pressure or even chemically by replacing the magnetic ions in the system and it is therefore more accessible experimentally and theoretically compared to other fields of frustration. Despite decades of research in frustrated magnetism, the field continues to surprise with the discoveries of emergent states of matter [56], topological order [15] and quantum entangled states [62].

Following the convention in ref. [40], frustrated compounds are divided into two categories: they are either overconstrained or underconstrained. In an *overconstrained* frustrated system, the system is unable to simultaneously satisfy competing interactions whilst obeying the anisotropy and lattice geometry. A generic example is AFM coupled collinear Ising spins on a triangle as shown in figure 2.1. It is not possible for these spins to form a *Néel state* where all spins are anti-parallel to its nearest neighbour (NN) spins and in this way minimise the AFM spin-spin-interactions whilst respecting the Ising anisotropy and the triangular lattice geometry. These systems are also called geometrically frustrated systems to underline the importance of the lattice geometry. A single triangle of AFM coupled Ising spins has a 6-fold degenerate ground state and the ground state of a real triangular lattice with 10^{23} spins is thus macroscopically degenerate.

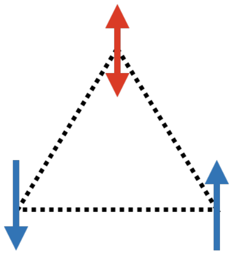

Figure 2.1: AFM coupled collinear Ising spins on a triangle. It is not possible to obtain a Néel state where all spins are anti-parallel to its nearest neighbour spins. The blue spins are anti-aligned, but the third spin (red) is parallel to one spin and anti-parallel to the other spin regardless of its orientation.

Spin ice is an example of an *underconstrained* frustrated system where a macroscopic amount of ground states all minimize the interaction energy whilst obeying the lattice geometry and anisotropy and as a result, there is no unique ordering pattern. The field has been heavily studied and is well presented in several reviews including refs. [15, 23, 28] and the classical spin ice compound $\mathrm{Ho_2Ti_2O_7}$ is described in chapter 5.

2.3.1 Experimental Signatures

The most obvious experimental feature in frustrated compounds is the absence of long-range magnetic order for temperatures $T < \theta_{\mathrm{CW}}$ when the temperature is lower than the energy scale of the interactions in the system. The amount of frustration in a system is often described by the *frustration index*, f, which describes the ratio between the ordering temperature, T_C and θ_{CW},

$$f = \left| \frac{\theta_{\mathrm{CW}}}{\mathrm{T}_C} \right|, \tag{2.26}$$

[45]. f thereby defines the temperature range of the correlated disordered phase, $T_c < T < \theta_{\mathrm{CW}}$.

An experimental signature in the correlated disordered phase is diffuse scattering where the system is characterized by broad, diffuse features in reciprocal space similarly to those found in a liquid. The similarity in scattering profile motivates the term *spin liquid* for a magnetically correlated disordered phase.

Spin liquids are generally divided into classical spin liquids, sometimes referred to as coorporative paramagnets, which order at a finite temperature, T_C, and quantum spin liquids.

In a quantum spin liquid, quantum fluctuations will prevent long range magnetic ordering and spontaneous symmetry breaking of the system even at T = 0 K. It is a truly quantum mechanical state where long range entanglement of the spins ensure that the total wave function is not a product of the wavefunctions of the individual spins thereby enabling non-local and fractional excitations [62, 11, 8]. The field of quantum spin liquids is currently developing rapidly both theoretically and especially experimentally searching for a realisation of a quantum spin liquid. The experimental signature of fractionalized excitations are diffuse continua in reciprocal space, but there is no experimental technique which directly measures quantum entanglement which is the main reason why a quantum spin liquid has not yet been found experimentally despite a large number of quantum spin liquid candidates such as $Na_4Ir_3O_8$ [64], $Yb_2Ti_2O_7$ [29, 41], $Tb_2Ti_2O_7$ [51] and Herbertsmithite, $ZnCu_3(OH)_6Cl_2$ [33].

Chapter 3

Neutron Scattering

Neutron scattering is a widely used technique to charactize the structure and dynamics of a vast range of materials. The following is largely based on the desriptions in ref. [46].

3.1 Motivation

Neutron scattering is a complimentary technique to other types of diffraction and spectroscopy especially using X-rays. X-ray sources are many orders of magnitude more intense than neutron sources, and X-rays interact more strongly with materials than neutrons and measurements with X-rays are therefore typically fast and have high counting statistics compared to neutron scattering experiments. However, neutron scattering has a number of advantages compared to X-ray scattering.

One advantage is exactly the weak neutron interaction with matter. This allows the neutrons to measure the sample bulk while surface effects are relatively weak. Bulk behaviour is typically easier to simulate theoretically and quantitative simulations of neutron scattering experiments is therefore often possible. In addition, the weak neutron interaction with matter allows the usage of bulky sample environment such as cryostats, magnets and pressure cells. Finally, it enables measurements at temperatures $T < 1$ K, which is not possible to reach in X-ray experiments to the knowledge of the author, due to radiation heating of the sample.

Neutrons interact with the nuclei in the sample with the strong nuclear force and with electrons in a sample with the electromagnetic force. This enable direct measurements of both the nuclear and magnetic structure of the sample, especially with the application of polarisation analysis which is further described in section 3.2.4.

Neutron scattering experiments are typically performed with cold or thermal neutrons which have wavelengths 0.6-40 Å in compliance with typical interatomic distances in most solids. The wavelengths correspond to energies in the range 0.05-200 meV where most structural and magnetic excitations occur which enables measurements of both structure and dynamics with the same experimental setup.

One final advantage of neutron scattering is its dependence on atomic elements and isotopes. The scattering probability, the *cross section*, of X-rays increases almost linearly with atomic number and X-rays therefore mostly scatter from heavy elements while light elements such as hydrogen are difficult to probe with X-rays. In contrast, the cross section of neutrons does not vary systematically with atomic number or even isotope. For instance, hydrogen, ^{1}H, has a coherent neutron scattering cross section of 1.7 barns, while deuterium, ^{2}H, has a coherent neutron scattering cross section of 5.6 barns. Chemical replacement of hydrogen with deuterium therefore allows studies of selected parts a molecule which is commonly used in soft matter science.

3.2 Principles in Neutron Scattering

Neutron scattering describes the event where an incoming neutron beam with initial wave vector $\mathbf{k}_i$ scatter from a sample volume as illustrated in figure 3.1. The neutrons scatter into all 4π directions, but only the neutrons which scatter into the area dA covering the solid angle dΩ with wave vector $\mathbf{k}_f$ are detected.

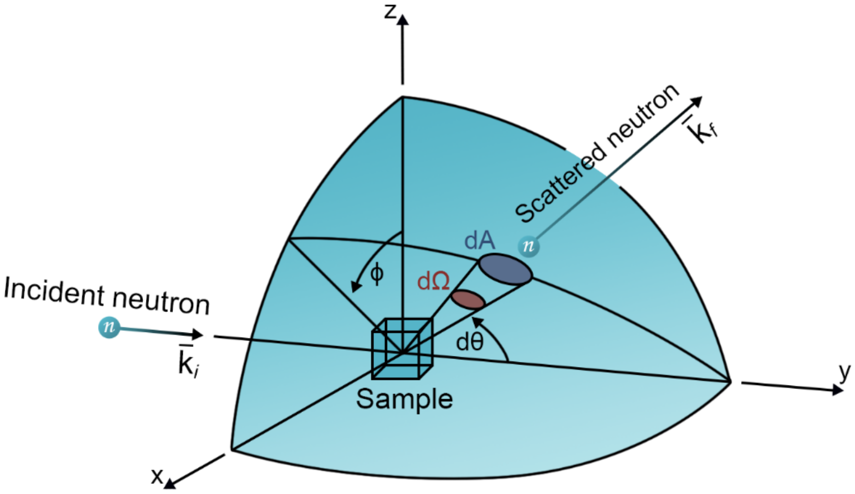

Figure 3.1: Schematic description of a scattering event where an incident (incoming) neutron beam scatter from a sample to a scattered (final) neutron beam into solid angle dΩ. Figure from [46].

In elastic scattering, where $|\mathrm{k_i}| = |\mathrm{k_f}| = \mathrm{k}$, interference between scattering from different nuclei and spins in the sample reveal nuclear and magnetic structure of the sample. Inelastic scattering, where an energy $\hbar\omega$ is transferred to the sample, probes the dynamics of the sample where the most commonly studied excitations are phonons and magnons.

The measured intensity in a neutron scattering experiment, the structure factor, S($\mathbf{Q}, \omega$) is defined by the *scattering cross section*, $\frac{d\sigma}{d\Omega}$ except for a factor of k_f/k_i which is unity in the case of the elastic scattering. Derivations of the expressions for the scattering cross section are long and only the results are stated here. The derivations are found in [65, 46].

3.2.1 Scattering Vector

Figure 3.2 describes an elastic scattering event where neutrons of wave vector $\mathbf{k_i}$ scatter an angle, 2θ, into the wave vector $\mathbf{k_f}$, however the defintion of $\mathbf{Q}$ is not limited to the elastic range. The scattering vector, $\mathbf{Q} = \mathbf{k_i} - \mathbf{k_f}$, yielding the relation,

$$Q = \mathrm{k}_i^2 - \mathrm{k}_f^2 - 2\mathrm{k}_i\mathrm{k}_f \cos(2\theta), \tag{3.1}$$

and in elastic scattering, this simplifies to

$$Q = 2\mathrm{k}\sin(\theta). \tag{3.2}$$

When the neutrons scatter from crystalline materials, which is the case for all materials in this thesis, the Bragg condition further implies

$$Q = \frac{2\pi}{d}, \tag{3.3}$$

where d is the lattice spacing orthogonal to Q. As a result, equation 3.3 and 3.2 relates the scattering angle with the crystalline structure, and they are thereby some of the basic equations in neutron scattering.

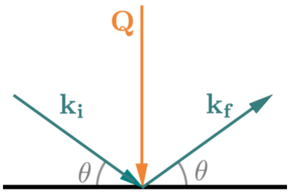

Figure 3.2: Schematic description of an elastic scattering event. Incoming neutrons of wave vector $\mathbf{k_i}$ interact with a sample and is scattered an angle, 2θ, and is described by the wave vector $\mathbf{k_f}$. The scattering vector, $\mathbf{Q}$ is also defined.

3.2.2 Static Structure Factor

In a neutron scattering experiment, the detector covers a certain angle, $d\Omega$, and the relevant quantity is therefore the probability of scattering neutrons with incoming flux Ψ into this solid angle. For elastic scattering, this gives the differential cross section,

$$\frac{d\sigma}{d\Omega} = \frac{1}{\Psi}\frac{W_{i\to f,d\Omega}}{d\Omega} = S(\mathbf{Q}), \tag{3.4}$$

where S(**Q**) is the static structure factor. The probability, W, of scattering from initial state, $|\psi_i\rangle$, to final state, $|\psi_f\rangle$, through the interaction potential, $\hat{V}$ into a solid angle dΩ, is described by *Fermi's Golden Rule*,

$$W_{i\to f,d\Omega} = \frac{k_f m_n}{(2\pi)^2\hbar^3} |\langle\psi_i|\,\hat{V}\,|\psi_f\rangle|^2 d\Omega, \tag{3.5}$$

where $m_n = 1.675 \cdot 10^{-27}$ kg is the neutron mass. This gives an expression for the differential cross section,

$$\frac{d\sigma}{d\Omega} = \frac{k_f}{k_i}\left(\frac{m_n}{2\pi\hbar^2}\right)^2 |\langle\psi_i|\,\hat{V}\,|\psi_f\rangle|^2, \tag{3.6}$$

where the factor $k_f/k_i = 1$ in the case of elastic scattering.

Nuclear Static Structure Factor

In nuclear scattering, the neutrons interact with the atomic nuclei through the strong nuclear force which is very short ranged, and the interaction potential is therefore well approximated by a delta function potential known as the Fermi pseudo-potential,

$$V_N(\mathbf{r}) = \frac{2\pi\hbar^2}{m_n}\sum_j b_j\delta(\mathbf{r}-\mathbf{R_j}), \tag{3.7}$$

where $\mathbf{R_j}$ is the position of the j'th nucleus. The nuclear *scattering length*, b$_j$ depends on both atomic number and isotope and describes the probablity of *coherent* scattering on a specific nuclei. In the event of coherent scattering from a single nucleus indexed j,

$$\left.\frac{d\sigma}{d\Omega}\right|_{\mathrm{coh}}^{\mathrm{N}} = |b_j|^2. \tag{3.8}$$

Coherent scattering from a system of nuclei depends on **Q** and describes correlations in the material. *Nuclear incoherent scattering* describes the stochastic deviation from the average scattering length, b$_j$ and it is a result of element and isotope disorder and temporal variations in the nuclear spin. Nuclear incoherent scattering gives a constant contribution in all directions which in most cases acts as a background. However, we have used the strong incoherent scattering from a vanadium sample, to calibrate the detector efficiencies before experiments at the neutron scattering instruments D7 and CNCS which are described in sections 3.3 and 3.4 respectively. Furthermore, incoherent scattering is only elastic, and it thereby shows the elastic energy resolution of the instrument.

The differential scattering cross section for nuclear elastic scattering from a crystalline material is found by inserting the Fermi pseudo-potential in equation 3.7 into equation 3.6. The derivation is performed in [46], and gives the result

$$\left.\frac{d\sigma}{d\Omega}\right|_{\mathrm{coh}}^{\mathrm{N}} = N\frac{(2\pi^2)}{V_0}e^{-2W}|F_N(\mathbf{Q})|^2\sum_\tau \delta(\mathbf{Q}-\tau), \tag{3.9}$$

Where N is the amount of unit cells in the system and $(2\pi)^3/V_0$ is the volume of the Brillouin zone. Thermal fluctuations in the nuclear positions are described by the Debye-Waller factor, $\exp\{-2W\} = \exp\{\langle\mathbf{Q}\cdot\boldsymbol{\mu}\rangle^2\}$, where $\boldsymbol{\mu}$ is the mean displacement from the average nuclear position. The reciprocal lattice vector, $\boldsymbol{\tau}$, describes the atomic positions and is generally described by the *Miller indices*, h, k and l, and the primitive vectors of the reciprocal lattice, $\mathbf{a}^*, \mathbf{b}^*$ and $\mathbf{c}^*$, according to $\boldsymbol{\tau} = h\mathbf{a}^* + k\mathbf{b}^* + l\mathbf{c}^*$. Finally, the nuclear structure factor, $F_N(\mathbf{Q})$, is given by

$$F_N(\mathbf{Q}) = \sum_j b_j \exp(i\boldsymbol{Q}\cdot\mathbf{R_j}), \tag{3.10}$$

where $\mathbf{R_j}$ is the position of the jth nucleus within the unit cell.

Magnetic Static Structure Factor

The neutron has a magnetic moment,

$$\boldsymbol{\mu} = \gamma\mu_N\boldsymbol{\sigma}, \tag{3.11}$$

where $\gamma = -1.9130$ is the neutron magnetogyric ratio, $\mu_N = e\hbar/2m_p = 5.0508\cdot 10^{-27}$ J/T is the nuclear magneton and $\boldsymbol{\sigma}$ consists of the three Pauli spin matrices. The neutron magnetic moment interacts directly with the magnetic field created by unpaired electrons, which enables magnetic neutron scattering.

The interaction potential for magnetic scattering, which is inserted in equation 3.6 in order to derive the differential cross section, describes the Zeeman interaction between the magnetic moment of the neutron, $\boldsymbol{\mu}$, and the magnetic dipole field created by an unpaired electron of spin $\mathbf{s_j}$ at position $\mathbf{r}_j$,

$$\hat{V_{\text{mag}}} = \sum_j \boldsymbol{\mu}\cdot\mathbf{B}_j = \frac{\mu_0}{4\pi} g\mu_B\gamma\mu_N \sum_j \boldsymbol{\sigma}\cdot\nabla\times\left(\frac{\mathbf{s_j}\times(\mathbf{r}-\mathbf{r_j})}{|\mathbf{r}-\mathbf{r_j}|^3}\right), \tag{3.12}$$

where $r_0 = e^2\mu_0/4\pi m_e = 2.8179$ fm, is the classical electron radius and $g = 2.0023$ is the electronic magneticogyric ratio also known as the g-factor and $\mu_B = e\hbar/(2m_e) = 9.2741\cdot 10^{-24}$ J/T is the *Bohr magneton*.

The differential scattering cross section for magnetic elastic scattering from a crystalline material is found by inserting this potential into equation 3.6. The derivation is performed in [46], and gives the result

$$\left.\frac{d\sigma}{d\Omega}\right|_{\text{coh}}^{\text{mag}} = N\frac{(2\pi^2)}{V_0}e^{-2W}|F_M(\mathbf{Q})|^2\sum_\tau \delta(\mathbf{Q}-\tau-\mathbf{Q'}). \tag{3.13}$$

In many systems, the magnetic unit cell differs in size compared to the structural unit cell which motivates the definition of the magnetic ordering vector, $\mathbf{Q'}$. The magnetic structure factor, $F_M(\mathbf{Q})$, is given by

$$F_M(\mathbf{Q}) = \sum_j b_{M,j} \exp(i\boldsymbol{Q} \cdot \mathbf{R_j}), \tag{3.14}$$

where the summation is performed over the magnetic unit cell. There is strong similarity between the expressions for nuclear and magnetic scattering in equations 3.9 and 3.13, but the complex form of the interaction potential is reflected in the magnetic scattering length, $b_{M,j}$, which is described by,

$$b_{M,j} = \gamma r_0 F(\mathbf{Q}) \frac{g}{2} \boldsymbol{\sigma} \cdot \boldsymbol{s_{j,\perp}}. \tag{3.15}$$

Equation 3.15 shows that magnetic scattering only depends on the electron spin components perpendicular to $\mathbf{Q}$, $\boldsymbol{s}_\perp = \hat{\boldsymbol{Q}} \times (\mathbf{s} \times \hat{\boldsymbol{Q}})$. In magnetic scattering, the neutrons scatter from electrons which are much less localised than nuclei. The scattering probability therefore depends on the Fourier transformed charge distribution, ρ, of the unpaired electrons, known as the magnetic form factor, $F(\mathbf{Q})$,

$$F(\mathbf{Q}) = \int \exp(i\mathbf{Q} \cdot \mathbf{r}) \rho(\mathbf{r}) d^3\mathbf{r}, \tag{3.16}$$

which decays homogeneously with $|\mathbf{Q}|$. Generally, the magnitude of the magnetic and nuclear scattering lengths is similar which enables simultaneous measurements of both nuclear and magnetic scattering. However, as a result of the form factor decay, magnetic neutron scattering has highest intensity for low $|\mathbf{Q}|$ while nuclear neutron scattering has similar intensity for all $|\mathbf{Q}|$. The total coherent scattering probability is described by the sum of the nuclear and magnetic scattering lengths,

$$\left.\frac{d\sigma}{d\Omega}\right|_{\text{coh}} = \left| \sum_j (b_j + b_{j,m}) \exp(i\boldsymbol{Q} \cdot \mathbf{r_j}) \right|^2 . \tag{3.17}$$

In the case of unpolarised neutrons, the cross terms involving both nuclear and magnetic scattering lengths cancel, and

$$\left.\frac{d\sigma}{d\Omega}\right|_{\text{coh}} = \left.\frac{d\sigma}{d\Omega}\right|_{\text{coh}}^{\text{N}} + \left.\frac{d\sigma}{d\Omega}\right|_{\text{coh}}^{\text{mag}} . \tag{3.18}$$

However, they do not cancel when polarised neutrons are used and the expressions therefore become more complex. The separation of the magnetic and nuclear contribution to the scattering with the use of polarisation analysis is described in section 3.2.4.

3.2.3 Dynamic Structure Factor

This thesis mostly focuses on elastic scattering, but we have also performed one inelastic neutron scattering experiment. In inelastic scattering, the neutrons scatter from an initial state, $|\psi_i\rangle$ with energy $E_i = \frac{(\hbar k_i)^2}{2m_n}$ into the final state $|\psi_f\rangle$ with energy $E_f = \frac{(\hbar k_f)^2}{2m_n}$ through the interaction potential $\hat{V}$. The neutron energy transfer is defined as $\hbar\omega = E_i - E_f$. The double differential cross section for inelastic neutron scattering strongly resembles the elastic expression in equation 3.6, but a delta function is included to ensure energy conservation and the prefactor $k_f/k_i \neq 1$, yielding

$$\frac{d^2\sigma}{d\Omega dE_f} = \frac{k_f}{k_i}\left(\frac{m_n}{2\pi\hbar^2}\right)^2 |\langle E_i\psi_i|\,\hat{V}\,|\psi_f E_f\rangle|^2\delta(\hbar\omega + E_i - E_f) = \frac{k_f}{k_i}S(\mathbf{Q},\omega), \qquad (3.19)$$

where $S(\mathbf{Q},\omega)$ is the dynamic structure factor. In the calculations, the interaction potentials are identical to the potentials used for the static structure factors, the pseudo Fermi potential in equation 3.7 and the Zeeman term in equation 3.12 for nuclear and magnetic scattering respectively. In the derivations, the nuclei are allowed to move and as a result, the expressions are more complex. The derivations and results of both nuclear and magnetic dynamic structure factor are shown in [46].

3.2.4 Polarisation Analysis

Polarisation analysis enables separation of the magnetic, nuclear and spin incoherent contributions to the total scattering. In a neutron scattering experiment which uses longitudinal polarisation analysis, also known as XYZ polarisation analysis, the initial neutrons are polarised, along either x, y or z as defined in figure 3.3. The polarisation of the scattered neutrons is also measured, and spins which have flipped polarisation are result in spin flip (indexed SF) scattering, while spins which have retained their initial polarisation result in non-spin flip (indexed NSF) scattering.

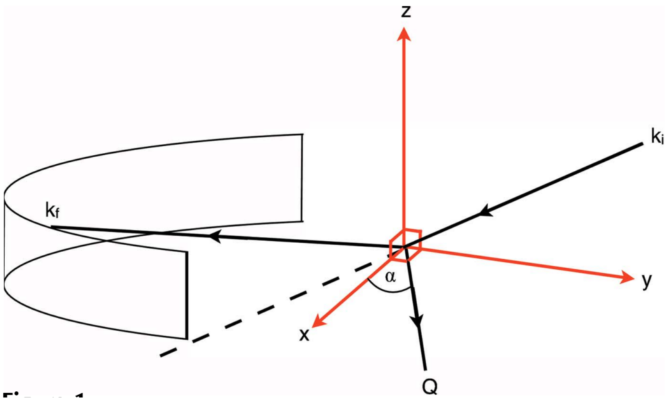

Figure 3.3: Scattering geometry used in polarisation analysis. Figure from [69]. The polarised neutron beam enters the instrument from the neutron guide. The neutron polarisation is then rotated into either the x, y or z direction before the neutrons scatter from the sample. When the scattering plane is spanned by the xy-plane, the angle, α, is used to separate the nuclear, magnetic and spin-incoherent scattering contributions.

The nuclear contribution (indexed N), which includes both coherent and isotope incoherent scattering, only appears in non-spin flip scattering. Oppositely, the nuclear-spin-incoherent (indexed si) and magnetic coherent (indexed mag) scattering appears in both the spin flip and non-spin flip scattering.

When the scattering plane equals the xy-plane in figure 3.3, it is possible to separate the three contributions to the total scattering based on the angle, α, between $\mathbf{Q}$ and the x-axis according to

$$\left(\frac{d\sigma}{d\Omega}\right)_x^{\mathrm{NSF}} = \frac{1}{2}\sin^2\alpha\left(\frac{d\sigma}{d\Omega}\right)_{\mathrm{mag}} + \frac{1}{3}\left(\frac{d\sigma}{d\Omega}\right)_{\mathrm{si}} + \left(\frac{d\sigma}{d\Omega}\right)_{\mathrm{N}}, \tag{3.20}$$

$$\left(\frac{d\sigma}{d\Omega}\right)_x^{\mathrm{SF}} = \frac{1}{2}(\cos^2\alpha + 1)\left(\frac{d\sigma}{d\Omega}\right)_{\mathrm{mag}} + \frac{2}{3}\left(\frac{d\sigma}{d\Omega}\right)_{\mathrm{si}}, \tag{3.21}$$

$$\left(\frac{d\sigma}{d\Omega}\right)_y^{\mathrm{NSF}} = \frac{1}{2}\cos^2\alpha\left(\frac{d\sigma}{d\Omega}\right)_{\mathrm{mag}} + \frac{1}{3}\left(\frac{d\sigma}{d\Omega}\right)_{\mathrm{si}} + \left(\frac{d\sigma}{d\Omega}\right)_{\mathrm{N}}, \tag{3.22}$$

$$\left(\frac{d\sigma}{d\Omega}\right)_y^{\mathrm{SF}} = \frac{1}{2}(\sin^2\alpha + 1)\left(\frac{d\sigma}{d\Omega}\right)_{\mathrm{mag}} + \frac{2}{3}\left(\frac{d\sigma}{d\Omega}\right)_{\mathrm{si}}, \tag{3.23}$$

$$\left(\frac{d\sigma}{d\Omega}\right)_z^{\mathrm{NSF}} = \frac{1}{2}\left(\frac{d\sigma}{d\Omega}\right)_{\mathrm{mag}} + \frac{1}{3}\left(\frac{d\sigma}{d\Omega}\right)_{\mathrm{si}} + \left(\frac{d\sigma}{d\Omega}\right)_{\mathrm{N}}, \tag{3.24}$$

$$\left(\frac{d\sigma}{d\Omega}\right)_z^{\mathrm{SF}} = \frac{1}{2}\left(\frac{d\sigma}{d\Omega}\right)_{\mathrm{mag}} + \frac{2}{3}\left(\frac{d\sigma}{d\Omega}\right)_{\mathrm{si}}. \tag{3.25}$$

$$\tag{3.26}$$

This allows for two different expressions for the magnetic scattering which can be derived either from the spin flip or the non-spin flip scattering:

$$\left(\frac{d\sigma}{d\Omega}\right)_{\mathrm{mag}} = 2\left(\frac{d\sigma}{d\Omega}\right)_x^{\mathrm{SF}} + 2\left(\frac{d\sigma}{d\Omega}\right)_y^{\mathrm{SF}} - 4\left(\frac{d\sigma}{d\Omega}\right)_z^{\mathrm{SF}}, \tag{3.27}$$

$$\left(\frac{d\sigma}{d\Omega}\right)_{\mathrm{mag}} = 4\left(\frac{d\sigma}{d\Omega}\right)_z^{\mathrm{NSF}} - 2\left(\frac{d\sigma}{d\Omega}\right)_x^{\mathrm{NSF}} - 2\left(\frac{d\sigma}{d\Omega}\right)_y^{\mathrm{NSF}}. \tag{3.28}$$

The nuclear and nuclear-spin-incoherent scattering contributions are derived from the total spin flip (TSF) and total non-spin flip (TNSF) cross sections according to

$$\left(\frac{d\sigma}{d\Omega}\right)_{\mathrm{N}} = \frac{1}{6}\left[2\left(\frac{d\sigma}{d\Omega}\right)_{\mathrm{TNSF}} - \left(\frac{d\sigma}{d\Omega}\right)_{\mathrm{TSF}}\right], \tag{3.29}$$

$$\left(\frac{d\sigma}{d\Omega}\right)_{\mathrm{si}} = \frac{1}{2}\left(\frac{d\sigma}{d\Omega}\right)_{\mathrm{TSF}} - \left(\frac{d\sigma}{d\Omega}\right)_{\mathrm{mag}}. \tag{3.30}$$

In samples without magnetic scattering, the nuclear and nuclear-spin-incoherent scattering contributions can be extracted from the spin-flip and non-spin flip scattering measurements along a single axis, which is known as Z-polarisation analysis.

Experiments where polarisation analysis is applied are especially sensitive to *multiple scattering* events, where a single neutron scatters several times in the sample. This is seen from the event where a neutron spin is flipped twice, in which case it is detected as non-spin-flip scattering in stead of spin-flip scattering. Multiple Bragg scattering is less likely when cold neutrons are used, which is the case at D7, but it is also important to consider the size and shape of the sample. Another limitation of XYZ polarisation analysis is the study of FM medium-range or long-range correlated materials since FM domains within the sample will depolarise the neutron beam.

3.3 D7

The D7 instrument at the Institute Laue-Langevin is a diffuse scattering instrument with polarisation analysis. We have used XYZ polarisation analysis for all 3 experiments performed at the instrument in this work. Figure 3.4 shows an overview of the D7 instrument. Key parts of the instrument are described here, while a more complete overview of the instrument is given in [69].

The incoming beam is polarised using a focusing supermirror polariser, which reflects one spin state and transmit the other, followed by a Mezei spin flipper. The Mezei spin flipper applies a field perpendicular to the initial neutron polarization and a field which is perpendicular to the initial neutron polarization which enables a 180 degrees spin flip of the neutron and a reversal of the neutron polarisation. The spin flipper is followed by a set of orthogonal coils which rotate the incoming neutron beam polarisation adiabatically into the x, y or z directions in order to polarise the neutron beam along three orthogonal directions.

A magnetic guide field of 1-2 mT inside the instrument ensures that the neutron polarisation is maintained through the instrument. The polarisation of the scattered neutrons is selected with polarisation analyser supermirrors in front of the detectors which cover -10° to +155° within the scattering plane (horizontal scattering) and ±10° outside the scattering plane (vertical scattering). It is possible to use the instrument as an inelastic time-of-flight spectrometer, like the CNCS instrument, but for the experiments presented in this work, the instrument was used as a diffuse scattering diffractometer with the Fermi chopper before the sample removed. As a result, the measured quantity is the energy integrated structure factor, $S(\mathbf{Q})$, which is not identical to the true static structure factor described in section 3.2.2, since it contains an unresolved dynamic contribution from $S(\mathbf{Q}, \omega)$. However, the dynamic contribution is generally several orders of magnitude smaller the static contribution to the neutron scattering, and the energy integrated $S(\mathbf{Q})$ is often interpreted as the elastic, static signal.

Before all three experiments at D7, we have performed a quartz measurement. Quartz is an amorphous silica which only has nuclear scattering and therefore no spin-flip scattering. A quartz measurement is therefore used to measure the polarisation error which origins from the polariser, the flipper and the analyser. The quartz measurement results in a *flipping* *ratio* for each detector, which is used to correct the measured spin-flip and non-spin-flip scattering.

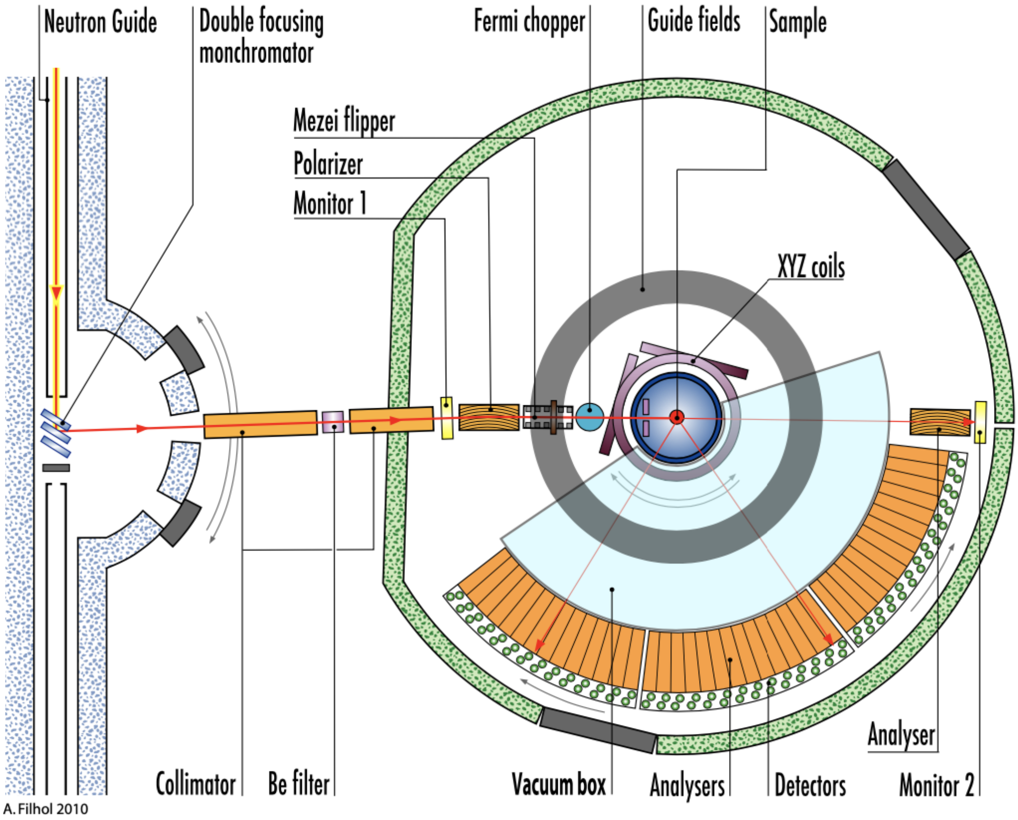

Figure 3.4: Overview of the D7 instrument. Figure from [69].

3.4 CNCS

The cold neutron chopper spectrometer (CNCS) at the Spallation Neutron Source is a *Time-of-flight* instrument with a direct geometry. A time-of-flight instrument uses the neutron flight time to select its energy as opposed to the energy associated with a scattering angle from the mirror monochromator at scattering instruments such as D7. At a time-of-flight instrument, the choppers which create short pulses of well defined energy therefore determines the flux and energy resolution of the instrument. At the CNCS, it is possible to tune the energy resolution from 1.2-10 % of the incident neutron energy.

Figure 3.5 shows an overview of the instrument. Key parts of the instrument are described here, while a more complete overview of the instrument is given in [21]. The neutron guide is curved in order to remove any background from high energy and thermal neutrons. The figure shows four choppers before the sample. First, a Fermi chopper shapes the incoming neutron beam. Then, two bandwidth choppers ensures that there is no overlap between the fastest and slowest neutrons in two adjacent pulses. Finally, a double disk chopper with two counter-rotating disks selects the incoming neutron energy from the phase difference between the double disk chopper and the Fermi chopper.

The scattered neutrons are detected in a scattering range -50° to +135° horizontal scattering and ±16° vertical scattering. The detection time of the neutrons within each pulse shows the energy transfer to the sample, and the measured quantity in a neutron scattering experiment is therefore the dynamic structure factor S($\mathbf{Q}$, ω) described in section 3.2.3.

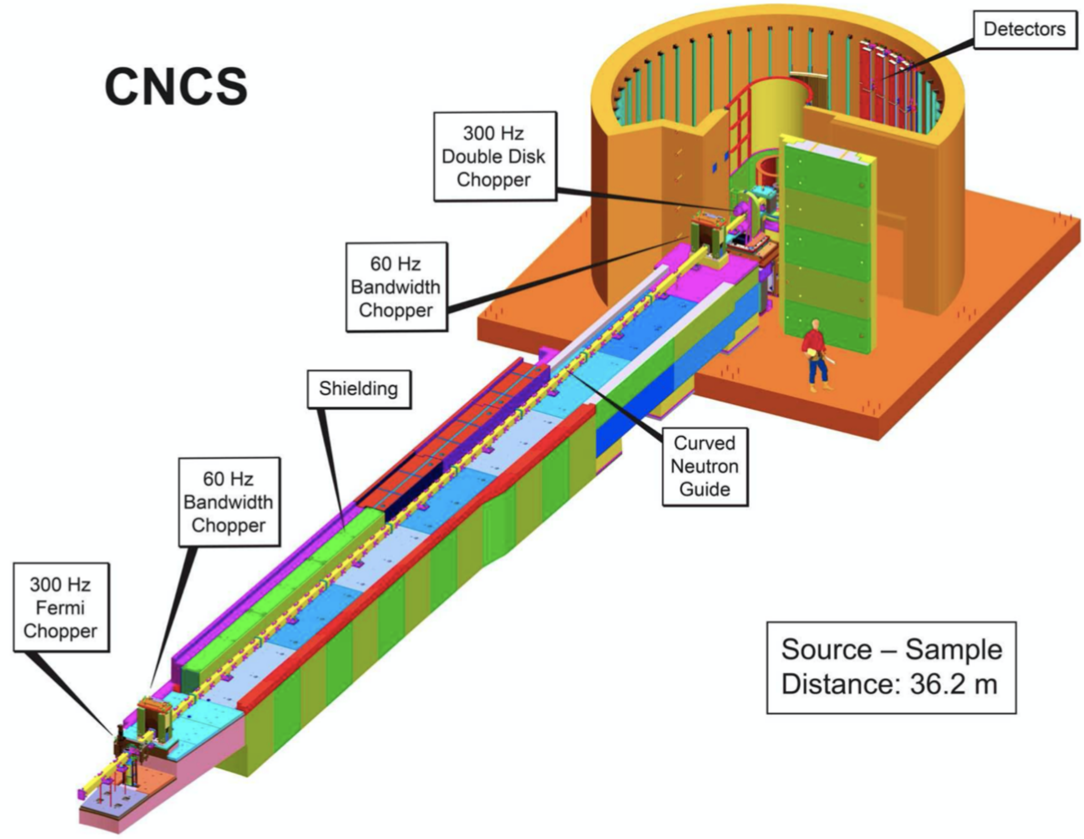

Figure 3.5: Overview of the CNCS instrument. Figure from [21].

Chapter 4

Uniaxial Pressure Cell

4.1 Introduction

Application of an external pressure offers an opportunity to perturb the balance between distance dependent interactions such as magnetic exchange interactions, dipolar interaction and crystal field anisotropy. This can drive materials, in general, into highly unconventional states of matter and is the case, in particular, for strongly correlated and frustrated systems. Indeed, Biesner et al. recently suggested that pressure offers a convenient way of tuning compounds in order to find quantum spin liquids and tuned quantum phase transitions [8]. In addition, external pressure simulates chemical pressure in a controlled and tunable way. Indeed, hydrostatic pressure has been used to study the quantum spin liquid candidates $Tb_2Ti_2O_7$ [51] and $Yb_2Ti_2O_7$ [41] and clarify the strong impact of even small levels of impurities on the ground state and dynamics of the compounds.

Hydrostatic pressure changes all bond lengths equally for cubic systems, but uniaxial pressure allows for an asymmetric distortion of the lattice thereby enabling direct tuning of certain bond lengths. This was recently described by Umeo et al. [71] who were able to increase or decrease the ordering temperature of the geometrically frustrated compound YbCuGe through the application of uniaxial pressure along different crystallographic directions. In contrast, the application of hydrostatic pressure did not affect the ordering temperature. The compound was studied with magnetisation measurements and specific heat measurements.

Similarly, Mirebeau et al. saw no pressure induced order when applying 6 GPa hydrostatic pressure to the classical spin ice compound $Ho_2Ti_2O_7$ (HTO) [50]. However, even low uniaxial pressures around 0.35 GPa do induce changes in HTO [19, 20] as described in this chapter.

Hydrostatic pressure has become a standard part of the sample environment in many neutron facilities. Most commonly are liquid/gas pressure cells, where the pressures typically below 1 GPa is applied from an external compressor typically with helium as the medium since its freezing pressure is higher than any other gas/fluid [44], and it is therefore possible to vary the pressure in-situ and measure the pressure from the external compressor. However, helium is able to penetrate most compounds including many samples. In addition, this unfortunate property of helium increases the effect of even small leaks especially at low temperatures.

Clamped McWhan pressure cells are most commonly used for neutron scattering pressure experiments for hydrostatic pressures in the range 1-3 GPa. Here, a sample is loaded into a capsule, most frequently a thin-walled Al cylinder, together with a pressure transmitting medium, typically Fluorinert liquid. The force is applied to the capsule with an external press through a piston in a cylinder and the force is locked mechanically. The design is thereby simple and compact, but it is not possible to change the pressure in-situ. Often, the pressure is estimated from the applied pressure at room temperature, but in order to obtain an accurate value for the pressure, a pressure marker with known equation of state such as NaCl or Pb can be applied. *Diamond anvil cells* (DAC) such as the wide angle DAC at the SNS [32], are used when even higher hydrostatic pressures up to 20 GPa for sample volumes ≈ 0.5 mm^3 are required. The design resembles the McWhan clamp pressure cell, but the pressure is applied to the sample with two opposing diamond anvils which enables larger pressures, but also smaller sample volumes. The optical transparency of the diamond anvils enables a determination of the pressure from the shift in fluorescent lines of ruby (Cr-doped Al_2O_3) under pressure [44].

A uniaxial pressure cell, which is aimed at susceptibility and heat capacity studies, was reacently developed by Umeo et al. [71] for sample disks of 2 mm in diameter and 0.5 mm height. In this cell, the pressure is measured with an indium (In) disk by using the pressure dependence of the superconducting transition temperature of In metal. The superconducting transition was measured from the diamagnetic signal of ac magnetic susceptibility. However, In also yields a neutron scattering signal and the method is therefore not ideal for our setup.

Hicks et al. has developed a uniaxial pressure cell which is aimed for studies with X-ray and μSR [34], where the force is applied to needle shaped samples of 0.3 mm in diameter, 3 mm length with a piezo-electric strain gauge which allows for in-situ changes of the applied force. The force is measured from variations in the capacitance between two plates. This design is very promising, but it is not possible to easily increase the applied force and thus the sample volume which makes neutron scattering experiments with the cell highly challenging. Additionally, the non-uniform cell background and the sample volume is likely to be a challenge for neutron scattering studies of magnetically frustrated compounds.

We here describe a setup to apply uniaxial pressure to crystals in neutron scattering experiments. Such a device requires the following experimental aims to be met:

E1 Apply highest possible uniaxial pressure to single crystal samples.

E2 Reach lowest possible temperatures at the sample position ($T < 50$ mK)

E3 Enable diffuse neutron diffraction from the pressurized sample.

E4 Enable inelastic neutron scattering from the pressurized sample.

E5 Ensure that the incident neutron spin is not depolarised to enable neutron polarisation analysis studies.

Experimental aim E1 is motivated by the scientific interest to drive the magnetic systems into unconventional states of matter through the application of uniaxial pressure. This aim is ultimately limited by the strenghs of the crystal bonds in the sample, and in reality the sample preparation where two planar and parallel surfaces of the crystal sample have to be polished.

Experimental aim E2: Typically, the frustrated systems only enter the correlated phases at extremely low temperatures when thermal fluctuations are low.

Experimental aim E3: The correlated and disordered phases that we target result in weak diffuse magnetic scattering, [56], [61]. In order to study these systems, we therefore need large opening angles both within and outside the scattering plane. Additionally, large samples are needed due to the weakness of the diffuse scattering profiles combined with the low interaction between neutrons and matter. The unconventional states of matter described above are typically studied with diffuse neutron scattering instruments and with cold inelastic neutron spectrometers, and instruments such as D7[69], CNCS[21], IN5[54], LET[7], DNS[3] and CAMEA[31] are kept in mind. A sketched illustration of a scattering experiment is presented in figure 4.1. Here, a divergent incoming neutron beam scatters from the cell and sample. The angular coverage of the detectors of D7 is used as an example, which shows the importance of a broad scattering range of the cell.

Experimental aim E4: Uniaxial pressure is expected to induce structural changes as well as changes in the dynamics of the systems, which are studied with inelastic neutron scattering. The intensity of inelastic neutron scattering is orders of magnitude smaller than the elastic signal, which again motivates large samples and a low and uniform background from the pressure cell.

Experimental aim E5: it is possible to separate magnetic and nuclear scattering through the use of polarisation analysis (PA) as described in chapter 3 and thereby resolve small pressure induced changes in the magnetic spin-spin correlations. However, any net ferromagnetic contribution in the sample environment will depolarise the neutron beam rendering PA impossible to use [24].

These experimental aims result in system requirements that are described in the next section. The pressure cells that are described later in this chapter are all discussed based on the requirements.

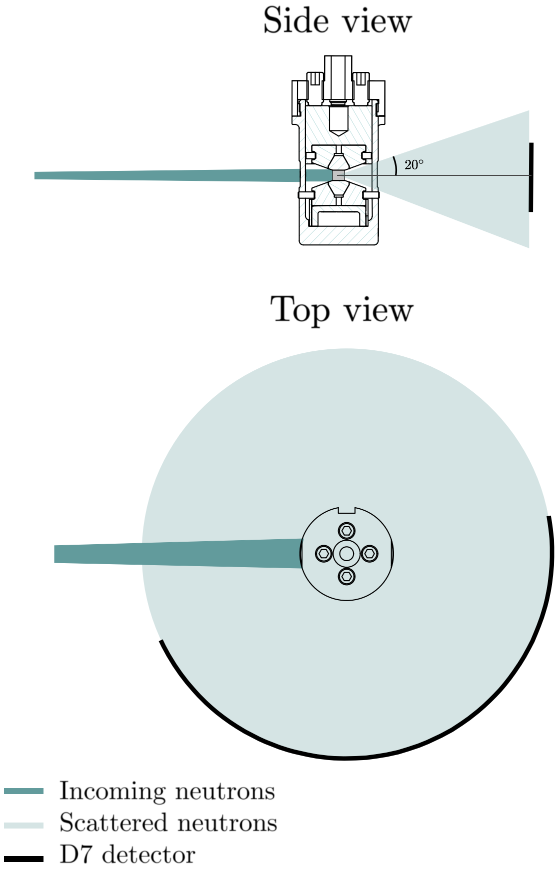

Figure 4.1: Sketched scattering on the cell D (section 4.7) for an incoming divergent neutron beam. Side view: the cell allows ± 20 degrees vertical scattering. This is compared to the vertical detector coverage of the D7 instrument at the ILL (± 10 degrees vertical scattering). Top view: the cell allows ± 180 degrees horizontal scattering. This is compared to the vertical detector coverage of D7 (-10 degrees, +155 degrees horizontal scattering). The sample-to-detector distances are not drawn to scale.

4.2 Cell Design

In order to meet the experimental aims defined in the previous section, we have defined the following system requirements:

S1 Keep 2 GPa uniaxial pressure constant within 5 % at the sample position during 24 hours. (experimental aim E1, E3, E4)

S2 Allow a broad scattering range of at least 180 degrees horizontal and ± 20 degrees vertical scattering. (experimental aim E3)

S3 Measure the applied force at cryogenic temperatures with less than 10 % error. (experimental aim E1, E2).

S4 Obtain uniform and low background from the cell (experimental aim E3, E4).

S5 Use materials that are thermally conducting even at cryogenic temperatures in order to cool the cell to cryogenic temperatures in less than 24 h. (experimental aims E3, E4 and E5).

S6 Use only materials that are non-magnetic (experimental aim E5).

S7 Accommodate several mm-size samples (experimental aim E3, E4).

S8 Obtain a cell with a maximum diameter of 45 mm so it fits into cryostats of common neutron scattering instruments (E4, E5).

S9 Use only materials that have low neutron activation (experimental aims E3, E4).

The cell design is based on the principles in a diamond anvil cell, but without any gaskets around the sample in order to obtain a uniaxial pressure. It is clear that leaving the crystal unconstrained, perpendicular to the application of pressure, will result in a Poisson expansion [44]. We have decided to accept such expansion since constraints on the crystal will limit the neutron scattering possibilities.

The development of the uniaxial pressure has been an iterative process where four cells (cells A-D) have been designed, constructed and tested. Cell A has large windows and the force is applied externally with a force press before the force is locked mechanically with the top screws. In cell B, the windows are removed and in stead the cell walls are thinned around the sample position in order to obtain a uniform cell background. Cells B and C have different force transducers with the aim to measure in-situ the applied force at low temperatures. In cell C, the force is applied mechanically with the top screws and not with an external force press in order to minimize the pressure loss. In cell D, the force is applied to the sample with cemented tungsten carbide anvils in cobber berrylium seats in order to obtain pressures above 350 MPa, the limit for the steel seats in cell A-C. In cell E, which has not yet been constructed and tested, the force is applied with a single top screw in order to obtain a true uniaxial pressure during force application to reduce tension in the sample.

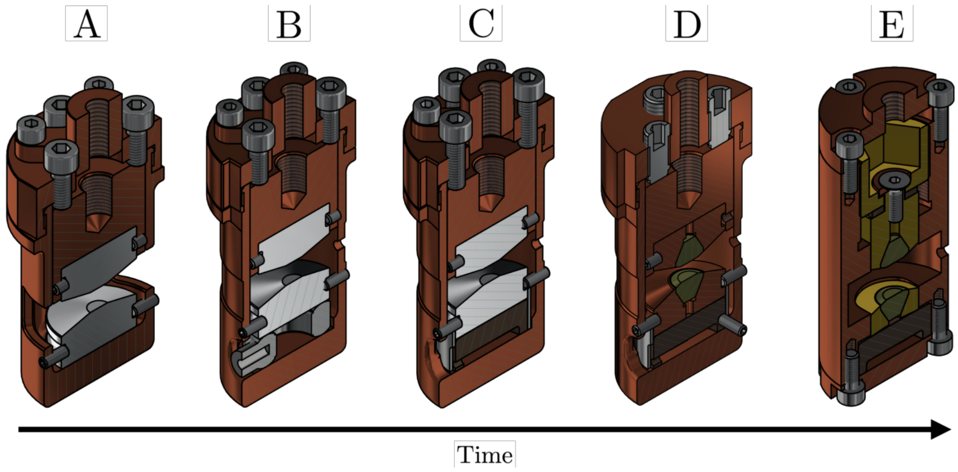

Figure 4.2: Illustration of the 5 iterations of the cell which are described in the this chapter where the cells are termed cell A to cell E. Cells A-D have been designed, calibrated and tested. Cell E is a suggested upgrade for the cell and it has not yet been constructed.

The following sections describe the materials of the cells and the design and tests of each cell are described and analysed. Finally, the results from all four cells are discussed. This section contains a description of each of the cells (cell A-D) along with a description of the changes in each iteration. Finally, the section contains a description of an improved design, cell E, which has not yet been constructed or tested.

4.2.1 Terms, Units and Basic Concepts

This section contains a description of the basic concepts and terminology which is used in the rest of the chapter. The notation and description is strongly based on ref. [44]. Figure 4.3(left) shows a generic example where a force F is applied to a material of length, L, resulting in an elongation ($\Delta L_1 > 0$) or compression ($\Delta L_2 < 0$) of the material depending on the sign of the force. The force is generally converted to *stress*, σ defined as the applied force, F, per area and is given in units of GPa. The response of the material, the *strain*, is generally defined as a dimensionless quantity, $\epsilon = \Delta L/L$. The stress-strain-curves of two different materials is shown in figure 4.3(right). At low applied stress, in the linear regime, there is no plastic deformation of the material, and

$$\sigma = E\epsilon, \tag{4.1}$$

where E is the *Young's Modulus* which is usually given in units of GPa. The stress which results in 0.2 % plastic deformation of the material is termed the *Yield Strength*. The *tensile strength*, σ_{T}, is the maximum stress that can be applied to a material and the *rupture length*, ϵ_{R} is the maximum strain of a material before it breaks. The two material curves in figure 4.3 are example of typical behaviour of the materials of similar yield strength, tensile strength and rupture strain. While the strain response of the orange curve varies smoothly for applied stress, $\sigma_{\ddot{\mathrm{Y}}} < \sigma < \sigma_{\mathrm{T}}$ while it has a dip in the blue curve due to work hardening.

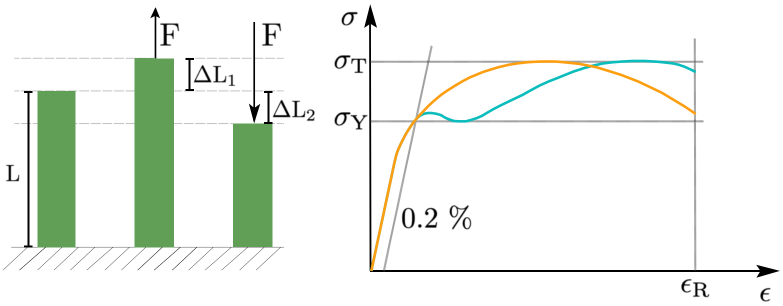

Figure 4.3: Left: A positive or negative force is applied to a rod (green) which results in $\Delta L_1 > 0$ and $\Delta L_2 < 0$ resulting in positive and negative strain respectively. Right: stress-strain curve modified from [44]. A stress, σ is applied to two different materials (orange and blue curves respectively). The two materials have identical yield strength, σ_{Y}, tensile strength, σ_{T}, and rupture strain, ϵ_{R}. The dip in the blue curve is a result of work hardening which is not seen in the orange curve. Stress-strain curves are generally measured for positive strain.

Materials are often described by their ductility which depends on the magnitude of E. *Ductile* materials can accommodate large deformations before fracturing while deformations of *brittle* materials are small. The strength of ductile materials is typically described by the yield strength, but the yield strength is difficult to determine experimentally for brittle materials and in addition it is often unreliable since there are large variations between specimen. In stead, brittle materials are charactized by their *transverse rupture strength*, related to the rupture length, and *hardness*. The exact definition of hardness varies, but it generally describes the indentation of a material when a large force is applied with a sharp object to a flat surface for a certain amount of time. Here, we use the *Vicker's hardness*, (HV), where a pyramid shaped diamond indenter whose sides have a 136° angle is used to apply a load for 10 or 15 seconds. The applied force, F, and the diagonal (in mm) of the indentation is used to define the hardness of the material according to,

$$\mathrm{HV} = \frac{0.189F}{d^2}, \tag{4.2}$$

as described in ref. [44]. The hardness is generally given in units of HV, although the formal unit is Pa. Another useful quantity in order to charactirize the strength of a mateiral is the *fracture toughness*, which measures the ability of a material to withstand the propagation of cracks under load.

4.3 Materials

All materials in the cell need high pressure capabilities, except the horizontal screws, in order to meet system requirements S1 and S7. Additionally, system requirements S5, S6 and S9 strongly limit the choice of materials.

Most parts of the cell are made from copper beryllium C17200 (CuBe), which consist of 1.8-2 % Be, 0.2-0.6 % Co+Ni, while the remaining part is Cu. It has a yield strength of 1240 MPa after heat treatment [42] when it is heat treated according to ref. [6]. The requirement for the CuBe yield strength is derived from the diameter of a typical cylindrical neutron scattering sample to be studied which is 4 mm, in which case 25 kN is required in order to obtain 2 GPa at the sample position. The highest possible sample diameter accommodated by the cells is 6 mm for which a force of 57 kN will provide a pressure of 2 GPa. The remaining parts of the cell have a larger cross section area and are therefore exposed to a lower pressure than the sample and the anvils which apply the force to the sample. For instance, the 2 mm thick cell wall in cells B-D at the sample position is exposed to a pressure of 208 MPa at an applied force of 57 kN, which is well below the yield strength of CuBe thus fulfillling scientific requirement S1. CuBe is non-magnetic and has a thermal conductivity of 108 W/mK at 300 K and 1.40 W/mK at 3 K, [63], which makes it possible to cool to cryogenic temperatures in compliance with scientific requirement S5. However, the thermal conductivity of CuBe is significantly lower than Cu with a factor of 3 at room temperature and at least a factor of 20 at 3 K which has to be considered during a neutron scattering experiment.

The exact amount of Co in CuBe is important with regards to neutron activation (system requirement S9), because the lifetime of Co-59 is 5.3 years and any neutron activation beyond the safety limit of a material which contains Co is therefore difficult to retrieve within a reasonable time frame. The data sheet of CuBe only states that the total amount of Co and Ni is within the interval 0.2 % to 0.6 % and the neutron activation will therefore have to be tested.

Screws and seats in the cells are made from steel 316 which is non-magnetic, has a yield strength of 200 MPa and a hardness of 225 HV. Steel 316 does not contain any Co, in contrast to most steels, providing an advantage in terms of activation (system requirement S9), and it has a room temperature thermal conductivity of 15 W/mK, see datasheet in appendix.

The anvils are in direct contact with the samples and apply the force to the sample. The anvils are therefore the cell components that experience the largest pressure identical to the sample pressure. The anvils are made from cemented tungsten carbide MT10MG (WC10) consisting of 10 % Co, 45 % W and 45 % C which is one of the hardest materials known to man. It has typical yield strengths between 3347 and 6833 MPa [49] and it will therefore not indent within scientific requirement S1. However, it is very brittle, and may therefore crack as a result of tension upon the application of large forces. WC10 has a hardness, of 1610 HV, a large transverse rupture strength of 4 GPa and a fracture toughness k_{1c} of 11.0, see data sheet in appendix.

Most types of tungsten carbide uses Co as a binder between W and C. WC10 contains 10 % Co which is an issue in regards to system requirement S9 due to neutron activation of Co. Cell parts which are made from WC10 must be covered completely in Cd or Gd in order to limit exposure since Cd and Gd are effective absorbers of cold neutrons. This will allow the users to retrieve the parts after an experiment. The room temperature conductivity of tungsten carbides like WC10 is approximately 50 W/mK, [37], which is better than many metals including steel 316. We can thus expect good thermal contact with the sample in compliance with system requirement S5.

4.4 Cell A

The force is applied externally to cell A with a force press. Once the external force is applied, a small additional force is applied with the top screws in order to maintain the force when the external press is released. The force readout from the external press is used as an indication of the force on the sample during the measurements and there is no pressure gauge in the cell. This section contains a description of the cell design along with a presentation and analysis of neutron scattering results.

Figure 4.4 shows the drawings of cell A in exploded view in addition to transparent and solid sideviews. The cryostat mounting screws (part 1) are used to attach the cryostat mounting (part 2) to the lid (part 4). The cryostat mounting contains an M6 screw hole which is used to attach the cell to the sample stick. The cryostat mounting screws only hold the weight of the cell and they are thereby not exposed to large forces. Part 3: the M5 top screws are tightened through the lid (part 4) and press down on the piston (part 5) in order to maintain the force once the external press is released. Part 4: the lid is screwed onto the cell cage (part 9) and the top screws are screwed through the lid. The force is applied to the piston (part 5) through a hole in the lid. There is a tight fit between the piston (part 5) and the cell cage (part 9) in order to obtain a uniaxial force on the sample. The fit is sufficiently tight that the piston does not fall out of the cell cage with the help of gravity if the cell is turned upside down. Part 6: the upper seat screws are used to hold the upper seat (part 7) in place. The seat screws (parts 6 and 10) therefore experience no large forces. There are two identical seats in the cell, the upper and lower seat, and the sample is placed between the seats at position 8. Part 9: the cell cage has two large windows with an opening angle of 70 degrees each. The windows were constructed as large as possible while keeping the pressure in the cell walls below the yield strength of CuBe. Part 10: There is not a tight fit between the lower seat and the cell cage, and the lower seat screws are used to align the lower seat and fix it when no force is applied.

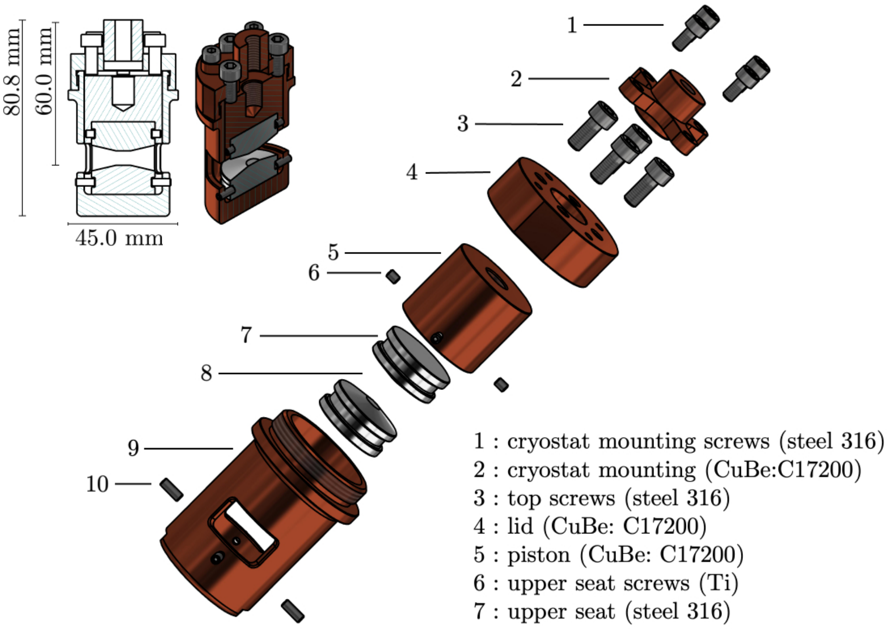

1 : cryostat mounting screws (steel 316)
2 : cryostat mounting (CuBe:C17200)
3 : top screws (steel 316)
4 : lid (CuBe: C17200)
5 : piston (CuBe: C17200)
6 : upper seat screws (Ti)
7 : upper seat (steel 316)
8 : sample position
9 : cell cage (CuBe: C17200)
10 : lower seat screws (Ti)

Figure 4.4: Drawings of cell A. Upper left corner: transparent views of the cell. The outer dimensions and the cell mounting-to-sample distance are marked. Center: exploded view of all parts of the cell which are numbered. Lower right corner: The cell parts are named and the materials are listed in parenthesis in the table.

4.4.1 Neutron Scattering Measurements

We have measured the neutron scattering profile of cell A at the diffuse scattering instrument D7 with neutrons of wavelength $\lambda = 4.9(1)$ Å, see section 3.3 for a description of the instrument. The experiment was performed on the spin ice compound $Ho_2Ti_2O_7$ (HTO), further details in chapter 2.3. HTO was chosen because of its well-known diffuse scattering profile and correlated disordered phase at ambient pressure.

Neutron scattering measurements were performed at 50 K, where HTO is in its paramagnetic phase and at 1.5 K in the correlated phase of HTO. In the paramagnetic phase, the sample scattering profile is a form factor decay, which is uniform under sample rotation and decreases in intensity with Q. In the correlated phase of HTO, the sample signal includes diffuse features and pinch points that follow the cubic crystalline symmetry.

Figure 4.5: Photo of cell A prior to the neutron scattering experiment at D7. The cell cage is covered with Cd outside the beam position and the seats are covered in Cd except at the sample position. A cylindrical HTO crystal of 1.5 mm in diameter is placed between the steel 316 seats with its cylindrical axis along the crystallographic c-axis.

Figure 4.5 shows a photo of the cell prior to the experiment. The seats are covered in Cd except at the sample position, and the cage is covered in Cd outside the beam position in order to reduce the cell background signal and to reduce neutron activation of the cell. A cylindrical HTO crystal of 1.5 mm in diameter was polished and placed between the seats with the pressure applied along the crystallographic c-axis. Neutron scattering measurements were performed at ambient pressure, with 2 kN and with 4 kN applied with the press which yields pressures of 1.1 GPa and 2.2 GPa respectively. The force was measured with the calibrated external press, but the actual force during the neutron scattering experiment is expected to be significantly lower, but was not determined.

Figure 4.6 shows the measured neutron scattering signal at 50 K and at 1.5 K. At 50 K, the signal is not uniform with sample rotation (azimuthal rotation in the figure). Instead, there is a distinct background pattern especially at low Q, where a low intensity region is marked by the line L_1 and a high intensity region is marked by the line L_2. The ellipses mark an asymmetry in the intensity even at higher Q which is less pronounced than the low Q features. At high Q, the intensity in the ellipse in the upper quadrant is higher compared to the intensity in the ellipse in the lower quadrant.

The measurements at 1.5 K have diffuse scattering and pinch points showing that HTO is indeed in its correlated phase. However, the profile is not symmetric in all four quadrants as expected from the cubic crystalline symmetry of HTO. In stead, the cell background marked by the lines L_1 and L_2 and the ellipses dominates. The pressure induced changes are predicted to be a few percent of the diffuse signal which is significantly weaker than the cell background and it is therefore difficult to retrieve the pressure induced signal. The noise level in the paramagnetic measurement is much larger than the diffuse features at

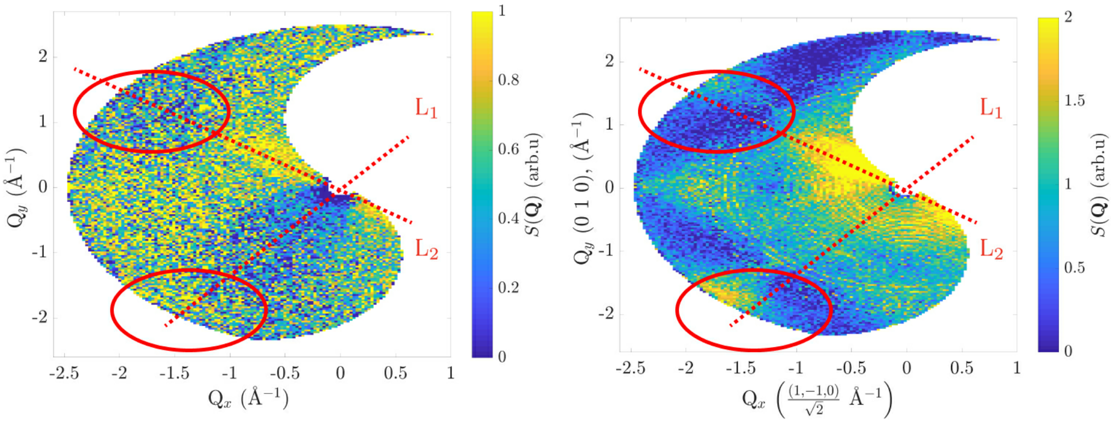

Figure 4.6: Pressurized spin flip neutron scattering measurements of cell A at D7 with a HTO cylindrical sample. Left: Measurement at 50 K in the paramagnetic phase of HTO. The profile is not uniform under sample rotation. For low Q, there is a region of low intensity along the line L$_1$ and high intensity along the line L$_2$. At high Q, the situation is reversed and the intensity is lower in the upper quadrant compared to the lower quadrant as marked by the ellipses. Right: Measurement at 1.5 K. Diffuse features and pinch points show that HTO is in its correlated phase. However, the background features observed in the paramagnetic signal also occur in the 1.5 K as marked by the same lines L$_1$, L$_2$ and the ellipses, and they are more intense than the diffuse features from HTO. The expected pressure induced changes are a few percent of the diffuse signal.

1.5 K due to low counting statistics. As a result, it is not possible to use the paramagnetic measurements directly as a background subtraction.

We have made a simulation of the cell attenuation in order to understand the origin of the cell background which was observed in figure 4.6 and to obtain a background subtraction. Figure 4.7 illustrates the principle of the attenuation simulation where a non-divergent neutron beam scatter from a point scatterer sample. The sample rotation determines if the beam is attenuated twice, once or zero times depending on the number of windows it passes. The neutron beam is attenuated exponentially when it passes through cell walls according to

$$\frac{I}{I_0} = \exp\left(-\mu_{\text{CuBe}} d\right), \tag{4.3}$$

where $d = 3$ mm is the thickness of the cell walls. The neutron linear attenuation factor of CuBe, $\mu_{\text{CuBe}} = 0.086\ \text{mm}^{-1}$, is determined from the online resource provided by NIST [67] and includes both neutron incoherent scattering and neutron absorption. The intensity of the neutron beam is thus reduced by 40 % if it passes two cell walls.

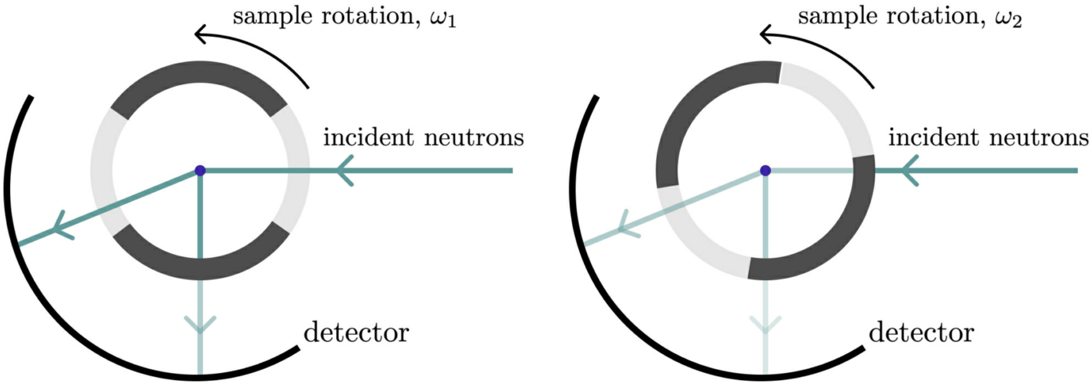

Figure 4.7: Sketch of the principle in the simulation of the cell background where a non-divergent neutron beam scatters from a point scatterer sample and is attenuated through the cell walls. The cell walls are coloured dark grey and the cell windows are light grey. The colour of the neutron beam represents its intensity. Left and right figures correspond to two different sample rotations. Left: the incident neutron beam pass through a cell window and is not attenuated before it scatters from the sample. The detected neutrons are scattered once or zero times. Right: the incident neutron beam pass a cell wall and is attenuated before it scatters from the sample. The detected neutrons are scattered twice or once.

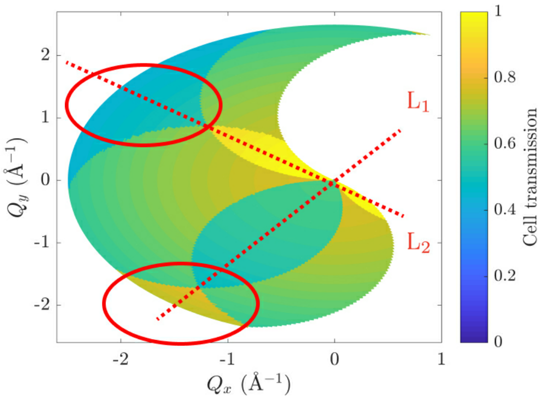

Figure 4.8: Attenuation simulation of the cell background based on the principles in figure 4.7. The cell attenuation results in a distinct pattern regions of three levels of intensity. These correspond to the neutron beam transmitting none, one or two windows when passing through the cell. A form factor decay of HTO has been included in the simulation in order to better compare the figure with the paramagnetic signal in figure 4.6. The two lines L_1 and L_2 and the two ovals are at similar positions to the lines in figure 4.6.

Figure 4.8 shows the neutron scattering profile of the attenuation simulation of the cell background. A form factor decay of HTO is included in the simulation in order to better compare with the paramagnetic signal in figure 4.6. There are three levels of intensity depending on the amount of cell walls that attenuate the neutron beam. The two lines L_1 and L_2 and the ovals that mark the cell background in figure 4.6 are also drawn in figure 4.8. The agreement is remarkable considering the simplicity of the model.

We have used this simple cell simulation without the form factor decay of HTO to renormalise the neutron scattering data in figure 4.6. Figure 4.9 shows the corrected paramagnetic profile. While the profile is more uniform under sample rotation compared to the uncorrected paramagnetic signal especially at high Q, the attenuation effects remains distinct in the low Q region.

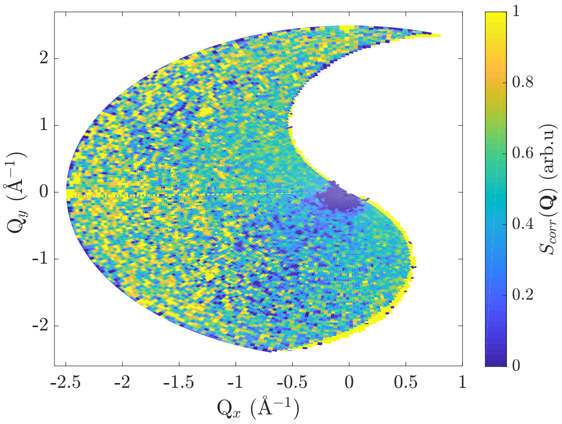

Figure 4.9: Paramagnetic spin flip neutron scattering data from figure 4.6 corrected with the cell simulation scattering profile in figure 4.8, $d_{\text{fit}} = 3.2$ mm. The signal is more uniform under sample rotation compared to the uncorrected data, but the profile of the neutron attenuation in the cell is still strong at low Q.

In the attenuation simulation, the thickness of the cell walls is assumed to be unaffected by the applied pressure. This is not realistic and a horizontal Poisson expansion is expected. The thickness of the cell wall, d_{CuBe} in equation 4.3 was allowed to vary with the aim of improving the background model. d_{fit} was determined as the distance which yielded the lowest χ^2 between the 2D scattering profile of the simulation and the paramagnetic scattering in figure 4.6. This yielded a wall thickness of $d_{\text{fit}} = 3.2$ mm. A horizontal expansion of 6.7 % at these low forces seems like a very large increase. It is possible that the variations in the wall thickness catch other features in the cell background that are not contained in the simple model. This is used as a motivation to perform a background subtraction with the cell simulation with a wall thickness described by d_{fit}.

Figure 4.10 shows the corrected spin flip neutron scattering data with pressure applied to the sample. Features of the cell attenuation are still observed especially at the edges of the window regimes, but the profile follows the cubic crystal symmetry much closer than the uncorrected data.

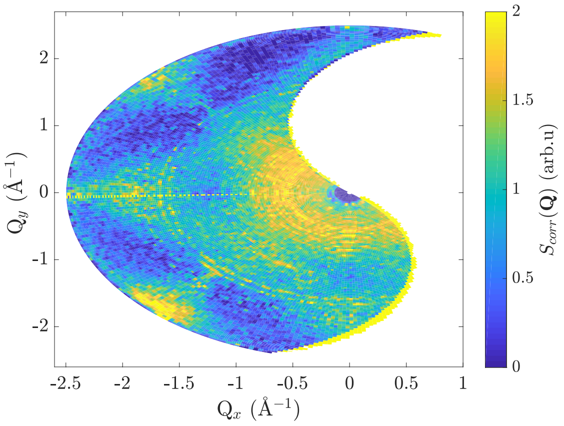

Figure 4.10: Pressurized spin flip neutron scattering data from figure 4.6 at 1.5 K corrected with the cell simulation scattering profile with a cell wall thickness of $d_{\text{fit}} = 3.2$ mm.

Figure 4.11 shows the relative difference in the data profiles at 1.5 K for ambient and pressurized corrected spin flip data along with a Monte Carlo (MC) simulation of the expected theoretical signal at 1.5 GPa. The relative difference data is defined as

$$\frac{\Delta S(\mathbf{Q})}{S(\mathbf{Q})} = \frac{S_{P>0} - S_{P=0}}{S_{P=0}}. \tag{4.4}$$

A qualitative agreement between data and simulation is marked by back circles at high Q. Oppositely, the low Q data is almost uniform unlike the theoretical prediction. This is possibly a result of the strong the cell attenuation effects for low Q. This underlines the necessity of reducing the cell background and the non-uniform attenuation.

4.4.2 Discussion

The most important result of the neutron scattering measurements of cell A was the unexpectedly large attenuation effects which were introduced by the difference between the attenuation in the cell walls and windows. This would not prevent studies of Bragg reflections or dispersion curves, but it makes it impossible to resolve the weak, diffuse scattering profiles that we target. The background is most pronounced for low Q which is especially unfortunate since the interesting magnetic correlations of the frustrated materials that we aim to study typically appear in the low Q region. Additionally, the form factor decay of magnetic neutron scattering will weaken the high Q signal. For this reason, many of the neutron scattering instruments that we target have detectors at both positive and negative scattering angles at low Q in order to obtain better statistics. It is therefore essential that the non-uniform cell background is minimum in this region, so we have removed the windows in later iterations of the cell.

The extracted pressure-induced changes in figure 4.11 are weaker than the simulation result. This is expected to be partly caused by smearing of the diffuse signal during the

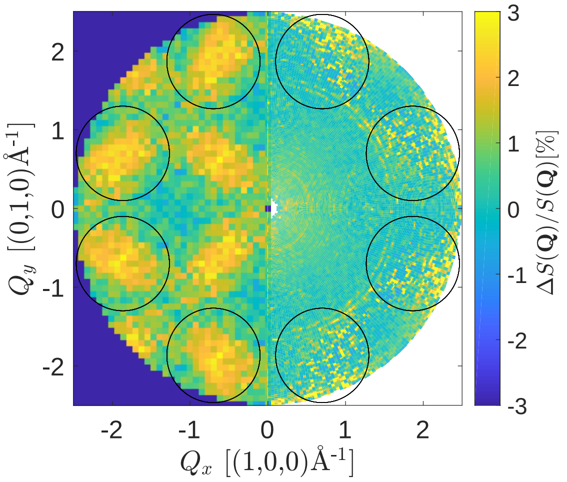

Figure 4.11: Comparison between Monte Carlo (MC) simulation (left) and neutron data (right) of the relative difference signal of pressurized HTO. Data has been corrected with the cell simulation scattering profile with $d_{\text{fit}} = 3.2$ mm. Black circles mark regions with agreement between data and simulation. Low Q data is almost uniform. Figure from [19].

background subtraction. Tbe MC simulation is made for a pressure of 1.5 GPa, but the actual pressure during the measurements is unknown. We have used the force readout from the external press, but additional force was applied with the top screws before the press was released. It is also expected that the force decreases when the external press is released. Furthermore, the piston had jammed after the experiment, possibly due to uneven force application with the top screws, and the friction between the piston and cell cage would reduce the force on the sample compared to the force readout from the external press. Finally, the temperature dependence of the force is unknown, and the experiment was performed at 1.5 K while the known force was applied at room temperature. All of the above arguments convinced us that an in-situ force measurement is necessary.

4.5 Cell B

The cell upgrade from cell A to cell B consists of:

- removal of windows in the cell cage in an attempt to obtain a uniform neutron scattering profile from the cell.
- introduction of the commercially available load gauge, KMR40 from HBM in order to measure the applied force below the sample and after release of the external force press.

This section contains a description of cell B with an emphasis on the KMR40 load gauge.

Figure 4.12 shows the drawings of cell B in exploded view as well as transparent and solid

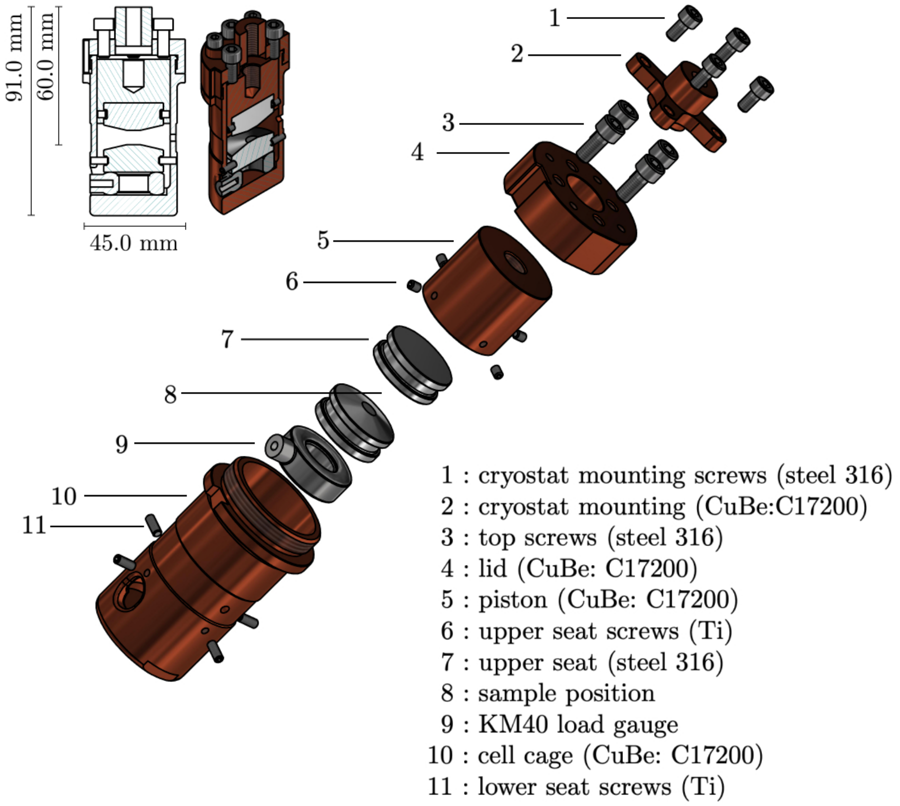

1 : cryostat mounting screws (steel 316)
2 : cryostat mounting (CuBe:C17200)
3 : top screws (steel 316)
4 : lid (CuBe: C17200)
5 : piston (CuBe: C17200)
6 : upper seat screws (Ti)
7 : upper seat (steel 316)
8 : sample position
9 : KM40 load gauge
10 : cell cage (CuBe: C17200)
11 : lower seat screws (Ti)

Figure 4.12: Drawings of cell B. Upper left corner: transparent views of the cell. The outer dimensions and the cell mounting-to-sample distance are marked. Center: exploded view of all parts of the cell which are numbered. Lower right corner: The cell parts are named and the materials are listed in parenthesis in the table.

sideviews. Parts 1-8 are identical to the corresponding parts in cell A except for a groove in the lid (part 4) which allows the load gauge wire to exit the cryostat. Part 9: KMR40 load gauge from HBM which has been inserted below the lower seat. Part 10: the cell cage which contains the remaining parts in the cell. The windows in the cell cage are removed in the upgrade from cell A to cell B, which increases the cross section area of the cell cage. This enables a thinning of the cell cage walls from 3 mm to 2 mm around the sample position while still maintaining the pressure in the walls significantly below the yield strength of CuBe. Finally, the cell cage extends further below the sample compared to the cell cage in cell A in order to accommodate the load gauge. Part 11 is the lower seat screws which are used to align the lower seat and fix the seats and load gauge in the cell when no force is applied.

4.5.1 KMR40 Load Gauge

The KMR40 load gauge has been developed and tested by HBM for forces up to 40 kN. It contains a large number of *strain gauges*, the principle of which is illustrated in figure 4.13. A strain gauge is a resistor that changes resistance when a force is applied along the specified axis while there is negligible change in resistance when a force is applied perpendicular to the axis. The change in resistance is positive or negative depending on the sign of the *strain* (compression or elongation). The strain is the material deformation that is caused by a mechanical stress. The field of strain gauge measurements is described in [36]

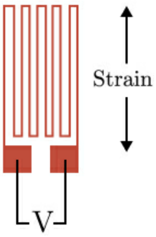

Figure 4.13: Schematics of a strain gauge. A strain which is applied along the specified axis changes the resistance in a strain gauge. Strains perpendicular to the axis will not induce any resistance changes.

Strain gauges are often connected in a *Wheatstone bridge* as illustrated in figure 4.14 in order to remove the effect of wire resistance, increase the temperature stability, reduce the sensitivity to non-vertical force components and increase the signal. In a Wheatstone bridge, an excitation voltage, V_e, is applied between the points B and C in the bridge, and an output voltage, V_0, is measured between points A and D in the bridge. If the bridge is balanced and 2 strain gauges are stretched and 2 strain gauges are compressed, the 4 strain gauge resistors fulfil the requirement

$$\frac{R_1}{R_2} = \frac{R_3}{R_4} \tag{4.5}$$

with the surface relaxed, and the output voltage is zero in that case. Any small deviation from the equilibrium state will induce a change in the output voltage, reflecting the surface strain caused by the applied force.

The KMR40 load gauge is not connected in a single Wheatstone bridge, but has a complicated electronic circuit with many strain gauges in order to better compensate for non-vertical force components and ensure a strong temperature stability. The drawings of the electronic circuit of the strain gauges have not been provided since KMR40 is commercially available. However, the KMR40 readout is given as a differential voltage similarly to the readout in a Wheatstone bridge. This differential voltage is then converted into a force with a linear calibration curve. Variations in temperature introduces a shift of the calibration curve while the slope is almost unaffected. The load gauge is only specified down to 263 K which is far from cryogenic temperatures, specified in system requirement S3. It is considered feasible to calibrate the KMR40 load gauge for cryogenic temperatures.

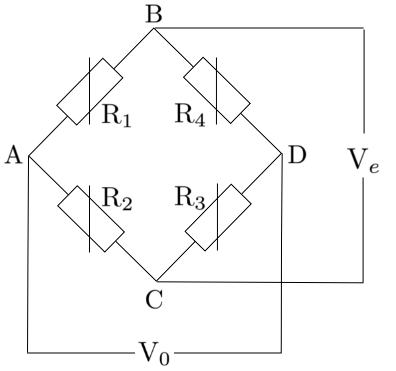

Figure 4.14: Schematics of the Wheatstone bridge circuit, which consists of 4 variable resistors (R_1 to R_4). The output is typically given as the ratio between the excitation voltage, V_e, applied between the points C and B in the bridge, and the output voltage, V_0, measured between the points A and D.

In addition to absolute force measurements, the load gauge is able to reveal friction between various parts of the cell, most importantly the piston and cell cage, from a discrepancy between externally applied force and measured force below the sample. We find that there is no significant discrepancy between the externally applied force and the KMR40 force readout at room temperature, leading to the conclusion, that the friction between the piston and cell cage is negligible in cell B.

In contrast, there is a large discrepancy between the measured force before and after removal of the external press. Despite application of additional force with all four top screws, the force is reduced by a factor of 8-10 when the external press is removed. In order to accommodate system requirement S1, application of 2 GPa pressure at the sample, we would need to apply much greater forces using the press prior to the experiment, and the crystal will often break under these conditions. Cell C addresses this.

In order to calibrate the load gauge at temperatures below 263 K, it was cooled to 75 K with different known forces applied with a gas membrane. These calibration measurements were primarily performed by Morten Haubro and his report on the measurements is included in appendix B.

The main effect of cooling was indeed a shift in the calibration curve which remained linear down to 75 K. However, there were many discrete spikes and jumps in the electronic signal during cooling which could indicate the appearance of cracks in the glue that is used to attach the strain gauges. Additionally, the signal became very noisy and unstable near liquid nitrogen temperatures with fluctuations orders of magnitude above the expected readout signal, making the KMR40 impossible to use at this temperature. One explanation to this behaviour is that air is trapped inside the cage of the load gauge. Condensation of the nitrogen in the air would introduce disturbances in the load gauge readout. Alternatively, a phase transition of a material in the load gauge could also drastically change the signal and possibly result in the appearance of cracks in the glue. It was not possible to obtain technical information on the glue and materials in the KMR40 load gauge since it is commercially available. The exact reason for the instability in the load gauge therefore remains unsolved. The load gauge did no longer respond to an applied force upon heating back to room temperature. We have cooled 2 different KMR40 force transducers and they both broke upon cooling to temperatures near liquid nitrogen.

Figure 4.15: Picture of KMR40 force transducer from HBM. Picture from the manual.

4.5.2 Discussion of cell B

The KMR40 force transducer worked well at room temperature, and we were therefore able to conclude that most of the force which was applied with the external press was lost once it was released despite application of additional force with the top screws. We therefore decide to apply the force directly with the top screws in later iterations of the cell in order to reduce the risk of breaking the crystal samples by applying a force which is many times larger than the force required during the experiment.

The KMR40 readout is linear and its main response to temperature variations is a shift in the calibration curve for temperatures down to 80 K. However, an issue occurs when the load gauge reaches 75-80 K which results in large fluctuations and eventually breaks the load gauge. Since we were unable to retrieve the technical specifications of the KMR40 load gauge, we have constructed our own load gauge in the upgrade to cell C in order to better adjust it to our purpose.

4.6 Cell C

The upgrade from cell B to cell C consists of:

- Introduction of a load gauge that can operate at cryogenic temperatures which allows to study the change in pressure upon cooling in a neutron scattering experiment.
- Pressure is applied directly with the top screws instead of an external press in order to reduce the pressure loss.

This section contains a description of the design, test and calibration of the load gauge along with stability tests of cell C at several temperatures. Additionally, the neutron scattering profile of cell C is presented and compared to the neutron scattering profile of cell A.

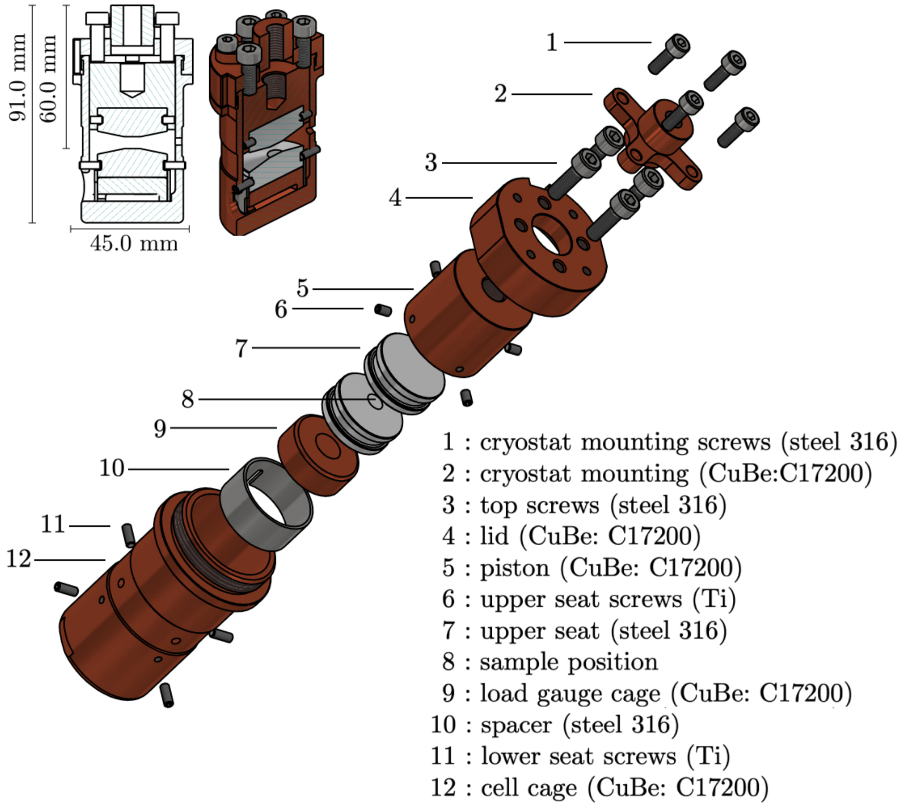

1 : cryostat mounting screws (steel 316)
2 : cryostat mounting (CuBe:C17200)
3 : top screws (steel 316)
4 : lid (CuBe: C17200)
5 : piston (CuBe: C17200)
6 : upper seat screws (Ti)
7 : upper seat (steel 316)
8 : sample position
9 : load gauge cage (CuBe: C17200)
10 : spacer (steel 316)
11 : lower seat screws (Ti)
12 : cell cage (CuBe: C17200)

Figure 4.16: Drawings of cell C. Upper left corner: transparent views of the cell. The outer dimensions and the cell mounting-to-sample distance are marked. Center: exploded view of all parts of the cell which are numbered. Lower right corner: The cell parts are named and the materials are listed in parenthesis in the table.

Figure 4.16 shows the drawings of cell C in exploded view in addition to transparent and solid sideviews. Parts 1-8 are identical to the parts in cell B, but in cell C, we now use the M5 top screws (part 3) directly to apply the force due to the large loss in force that was observed in cell B upon relaxation of the external press. For the load gauge calibrations the force is still applied with a calibrated external press through the hole in the lid in order to apply a known force and the top screws are thereby not used for these calibrations. Part 9, is the CuBe load gauge, and part 10 is a spacer which aligns the CuBe load gauge with respect to the cell cage (part 12). The groove in the spacer allows the wires to exit the cell cage.

4.6.1 Load Gauge Design

The KMR40 load gauge that was used in cell B accurately measured the force and seemed resistant to temperature changes except at liquid nitrogen temperatures. However, the challenges at this specific temperature is believed to be caused either by condensation of air in the load gauge cage, or a phase transition in the load gauge materials which causes the glue to crack. With better technical knowledge of the load gauge, it is possible to overcome these challenges which motivated a continued use of strain gauges when developing a load gauge for cell C.

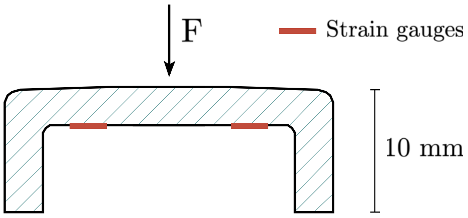

Figure 4.17: Schematics of the load gauge used in cell C. The load gauge cage is a cylinder with a slightly conical lid, that is here seen from the side. Four cryogenic strain gauges are glued onto the back of the lid in a Wheatstone bridge circuit (figure 4.14). When a force is applied, the load gauge lid deforms, which induces an electronic signal in the strain gauges. More details on the load gauge is found in figure 4.18.

Figure 4.17 illustrates the principle of the load gauge for cell C. The cage of the load gauge is made from CuBe and it is designed as a cylinder with a conical lid. When a force is applied vertically, the lid deforms which induces an electronic signal in four strain gauges that are glued onto the lid of the load gauge and connected in a Wheatstone bridge. Figure 4.18 shows a photo of the load gauge lid with four CFLA-1-350 strain gauges attached with adhesive type C-1 from Tokyo Measuring Instruments Lab. The strain gauges are calibrated for relative strain up to 0.1 % and for temperatures down to 4 K. We expect that there are no challenges in accomodating mK temperatures once 4 K has been reached. The photo in figure 4.18 also shows a PT100 thermometer which is used during the calibration of the load gauge. It is specified down to 74 K and it is therefore not intended to be used during neutron scattering measurements.

The positioning of the strain gauges is based on a *finite element analysis* (FEA) of the strain in the load gauge cage at 25 kN which corresponds to 2 GPa pressure on a cylindrical 4 mm diameter sample. Typical samples are expected to be 3-4 mm in diameter and the load gauge is therefore designed and tested with this in mind. FEA uses numerical finite element methods to calculate structural behaviour such as the stress and strain of a material under a given load as described in [26]. Figure 4.18 presents the relative strain of the load gauge lid based on the FEA along with the strain active areas of the strain gauges. The simulation shows that the lid only experience positive strain and it is therefore not possible to expose two strain gauges to positive strain and two strain gauges to negative strain and take full advantage of the Wheatstone bridge. Instead, two strain gauges are placed near the edge of the lid where the strain is close to zero. These two strain gauges thereby mostly contributes to temperature stabilisation, they adjust for non-vertical components of the applied force, and they adjust for differences in the resistances in the wires. The two remaining strain gauges are placed near the center of the lid where they experience a large strain which slightly exceeds the 0.1 % limit for relative strain.

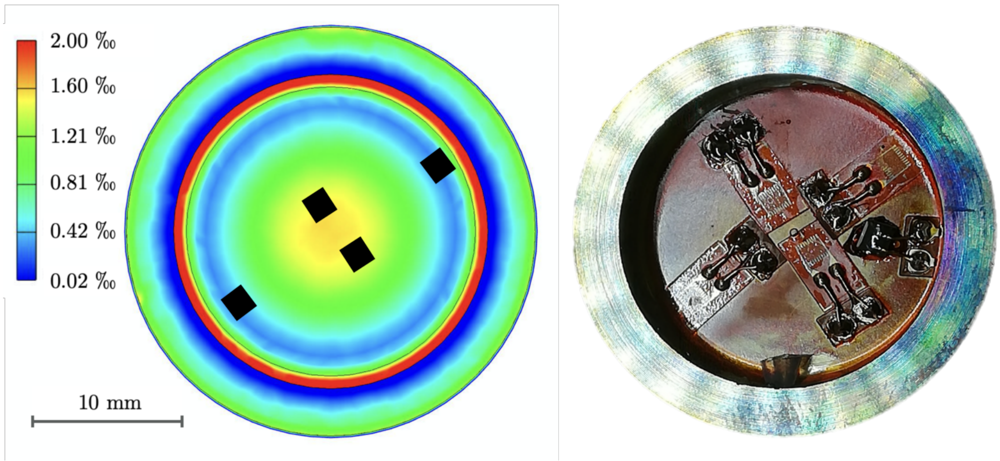

Figure 4.18: Left: Finite element analysis of the load gauge lid with 25 kN load applied. The colour scale describes the relative strain of the lid. The strain active areas of the strain gauges are marked by dark grey squares. Right: Photo of the load gauge lid with four strain gauges and a PT100 thermometer. Photo taken before wires were soldered.

Reliability is shown after numerous load applications during calibrations and tests of the cell and load gauge and no systematic changes are observed upon pressurization. We therefore conclude that the adhesive and strain gauges are not damaged by force applications of this magnitude. If larger forces are required at a later point, it is possible to increase the thickness of the lid in order to reduce the strain of the lid, but this will also reduce the signal in the strain gauges and the current lid thickness is thereby ideal for the forces which we target.

4.6.2 Room Temperature Force Calibration of CuBe Load Gauge

The CuBe load gauge has been calibrated at 300 K, at 195 K (cooled with dry ice), at 125 K (cooled with liquid nitrogen) and at 80 K (cooled with liquid nitrogen). This section contains a description and analysis of the room temperature calibrations, while calibrations for temperatures below room temperature is described in section 4.6.3.

The CuBe load gauge is calibrated with an external force press. Initially, the load gauge was placed directly in the press, but we obtained significantly different calibration curves depending on the exact position of the load gauge with respect to the press. In order to reduce the horizontal force components and simulate the experimental situation during a neutron scattering experiment, the load gauge was placed in cell C during the calibrations and the force was applied with an external press through the hole in the lid of cell C.

The load gauge is highly sensitive, and even small forces of less than 1 N applied with a finger is clearly seen in the differential voltage readout. Similarly, there are spikes in the signal if someone walks by the experimental setup. The load gauge sensitivity to horizontal force components is surprising since the Wheatstone bridge should compensate for it. It is believed to be a result of a slight tilt of one of the strain gauges as seen in figure 4.18.

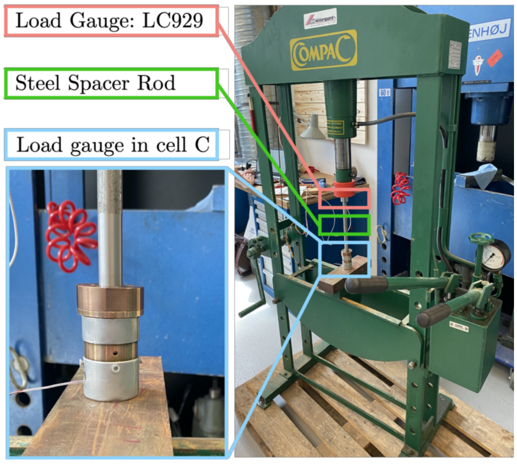

Figure 4.19: Photo of the experimental setup which was used to calibrate the load gauge at room temperature with an external press (in green). The red square frames the reference load gauge LC929 which was used to measure the applied force. The green square frames the steel spacer rod which was used to thermally disconnect the reference load gauge from the cell (important for calibrations at temperatures below -10 °C). The blue square circles cell C which contains the CuBe load gauge.

Figure 4.19 shows the experimental setup that was used for the room temperature calibration of the load gauge. The external press is calibrated with a reference load gauge LC929 which is specified down to 263 K. Consequently, it is necessary to thermally disconnect the cell and press during calibration below this temperature. In order to create similar experimental conditions for all calibrations, the force was applied from the press to the cell piston through a steel rod, as shown in the photo, even at room temperature. The zoom on the cell shows that the top screws were not used during the load gauge calibration, but all other parts of cell C except for the cryostat mounting was contained in the cell cage as specified in figure 4.16.

The reference load gauge LC929 is specified up to 22 kN, and this was therefore the upper limit for the calibration. We expect to be able to extrapolate the force up to 25 kN as specified in system requirement S1 for a 4 mm diameter sample. The room temperature calibration was repeated 6 times where the force was increased from 0 kN to 22 kN and returned to 0 kN 3 times, which we term one data set. The cell was disassembled between each data set.

Figure 4.20 shows an example of the differential voltage readout of a single data set (data set 1). There are three distinct increases in signal when the force is applied with the external press. The force is applied manually by pumping with a handle and it is apparent that it is not applied with the same rate for each of the three force increases. The force increase is slower than the force decrease where the press is released by opening a valve.

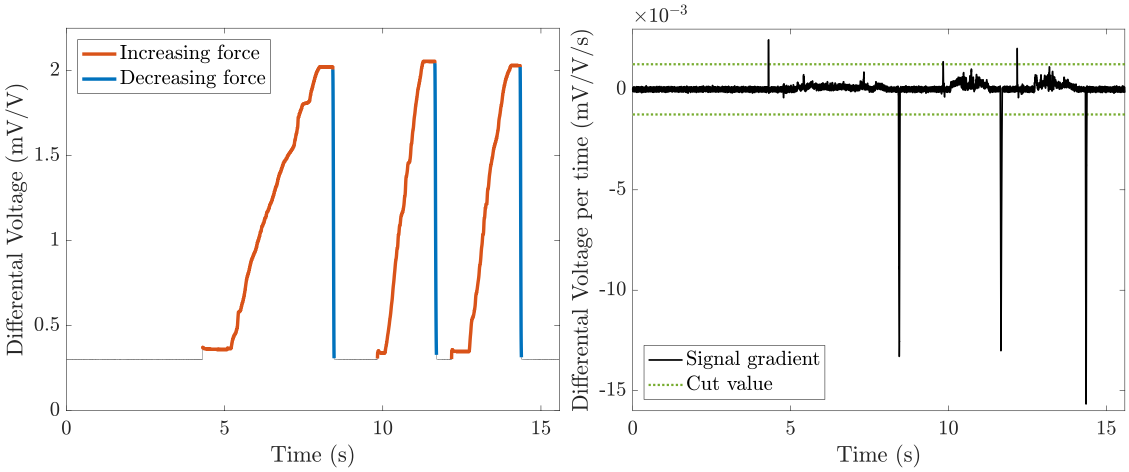

Figure 4.20: Left: induced response in differential voltage when the externally applied force is increased to approximately 22 kN 3 times (data set 1). The red and blue lines mark the data which is used as increasing and decreasing force respectively based on the gradient of the signal (right). The marked cut values of the gradient are used to separate the signal into increasing and decreasing force.

Figure 4.20 also shows the gradient of the differential voltage signal, which is used to separate the signal into increasing and decreasing force when the gradient crosses the marked cut values. While there is a sharp negative peak in the gradient when the force is released with the valve, there is only a small positive peak at the start of the increasing force curve. There is also no clear gradient signal at the top of the force curve, and the plateau at the top of the force curve is therefore included in the increasing force curve despite a slight decrease in force due to a drift of the hydraulic press.

Figure 4.21 shows the calibration curve of data set 1 where the calibration curve has been separated into increasing and decreasing force as described in figure 4.20. There is hysteresis in the system between increasing and decreasing force and the two sets of calibration curves have therefore been separated and treated independently. The curves presented here are the increasing force curves, since these are the curves that are relevant when force is applied to the cell prior to an experiment.

Figure 4.22 shows six room temperature calibration data sets, data sets 1-6. The zoom inset in figure 4.22 shows that variations between each dataset is larger than variations within each dataset indicating that the cell assembly method is crucial in order to reduce the systematic errors on the calibration curve. Data sets are taken both before and after temperature calibrations of the load gauge as described in section 4.6.3. Data sets 1-3 are

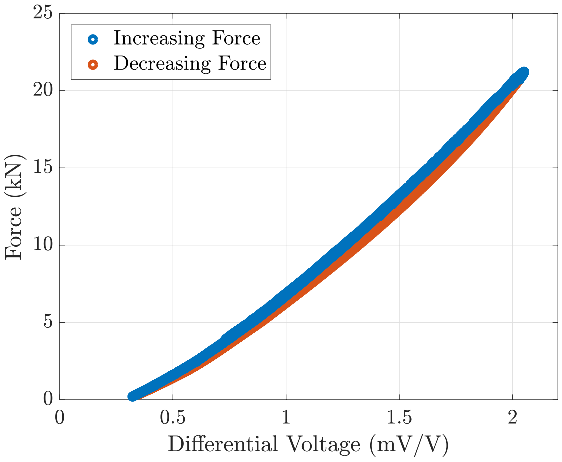

Figure 4.21: Dataset 1 where the force has been increased from 0 kN to 22 kN and decreased back to 0 kN three times. There is hysteresis between increasing and decreasing force, and increasing force calibration curves are therefore used in this thesis unless otherwise stated.

taken prior to calibrations at low temperatures, data sets 4-5 are taken between cooling with dry ice and liquid nitrogen and data set 6 is taken after cooling with liquid nitrogen. There is no systematic change in the calibration curves upon cooling and stress testing the load gauge which shows its robustness and stability and we therefore combine the data from all 6 data sets into a single room temperature calibration curve.

Figure 4.23 presents the data from all six data sets in addition to a third degree polynomial fit which that be used as a room temperature calibration curve. The inset figure shows the relative residual difference between data and fit defined as

$$dF_{\text{rel}} = \frac{F_{\text{fit}} - F_{\text{data}}}{F_{\text{data}}}, \tag{4.6}$$

which is interpreted as the error on the calibration curve termed the calibration error. The calibration error is less than 5 % for forces above 15 kN, corresponding to 2 GPa pressure on a 3.1 mm diameter sample, but it is substantial when low forces are applied since the strain gauge signal is smaller in this range. If there is a need to use the cell for low applied forces, it is possible to design a load gauge which is very similar to the current load gauge and which fits into the cell, but has a thinner lid and thereby a larger strain.

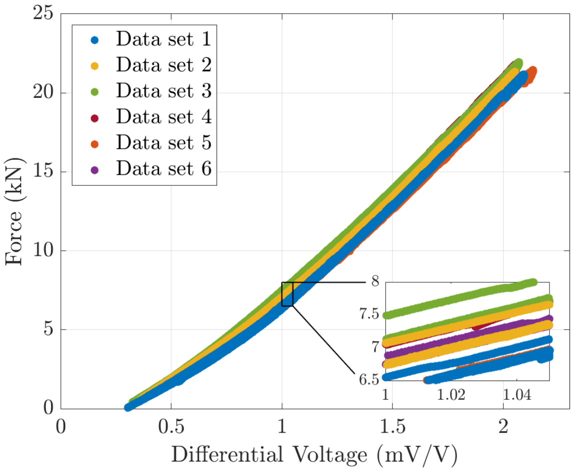

Figure 4.22: Room temperature calibration curves for increasing force of each cell assembly termed dataset. The force was increased to 22 kN 3 times within each dataset. There is no systematic change in the calibration curves. The descrepancy between each dataset is larger than the discrepancy within each dataset.

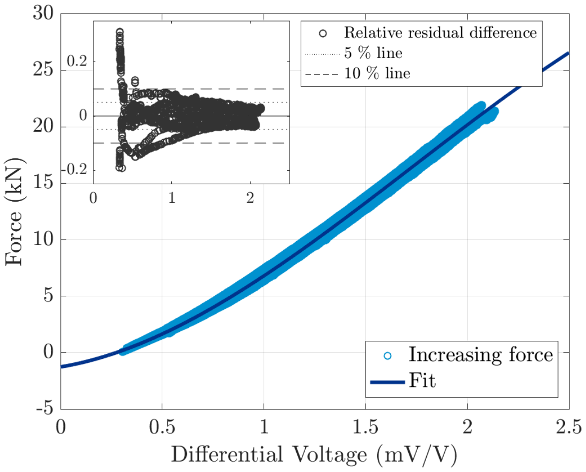

Figure 4.23: Data from all 6 datasets along with a 3rd degree polynomial fit which will be used as the room temperature calibration curve. Fit parameters are presented in table 4.1. The inset figure shows the relative residual difference between data and fit along with 5 % and 10 % lines. The relative residual difference is less than 5 % for forces above 15 kN.

4.6.3 Low Temperature Force Calibration of CuBe Load Gauge

This section contains a description of the load gauge calibrations that were performed at temperatures below room temperature. Figure 4.24 shows the experimental setup that was used for these calibrations. The setup strongly resembles the room temperature calibration setup that was presented in figure 4.19, but the cell is placed in a container which is filled with either dry ice or liquid nitrogen. The force is applied through a steel rod in order to thermally disconnect the reference load gauge and the cell. A PT100 thermometer on the reference load gauge showed that the temperature was above 278 K degrees at all times and thereby well above 263 K which is the lower temperature limit specified for the reference load gauge. The force was only applied once the system had reached thermal equilibrium.

It took approximately 1 hour to reach thermal equilibrium both when cooling from 300 K to 77 K with liquid nitrogen and when cooling from 300 K to 195 K with dry ice. This is much faster than in a typical cryostat and it thereby provides a stress test of the load gauge. While the signal fluctuated a lot during temperature variations it recovered well once it had reached thermal equilibrium. Fluctuations are expected due to temperature gradients in the load gauge during cooling.

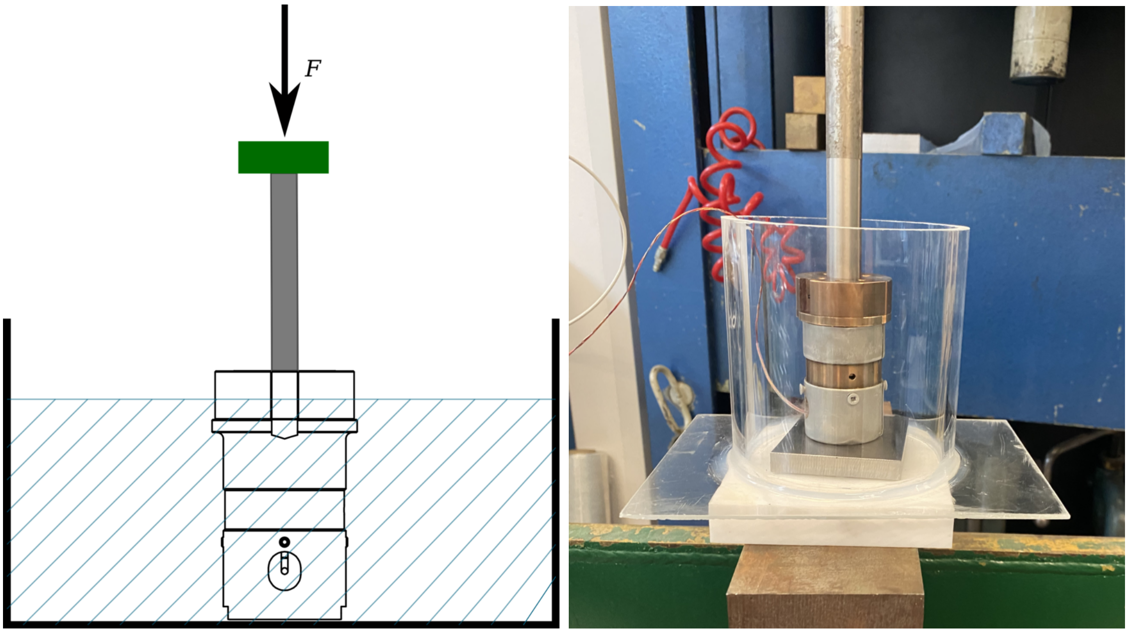

Figure 4.24: Experimental setup during the temperature dependent force calibrations of the load gauge in a sketch format (left) and a photo where the container is empty (right). The load gauge is inside the cell which is placed in an container. The container is filled with liquid nitrogen or dry ice during the force calibrations. Once the system has reached thermal equilibium, the force is applied externally with a force press through a stainless steel spacer rod which thermally disconnects the cell from the calibrated reference load gauge LC929 (green square in the sketch).

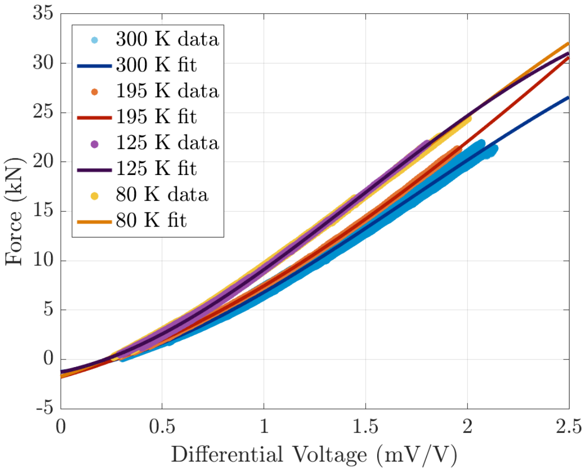

Figure 4.25: Force calibrations of the load gauge at temperatures: 300 K, 195 K, 125 K, 80 K. Each calibration curve has been fitted to a third degree polynimial fit. Fit parameters are presented in table 4.1. The temperature dependence is most pronounced for large forces and is smaller than the calibration error when no force is applied. The 300 K calibration curve consists of 6 datasets while the remaining curves consists of 1 dataset each. The calibration curves at 125 K and 80 K coincide.

Figure 4.25 shows the calibration curves obtained at low temperatures in addition to the room temperature calibration curve that was presented in section 4.6.2. The room temperature calibration curve consists of 6 data sets while the calibration curves at the other temperatures consists of a single data set each. This explains the larger spread of the room temperature curve compared to the other calibration curves where a similar spread is anticipated if more data sets are produced.

A temperature reduction primarily changes the slope of the calibration curve and temperature variations between the calibration curves is therefore most pronounced for large forces while it is less than the calibration error when no force is applied. This is opposite to the observation of the KMR40 load gauge that was used in cell B where temperature variations predominately induced a shift in the calibration curves.

Figure 4.25 also shows that the calibration curves at 125 K and 80 K almost coincide,

	a	b	c	d
300 K	-1.214(73)	6.29(27)	2.98(30)	-1.261(95)
195 K	-0.399(3)	3.887(11)	5.739(11)	-1.788(3)
125 K	-1.795(10)	7.976(32)	4.221(31)	-1.308(9)
80 K	-1.005(11)	5.213(35)	6.772(34)	-1.740(10)

Table 4.1: Fit parameters of third degree polynomial fit ($ax^3 + bx^2 + cx + d$) to load gauge calibration data presented in figures 4.25 and 4.23.

indicating that the material properties of CuBe, especially the elastic modulus, do not change significantly below this temperature. We will therefore use the 80 K calibration curve to estimate the applied force at helium temperatures. Table 4.1 shows the fit parameters of third degree polynomials which have been fitted to all four calibration curves. The purpose of the calibration curves is to describe the data and there is no direct physical interpretation of the parameters with this model. These fitted curves will be used to convert the differential voltage readout to force and the error will be given by the calibration error of the corresponding force based on the room temperature calibrations.

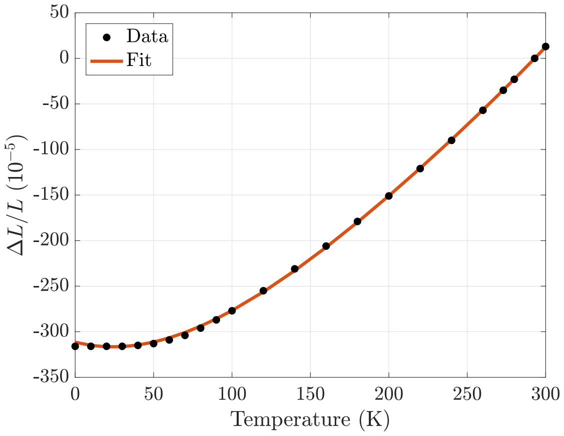

Figure 4.26: Thermal expansion of CuBe C17200, data from [16], fit from [68]. The thermal expansion is very small below 77 K.

The pressure will change upon cooling from room temperature to cryogenic temperatures due to differences in the thermal contraction of the cell materials, primarily steel 316, CuBe and the sample. The thermal contraction of many common materials such as steel is very small below liquid nitrogen temperatures [18] and figure 4.26 shows that this also applies to CuBe. It is therefore sufficient to determine the temperature induced force change down to liquid nitrogen temperatures.

In order to investigate the load gauge response at even lower temperatures, it was cooled in a closed cycle refrigerator (CCR) without any applied load. Figure 4.27 shows the load gauge readout as a function of time. The temperature is reduced in steps and allowed to stabilise before it is reduced further. The temperature and differential voltage readouts in figure 4.28 are found as the average of the marked data in each plateau in figure 4.27.

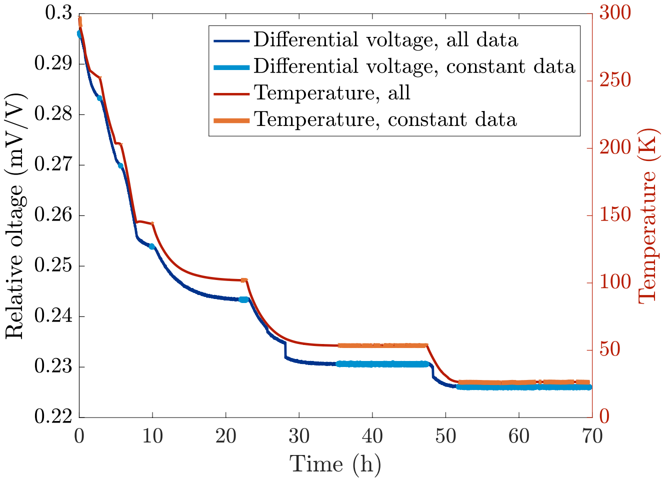

Figure 4.27: Change in differential voltage (left axis) and temperature (right axis) upon cooling the unloaded load gauge and cell from 300 K to 26 K. The marked constant temperature data is used to generate the data of the first cooling in figure 4.28.

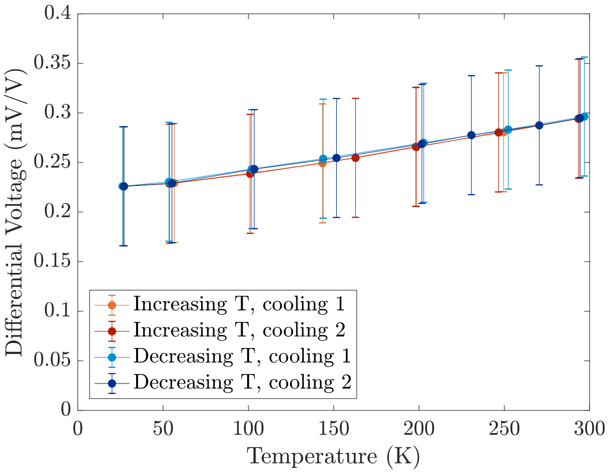

Figure 4.28: The temperature induced change in load gauge response without any applied force. The load gauge has been placed inside the cell and cooled from 300 K to 26 K and heated back to 300 K twice. The plotted room temperature calibration errors are larger than the induced variations.

Figure 4.28 shows the differential voltage readout as a function of temperature for two temperature decreases and two temperature increases. The calibration error is larger than the temperature induced change in the differential voltage readout and the small hysteresis between increasing and decreasing temperature is difficult to resolve. The change in differential voltage is close to linear even at the lowest temperatures, but the temperature dependence is very weak compared to the calibration curves in figure 4.25. The signal changes by approximately 0.07 mV/V in the entire temperature range, which is approximately 30 times less than the differential voltage readout at 22 kN and the change below 100 K is only 0.002 meV which is orders of magnitude less than the calibration error and therefore insignificant in comparison. This shows that the temperature induced changes without applied force are minimal and can be neglected below the 100 K.

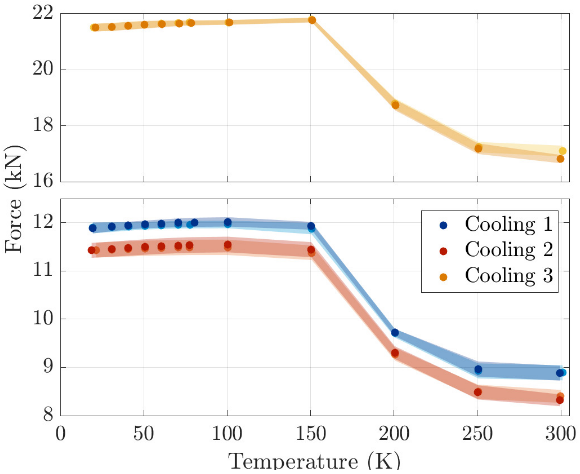

Figure 4.29: Three different forces have been applied to cell C at room temperature. This figure shows the force response when the cell is cooled from 300 K to 21-24 K and heated back to 300 K in the CCR for all three forces. There is a very low level of hysteresis between heating and cooling, the curves coincide except for the room temperature point of cooling 3 where there is a small discrepancy. The differential voltage readout is converted to force with the calibration curve which is closest in temperature in figure 4.25.

The loaded cell was cooled without sample in a CCR in order to simulate the force response to temperature in a neutron scattering experiment. Figure 4.29 shows the temperature induced force change when the cell is cooled from 300 K to 21-24 K and back to 300 K without sample for three different applied forces. The curves are separated into increasing temperature (dark colour) and decreasing temperature (light colour) and are converted from differential voltage readout to force with the calibration curve in figure 4.25 which is nearest in temperature. Below 150 K, the force is almost stable in compliance with the expectation that the thermal contraction of the cell materials is small below 100 K.

The system shows very small hysteresis between increasing and decreasing temperature and only the room temperature data, upon cooling 3, differ by approximately 1 errorbar, while the remaining data points coincide. The shapes of the curves are similar, and it reflects the relative thermal coefficients of the materials in the cell: steel 316 and CuBe. During a neutron scattering experiment, the dominant contribution to the change in force is the relative ratio between the contractions of CuBe, steel 316 and the sample, and it is therefore not possible to create a sample independent estimate of the shape of the curve, except for the expectation that it is likely to stabilise for temperatures below approximately 100 K. This is why the in-situ force measurement is essential to the experiment.

Figure 4.30 shows the temperature and differential voltage readout as a function of time during the first cooling in figure 4.29. The average of the marked data in each plateau was used to generate the data in figure 4.29. The cell is cooled from 300 K to 21 K in less than 30 hours with 12 intermediate steps where the temperature has been allowed to stabilise. This shows that it is indeed possible to cool the cell to cryogenic temperatures in less than 24 hours in compliance with system requirement S5.

Figure 4.30 shows large increases in force readout while the temperature changes most rapidly. This was not observed in figure 4.27 when cooling the unloaded cell, and it is therefore thought to reflect an actual force increase of approximately 1-2 kN caused by the temperature gradient within the cell. This dramatic response to cooling is important to keep in mind during a neutron scattering experiment where the system should be allowed to cool slowly in order to limit any additional force on the sample which might break it.

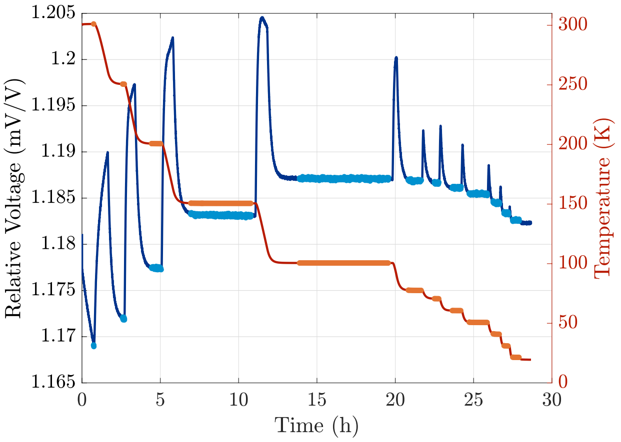

Figure 4.30: Change in differential voltage (left axis) and temperature (right axis) during cooling of the loaded cell in a CCR. The cell is cooled from 300 K to 21 K in less than 30 hours with 12 intermediate steps where the temperature is allowed to stabilise. The marked data is used to generate measurement 1 in figure 4.29. The differential voltage readout increases dramatically during cooling corresponding to a rapid force change of 1-2 kN when there is a temperature gradient in the cell and then stabilises at a lower level.

4.6.4 Stability Test of cell C

Stability tests have been performed for temperatures between 300 K and 250 K in order to check if the cell meets system requirement S1. Figure 4.31 shows a stability test at room temperature with 8.3 kN applied initially. The force drops by 2.5 % during 30 hours which is half the accepted drift.

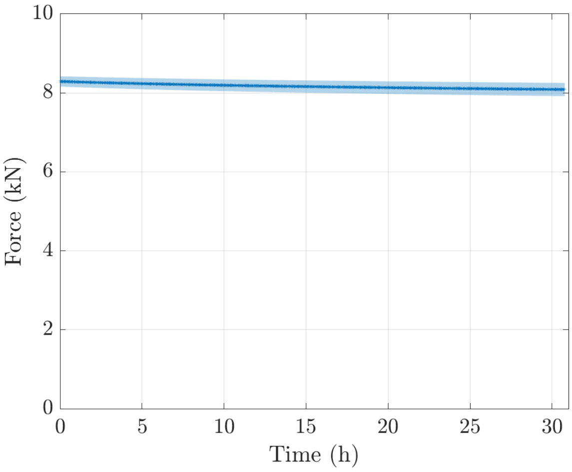

Figure 4.31: Stability test of cell C at room temperature which shows force as a function of time. The force decreased by 0.21 kN during 30 hours which corresponds to 2.5 % of the initially applied force. This is less than the room temperature calibration error.

Figure 4.32 shows the drift of cell C at temperatures from 300 K to 250 K in 10 K steps. All six differential voltage readout curves are converted to force with the room temperature calibration curve in figure 4.23. The force reduction is linear and the slope decreases when the temperature is reduced. All six curves are fitted with linear fits and the slopes are plotted as a function of temperature in figure 4.32(right). The temperature induced change in slope is well described by a fitted exponential,

$$\text{slope} = A \exp\left(\frac{T}{T_0}\right), \tag{4.7}$$

where T_0 = 9 K ± 1 K and A = (-7 ± 20) $\cdot 10^{-18}$ kN/min showing that the effect is thermally activated. The error on A is larger than its value, but the lifetime, T_0 seems reasonable and describes well that the cell keeps the force very stable when the temperatures is decreased below 260-270 K.

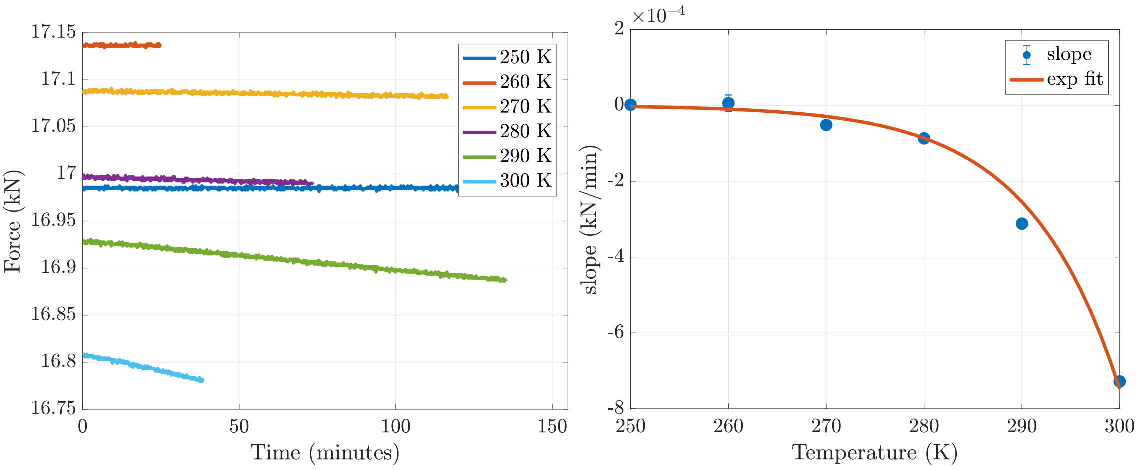

Figure 4.32: Stability test of cell C at temperatures from 300 K to 250 K in 10 K steps. Left: force curves as function of time at the different temperatures. The room temperature calibration error is approximately 0.18 kN for the applied forces and it is therefore not included in the plot to enhance graphical clarity. Right: The slope of linear fits to the force curves in the left figure along with an exponential fit to the slope according to equation 4.7 with $T_0 = 9$ K ± 1 K.

4.6.5 Neutron Scattering Measurements at Room Temperature

We have measured the neutron scattering profile of cell C at the diffuse scattering instrument D7 at the ILL. The experimental conditions are very similar to the measurements that were performed on cell A described in section 4.4 including the sample, which was again HTO. This section contains a description of the room temperature background measurements of cell C, while measurements at 1.5 K are described in the next section.

Figure 4.33 shows a photo of cell C where the cell cage and seats are covered with Cd outside the neutron beam position as it was described for cell A in section 4.4. The HTO sample is hidden inside the cell. The load gauge was placed in the cell during the measurements, but it is not present in the photo.

Figure 4.34 shows the neutron scattering background of cell C, which was measured with an Al nut at room temperature. The figure contains both the spin flip measurements, which contain information on spin incoherent and magnetic scattering profiles, and the non spin flip measurements, which additionally contains information on the nuclear neutron scattering. Both measurements are uniform under sample rotation and thereby fulfil system requirement S4. The rings reflect small variations in detector efficiencies.

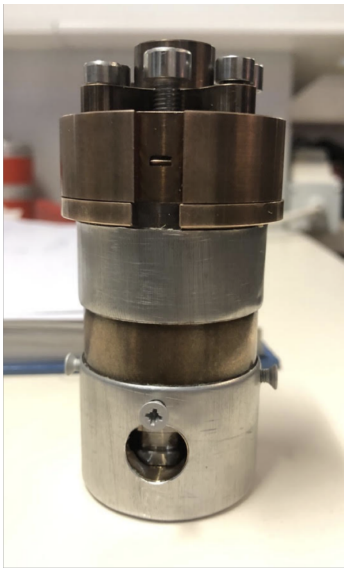

Figure 4.33: Photo of cell C. The cell cage is covered with Cd except around the sample and the seats are covered in Cd except at the sample position (hidden inside the cell). A cylindrical HTO crystal is placed between the steel 316 seats (hidden inside the cell). The photo also shows a hole in the cell cage and a groove in the lid which allows the load gauge wires to exit the cell. The load gauge is not present in the cell on the photo.

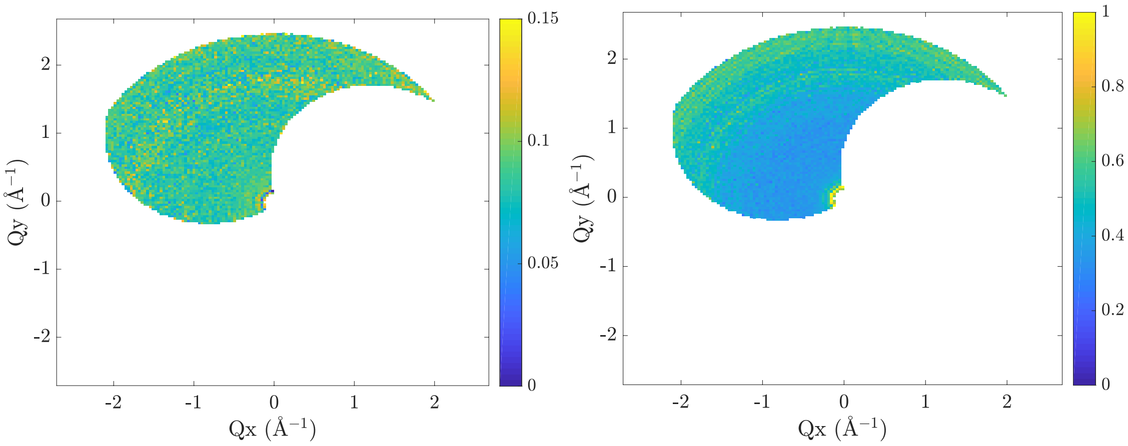

Figure 4.34: Spin flip (left) and non spin flip (right) neutron scattering background measurement of cell C with an Al nut at room temperature. The intensity is plotted on a colour scale as a function of the two components of **Q** in the scattering plane. The cell signal is very uniform with sample rotation (azimuthal rotation in the figures). The rings reflect variations in detector efficiencies. The high intensity for very low scattering angle is caused by the direct beam of unscattered neutrons.

4.6.6 Neutron Scattering Measurements at Cryogenic Temperatures

This section contains a description of the neutron scattering measurements of HTO which were performed at 1.5 K. The measurements were performed at ambient pressure and with 350 MPa applied uniaxially to the sample with cell C.

Figure 4.35 shows the resulting spin flip scattering pattern at ambient pressure (left) and with 350 MPa pressure applied to the sample (right). Unfortunately, we were unable to obtain similar counting statistics for the two setups which is apparant from a larger noise level in the ambient pressure data. The azimuthally averaged SF background signal in figure 4.34 has been subtracted from both data sets in figure 4.35. The diffuse scattering patterns and pinch points which are seen in the figure reveal that HTO is indeed in its correlated phase as expected at 1.5 K. Comparison of the two figures also show that the pressure induced changes are very small.

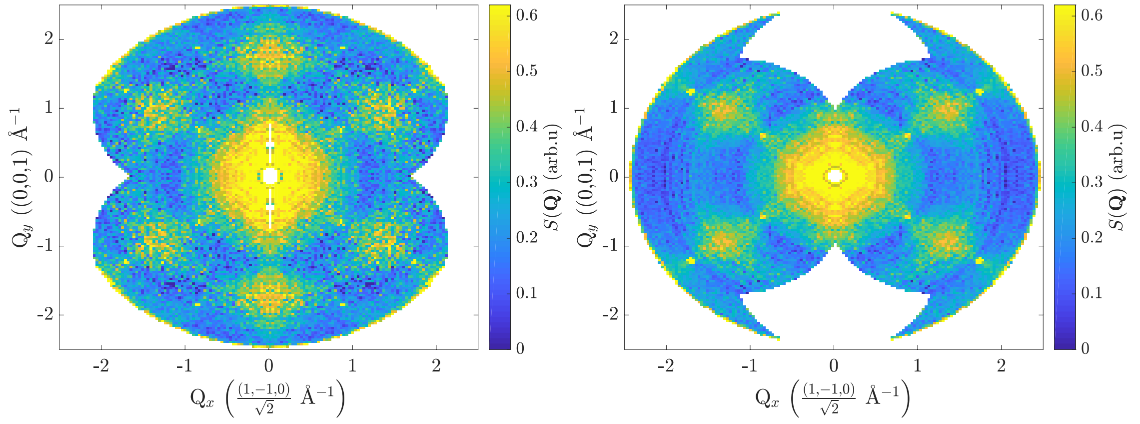

Figure 4.35: 2D spin flip neutron scattering profile of HTO in its correlated phase at 1.5 K at ambient pressure (left) and with 350 MPa pressure applied (right). Both data sets have been symmetrized. The diffuse features and pinch points is well resolved in both figures despite less counting statistics for the ambient pressure data compared to the pressurized data.

Figure 4.36 shows an MC simulation of the scattering profile from pressurized HTO. The simulation has been made by Richard Edberg, and it is described in ref. [20]. The data in figure 4.35 is in arbitrary units, and in order to compare with the simulation, the data has been normalised to the averaged intensity across the high Q diffuse peak. Figure 4.36 shows the 2D difference between the scattering profiles of pressurized, $S_P(Q)$, and non-pressurized data, $S_0(Q)$, defined as

$$\Delta S(Q) = S_P(Q) - S_0(Q). \tag{4.8}$$

For $Q < 1$ Å^{-1} there is qualitative agreement with increased intensity horizontally where $Q_y = 0$ Å^{-1} and reduced intensity outside this region where $Q_y \neq 0$ Å^{-1}. For $Q > 1$ Å^{-1}, the situation is reversed with suppressed intensity at low angles from the horizontal line and high intensity outside this region. The absolute value of the intensity difference is larger for high Q compared to low Q, and it is more noisy.

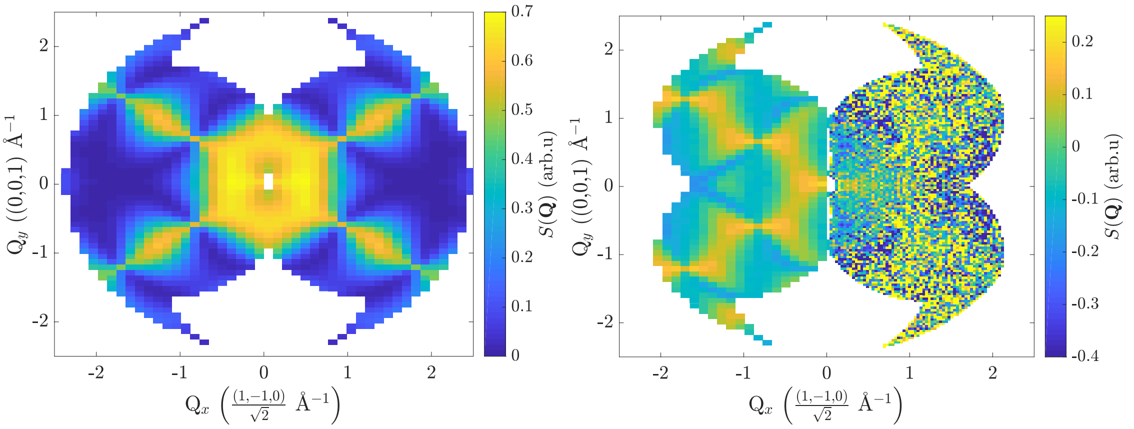

Figure 4.36: Left: MC simulation of the pressurized and non-pressurized S($\mathbf{Q}$) plotted on a colour scale. Right: simulated (left) and measured (right) ΔS($\mathbf{Q}$) obtained from the data in figure 4.35.

Figure 4.37 (left) shows the signal of the data in figure 4.35 integrated across all Q as a function of angle (zero degrees is horizontal). The left figure shows the integrated intensity for the pressurized and non-pressurized data in figure 4.35. The pressure induces a narrowing of the peaks centered at 35 degrees with a possible shift to lower angles. The pressure induces a reduction of the signal at low angles and at $Q_y = 0$ Å^{-1} (zero degrees), there are large fluctuations in both pressurized and non-pressurized data.

Figure 4.37 (right) shows the difference signal between both the data in the left figure and the corresponding Q-integrated MC simulations. The agreement between data and simulation is remarkable and the data is well described by the simulation in all directions. This is especially evident in the region 0-30°. The shift of the 35° peak that was observed in 4.37 (left) is not reproduced by the simulation, and a small discrepancy between difference data and simulation is therefore seen from 30-50°.

Figure 4.38 shows the Q integrated scattering profile when integration is performed for Q < 0.6 Å^{-1} as marked in the left figure. The right figure shows a pressure induced reduction of the signal at high angles, while it slightly increases at low angles.

Figure 4.39 shows the difference curves of both data and MC simulation which have been integrated across low Q (Q < 0.6 Å^{-1}). There is good qualitative agreement between data and simulation in all directions and ΔS(Q) is positive for low angles and negative for large angles for both data and simulation. However, there is a constant offset between data and simulation, ans data is consistently 0.08 below the difference simulation. This could be an effect of a difference in the cell background in pressurized and non-pressurized data. Due to the Poisson effect, the thickness of the cell walls will increase in the pressurized cell compared to the non-pressurized data increasing the neutron absorption in the cell. In addition, the idealized nature of the simulation along with boundary effects might result in

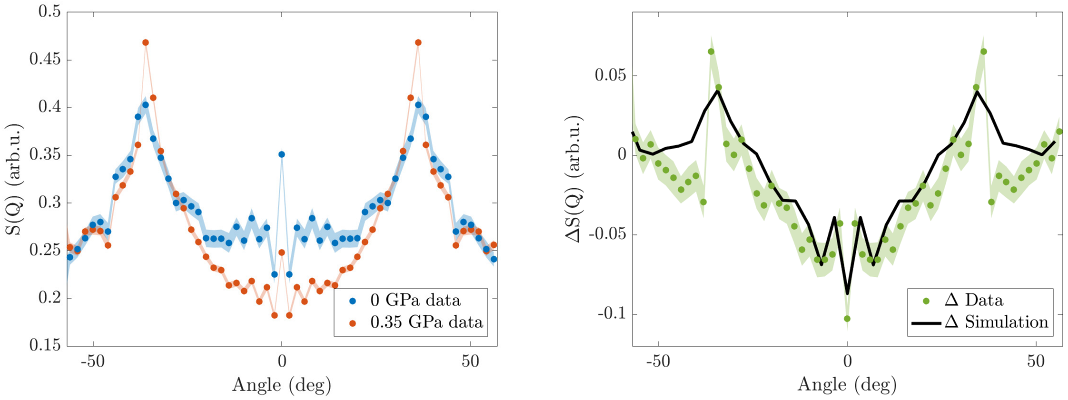

Figure 4.37: Left: angular dependent S(Q) pressurized and non-pressurized data obtained from integration of S(**Q**) in figure 4.35 over all Q. Right: ΔS(Q) difference data between pressurized and non-pressurized S(Q) in the left figure. ΔS(Q) is compared the a simulated ΔS(Q) integrated for the same region in Q.

a small offset in the simulation which becomes important at these small pressure induced signals.

There is a dip in the difference data at 30-40° which is not described by the simulation. This may be an effect of poor resolution in the simulation, which is ultimately limited by the size of the simulated system [20]. However, it could also be a result of a true difference between the simulation and data, possibly due to the simulation limitations described above.

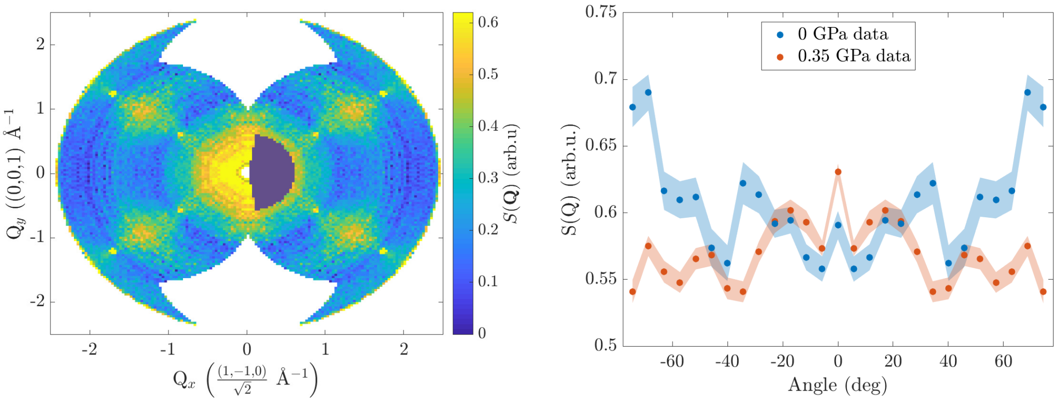

Figure 4.38: Left: S(**Q**) has been integrated for the marked low Q region ($Q < 0.6$ Å^{-1}). Right: angular dependent pressurized and non-pressurized S(Q) integrated for marked low Q region ($Q < 0.6$ Å^{-1}).

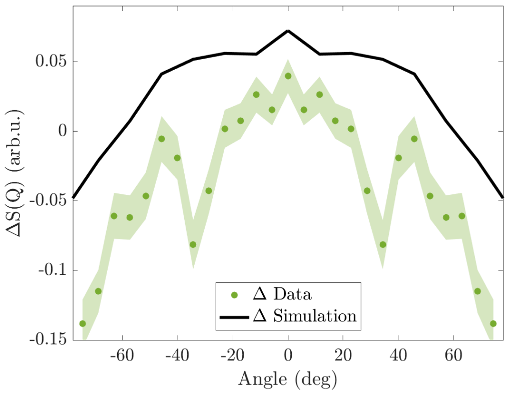

Figure 4.39: Angular dependent difference signal, ΔS(Q) between the pressurized and non-pressurized S(Q) in figure 4.38 where integration has been performed for $Q < 0.6$ Å^{-1}. ΔS(Q) is compared to the the simulated S(Q) integrated for the same region in Q.

4.6.7 Discussion of cell C

Cell C has a uniform neutron scattering background and thus fulfils system requirement S4. The yield strength of steel 316 is 200 MPa, but we were able to apply up to 350 MPa pressure to a cylindrical HTO sample. However, the seats were heavily deformed after the experiment and we will therefore design new seats which resemble the seats and anvils in diamond anvil cells.

We also experienced indentation issues at the tips of the top screws that were used to apply the force. The thread of the screws did not deform, suggesting that the pressure is only slightly above the yield strength. We will therefore increase the screw diameter without changing the material of the top screws in the upgrade to cell D.

Despite indentation issues of the cell, the HTO experiment was highly successful, and we were able to show clear evidence of pressure induced effects through the application of a uniaxial pressure of 350 MPa, whilst no changes were observed when hydrostatic pressure up to 6 GPa was applied [50].

The applied force of cell C decreased by approximately 2.5 % in 30 hours which is below the specifications in system requirement S1. The reduction in force is thought to be caused by small movements of the screws. The difference in thermal contraction between the CuBe lid and the steel screws will increase the friction upon cooling which would increase the stability of the force as it was seen in figure 4.32. The force is almost constant for temperatures below 260-270 K showing that the pressure will be very stable during a neutron scattering experiment at cryogenic temperatures.

4.7 Cell D

The upgrade from cell C to cell D consists of:

- Replacement of the M5 top screws with M8 pinol top screws in order to avoid indentation whilst fulfilling system requirements S1 and S8.
- Replacement of the steel 316 seats with CuBe seats and WC10 anvils in order to fulfill system requirement S1.

This section contains a description of cell D with a special emphasis on the seats and anvils. Additionally, a stability test of the cell is presented along with neutron scattering results measured at the Thales instrument at the ILL, though with steel anvils.

Figure 4.40 shows all parts of the cell D in exploded view in addition to transparent and solid sideviews. Part 1: M8 top screws are used to apply the force. The screw heads do not fit within the size specifications in system requirement S8 and the screws are therefore pinol screws. Part 2: The lid is screwed onto to the cell cage (part 9) and the top screws are screwed through the lid in order to apply the force to the lid and piston (part 3). The cell is mounted on the cryostat by screwing the lid onto an M6 screw. Part 3: The piston transfers the force from the top screws to the upper seat. Part 4: upper seat screws fix the upper seat to the piston. Part 5: there are two identical seats in the cell, the upper and the lower seat. The seats transfer the force to the anvils and reduce the horizontal stress in the anvils as described later in this section. Part 6: sample position. Part 7: the anvils transfer the force to the sample. The highest pressure in the cell for a given applied force is obtained between the anvils and the sample. The remaining parts 8-11 are identical to the similar parts in cell C.

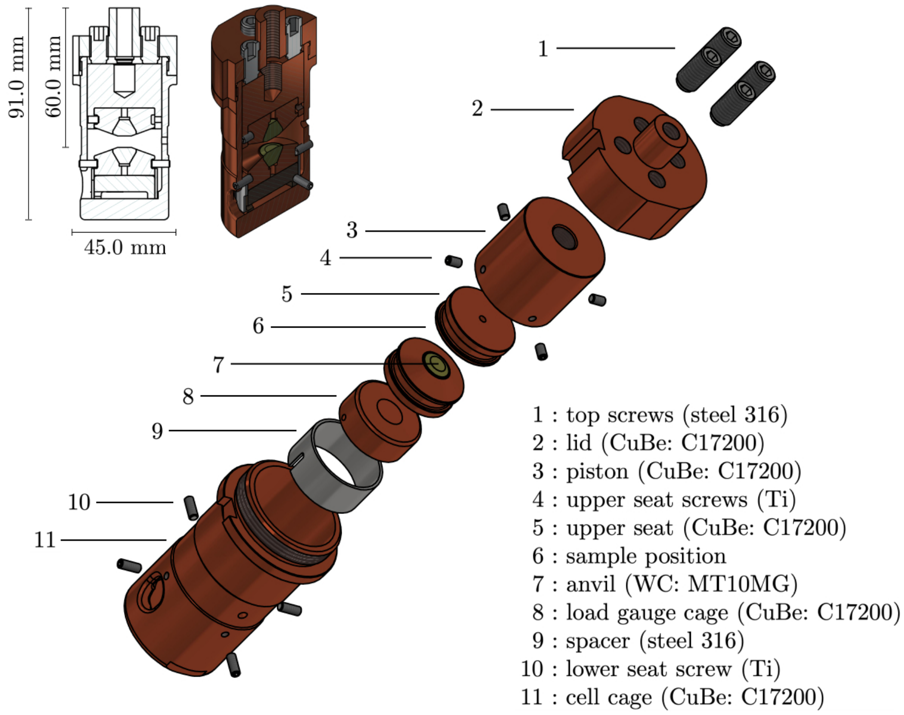

1 : top screws (steel 316)
2 : lid (CuBe: C17200)
3 : piston (CuBe: C17200)
4 : upper seat screws (Ti)
5 : upper seat (CuBe: C17200)
6 : sample position
7 : anvil (WC: MT10MG)
8 : load gauge cage (CuBe: C17200)
9 : spacer (steel 316)
10 : lower seat screw (Ti)
11 : cell cage (CuBe: C17200)

Figure 4.40: Drawings of cell D. Upper left corner: transparent views of the cell. The outer dimensions and the cell mounting-to-sample distance are marked. Center: exploded view of all parts of the cell which are numbered. Lower right corner: The cell parts are named and the materials are listed in parenthesis in the table.

4.7.1 Anvils

An important part of the upgrade from cell C to cell D is the introduction of anvils in the seats in order to reach pressures up to 2 GPa as specified in system requirement S1. The design of seats and anvils are strongly based on the design in a DAC, and the naming convention of DAC anvils that are specified in figure 4.41 are used in the section. Figure 4.41 shows the principle of the seats and anvils. The anvils are made from WC10 that was described in section 4.3, which is very hard, but also brittle. It will not indent in the specified pressure range, but it needs support from the side in order to reduce the horizontal stress in the anvils. This is insured by the design of the CuBe seats which support the anvils around the girdle and lower pavillion. Furthermore, the area is increased by at least a factor of 2 from the culet to the cross section area of the side of the lower pavillion thereby reducing the pressure correspondingly and avoiding indentation of the seats.

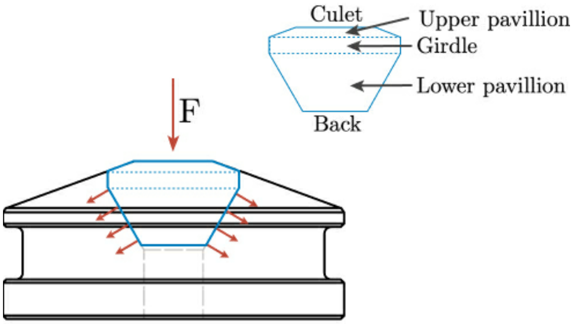

Figure 4.41: Sketch of the principle of the anvils and seats. Left: a vertical force is applied to the culet of the anvil. The force is transferred to the seat through the lower pavillion. The anvil is confined within the seats which reduces the horizontal stress in the anvil. Right: definition of the naming of the different parts of the anvil.

4.7.2 Stability Test of cell D

A stability test displayed in figure 4.42 shows that cell D is able to maintain the applied force within 1 % of the initially applied 12.60 kN in almost 60 hours at room temperature. The cell thereby exceeds the aim in system requirement S1 by a factor of 5. There is a gap in data starting after 19.4 hours because the data files were overwritten in this time period.

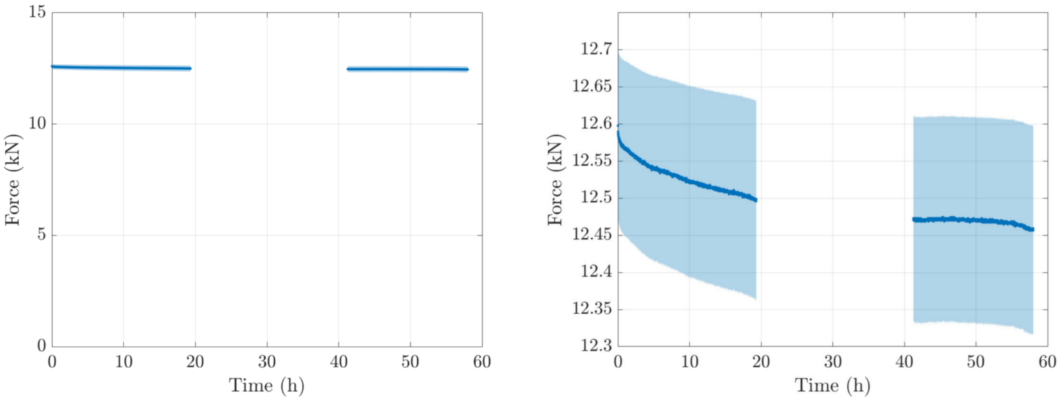

Figure 4.42: Stability test of cell D with full force range (left) and zoom on force axis in order to see the force change. During almost 60 hours the force decreases from 12.60 kN to 12.46 kN which is approximately 1 % of the initially applied force. After 19.4 hours, the data files were overwritten and not logged properly. This error was only corrected 21.6 hours later which is the reason for the missing data points in that time interval.

4.7.3 Neutron Measurement

A neutron scattering experiment was performed with cell D at Thales at the ILL in October 2021 on pressurized $La_{2-x}Ba_xCuO_4$ (LBCO), x = 0.115. At 25 MPa a gradual structural transition measured with μSR shifts the superconducting transition temperature, T_C [4]. The physics of LBCO is both rich and highly unusual, especially around the doping x = 1/8 as described in i.e. ref [70], [48] and [4], but it is outside the scope of this thesis and the analysis on the pressure induced effects on T_C has not been a part of the work of this thesis. Thales is a triple axis spectrometer with a higher spatial resolution than the diffuse scattering spectrometer D7. This enables a direct measurement of the compression of the pressurized LBCO crystal which is the focus of this section.

In the neutron scattering measurements, 30 MPa pressure was applied along the $(1\bar{1}0)$ tetragonal direction of a cylindrical crystal of LBCO with x = 0.115. The crystal had a diameter of 5 mm, a height of 3.9 mm and weight of 0.76 g. The pressure was applied with the steel seats of cell A-C in the neutron scattering experiment, but tests prior to the experiment were performed with the WC10 anvils.

Figure 4.43 shows the $(002)_T$ and $(110)_T$ Bragg peaks at 2 K with and without applied pressure. Unfortunately, the peaks at ambient pressure were measured without collimators, while the beam was collimated at the 30 MPa measurements and the ambient measurements at ambient pressure are therefore significantly broader. Additionally, different counting statistics were obtained, and all peaks in the figure are therefore normalised. The amplitude has been fixed to 1 for all four Gaussian fits while the remaining fit parameters are presented in table 4.2.

Evidently, both Bragg peaks shift when pressure is applied which is a result of a change in lattice parameters a, b, and c, where lattice parameters of the non-pressurized crystal are indexed 0 and lattice parameters of the pressurized crystal are indexed P:

$$a_0 = b_0 = 3.7679(5)\text{Å}, c_0 = 13.2764(6)\text{Å}$$
$$a_P = b_P = 3.7802(2)\text{Å}, c_P = 13.1287(6)\text{Å}$$

The lattice parameters thereby increase by 0.3 % in the ab-plane and decrease by 1.1 % along the c-axis. That the (110) parameters increase seems unexpected, but it is caused by the tetragonal coordinate system. Pressure along $(1\bar{1}0)_T$ introduces an orthorombic splitting and will thereby reduce $(100)_O$ and increase $(010)_O$ and $(001)_O$). The diagonal 110_O (*i.e.* the 100_T) will increase which is consistent with the observation.

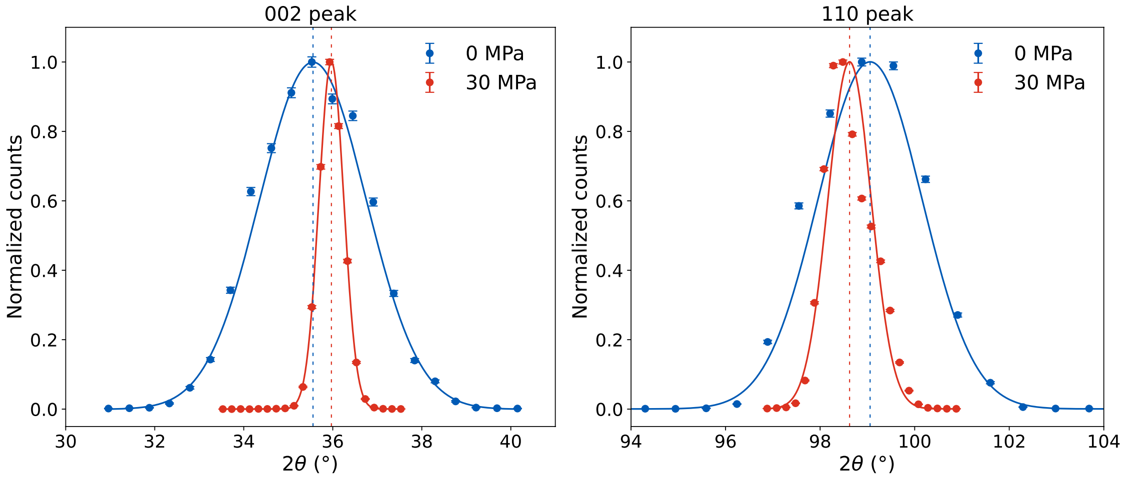

Figure 4.43: Gaussian fits of Bragg peaks (0 0 2) (left) and (1 1 0) (right) at ambient pressure and with 30 MPa pressure applied to a LBCO sample. Fit parameters are presented in table 4.2. All measurements are taken at 2 K at the Thales intrument. The shift in peak positions show that the lattice parameter has increased by 0.3 % in the ab-plane and 1.2 % along the c-axis as a result of the applied force. Figure made by Machteld Kamminga.

Parameter Name	Ambient Pressure Fit	Pressurized Fit
μ_{002}	35.556 ± 0.007	35.964 ± 0.001
σ_{002}	1.194 ± 0.004	0.2784 ± 0.0007
B_{002}	$(0.5 \pm 0.3) \cdot 10^{-3}$	$(0.27 \pm 0.04) \cdot 10^{-3}$
μ_{110}	99.057 ± 0.006	98.6223 ± 0.001
σ_{110}	1.097 ± 0.003	0.4564 ± 0.0008
B_{110}	$(0.5 \pm 0.1) \cdot 10^{-3}$	$(0.6 \pm 0.1) \cdot 10^{-3}$

Table 4.2: Fit parameters of Gaussian fits $(S(Q) = \exp\left(\frac{(x-\mu)^2}{\sigma^2}\right) + B)$ to data presented in figure 4.43.

4.7.4 Discussion of cell D

We have applied 32 kN to the cell without indentation or crack formation of any parts of cell D. The force was applied without any sample substitute, but it corresponds to 2 GPa pressure applied to a 4.5 diameter sample in compliance with system requirement S1. We have also applied up to 800 MPa pressure to a polished cylindrical LBCO crystal of 5 mm in diameter with cell D during testing prior to the experiment. However, the LBCO crystals cracked explosively when force was applied as illustrated in figure 4.44. Other polished cylindrical LBCO crystals exploded at significantly lower pressures down to 50 MPa whereas the polished cylindrical crystal used in the Thales experiment with steel seats was unharmed. In studies of HTO with previous iterations of the cell, vertical cracks have appeared, but the crystal pieces have remained between the anvils, and we have been able to continue the neutron scattering experimen,t since the pieces remain essentially aligned. This is not possible when the crystal cracks like LBCO in figure 4.44 since the crystal pieces are no longer aligned and all pressure on the sample is lost. There are several possible explanations to the discrepancy between the observations with HTO and LBCO. It could be a property of LBCO that it is more brittle compared to HTO.

Figure 4.44: Cell with cracked LBCO crystal after pressurization with 800 MPa viewed from the top of the cell. The crystals cracked dramatically and almost turned into powder upon application of pressure.

Finally, the WC10 anvils are very hard and rigid compared to the steel 316 seats that were used for studies of HTO and they deform very little elastically. Steel 316 can deform elastically and even indent slightly and in this way compensate for any non-parallelism of the sample or cell. It is highly challenging to obtain two planar and parallel surfaces of the sample, and it seems likely that this is even more critical when the WC10 anvils are used instead of the steel 316 seats of cell A-C. It is possible that the applied force is not entirely uniaxial whilst it is applied since it is applied with four screws that are not tightened simultaneously. This will also introduce a small tilt of the piston, seat and anvil, and this will increase the tension in the sample when the WC10 anvils are used compared to the steel seats. The steel seats fit in cell D, and it is therefore advantageous to use these seats if pressures below 300 MPa are desired in order to accommodate small non-parallelisms in the sample or cell. Eventually, this motivated us to use the steel seats for the LBCO Thales experiment after unsuccessful tests had been performed with the WC10 anvils.

4.8 Discussion

We have designed, constructed and tested 4 uniaxial pressure cells, cell A-D that are discussed in this section based on the system requirements. The system requirements of the cells that were specified previously in this chapter are here repeated :

S1 Keep 2 GPa uniaxial pressure constant within 5 % at the sample position during 24 hours.

S2 Allow broad scattering range of at least 180 degrees horizontal and ± 20 degrees vertical scattering.

S3 Measure the applied force at cryogenic temperatures with less than 10 % error.

S4 Obtain uniform and low background from the cell.

S5 Use materials that are thermally conducting even at cryogenic temperatures in order to cool the cell to cryogenic temperatures in less than 24 h.

S6 Use only materials that are non-magnetic.

S7 Accommodate mm-size samples.

S8 Obtain a cell with a maximum diameter of 45 mm so it fits into cryostats of common neutron scattering instruments.

S9 Use only materials that have low neutron activation.

System requirement S1

We have applied 32 kN force to cell D without any cracks or indentation of the cell. Cell C kept 8.30 kN initially applied force constant within 2.5 % during 30 hours, while cell D kept an initially applied force of 12.60 kN constant within 1 % during almost 60 hours. We therefore conclude that cells C and D fulfil system requirement S1 in terms of magnitude and stability of the applied force. However, the force is not completely uniaxial during application, since it is applied with 4 screws. The screws are cross tightened with a torque wrench in small steps and the non-uniaxial component is thereby reduced and close to zero when all four screws are tightened. The piston in cell A had a very tight fit with the cell cage in order to ensure uniaxial pressure on the sample, but the fit was made less tight in later cell iterations to avoid jamming issues that were observed in cell A. This introduces a risk of small horizontal force components which increases the stress in the sample and might break it. The LBCO samples in cell D broke very explosively which might be a result of small non-uniaxial components to the force that are not accomodated by the cell due to the hardness of the WC10 anvils. However, it could also be a result of the sample preparation or internal properties of LBCO.

System requirement S2

All four iterations of the cell allows ± 20 degrees vertical scattering and ±180 degrees horizontal scattering and they thereby fulfill system requirement S2.

System requirement S3

Cells B-D contain a load gauge and is thereby able to measure the applied force in-situ. Cell B contains a commercial load gauge KMR40, which is able to accurately measure the applied force at room temperature, but it breaks whenever it is cooled below 75 K - 80 K. This is most likely caused by condensation of air in the load gauge cage or a phase transition of some of the solid materials in the load gauge which causes the strain gauge glue to crack or losen. However, we were not able to obtain a detailed technical description of the load gauge since it is commercially available. Instead, we designed, constructed, tested and calibrated a load gauge which works well at cryogenic temperatures and was used in cells C and D. The load gauge is highly sensitive and can register relative changes in force below 1 N when applied with a finger. However, non-uniaxial components introduced by small variations in the cell assembly cause slightly different calibration curves which results in a larger calibration error. The load gauge determines the force most accurately for forces in the range 15 kN to 25 kN where it has a relative uncertainty below 5 %. 15 kN corresponds to 2 GPa pressure to a sample of 3.1 mm in diameter while 25 kN corresponds to 2 GPa pressure on a 4 mm diameter sample and typical samples are expected to have dimensions in this range. The load gauge fulfils system requirement S3 for forces above 5 kN where it has relative uncertainty below 10 %.

System requirement S4

Cell A was designed with large windows with an aim to reduce the background signal. However, this resulted in a very distinct and non-uniform background caused by attenuation effects in the cell. These effects were more significant than the diffuse profiles of HTO, and the windows were therefore removed in later iterations of the cell. In cells B-D, the cell wall is thinned from 3 mm to 2 mm around the sample position which reduces the absorption from approximately 40 % in cell A to 30 % in cell B-D. The neutron scattering background of cell C measured at D7 was very uniform with sample rotation and it was possible to clearly resolve the diffuse features of HTO in its correlated phase, and also extract pressure induced changes in the diffuse features. With the increased flux that will soon be accessible in new neutron sources such as the European Spallation Source, a uniform background is valued above absorption. The neutron scattering background of cells

B and D are expected to be highly similar to cell C, since they have identical cell cages and the remaining part of the cells are shielded by Cd. Cells B-D thereby fulfil system requirement S4.

System requirement S5

We were able to cool cell C from room temperature to 21 K in approximately 30 hours with many intermediate steps in order to allow the system to reach thermal equilibrium before measuring the load gauge readout. The room temperature thermal conductivity of WC10 is more than 3 times larger than steel 316 which was used in cell C, and we therefore expect that all four cells comply with system requirement S5.

System requirement S6

All materials that are used in the cells are non magnetic, with a magnetic permeability less than 1.01, and can be used in conjunction with polarisation analysis. This was shown by the two successful experiments at the D7 at the ILL, where polarisation analysis was applied.

System requirement S7

All four cells can accommodate samples that are up to 8 mm high and 6 mm in diameter thereby fulfilling system requirement S7.

System requirement S8

All four cells have an outer diameter of 45 mm and thereby fit into the most commonly used cryostats. Furthermore, the distance from sample position to the top of the cell where it is attached to the sample stick is 60 mm which is also in compliance with commonly accepted distances. Specifically, successful neutron scattering experiments were performed at the D7 and Thales instruments at the ILL.

System requirement S9

The amount of Co in CuBe is informed by the manufacture to be in the range 0-0.6 %, but the exact amount of Co is important with regards to neutron activation due to the large amount of CuBe. If the cell is active, one cannot remove it from the facility and transport it elsewhere. Considering a Co content of 0.6 % would give rise to a very high activation rate, upon 5 days of beamtime on D7, such that it would take 38 years before the cell had less than $5 \cdot 10^{-4} \mu$Ci. We covered the cell in Cd and therefore protected the cell from activation such that we were able to retrieve cell C within weeks after a 5 day experiment at D7 in October 2019 and it is therefore not a problem in regards to system requirement S9. However, the anvils contain 10 % Co. It is not possible to cover the culets of the anvils with Cd and we will therefore construct several pairs of seats and anvils which are stored at the facilities since they are expected to be difficult to retrieve due decay time of Co which is 5.3 years.

4.8.1 Outlook: Cell E

It is very important to ensure that the applied force is as uniaxial as possible when using the WC10 anvils. We therefore suggest a new design, cell E, where the force is applied with a single top screw. Cell E has currently only been designed, and this section therefore contains a description of the design and the ideas behind the design as well as a discussion on possible challenges with this design.

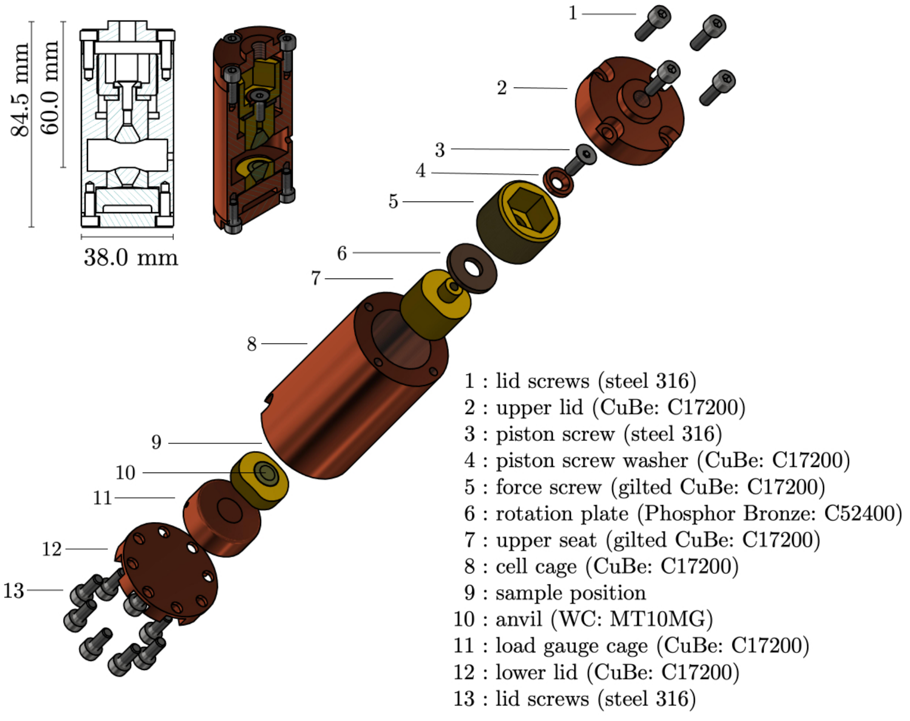

1 : lid screws (steel 316)
2 : upper lid (CuBe: C17200)
3 : piston screw (steel 316)
4 : piston screw washer (CuBe: C17200)
5 : force screw (gilted CuBe: C17200)
6 : rotation plate (Phosphor Bronze: C52400)
7 : upper seat (gilted CuBe: C17200)
8 : cell cage (CuBe: C17200)
9 : sample position
10 : anvil (WC: MT10MG)
11 : load gauge cage (CuBe: C17200)
12 : lower lid (CuBe: C17200)
13 : lid screws (steel 316)

Figure 4.45: Drawings of cell E. Upper left corner: transparent views of the cell. The outer dimensions and the cell mounting-to-sample distance are marked. Center: exploded view of all parts of the cell which are numbered. Lower right corner: The cell parts are named and the materials are listed in parenthesis in the table.

Figure 4.45 shows cell E in an exploded view as well as transparent and solid sideviews. Part 1: the lid screws are used to connect the lid (part 2) and cell cage (part 8). The force on the lid screws origin from the cell gravity and they are thereby not exposed to large forces. Part 2: the cell is mounted on a sample stick with the M6 screw hole in the upper cell lid. Part 3: the piston screw connects the force screw (part 5) and the upper seat (part 7). It does not need high pressure cababilities. Part 4: piston screw washer. Part 5: the force is applied with the force screw. There is a thread on the outside of part 5 which matches the thread on the inside of the cell cage (part 8). The force screw is gilted in order to prevent cold welding of the force screw and cell cage due to the large friction between them. Part 6: the rotation plate allows the force screw to rotate when force is applied without transferring a large torque to the upper seat (part 7) in order to prevent rotation of the upper seat and anvil with respect to the sample. Part 7: The upper seat transfers the vertical force from the rotation plate to the anvil. The oval shape of the upper seat and inside of the cell cage (part 8) absorbs the torque that is transferred from the force screw to the upper seat through the rotation plate. Any small rotation of the upper seat will occur at very low forces when the initial force is applied and the seat rotates slightly with respect to the cell cage. The upper seat is gilted in order to prevent cold welding of the upper seat and cell cage due to the large friction between them. Part 8: the cell cage. The cross section of the inside of the cell cage is circular at the top and bottom of the cage where the force screw (part 5) and load gauge (part 11) are contained respectively. The cross section of the inside of the central part of the cell cage is oval in order to increase the friction between the seats and cell cage in order to minimize any torque on the sample. The sample is placed at position 9. Part 10: the anvils are similar to the anvils in cell D. Part 11: the load gauge is similar to the load gauge in cell C and D. Part 12: the introduction of a lower lid makes it easier to insert the load gauge since the load gauge wires can exit a groove in the cell cage in stead of a hole. This allows for a tighter fit between the load gauge and the inside of the cell cage which reduces the calibration error of the load gauge. Part 13: The lower lid screws attach the lower lid to the cell cage.

Application of the force with a single screw removes the risk of horizontal components to the force, but it introduces a risk of applying a torque to the sample from the upper anvil. Figure 4.46 shows a top view of the cell with the seat in orange and the inner part of the cage in blue. The oval fit creates a large rotational friction between the two parts which prevents rotation of the seat. Any small rotation will occur when the force is initially applied, and the torque on the sample is therefore expected to be minimal.

75 Nm is needed to apply 22 kN which is close to the limit when force is applied by hand even if the wrench has a long arm. If larger forces are required, gearing is needed, but this will further complicate the design - especially due to the size specifications of system requirement S8. Gearing is therefore not suggested for cell E.

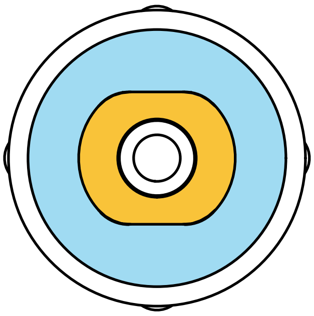

Figure 4.46: Top view of cell E which shows the oval shape of the inner side of the blue cell cage (part 8 in figure 4.45) and the yellow upper seat (part 7 in figure 4.45). The oval fit is designed to prevent rotation of the upper seat with respect to the sample.

4.9 Conclusion

We have managed to create a uniaxial pressure cell which is suited for the study of strongly correlated and frustrated magnetic materials by neutron scattering techniques. The cell has a highly uniform neutron scattering background which enables detection of pressure induced changes that are just a few percent of the weak diffuse scattering profile of HTO. We are able to apply 32 kN with the cell, corresponding to 2 GPa on a 4.5 mm sample without any indentation of crack formation of any parts of the cell. The most up to date pressure cell, cell D, has been used to study magnetic variations in LCBO upon the application of 800 MPa uniaxial pressure. Suggestions are made to optimise the uniaxial nature of the pressure cell with cell E. For pressures up to 350 MPa, the cell is able to meet all system requirements and can be used directly for neutron scattering experiments, both elastic and inelastic, and with the application of polarisation analysis.

Chapter 5

Spin Ice Under Uniaxial Pressure

This chapter is a short introduction to the physics in classical spin ice compounds and the effects of applying uniaxial pressure to $Ho_2Ti_2O_7$ (HTO) and $Dy_2Ti_2O_7$ (DTO) with an emphasis on HTO, This work resulted in the publications [19, 20]. Additional two manuscripts, [60] and [27] will be submitted shortly.

5.1 Spin Ice

Spin ice is an example of an underconstrained system where a macroscopic amount of ground states all minimize the interaction energy whilst obeying the lattice geometry and anisotropy. The field has been heavily studied and is well presented in several reviews including refs. [15, 23, 28]. The following is a short summary of the results in the field.

Structure

In spin ice compounds, magnetic ions occupy the pyrochlore lattice consisting of corner-sharing tetrahedra as illustrated in figure 5.1(left). The crystal field creates a strong easy axis which connects the centres of adjacent tetrahedra (defined as the local (111)-axis), and the spins are therefore well approximated by Ising spins. AFM NN interactions is at the origin of the frustration in many frustrated compounds, for instance AFM coupled collinear Ising spins on a triangle as it was described in chapter 2.3. However, in spin ice compounds, AFM NN interactions result in a non-frustrated all-in-all-out state, where all spins on a tetrahedron point either *in* towards the centre or the *out*, away from the centre. In contrast, FM NN interactions result in a highly frustrated ground state manifold which follows the *ice rules*. The rules dictate that for each tetrahedron, two spin must point *in* towards the centre and two spins must point *out* away from the center in a two-in-two-out state.

There is a macroscopic amount of states which fullfill the ice rules on the pyrochlore lattice, and fluctuations between the states suppress long range order. One state which obeys the ice rules is illustrated in figure 5.1(left) for the pyrochlore lattice. In order to enhance graphical clarity, a 2D projection of the pyrochlore lattice is presented in figure 5.1 where each cross represents the centre of a tetrahedron and spins are restricted to point along the lines of the square lattice.

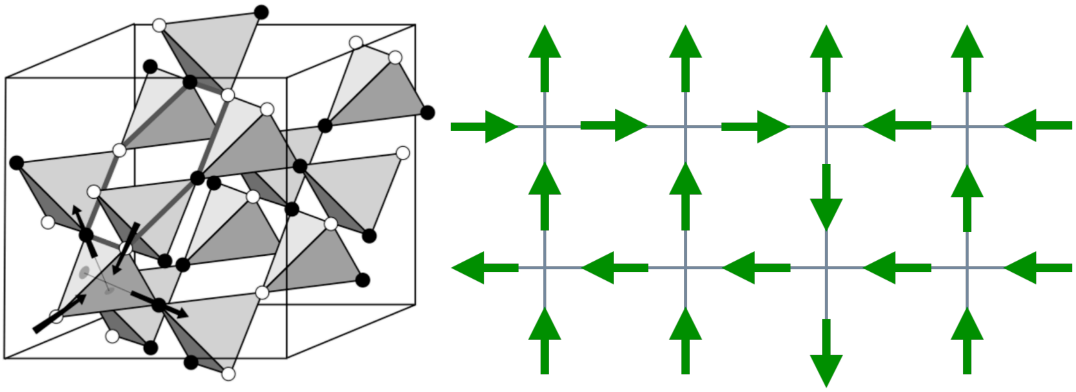

Figure 5.1: Left: The pyrochlore lattice which consists of cornersharing tetrahedra. Arrows mark spins in a two-in-two-out state of a single tetrahedron and the spin orientations of the remaining spins are marked by black or white colours of the spin sites. Figure from [10]. Right: 2D square spin ice where the pyrochlore lattice has been projected onto a 2D square lattice. Crosses in the lattice represent the centres of each tetrahedron and spins are restricted to point along the lines. One spin configuration from the ground state manifold is sketched which follow the ice rules, two-in-two-out configuration.

Famous examples of *classical spin ice compounds* are $Ho_2Ti_2O_7$ (HTO) and $Dy_2Ti_2O_7$ (DTO) where the magnetic rare earth ions Ho^{3+} with J = 8 and Dy^{3+} with J = 15/2 respectively occupy the pyrochlore lattice. Interestingly, both HTO and DTO have AFM NN exchange interactions, but these are very weak, and dipole interactions therefore ensure effective FM NN interactions in these systems resulting in a frustrated spin ice state. HTO and DTO are therefore also referred to as dipole spin ice compounds.

Excitations

One of the main reasons for the intense interest in spin ice compounds are the excitations which are well described as magnetic monopoles and an emergent gauge field [38, 15]. Figure 5.2 shows the principle described with an excitation from the 2D square spin ice state illustrated in figure 5.1(right). Initially, the circled spin is flipped which creates a 3-in-1-out state and 1-in-3-out state of the two adjacent tetrahedra which are mapped as a positively and negatively charged magnetic monopole respectively. Without adding any additional energy to the system, the spins of these two tetrahedra can now flip resulting in a translation of the magnetic monopoles.

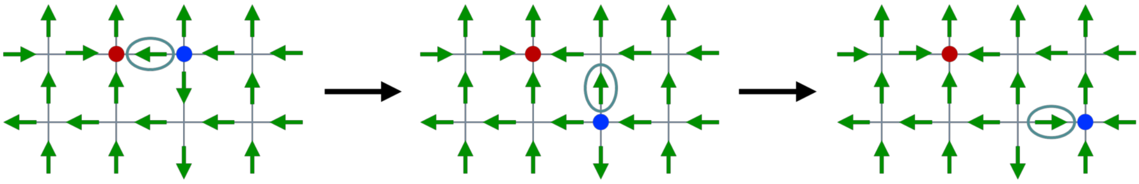

Figure 5.2: Illustration of the fractional excitations which are described as magnetic monopoles. Left: the marked spin is flipped which causes the two adjacent tetrahedra to have states tre-in-one-out (red) and one-in-three-out (blue) which are described as a magnetic positive and negative monopole respectively. Flipping spins within the monopole tetrahedra will move the monopoles to other tetrahedra as shown in the center and right figure without increasing the energy of the system. The two fractional monopole excitations are thereby delocalized.

5.2 Spin Ice Under Uniaxial Pressure

As discussed in chapter 4, uniaxial pressure changes the crystal symmetry in contrast to hydrostatic pressure, and even low uniaxial pressures can therefore strongly pertube the balance between competing interactions in a magnetically frustrated compound. HTO and DTO have been heavily studied during the past 15 years, and as a result they are very well characterized and understood at ambient pressure. This is an excellent starting point when the balance between the interactions are changed upon application of uniaxial pressure which motivated the choice of HTO and DTO for these studies. Figure 5.3 shows a single tetrahedron in the pyrochlore lattice which is exposed to pressure from 3 different directions.

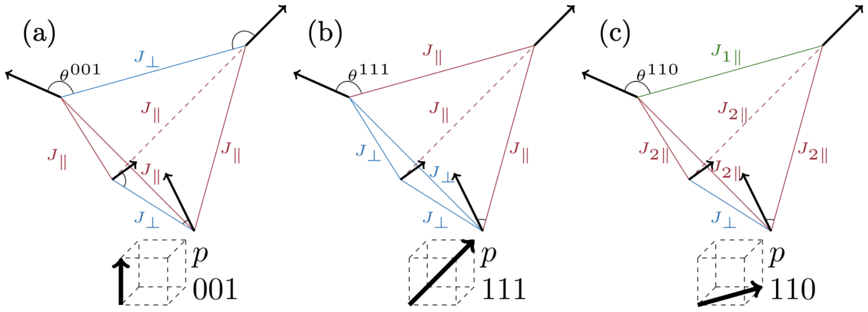

Figure 5.3: Sketch of the effect of application of uniaxial pressure to a single tetrahedron with pressure applied along the specified crystallographic directions. Blue bonds are orthogonal to the pressure directions and do not change in the simulations. Red and green bonds both have parallel components to the applied pressure and interactions across these bonds vary with pressure in the simulations. Spins are restricted to point towards the centre of the tetrahedra defined by the pressure dependent angle θ. Figure by Richard Edberg from [20].

In the MC simulations, which were performed by our collaborators, the system is assumed to have zero Poisson ratio, as described in chapter 4, meaning that only bonds which have spatial components along the direction of the applied pressure will change. The optimised Hamiltonian include nearest neighbour exchange interactions and long-range dipolar interactions described in chapter 2. In the simulation, Ising spins are restricted to point towards the centre of the tetrahedra, thereby altering the local (111) direction by a pressure dependent angle, θ, as defined in figure 5.3.

5.2.1 Magnetisation Measurements

MC simulations of DTO have been compared to magnetisation measurements performed by Mito et al. [52]. The local anisotropy angle, θ, changes the magnetic moments parallel to the applied magnetic field and thereby the magnetic saturation at high fields which can be used to determine the crystallographic compression in the simulation.

Figure 5.4 shows that the simulations are able to reproduce the magnetisation measurements of DTO when pressure is applied along the (001) and (111) directions. When pressure is applied along the (110) direction, there is good agreement for low applied magnetic fields (B < 1.5 T), but the measured change in magnetization is not saturated even at the highest applied fields, while this is the case for the simulated result.

As discussed in [20], alignment of the crystal, pressure and the magnetic field is especially important along the (110) direction, because half the spins have a local (111) direction perpendicular to the magnetic field at ambient pressure. In fact, very small misalignments of less than 1° results in a significant change in the saturation field as discussed for the HTO results later in the section.

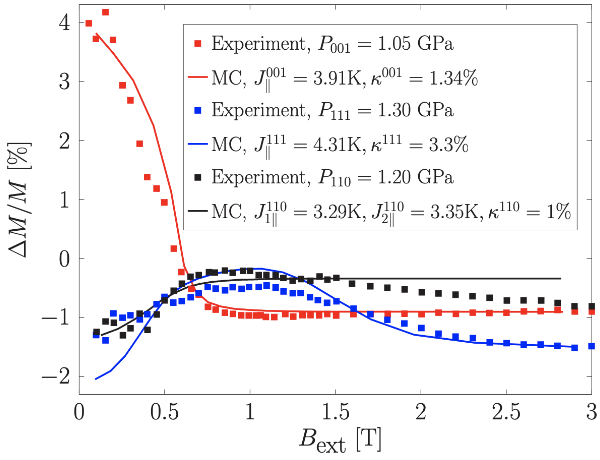

Figure 5.4: Magnetisation measurements from ref. [52] and MC simulations of DTO under uniaxial pressure along three different crystallographic directions. Figure by Richard Edberg from [19].

We have performed magnetization measurements on polished cylindrical HTO crystals of height 3.0(5) mm and diameter 2.0(5) mm at a superconducting quantum interference device (SQUID) magnetometer (Quantum Design MPMS-XL) using a piston-cylinder type of pressure cell (CR-PSC-KY05-1, Kyowa-Seisakusho Co., Ltd.) [20] with the same experimental setup that was used by Mito et al. to make the magnetization measurements of DTO presented in figure 5.4.

We have grown the crystals using the floating zone technique with 3 mm/h growth speed. The high quality of the HTO single crystals, indicated by visual inspection as seen in figure 5.5(left), were confirmed by diffraction measurements at the D9 instrument at the ILL as described in [27]. The crystals were polished into cylindrical samples as shown in figures 5.5(center) and 5.5(right).

Figure 5.5: Left: As-grown HTO rod using the floating zone technique. The central part of the rod (from 2 mm to 13 mm on the scale) is a single crystal while the top and bottom part is polycrystalline. Center: polished, cylindrical HTO single crystal shows the high quality of the crystal polishing. The sample has diameter 2.0(5) mm and height 3.0(5) mm (used for magnetisation measurements). Right: cylindrical polished HTO crystal placed on the seats and piston of cell C (used for neutron scattering measurements). The sample has a diameter of 3.0(5) mm and a height of 3.0(5) mm.

Figure 5.6 shows the measured and simulated relative change in magnetization when pressure is applied along the crystallographic directions (001) and (110). Figure 5.6(left) shows that the MC simulations capture well the measured pressure induced changes along the (001) direction. Figure 5.6(right) shows that there is qualitative agreement between simulations and data when pressure is applied along the (110) direction, but again the simulations show saturated magnetizations while this is not observed in data.

Figure 5.6(right) contains two different simulations, one where the alignment between magnetic field and crystal is assumed perfect, and one where there is a small angle, $\delta\phi$, between them. Even very small angles less than 1° has a large effect on the magnetization curves along the (110) direction, while similar effects are not seen along the (001) and (111) directions where all spins have components parallel to the applied field. The alignment uncertainty in the experimental setup is approximately 5°, and the discrepancy between data and simulations along the (110) direction for both DTO and HTO is therefore assigned to a small misalignments during the experiment within the uncertainty. However, despite the inclusion of misalignment effects in the simulations, they do not capture all features in data along the (110) direction.

A comparison between the high field magnetization curves in figures 5.4 and 5.6(left) when pressure is applied along the (001) direction shows that DTO and HTO have different saturation magnetizations (1.34 % and 0.8 % for DTO and HTO respectively) indicating that the compounds have different compressibility. The magnetization curve in figure 5.4 shows an increase of the effective magnetic moment of Dy^{3+} along the (001) with ΔM/M = 4 % when 1.05 GPa pressure is applied along the crystallographic (001) direction. When pressure is applied along the (001) direction, the MC simulations show that the ground state manifold is split into two different manifolds with spin chains parallel and perpendicular to the applied field respectively. The increased magnetization for DTO shows that the parallel spin chain states have lower energy thereby reducing the amount of degeneracy in the system. Interestingly, figure 5.6(left) shows that the magnetic moment along (001) decreases for HTO by approximately 2 % when 1 GPa pressure is applied along the same crystallographic. This difference is assigned to the ratio between exchange and dipolar interactions in HTO and DTO, where exchange interactions are stronger in DTO than in HTO compared to the dipolar interactions and different ground states in the ground state manifold are thereby selected for HTO compared to DTO.

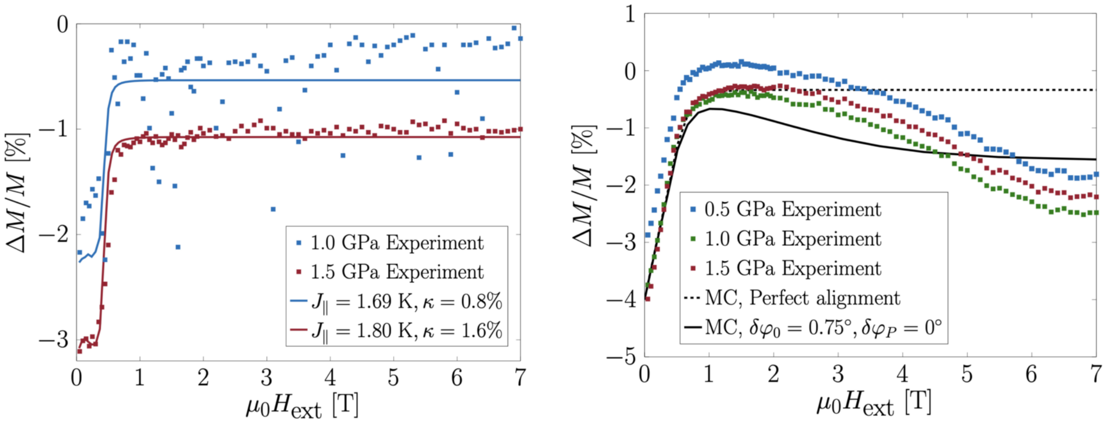

Figure 5.6: Magnetization measurements of HTO with uniaxial pressure applied. Left: Change in magnetization when uniaxial pressures of 1.0 GPa and 1.5 GPa applied along (001). Right: Change in magnetization when uniaxial pressures of 0.5 GPa, 1.0 GPa and 1.5 GPa applied along (110). MC simulations of pressure applied along (110) have been performed with perfect alignment between crystal and magnetic field and where an angle, $\delta\phi$, between the field and crystal orientation is a varied. The exchange parameters in the right figure are $J_{||} = 1.2$ K and $\kappa = 1$ %. Figures by Richard Edberg from [20].

5.2.2 Neutron Scattering Measurements of HTO

Two different neutron scattering experiments have been performed at the D7 instrument at the ILL with uniaxial pressure applied to HTO single crystals. In both neutron scattering experiments, pressure was applied to polished, cylindrical HTO samples of height 3.0(5) mm and diameter 3.0(5) mm as discussed in detail in sections 4.4 and 4.6.

Natural Dy^{3+} is a very strong neutron absorber (994 barn for 2200 m/s neutrons [22]) and isotopically enriched Dy^{3+} such as $^{162}Dy^{3+}$ with a much lower neutron absorption is highly expensive. Many crystal samples crack upon pressure application rendering neutron scattering experiments with uniaxial pressure applied to enriched DTO unrealistic at this moment in time. Fortunately, Ho^{3+} is not a strong neutron absorber (65 barn for 2200 m/s neutrons [66]) enabling neutron scattering experiments with HTO samples which are isostructural to DTO and displays much of the same physics as DTO.

In the first neutron scattering experiment in 2018, pressure was applied along the (001) direction (figure 5.3.a) with pressure cell A and resulted in the publication [19]. The neutron scattering experiments and the publication was made prior to the HTO magnetization measurements and the MC simulations were therefore based on the results of DTO. HTO and DTO are isostructural and are both classical spin ice compounds and they were therefore assumed to have equal compressibility. This enabled a direct application of the results of the MC simulations of DTO to simulate the expected neutron scattering response of HTO to uniaxial pressure. In the MC simulations of HTO, only the exchange interaction, parametrized by $J_{||}$ defined in figure 5.3, was varied. The extensive efforts to perform a background subtraction was discussed in section 4.4 and qualitative agreement between data and MC simulations was obtained at high Q while background effects dominated the low Q region.

The crystal alignment with pressure applied along the (001) direction was chosen based on the large response in magnetization measurement of DTO compared to pressure applied along (110) and (111). However, the magnetization measurements of HTO presented in figure 5.6 show that the difference in relative strength of the dipolar and exchange interaction reduce the energy in different spin ice states from the ground state manifold. As a result, application of pressure along the (110) direction induces the strongest response in magnetization measurements and pressure was applied along this direction in the second neutron scattering experiment, which was performed at D7 in October 2019.

A reduction of the degeneracy in the ground state manifold will primarily result in a narrowing of the observed neutron scattering diffuse features. There is a directional dependence of magnetic neutron scattering, which is only sensitive to spins in the scattering plane perpendicular to $\mathbf{Q}$. However, all spins have spin components perpendicular to the (110) direction, and neutron scattering measurements are therefore less sensitive to the alignment issues presented in the magnetization measurements for pressures along (110).

In the second neutron scattering experiment, 0.35 GPa pressure was applied along the (110) (figure 5.3.c) direction with the optimised pressure cell C as described in section

4.6. This resulted in publication [20], but additional unpublished results were presented in section 4.6 which will be published in [60]. These results show distinct pressure induced changes which are well described by the MC simulations.

5.3 Conclusion

Neutron scattering measurements of HTO under uniaxial pressure show distinct pressure induced features. These have been MC simulated by our collaborators based on magnetization measurements of HTO and DTO showing that the ground state manifold of spin ice states is split and the degeneracy is reduced upon application of uniaxial pressure.

Chapter 6

Ytterbium Gallium Garnet

6.1 Introduction

Three dimensional (3D) geometrically frustrated compounds with rare earth ions have been shown to display novel and emergent behaviour in recent years as a result of the interplay between the spin-spin interactions and the anisotropy. One example is the classical spin ice compound $Ho_2Ti_2O_7$ (HTO), described in chapter 5, where the rare earth ions occupy the pyrochlore lattice formed by cornersharing tetrahedra. In HTI, it is possible to model the excitations as magnetic monopole excitations.

Another 3D lattice which often results in frustration is the *garnet* lattice, which consists of two interpenetrating *hyperkagome* lattices illustrated in figure 6.1. In $Gd_3Ga_5O_{12}$ (GGG), where Gd^{3+} ions occupy the two hyperkagome lattices, a long range hidden order has been found where the collective spin of each 10-ion loop, called the *director*, shows long range correlations despite absence of any long range correlations of the individual spins [56]. The director, $\mathbf{L}$, of position $\mathbf{rc}$ is defined as,

$$\mathbf{L}(\mathbf{rc}) = \frac{1}{10}\sum_{n}\cos(n\pi)\mathbf{S}_n(\mathbf{r}), \tag{6.1}$$

where $\mathbf{S}_n(\mathbf{r})$ is the n'th normalised spin on the 10-ion loop centered in $\mathbf{rc}$ marked by the orange ion in figure 6.1. The long range correlations of the director state in GGG governs both magnetic structure [56] and dynamics [5]. NN spins in GGG couple antiferromagnetically (AFM) and have an easy plane anisotropy in the local XY plane defined in figure 6.1.

$Yb_3Ga_5O_{12}$ is isostructural to GGG. It has a unit cell of dimensions a = 12.204(4) Å. There are two characteristic distances across 10-ion loop in figure 6.1, 8 of the ions are separated by 11.210 Å while there is 12.204 Å between one pair of ions in each loop. A strong spin orbit coupling in the ground state level $^2F_{7/2}$ of the Yb^{3+} ions could result in a strong anisotropy. Furthermore, the ground state Kramers doublet, which has an effective

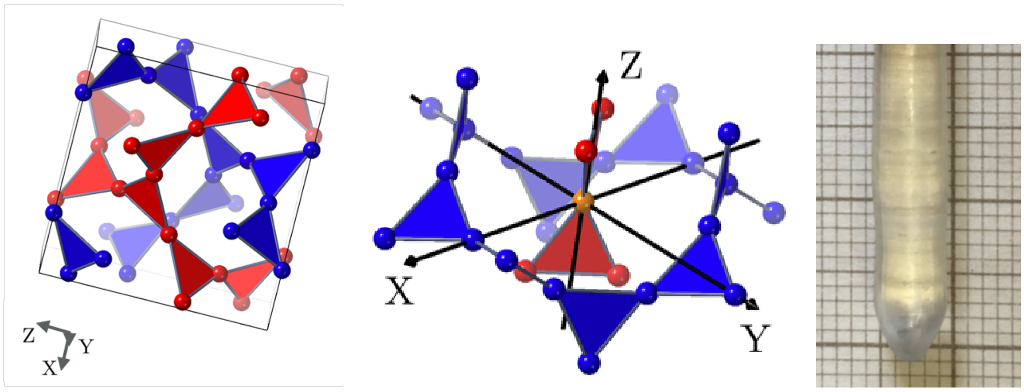

Figure 6.1: Left: 24 Yb^{3+} ions of the YbGG unit cell. The colour represent two different interpenetrating hyperkagome lattices. Triangle surfaces between neighbouring Yb^{3+} ions are coloured. The two nearest neighbours are within the same hyperkagome lattice, while third nearest neighbours belong to opposite hyperkagome lattices. Center: Definition of the local coordinate system of the central orange Yb^{3+} ion which is a part of the red hyperkagome lattice. Right: Photo of the single crystal YbGG which was used for the neutron scattering measurements described later in the chapter.

spin S = 1/2, is well isolated from the first excited Kramer's doublet predicted to be found 63.5 meV (736 K) [59] above the ground state, enabling strong quantum effects in YbGG. Quantum effects are widely expected to generate novel states of matter including quantum spin liquid states and topological order [11].

Figure 6.2 shows the temperature dependence of the heat capacity measurements by Filippi et al [25]. It resembles the temperature dependence of the heat capacity of HTO, DTO and GGG, in particular the broad peak centred at 180 mK and extending up to 600 mK which represents the correlated spin ice phase of HTO and DTO[28] and the correlated director state in GGG [56]. Below the broad peak in figure 6.2, the heat capacity has a lambda transition at 54 mK which was originally assigned to a magnetic ordering [25], but later attempts to confirm the magnetic order with muon spin resonance and Mössbauer spectroscopy showed a disordered magnetic moment down to 36 mK [17, 35].

Figure 6.1 shows a photo of a large single crystal YbGG grown using the floating zone method in an Ar + O_2 gas atmosphere with a growth rate of 10 mm/h [43]. The quality and size of the crystal has enabled us to study YbGG with cold elastic and inelastic neutron scattering.

In this section we show the results of a reinvestigation of the crystal field levels of YbGG with thermal inelastic neutron scattering and susceptibility measurements along with results and analyses of cold elastic and inelastic neutron scattering measurements. These results lead to the publication ref. [61].

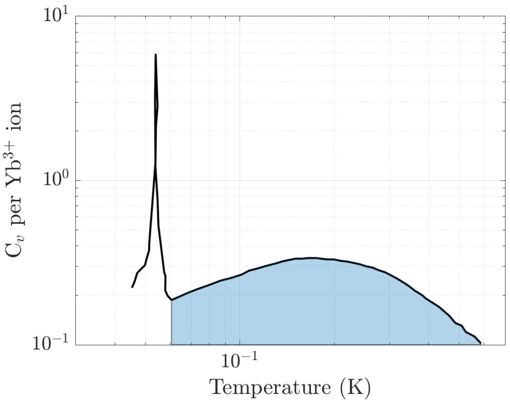

Figure 6.2: Heat capacity measurement of YbGG by Filippi et al Figure reproduced from ref. [25]. Above the lambda transition at 54 mK, there is a broad feature marked in blue which resembles the broad feature in the spin ice compounds HTO and DTO where it represents a short range correlated state. Both axes are logarithmic.

6.2 Crystal Field Interactions

This section contains a description of the crystal field interactions in YbGG which are able to predict the three lowest crystal field excitations measured with thermal inelastic neutron scattering and the magnetic susceptibility except at the very lowest temperatures.

Pearson et al. calculated the Stevens parameters where they neglect all spin-spin interactions including exchange [59]. The calculations were been optimized to infrared absorption spectroscopy measurements by Buchanan et al. [13]. This yields a predicted splitting of 63.5 meV (736 K) between the first crystal field excitation and the ground state doublet, and the ground state Kramers doublet, $^2F_{7/2}$ is thereby well isolated from a series of excited Kramers doublet states. The *Kramers theorem* states that for a system with an odd number of fermions, all energy levels are at least two-fold degenerate in the absence of a magnetic field. Because these two energy levels are time reversed versions of each other, it is possible to split lift the degeneracy of a Kramers doublet with a magnetic field, but not an electric field [9]. There are 13 electrons the in 4f orbital of Yb^{3+} and it therefore qualifies as a Kramers ion. The effective spin $S = 1/2$ of the ground state doublet presents the possibility of quantum effects at low temperatures.

6.2.1 Thermal Inelastic Neutron Scattering

We have used thermal inelastic neutron scattering measurements at the time-of-flight instrument, IN4 at the ILL, to probe the three lowest lying crystal field excitations. Measurements were performed with incoming energy, $E_i = 113$ meV at a temperature of 1.5 K in three different orientations showing no directional variations. The datasets from all three orientations are therefore combined into a single dataset which is presented in this section.

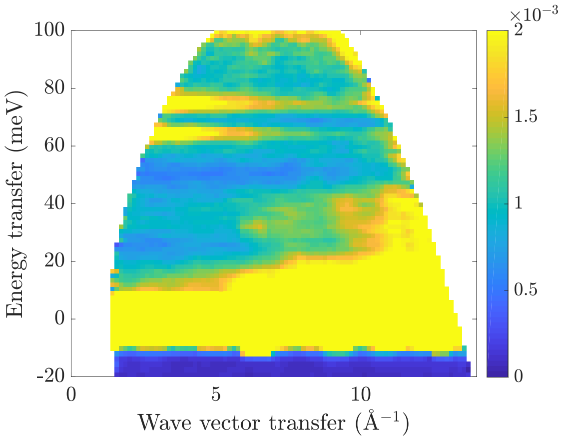

Figure 6.3: 2D Scattering profile S(Q,ω) of crystal field excitations in YbGG measured with the IN4 instrument, ILL. The colour represents neutron scattering intensity. The excitations are well separated from the ground state doublet.

Figure 6.3 shows the 2D scattering profile of YbGG. The ground state is well separated from the crystal field excitations which are predicted to be at 63.5 meV, 72.7 meV, 79.4 meV respectively [13]. The two upper crystal field excitations, E_1 and E_2 are not resolved in the colour plot in figure 6.3. The excitations decay homogeneously with Q as it is expected for a single ion effect which has a form factor dependence on **Q** reflecting the spatial distribution of the 4f electrons of Yb^{3+}.

Figure 6.4 shows the integrated data for $4 \leq Q \leq 5$ Å^{-1} as a function of energy along with Gaussian fits used to extract the energy and intensity of the excitations. The Q region represents the lowest region in Q where all three excitations are accessible with $E_i = 113$ meV. Excitation E_1 is well separated from the remaining two excitions, E_2 and E_3, and it is fitted with a Gaussian lineshape yielding $E_1 = 63.8 \pm 0.2$ meV. The positions of the excitations E_2 and E_3 are resolved with a double Gaussian lineshape where the widths of both Gaussian contributions are fixed to the energy resolution obtained from the Gaussian fit of E_1, $\mathrm{FWHM}_1 = 4.2 \pm 0.5$ meV. Figure 6.4 contains an energy diagram with the position of all three excitations.

The energy levels of the three excitations are within 2 error bars identical to the first three crystal field excitations calculated by Pearson et al. [59] based on the calculated Stevens parameters. In addition to the form factor like Q-dependence of the excitations in figure 6.3, this shows that the ground state is indeed a well separated Kramers state doublet of spin S = 1/2 and the Steven parameters calculated by Pearson et al. describe the crystal field well.

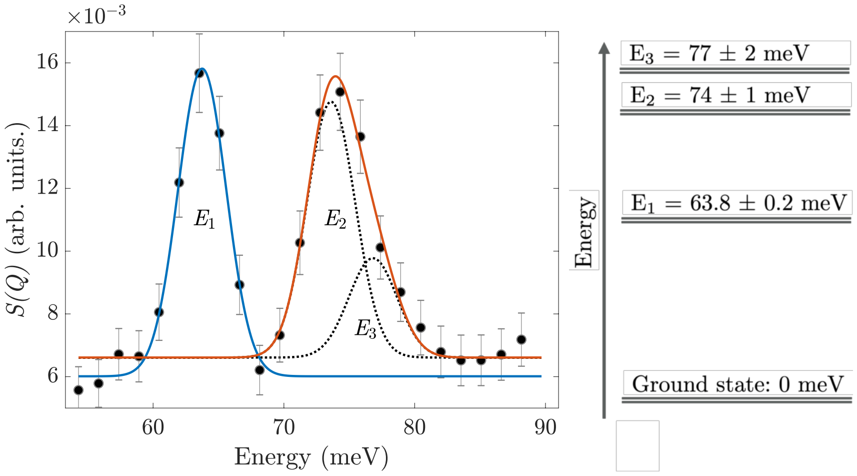

Figure 6.4: Left: Integrated data for $4 \leq Q \leq 5$ Å^{-1} as a function of energy transfer shows three crystal field excitations. The first excitation, E_1 is well separated from E_2 and E_3 and is fitted with a single Gaussian. The upper excitations E_1 and E_2 are resolved using a double Gaussian lineshape. Right: Energy diagram obtained from the Gaussian fits in the left figure. The energy axis is not linear.

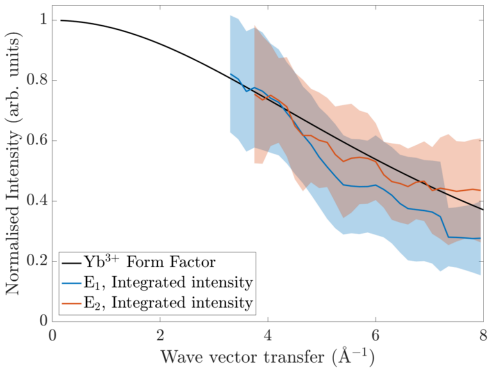

Figure 6.5: Intensity of E_1 and E_2 obtained from the integrated intensity of the Gaussian fits to each position in Q. While the result is noisy, there is qualitative agreement with the plotted form factor decay of Yb^{3+} indicating that the excitation is a single ion effect.

The Q dependence of the intensity of the excitations is analysed by fitting the three energy levels with Gaussians at each position in Q. The amplitude and background of the Gaussians are fitted while the position of the three Gaussians are fixed to the positions obtained in figure 6.4 and the widths are fixed to the energy resolution as obtained from the width of E_1. Figure 6.5 shows the integrated intensity of the Gaussian fits of E1 and E_2 as a function of Q along with the form factor decay of Yb^{3+}. The intensity has been normalised to the form factor decay. There is qualitative agreement indicating that the excitations do represent a single ion effect, but there is a high level of noise. E_3 which has much lower intensity than E_1 and E_2 which results in a very noisy intensity when plotted as a function of Q, and it is therefore not included in figure 6.5.

6.2.2 Susceptibility Mesurements

Susceptibility measurements have been performed for 1.8 K $< T <$ 300 K at the Technical University of Denmark on a 0.29 g YbGG single crystal using the VSM and AC-MSII options on a Quantum Design Dynacool PPMS with 0.1 T applied magnetic field. The crystal was not aligned during the experiment, but susceptiblity measurements were performed with the crystal oriented along 2 orthogonal directions with very similar results which is expected due to the highly three dimensional structure of the crystal. We here present only 1 of the measurements.

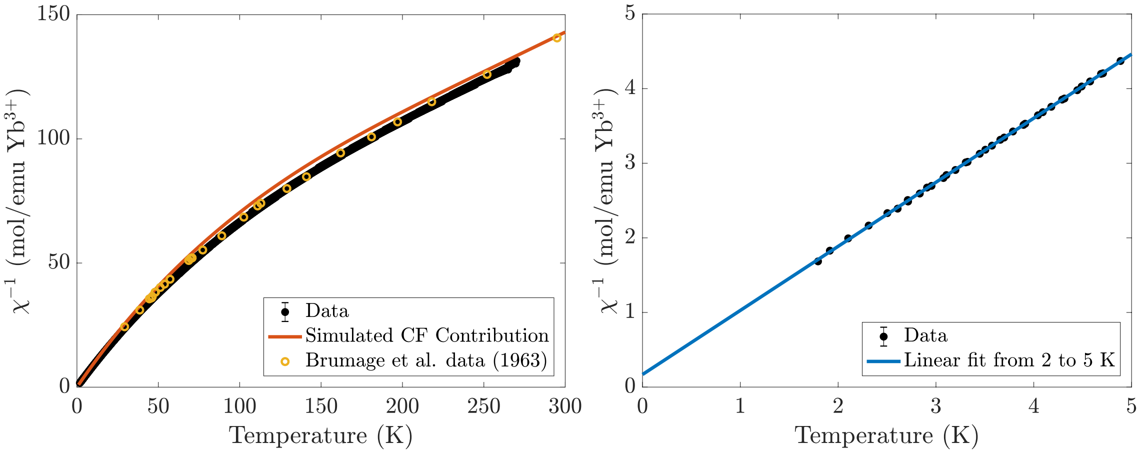

Figure 6.6: Magnetic susceptiblity of YbGG. Left: Measured susceptiblity in addition to the simulated crystal field contribution to the magnetic susceptiblity. The simulation is based on the Stevens parameters obtained by Pearson et al. [59]. The figure also contains the susceptiblity measurements by Brunage et al. [12] from 1963, which coincide with our measurements. Right: Linear fit for T $\leq$ 5 K yields θ_{CW}=-0.2(1) K. Errorbars are contained within the plotted linewidth.

Figure 6.6 shows the temperature dependence of the inverse susceptiblity. The left figure shows the entire measured temperature range along with previous susceptibility measurements by Brumage et al. [12]. There is excellent agreement between the measurements. Additionally, the left figure contains the simulated crystal field contribution to the magnetic susceptiblity based on the Stevens parameters calculated by Pearson et al. [59]. The crystal field contribution is able to reproduce data very well which shows that the crystal field is the dominant contribution to the magnetic susceptibility except at very low temperatures. This justifies the exclusion of exchange interactions in the crystal field calculations performed by Pearson et al.

Figure 6.6(right) shows a linear fit to the inverse susceptibility for temperatures $T \leq 5$ K. The data is well represented by the linear fit which shows that exchange interactions govern the magnetic susceptibility at these temperatures. The Curie Weiss temperature, θ_{CW}, obtained from the fit is - 0.2(1) K, indicating weak AFM interactions. This contradicts the results by Filippi et al who obtained a positive $\theta_{\mathrm{CW}} = 45 \pm 5$ mK indicating weak FM interactions [25]. Recently, l'Hotel et al. reported a positive $\theta_{\mathrm{CW}} = 97$ mK [47]. These results are thereby inconsistent, but they all show very weak spin-spin interactions in the mK regime which is approximately three orders of magnitude less than the crystal field excitations.

6.3 Cold Neutron Scattering Measurements

The energy scale of the magnetic correlations in YbGG are in the mK range and we have therefore studied them using cold neutron scattering. The experiments were performed on a 1.9 g single crystal YbGG at the CNCS and D7 instruments described in sections 3.4 and 3.3 respectively. Figure 6.7 shows a photo of the mounted crystal prior to the measurements at the CNCS. Both experiments were performed with $\mathbf{Q}_x$ = (L, L, 2L) and $\mathbf{Q}_y$ = (2H, -2H, 0) spanning the scattering plane. The temperature during the measurements were stable and experimentally measured to be 50 mK. However, the actual sample temperature is expected to be higher, most likely in the range $0.07 \text{ K} < T < 0.6 \text{ K}$ due to the low thermal conductivity of rare earth garnet compounds, particularly at low temperatures and a limited thermal contact between sample and thermal bath. We therefore expect to be in the temperature range where heat capacity measurements show short range correlations. The long range order expected for temperatures below the lambda transition at 54 mK in heat capacity measurements in figure 6.2 was not observed in the neutron scattering data.

This sections describes extraction of the elastic and inelastic magnetic scattering profiles, S($\mathbf{Q}$, E) of YbGG from the CNCS data sets. The data obtained from measurements at D7 is described, and differences between the D7 and CNCS data are discussed. Finally, the magnetic elastic data from the CNCS measurements and the magnetic energy integrated data from the D7 measurements are analysed with a reversed Monte Carlo technique (RMC), and these results are discussed.

Figure 6.7: Photo of the mounted YbGG single crystal prior to neutron scattering measurements with the CNCS instrument.

6.3.1 Neutron Scattering Measurements with the CNCS Instrument

We have performed neutron scattering measurements with the CNCS instrument using 2 different incoming neutron energies, $E_i = 1.55$ meV and $E_i = 3.32$ meV, which we term data set 1 and data set 2 respectively. The energy of the incoming neutrons is lower for data set 1 compared to data set 2, and it therefore probes a smaller region of reciprocal space and energy transfer, but with a better resolution compared to data set 2. The elastic energy resolutions obtained from the incoherent scattering of a vanadium scatterer are $\delta E = 0.037(5)$ meV and $\delta E = 0.109(2)$ meV for data sets 1 and 2 respectively. The energy resolution of a time-of-flight instrument like the CNCS generally increases as $(k_i/k_f)^3$ for inelastic scattering compared to the elastic line [53]. Neutron scattering measurements were performed at 50 mK, where magnetic correlations are expected, and at 13 K in the paramagnetic regime of YbGG. The high temperature profile is used to perform a background subtraction in order to extract the correlated magnetic scattering profile which we term $S(\mathbf{Q},E)$. Subscripts 1 and 2 refer to data sets 1 and 2 respectively. The total scattering (nuclear, paramagnetic and correlated magnetic scattering) is termed $S^{13\text{ K}}(\mathbf{Q},E)$ and $S^{50\text{ mK}}(\mathbf{Q},E)$ for measurements at 13 K and 50 mK respectively.

Extracting Data

Figure 6.8 shows $S_2(\mathbf{Q},E)$ in order to illustrate the data format of the CNCS data. $S(\mathbf{Q},E)$ is three dimensional with the axes defined by the two components of $\mathbf{Q}$ spanning the scattering plane along with the energy transfer. Figure 6.8 contains two 2D slices of the 3D data set, a horizontal and a vertical slice. The horizontal slice has constant energy transfer and shows the elastic line. The intensity of the elastic line is saturated despite a logarithmic colour scale. The vertical slice has constant $\mathbf{Q}_x$ = (L, L, 2L) and shows a gapped, dispersionless soft mode excitation, INS3, which is further described later in the section. The detectors at the CNCS allow neutron scattering measurements of reciprocal space ±16° outside the scattering plane, but technical data reduction challenges at the

SNS made this information unavailable for these data sets.

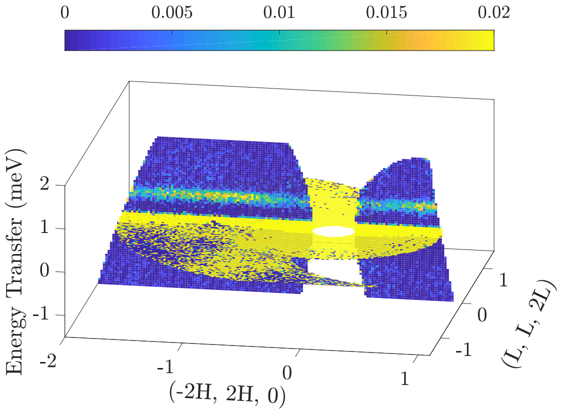

Figure 6.8: Illustration of the data format of the CNCS data with $\mathrm{S}_2(\mathbf{Q},\mathrm{E})$. The data is three dimensional and contains information along the energy transfer and two components of $\mathbf{Q}$ which span the scattering plane, $\mathbf{Q}_x$ = (L, L, 2L) and $\mathbf{Q}_y$ = (-2H 2H 0). The intensity is plotted on a logarithmic colour scale. The figure contains two 2D slices, a horizontal slice showing the elastic line with constant, zero energy transfer and a vertical slice where $\mathbf{Q}_x$ = (L, L, 2L), L = -0.23. The intensity of the elastic line is saturated.

Figure 6.9 shows the energy transfer dependent $\mathbf{Q}$ integrated scattering profiles $\mathrm{S}_1^{13\ \mathrm{K}}(\mathrm{E})$ and $\mathrm{S}_1^{50\ \mathrm{mK}}(\mathrm{E})$. $\mathrm{S}_1^{50\ \mathrm{mK}}(\mathrm{E})$ contains three peaks marked by vertical dashed lines which are absent in $\mathrm{S}_1^{13\ \mathrm{K}}(\mathrm{E})$ showing that these are magnetic excitations. The excitations, named INS1-INS3, are found at energy transfers $\mathrm{E}_{\mathrm{INS1}} = 0.062(5)$ meV, $\mathrm{E}_{\mathrm{INS2}} = 0.13(3)$ meV and $\mathrm{E}_{\mathrm{INS3}} = 0.69(5)$ meV respectively. The inset of figure 6.9 is a vertical 2D slice of data set 2 with constant $\mathbf{Q}_x$ showing directly the dispersionless nature of INS3. INS1 and INS2 are also dispersionless as discussed later in the section. The scattering profiles $\mathrm{S}_1(\mathbf{Q}, 0)$, $\mathrm{S}(\mathbf{Q}, \mathrm{E}_{\mathrm{INS1}})$ and $\mathrm{S}(\mathbf{Q}, \mathrm{E}_{\mathrm{INS2}})$ are extracted from data set 1 while $\mathrm{S}_2(\mathbf{Q}, 0)$ and $\mathrm{S}(\mathbf{Q}, \mathrm{E}_{\mathrm{INS3}})$ are extracted from data set 2.

Three Gaussians are fitted to energy cuts in $\mathrm{S}_1^{50\ \mathrm{mK}}(\mathbf{Q}, \mathrm{E})$ for each bin in $\mathbf{Q}$ as illustrated in figure 6.10. The widths of the elastic line and INS1 are fixed to the elastic energy resolution to reduce the number of fit parameters. This is justified by the proximity of INS1 to the elastic line and the energy resolution of INS1 does therefore not vary significantly from the elastic energy resolution. A single Gaussian is fitted to $\mathrm{S}_1^{13\ \mathrm{K}}(\mathbf{Q}, \mathrm{E})$ to energy cuts for each bin in $\mathbf{Q}$ to extract the elastic nuclear and paramagnetic contribution. $\mathrm{S}_1(\mathbf{Q}, 0)$ is found from the difference between the integrated intensities of the Gaussian fits to the elastic lines in each $\mathbf{Q}$ bin in $\mathrm{S}_1^{50\ \mathrm{mK}}(\mathbf{Q}, \mathrm{E})$ and $\mathrm{S}_1^{13\ \mathrm{K}}(\mathbf{Q},\mathrm{E})$. $\mathrm{S}(\mathbf{Q}, \mathrm{E}_{\mathrm{INS1}})$ and $\mathrm{S}(\mathbf{Q}, \mathrm{E}_{\mathrm{INS2}})$ are determined as the integrated intensity of the corresponding Gaussian fits to each point in $\mathbf{Q}$ in $\mathrm{S}_1^{50\ \mathrm{mK}}(\mathbf{Q}, \mathrm{E})$.

The dispersionless natures of both INS1 and INS2 are seen from the small variations in the fitted peak position compared to the elastic energy resolution. $\mathrm{E}_{\mathrm{INS1}}$ and $\mathrm{E}_{\mathrm{INS2}}$ are determined from the average peak position across all $\mathbf{Q}$, and the errors are determined form

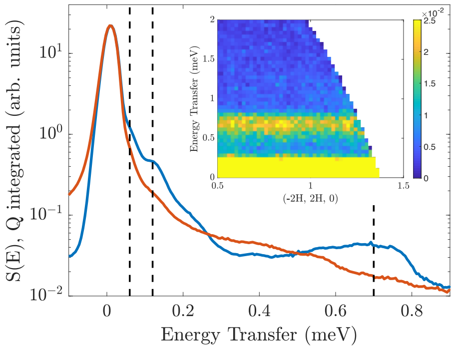

Figure 6.9: Energy dependent Q integrated $S_1^{50\text{ mK}}(E)$ (blue) and $S_1^{13\text{ K}}(E)$ (red). Three excitations, INS1-3 at $E_{\text{INS1}} = 0.062(5)$ meV, $E_{\text{INS2}} = 0.13(3)$ meV and $E_{\text{INS3}} = 0.69(5)$ meV respectively marked by vertical dashed lines are observed at 50 mK, but are absent at 13 K. The inset figure shows a vertical 2D slice of data set 2 with constant $\mathbf{Q}_x$ = (L, L, 2L), L = 0.23. This shows the dispersionless nature of INS3. Figure from [61].

the spread in fitted peak position. The total fit plotted in figure 6.10 has systematically lower intensity than data for energy transfers near 0.2 meV indicating the possible existence of an additional excitation. The intensity of such a possible excitation is an order of magnitude lower than the intensity of INS2, and it is therefore not included in the model.

S($\mathbf{Q}$, E_{INS3}) is determined from the difference between the energy integrated data from 0.5 meV to 0.9 meV to each bin in $\mathbf{Q}$ in $S_1^{50\text{ mK}}(\mathbf{Q},E)$ and $S_1^{13\text{ K}}(\mathbf{Q},E)$. E_{INS3} is found from the peak position of a skewed Gaussian fit in the range 0.5 meV $< E <$ 0.9 meV to the intensity of the $\mathbf{Q}$ integrated data, $S_1^{50\text{ mK}}(E)$.

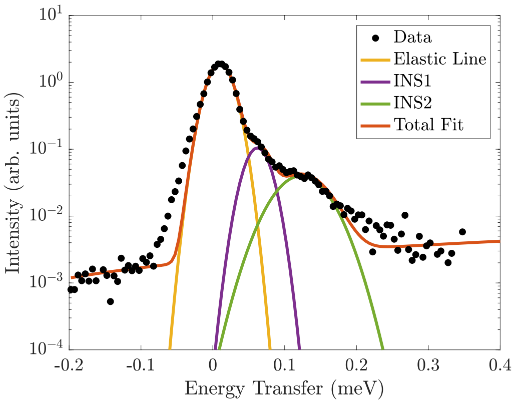

Figure 6.10: Intensity as a function of energy transfer in an energy cut of $S_1^{50\text{ mK}}(E)$ for a single $\mathbf{Q}$ bin. Three Gaussians are fitted to data thus resolving the elastic line, INS1 and INS2 respectively. The intensity is plotted on a logarithmic scale.

Elastic Data

Figures 6.11 and 6.12 show $S_1(\mathbf{Q},0)$ and $S_2(\mathbf{Q},0)$, respectively. Both figures show distinct diffuse 6-fold symmetric features following the crystal symmetry. The short range nature of the diffuse features is consistent with the broad feature in the heat capacity in figure 6.2 for 54 mK $<$ T $<$ 600 mK.

Figure 6.11(left) shows $S_1(\mathbf{Q},0)$ which contains a hexagon marked **A** for $|Q| \leq 0.63$ Å^{-1}. Figure 6.11(right) shows a linecut with $\mathbf{Q}_y$ = (-2H, 2H, 0), H = 0. The figure contains a dominant single peak which is the feature **A**. A Gaussian fit yields a peak position at $|Q| = 0.30(3)$ Å^{-1} corresponding to a lattice distance, $d = 2\pi/Q = 20(2)$ Å. This is approximately twice the short distance across a 10-ion loop, which is 11.210 Å at room temperature. Both figures 6.11(left) and (right) show that the scattering intensity of the hexagon decreases for $\mathbf{Q} \rightarrow 0$ Å^{-1} indicating that these correlations are AFM. The correlation length, determined from the FWHM of the fitted Gaussian, is 12(2) Å and the correlations are thereby very short range. Figure 6.11(left) contains weak circular features extending from the sides of the hexagon marked by **B** → **C**. $S_1^{50\text{ mK}}(\mathbf{Q},\mathrm{E})$ is discussed in section 6.3.4 where it is related to an RMC simulation.

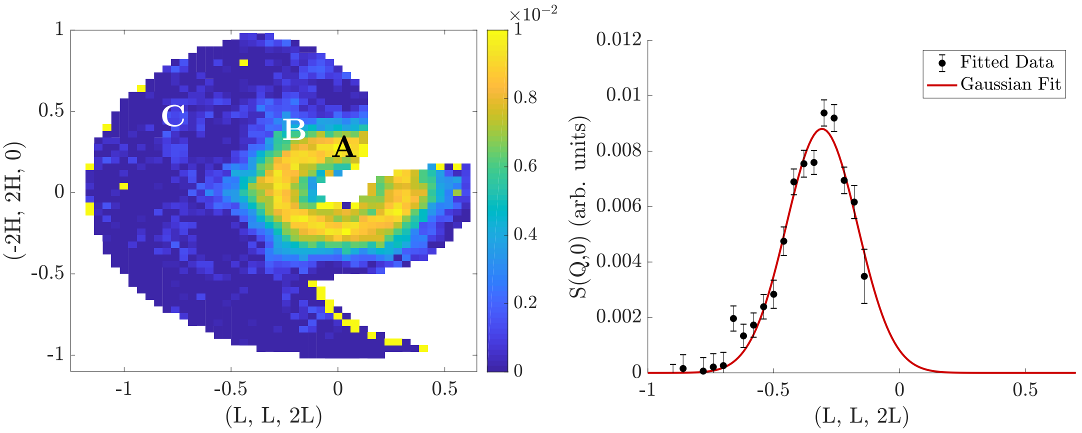

Figure 6.11: Left: $S_1(\mathbf{Q},0)$ ($E_i = 1.55$ meV). A low Q hexagon is marked by **A**. The intensity of the hexagon is reduced for $\mathbf{Q} \rightarrow 0$ Å^{-1}. Weak ring-like diffuse features extend from the edges of the hexagon for **B** → **C**. Right: linecut of the 2D data where $\mathbf{Q}_y$ = (-2H, 2H, 0), H = 0. Fit parameters are listed in table 6.1.

Figure 6.12(left) shows $S_2(\mathbf{Q},0)$. The data extends further into |Q| compared to $S_1(\mathbf{Q},0)$ because E_i is higher. The low **Q** hexagon marked **A** is visible in the figure, but the decreased intensity for Q $\rightarrow$ 0 Å^{-1} is not clearly resolved. Diffuse peaks appear between the three marked Bragg peaks B: (-2, 1, -1), C: (-3, 2, -1), D: (-1, -2, -3) and symmetry equivalent reflections.

Figure 6.12(right) shows a linecut with $\mathbf{Q}_y$ = (-2H, 2H, 0), H = 0, and $\mathbf{Q}_x$ = (L, L, 2L), L $<$ 0. The low **Q** feature **A** and the high **Q** diffuse peaks between **B**, **C** and **D** are seen in the linecut. A Gausian fit to the linecut of the high **Q** diffuse peak yield a peak position at 1.86(9) Å^{-1} corresponding to a lattice spacing, $d = 2\pi/Q = 3.4(2)$ Å^{-1}. This is close to the NN distance which is 3.737 Å at room temperature. The correlation length is obtained from the FWHM to be 11(5) Å consistent with the short and long distance across the 10-ion loop which is 11.210 Å and 12.204 Å respectively. The ring-features that were observed to extend from the sides of the feature **A** in S$_1$(**Q**,0) in figure 6.11 are not resolved in S$_2$(**Q**,0) in figure 6.12.

The signal-to-noise in data set 2 is lower than in data set 1, which is seen in the linecut in figure 6.12(right) where errorbars are plotted. However, the errorbars seem very large compared to the variations in signal. It is possible that they were not correctly scaled in the data reduction that was performed at the SNS since the errors in the inelastic channels of data set 2 are also very large compared to the variations in signal as discussed later in this section.

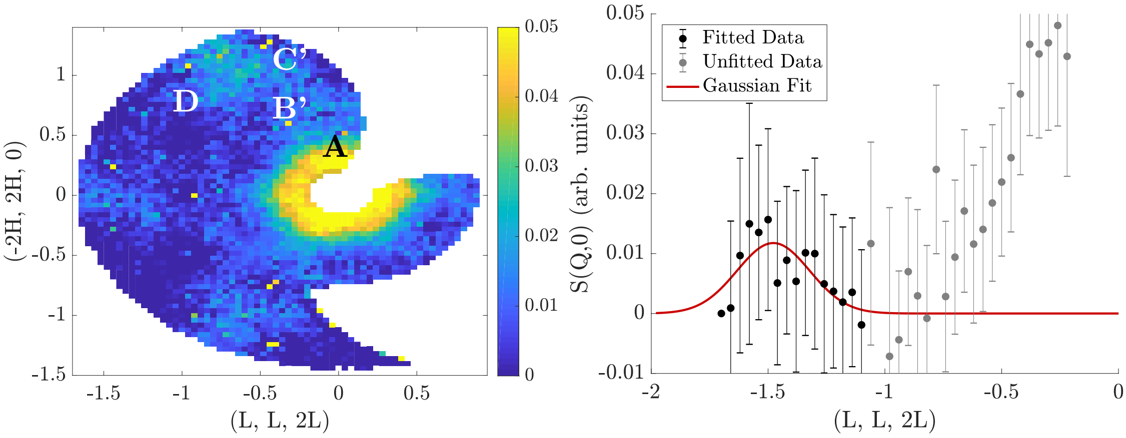

Figure 6.12: Left: S$_2$(**Q**,0) (E$_i$ = 3.32 meV). A low Q hexagon, marked A, is observed. Diffuse peaks are seen between the three Bragg peaks marked by B, C, D, corresponding to the reflections B: (-2, 1, -1), C: (-3, 2, -1), D: (-1, -2, -3). and symmetry equivalent positions in the scattering range. Right: line cut where $\mathbf{Q}_y$ = (-2H, 2H, 0), H = 0 and $\mathbf{Q}_x$ = (L, L, 2L), L < 0. A Gaussian is fitted to the high **Q** diffuse peak which extends between **B**, **C** and **D** in the left figure. Selected fit parameters are listed in table 6.1.

Data set 1 ($E_\mathrm{i} = 1.55$ meV)	
Gaussian Peak Position	0.30 ± 0.03 Å^{-1}
Distance (from peak pos)	20 ± 2 Å
FWHM	0.52 ± 0.09 Å^{-1}
Correlation Length (from FWHM)	12 ± 2 Å
Data set 2 ($E_\mathrm{i} = 3.32$ meV)	
Gaussian Peak Position	1.86 ± 0.09 Å^{-1}
Distance (from peak pos)	3.4 ± 0.2 Å
FWHM	0.55 ± 0.25 Å^{-1}
Correlation Length (from FWHM)	11.5 ± 5.2 Å
Data set 3 ($E_\mathrm{i} = 8.11$ meV)	
Gaussian Peak Position	1.95 ± 0.08 Å^{-1}
Distance (from peak pos)	3.2 ± 0.1 Å
FWHM	1.6 ± 0.2 Å^{-1}
Correlation Length (from FWHM)	4.0 ± 0.6 Å

Table 6.1: Selected fit parameters of the Gaussian fits in figures 6.11, 6.12 and 6.15. Data set 3 is obtained from neutron scattering measurements at D7 described in section 6.3.2. Parameters have been converted from dimensionless recoprocal lattice vectors to units of Å^{-1} and Å in order to relate to dimensions in the crystal.

Inelastic Data

We have measured three dispersionless, gapped, soft mode exciations, INS1-INS3 as described previously in the section. A softmode excitation is here used to describe a dispersionless excitation which is not a single ion effect. This section contains a description of S($\mathbf{Q}$) for each excitation.

Figure 6.13(left) shows S($\mathbf{Q}$, $\mathrm{E_{INS1}}$). INS1 has reduced intensity as $\mathbf{Q} \rightarrow 0$ Å^{-1} and a diffuse hexagon which peaks at 0.90(2) Å^{-1}. Diffuse peaks extend from the corners of the hexagon and has peak positions at **A**, **B** and **C** corresponding to the three symmetry equivalent Bragg reflections (-2, 1, -1), (-1, -1, -2) and (1, -2, -1) respectively in the elastic line.

Figure 6.13(right) shows S($\mathbf{Q}$, $\mathrm{E_{INS2}}$) which is azimuthally symmetric, but its intensity increases with increasing $\mathbf{Q}$ oppositely to a form factor decay and it is therefore not a single ion effect. In order to study INS2 more carefully, an experiment with a similar Q resolution, but larger neutron incoming energy should be performed in order to access higher $\mathbf{Q}$-regions.

Figure 6.14(left) shows S($\mathbf{Q}$, $\mathrm{E_{INS3}}$). The intensity is low for $\mathbf{Q} \rightarrow 0$ Å^{-1} marked **A**, and increases in a diffuse hexagon marked **B** before it decreases beyond the hexagon. Figure

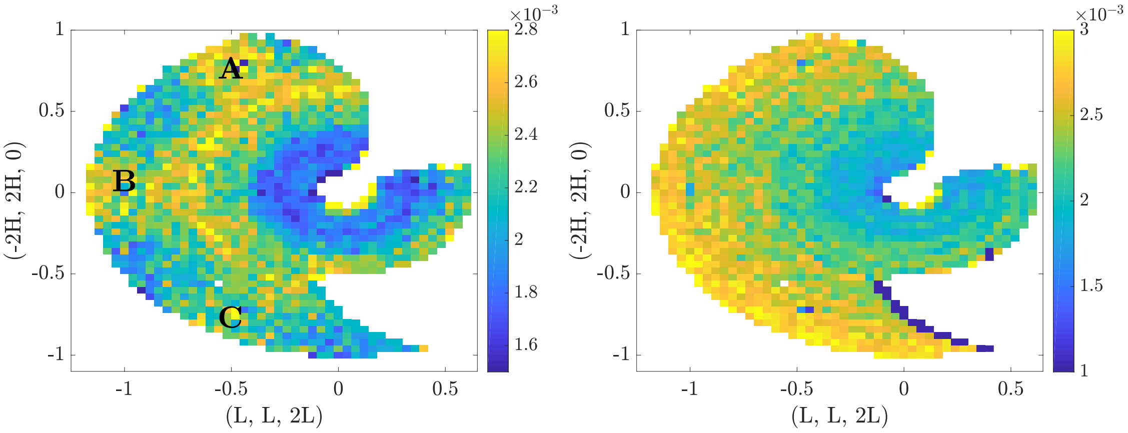

Figure 6.13: S($\mathbf{Q}$, E_{INS1}) (left) and S($\mathbf{Q}$, E_{INS2}) (right) obtained from Gaussian fits to energy transfer dependent linecuts for each bin in $\mathbf{Q}$ in $S_1^{50\text{ mK}}(\mathbf{Q}, E)$. S($\mathbf{Q}$, E_{INS1}) contains a diffuse high intensity hexagon and low intensity for $\mathbf{Q} \rightarrow 0$ Å^{-1}. Three diffuse peaks extend from the corners of the hexagon and are centered at the positions **A**, **B** and **C** which correspond to the symmetry equivalent nuclear Bragg reflections (-2, 1, -1), (-1, -1, -2) and (1, -2, -1) in the elastic line respectively. S($\mathbf{Q}$, E_{INS2}) is uniform in all directions of $\mathbf{Q}$ in the scattering plane, but its intensity increases with Q oppositely to a form factor dependence.

6.14 shows the Q integrated signal across the feature **B** as a function of azimuthal angle. The errors are very large compared to the variations in signal similarly to the elastic signal of data set 2. The integrated data follow a 6-fold symmetry associated with a hexagonal pattern. This is confirmed by a fitted sine function with a constant background which yields a fitted periodicity of 57(2) degrees, see figure 6.14(right).

Inelastic neutron scattering measurements of YbGG were recently published by l'Hotel et al. [47]. These measurements describe the inelastic spectrum along two different $\mathbf{Q}$ directions and they obtain very similar results with three dispersionless excitations at 0.032(5) meV, 0.100(6) meV and 0.70(5) meV respectively giving confidence in the results presented in this section.

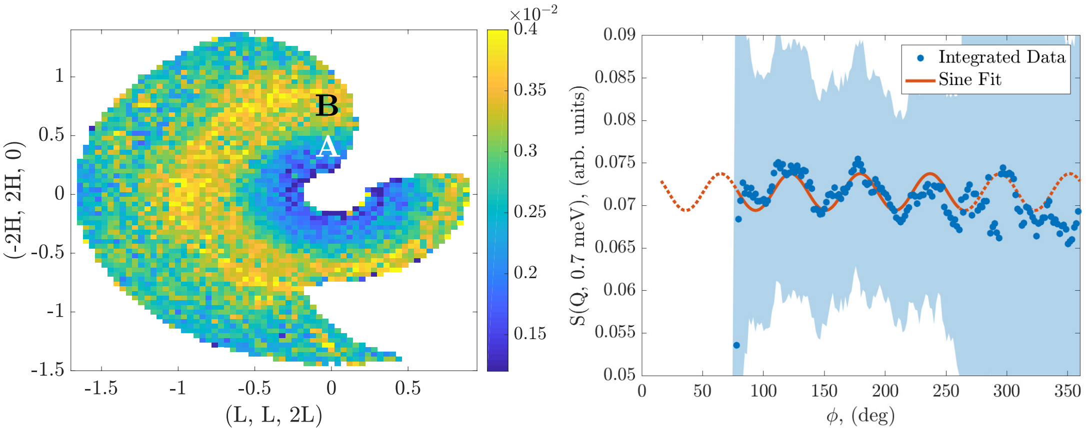

Figure 6.14: Left: S(**Q**, $\mathrm{E}_{\mathrm{INS3}}$) has low intensity for $\mathbf{Q} \rightarrow 0$ Å^{-1} marked **A**, while a diffuse hexagon follows at higher **Q** marked **B**. The intensity of S(**Q**, $\mathrm{E}_{\mathrm{INS3}}$ decreases beyond the feature **B**. Right: Angle dependent integrated intensity along **Q** across the feature **B**. A sine function with a constant background has been fitted to data in the range with a solid line. While there is no clear hexagonal symmetry in the 2D data, the integrated data shows a 6-fold symmetry with a fitted periodicity of 57(2) degrees.

6.3.2 Neutron Scattering Measurements with the D7 Instrument

We have performed neutron scattering measurements with polarisation analysis (PA) at the D7 diffuse scattering diffractometer instrument with incoming energy 8.11 meV thus probing a larger Q region compared to data sets 1 and 2. The experiment was performed with the same 1.9 g single crystal that was used for the CNCS experiment at 50 mK, and a similar crystal alignment. This section contains a description of the results from this experiment, which we term data set 3.

PA enables extraction of the energy integrated 2D total magnetic scattering profile, $\mathrm{S}_3(\mathbf{Q})$ which is shown on figure 6.15(left). The figure shows a low **Q** hexagon, marked **A** consistent with the feature **A** in $\mathrm{S}_1(\mathbf{Q},0)$ and $\mathrm{S}_2(\mathbf{Q},0)$ in figures 6.11 and 6.12 respectively. Figure 6.15(left) shows slightly increased intensity beyond the feature **A** consistent with the ring-like features marked **B** → **C** in figure 6.11, but it is not fully resolved in $\mathrm{S}_3(\mathbf{Q})$. Figure 6.15(left) also shows three symmetry equivalent diffuse peaks marked **B**, and at the highest **Q** weak ring-like features extend from the diffuse peaks **B** towards **C**.

Figure 6.15(right) shows a linecut where $\mathbf{Q}_y$ = (-2H, 2H, 0), H = 0. The feature **A** is seen in the linecut which also shows a reduced intensity for $\mathbf{Q} \rightarrow 0$ Å^{-1} in compliance with the observations in $\mathrm{S}_1(\mathbf{Q},0)$ and $\mathrm{S}_2(\mathbf{Q},0)$ and the three data sets are thereby consistent in the **Q**-region they all probe. A Gaussian lineshape has been fitted to the feature **B** which shows a peak position at 1.95(8) Å^{-1}. This corresponds to a lattice spacing, $d = 2\pi/Q = 3.2(1)$ Å which is less than the nearest neighbour distance of 3.737 Å at room temperature. The correlation length as determined from FWHM of the Gaussian is 4.0(6) Å.

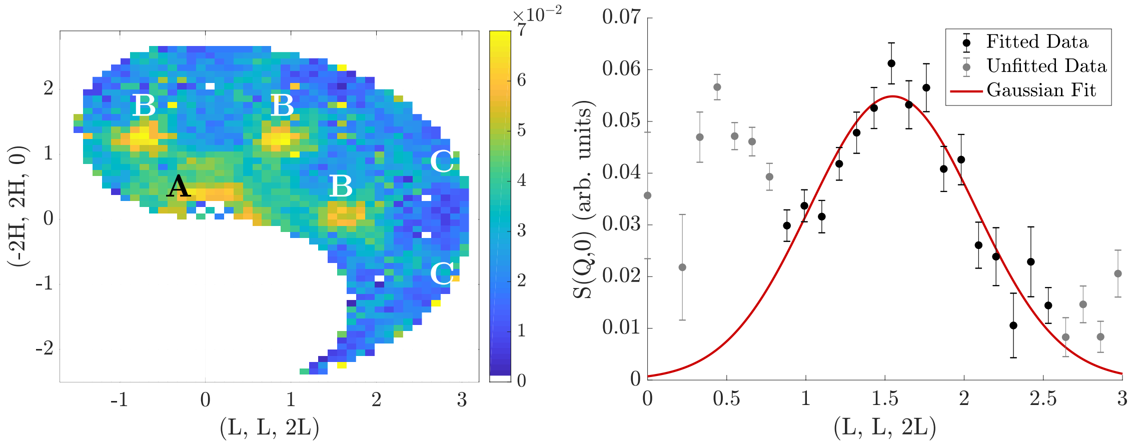

Figure 6.15: Left: $S_3(\mathbf{Q})$ (energy integrated). There are three symmetry equivalent diffuse peaks marked **A** and a low Q hexagon marked **B**. Weak ring features extend from **A** → **C**. Right: A linecut where $\mathbf{Q}_y$ = (-2H, 2H, 0), H = 0. A Gaussian lineshape has been fitted to data, fit parameters in table 6.1.

Figure 6.16 shows the spin incoherent 2D scattering profile, $S_{SI}(\mathbf{Q})$ which is homogeneous if the PA is perfect. There are diffuse features in $S_{SI}(\mathbf{Q})$, especially at the positions of the diffuse peaks marked **B** in figure 6.15 where the intensity is low, and between the diffuse peaks, where the intensity is high. Additionally, the ring-like features that extended from **B** → **C** are reproduced in figure 6.16 as lines of low intensity and high intensity inside the rings. The intensity variations in the features of $S_{SI}(\mathbf{Q})$ is a factor of 2-3 lower than the intensity variations in $S_3(\mathbf{Q})$.

The non-homogeneous spin incoherent scattering profile shows that the PA is not perfect, which is typically a result of a net FM contribution or preferential alignment of AF moments depolarising the neutron beam. No FM materials were used in the sample environment, and the imperfect PA is therefore most likely caused by a FM contribution from the sample. This is surprising, since we the system only has short range correlations are observed in figure 6.15 and no depolarisation of the scattered beam was observed during the experiment which would also typically indicate a successful PA.

All features in $S_{SI}(\mathbf{Q})$ in figure 6.16 are at the same positions in $\mathbf{Q}$ as the features in $S_3(\mathbf{Q})$ in figure 6.15, and only the relative intensities of the observed magnetic features are therefore affected, not the positions of the features. This will affect the results of the RMC simulations presented in section 6.3.4, but the distances between the correlated spins will reflect the true distances. This is further discussed in section 6.3.4.

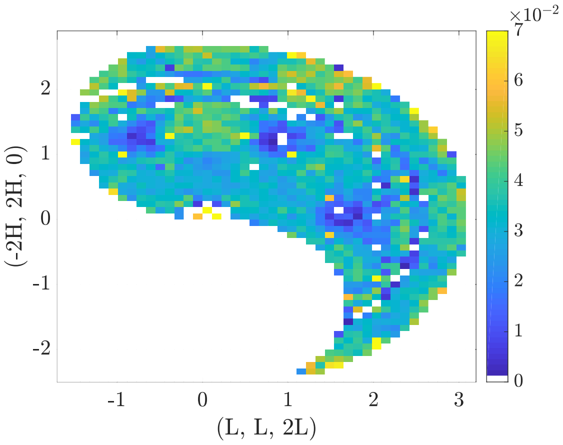

Figure 6.16: Spin incoherent scattering profile of data set 3, $S_{SI}(\mathbf{Q})$. There are features at the diffuse peaks marked **B** in $S_3(\mathbf{Q})$ in figure 6.15. $S_{SI}(\mathbf{Q})$ is reversed compared to $S_3(\mathbf{Q})$ with reduced intensity at the features **B** and increased intensity between the them. Additionally, the ring-like features that extend from **B** → **C** in figure 6.15 are retrieved with high intensity inside the rings and reduced intensity along the edge of the rings. The colour scale of this figure is identical to the colour scale of the total magnetic scatting in figure 6.15(left). There are many white bins with zero counts.

6.3.3 Comparison of D7 and CNCS data

Upon first considering data set 1 and 3 it is difficult to reconcile the two data sets until one places them on an absolute **Q** scale, figure 6.17 which shows $S_1(\mathbf{Q}, 0)$ and $S_3(\mathbf{Q})$.The figure shows that the two data sets probe different regions in **Q** and they are thereby sensitive to correlations at different length scales in the sample. Data set 1 has $0.13 < L < 1.2$, $0.1 < H < 0.95$ and data set 3 has $0.2 < L < 3.1$ and $0.3 < H < 2.8$.

Another difference between the data sets is the measurement method. $S_1(\mathbf{Q}, 0)$ and $S_2(\mathbf{Q}, 0)$ are extracted from the scattering within the instrumental energy resolution and it is therefore considered static. $S_3(\mathbf{Q})$ is the magnetic contribution to the energy integrated scattering and it thereby contains a dynamic contribution whose intensity is 1-3 orders of magnitude lower than the elastic contribution for INS1-INS3 based on the Q integrated $S_1(E)$ in figure 6.9.

Finally, a large paramagnetic contribution has been subtracted from the base temperature scattering profiles of data sets 1 and 2, while data set 3 represents the full magnetic scattering profile. The difference between the magnetic scattering profile, $S_{\text{sub}}(Q)$, obtained from subtraction of a high temperature signal where all spins are uncorrelated, and the full magnetic scattering profile, $S(Q)$, is a constant term which represents the self-correlations,

$$S_{\text{sub}}(Q) = S(Q) - \frac{2}{3}C\left(\mu_{\text{eff}} f(Q)\right)^2, \qquad (6.2)$$

where the proportionality constant $C = 0.07265$ barns, μ_{eff} is the effective magnetic mo-

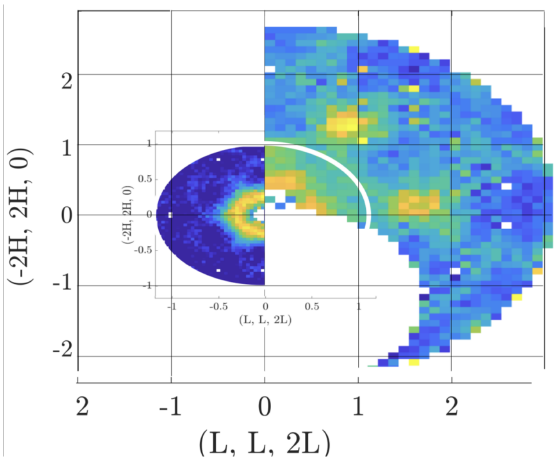

Figure 6.17: $S_1(\mathbf{Q}, 0)$ (left) and $S_3(\mathbf{Q})$ (right) showing the difference in the probed **Q**-range. The two scattering profiles are plotted on different colour scales as used in figures 6.11 and 6.15 for $S_1(\mathbf{Q}, 0)$ and $S_3(\mathbf{Q})$ respectively.

ment and $f(Q)$ is the form factor decay [57]. As a result of this difference, $S_1(\mathbf{Q}, 0)$ and $S_2(\mathbf{Q}, 0)$ can contain negative intensities which is not physically reasonable for $S_3(\mathbf{Q})$. This difference in type of magnetic scattering data is included in the RMC simulations presented in section 6.3.4.

6.3.4 Reverse Monte Carlo

We have performed reversed Monte Carlo (RMC) simulations on $S_1(\mathbf{Q}, 0)$, $S_2(\mathbf{Q}, 0)$ and $S_1(\mathbf{Q})$ using the *Spinvert* refinement algorithm [55]. The algorithm minimizes the residual difference between the measured and simulated structure factor S(Q) unlike a conventional Monte Carlo simulation (MC) where the energy of the system is minimized and the spin-spin interactions are therefore not provided by an RMC simulation. A strength of RMC compared to other simulation methods is that no symmetry is enforced on the system apart from the crystallographic structure and periodic boundary conditions. We have simulated 8×8×8 unit cells corresponding to $24 \cdot 8^3 = 12288$ spins, thus obtaining the real space spin-spin correlations from the neutron scattering data.

Minimising directly the residual difference between 2D $S(\mathbf{Q})$ in an RMC simulation leaves all points in **Q** outside the scattering plane unconstrained leading to unphysical results which are discontinuous and do not respect the crystal symmetry. In order to avoid this, we have created an isotropic scattering distribution S(Q) by integrating $S(\mathbf{Q})$ across identical $|Q|$ thereby constraining the out-of-plane points in **Q** to the scattering profile of the scattering plane. We shall term S(Q) the powder averaged data.

In order to reduce the risk of erroneous minimizations, we have used the average of 400 RMC simulations to describe a single data set, and we perform simulations of $S_1(\mathbf{Q}, 0)$, $S_2(\mathbf{Q}, 0)$ and $S_3(\mathbf{Q})$ where different regions in **Q** are probed and where different neutron scattering instruments are used and compare the results of the different RMC simulations. Based on the simulations of the powder averaged signals, we have recalculated $S(\mathbf{Q})$ and compared it the original data. All of these efforts combined gives great confidence in the RMC simulation results.

Simulation Results

Figure 6.18 shows the results of the RMC simulation of data set 1. Figure 6.18(left) shows the powder averaged input data, $\mathrm{S}_1(\mathrm{Q})$ in addition to the simulated $\mathrm{S}_1^{\mathrm{sim}}(\mathrm{Q})$. The two curves coincide throughout the Q-range except at the very lowest Q where the errors on data are large, reflecting the proximity of the direct neutron beam.

The spin structure which is obtained from the RMC refinement of $\mathrm{S}_1(\mathrm{Q})$ is used to calculate the 2D scattering profile, $\mathrm{S}_1^{\mathrm{calc}}(\mathbf{Q},0)$. Figure 6.18(right) shows $\mathrm{S}_1^{\mathrm{calc}}(\mathbf{Q},0)$ along with the measured $\mathrm{S}_1(\mathbf{Q},\,0)$. The agreement is remarkable both at low $\mathbf{Q}$ where the position of the hexagon is well described, and at higher $\mathbf{Q}$ where the weak features extending from the sides of the hexagon are well reproduced by the simulation. The ability of the obtained spin structure to describe $\mathrm{S}_1(\mathbf{Q},\,0)$ based on the simulation of $\mathrm{S}_1(\mathrm{Q})$ gives great confidence in the RMC spin structure which has been simulated for data set 1.

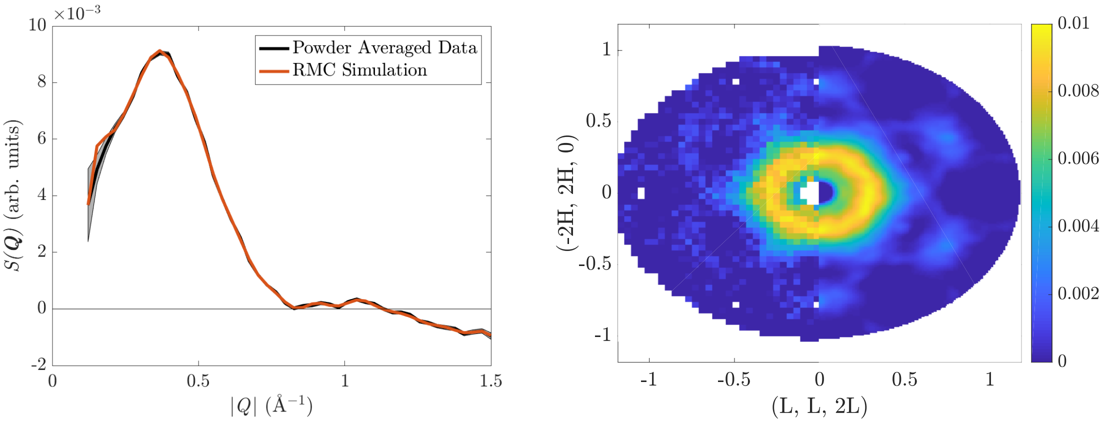

Figure 6.18: RMC simulation results of data set 1. Left: powder averaged input data, $\mathrm{S}_1(\mathrm{Q})$ and RMC simulated $\mathrm{S}_1^{\mathrm{sim}}(\mathrm{Q})$. The simulation coincides with data throughout the available Q range. Right: $\mathrm{S}_1^{\mathrm{calc}}(\mathbf{Q},0)$ (right) along with the measured $\mathrm{S}_1(\mathbf{Q},\,0)$ (left).

Figure 6.19 shows the results of the RMC simulation of data set 2. Figure 6.19(left) shows the powder averaged input data, $\mathrm{S}_2(\mathrm{Q})$ in addition to the RMC simulated $\mathrm{S}_2^{\mathrm{sim}}(\mathrm{Q})$. While there is qualitative agreement between $\mathrm{S}_2(\mathrm{Q})$ and $\mathrm{S}_2^{\mathrm{sim}}(\mathrm{Q})$ in terms of the shape of the two S(Q) curves, there are also distinct discrepancies, particularly for $|Q| > 0.8$ Å^{-1}, where there is a constant offset between data and simulation that is not seen at low Q. The offset remains constant except near the upper limit of the Q range at 2 Å^{-1} where data and simulation again coincide.

Figure 6.19(right) compares $S_2^{\rm calc}(\mathbf{Q},0)$ along with the measured $S_2(\mathbf{Q}, 0)$. The figure shows clear similarity especially at low Q, where the measured diffuse hexagon is well reproduced. The high **Q** diffuse peaks have a triangular lineshape in the simulation which is not resolved in data. The ring-like features which were observed to extend from the sides of the hexagon in $S_1(\mathbf{Q},0)$ are reproduced by $S_2^{\rm calc}(\mathbf{Q},0)$ despite the inability to visually resolve these features in $S_2(\mathbf{Q},0)$. This shows the robustness of the RMC simulation and gives confidence in the results.

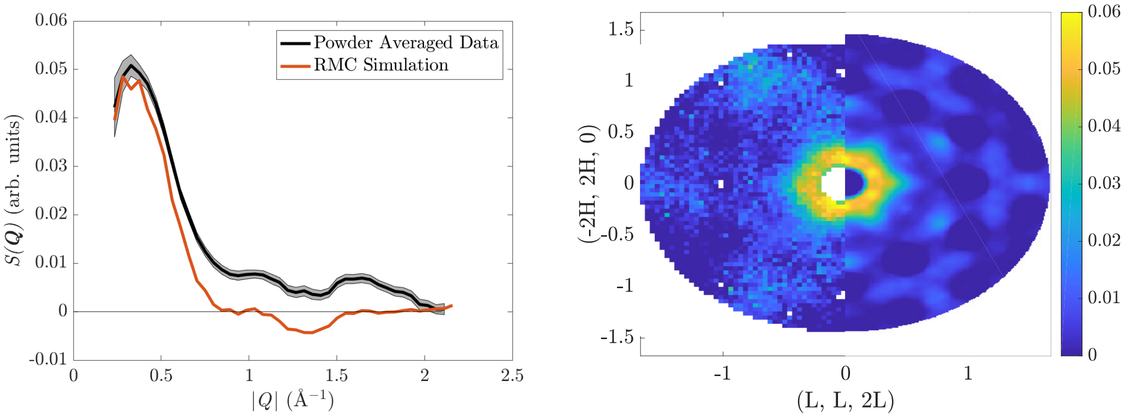

Figure 6.19: RMC simulation of data set 2. Left: powder averaged input data, $S_2(Q)$ and RMC simulated $S_2^{\rm sim}(Q)$. There is qualitative agreement between the shape of the powder averaged data and simulation, but there is an offset in intensity of approx 0.01 for $Q > 0.8$ Å^{-1}. Right: $S_{\rm calc,2}(\mathbf{Q},0)$(right) along with the measured $S_2(\mathbf{Q}, 0)$(left). There is good agreement between data and simulation, particularly at low **Q** where the diffuse hexagon is well reproduced. The high **Q** diffuse peaks are also produced by the simulation with a triangular lineshape. Circular features extend from the sides of the hexagon in the simulation. This feature is not resolved in data, but it was seen in $S_1(\mathbf{Q}, 0)$ (figure 6.18).

Figure 6.20 shows the results of the RMC simulation of $S_3(\mathbf{Q})$. Figure 6.20(left) shows the powder averaged input data, $S_3(Q)$ in addition to the simulated $S_3^{\rm sim}(Q)$. There is good agreement between data and RMC simulation for $|Q| < 1$ Å^{-1} and $|Q| > 2.5$ Å^{-1}. In the intermediate Q range, there is an offset and a small shift in $|Q|$ of the diffuse features indicating that all correlations in the simulation do not represent the measured correlations. The is supported by a comparison between $S_3^{\rm calc}(\mathbf{Q},0)$ and $S_3(\mathbf{Q})$ in figure 6.20(right) which shows qualitative agreement, but $S_3^{\rm calc}(\mathbf{Q},0)$ contains peaks extending from the corners of the low **Q** hexagon which are not observed in $S_3(\mathbf{Q})$.

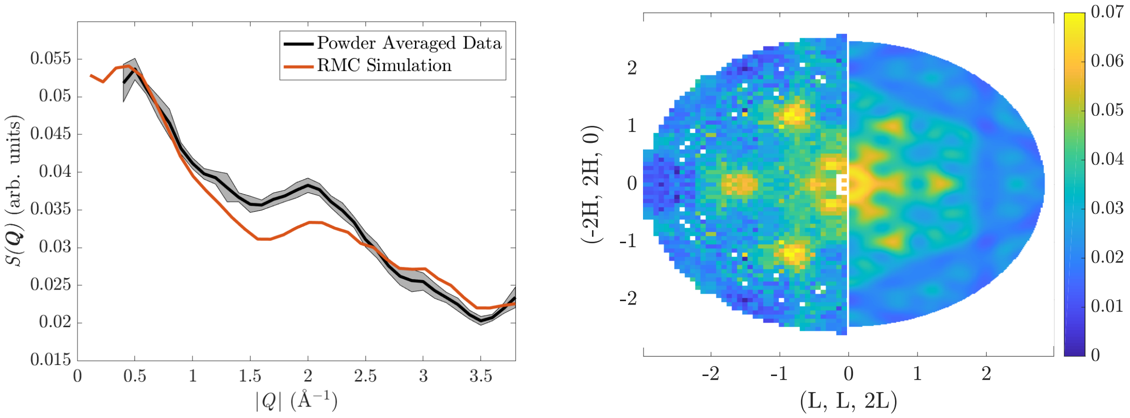

Figure 6.20: RMC simulation of data set 3. Left: powder averaged input data, $S_3(Q)$ and RMC simulated $S_3\text{sim}(Q)$. There is good agreement between data and simulation for $Q < 1$ Å^{-1} and for $Q > 2.5$ Å^{-1}, but there is a vertical offset and a shift in Q between data and simulation in the intermediate region. Right: $S_{\text{calc},3}(\mathbf{Q}, 0)$(left) along with the measured $S_3(\mathbf{Q})$(right).

Correlation Functions and Local Anisotropy

This section studies the correlations and anisotropy derived from the averaged spin configurations that have been obtained in the RMC simulations. Figure 6.21 shows the histograms of the correlations between spins as a function of distance for alle three data sets. Positive values of the correlation are interpreted as FM spin correlations and negative values of the correlation are interpreted as AFM spin correlations. All three data sets obtain FM correlations between NN spins where the average angle is approximately 73° in the simulation of data set 1 and 3 while it is 53° in the simulations of data set 2. Additionally, all three simulations observe AFM correlations between spins separated by 8-12 Å corresponding to the distance across the 10-ion loop (11.210-12.204 Å at room temperature). The correlation length is longer in data set 2 and 3 compared to data set 1 which is seen as a non-zero average angle between spins that are 15-25 Å apart. The simulation of data set 3 shows a strong AFM correlation at 6.1 Å which is not seen in the simulations of data set 1 and 2. For data set 1 the same distance has FM correlations, while it is AFM in data set 2, but the correlations at 6.1 Å are much weaker in both data set 1 and 2 compared to data set 3.

The rest of the section focuses on data set 1, since the spin configurations of the RMC simulation of data set 1 are able to completely reproduce data while there are discrepancies for data sets 2 and 3. However, the spin anisotropy and director state obtained from data sets 2 and 3 are equivalent to the results presented in the following [61].

Figure 6.22 shows the spin probability distribution of the spin configurations obtained in the RMC simulation of data set 1, plotted in local coordinates. The local coordinates were defined in figure 6.1 and is shown again in figure 6.22. The spin probability distribution

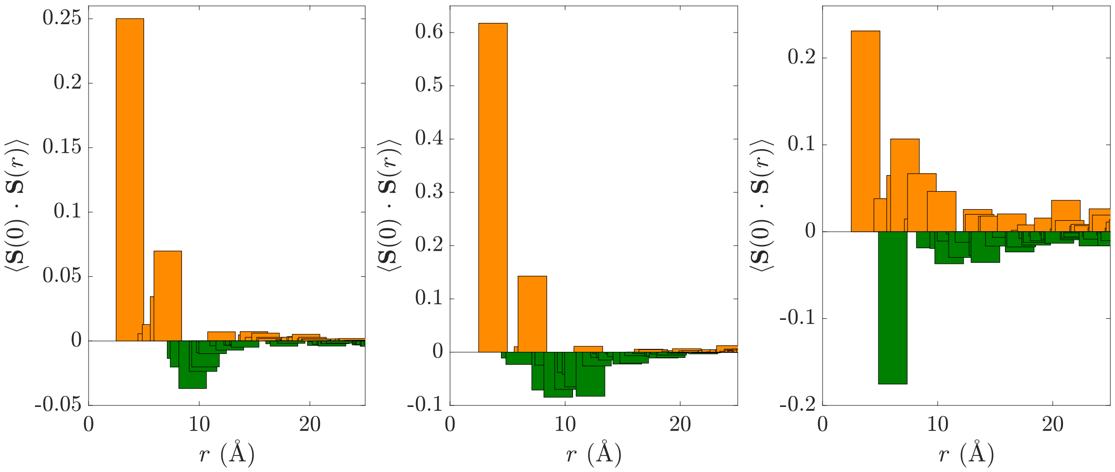

Figure 6.21: Spin correlations obtained from the RMC simulation of data set 1 (left), data set 2 (center) and data set 3 (right). Positive scalars are orange, negative scalars are green. NN correlations are positve (FM) in all three simulations although the value of the correlation is much larger for data set 2 compared to data sets 1 and 3. There are negative (AFM) correlations across the 10-ion loop (10-12 Å). In data set 3, there is a strong AFM correlation at 6.1 Å. The same distance has positive (FM) correlations in the simulation of data set 1 and slightly negative (AFM) correlations for data set 2.

shows an easy axis along the local z-direction connecting the centres of two adjacent triangles.The spin configuration of the RMC simulations of data set 2 and 3 also has an easy axis along the local z-direction, which is stronger in data set 2 compared to data set 1.

Figure 6.23 shows the averaged correlations and anisotropy of the total spin of each 10-ion loop, termed the director, **L**. The correlation function, $g_L = 2\langle|\mathbf{L}(0)\cdot\mathbf{L}(r)|\rangle - 1$ describes the relative orientation of the directors which are collinear if g_L = 1 and orthogonal if g_L = -1. g_L is positive for all distances indicating a collinear director state within the first unit cell, 12.204 Å, while $g_L \approx 0$ outside the first unit cell showing that the director correlations are short ranged.

Figure 6.23(right) shows the probability distribution of the directors, which is very similar to the distribution of the spins in figure 6.22, with an easy axis along local z, but the easy axis is weaker for the directors compared to the spins as seen from the limits on the colour scales in figures 6.22 and 6.23. The director correlations and anisotropy obtained from the RMC simulations of data sets 2 and 3 are equivalent to those presented in figure 6.23.

Figure 6.24 illustrates the results of the RMC simulations. Ising spins are restricted to point along the local z-axis and NN spins couple FM. This results in a large amount of degenerate ground states, one of these is presented in the figure. The figure also shows a director state in red which is restricted to point along the local z-direction of the centre of the 10-ion loop marked marked by a single ion from the opposite hyperkagome lattice.

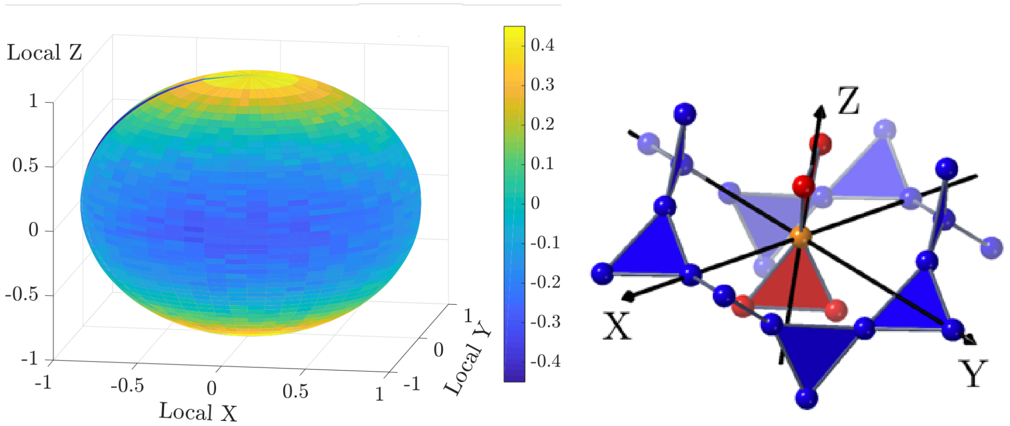

Figure 6.22: Left: Spin probability distribution of the RMC simulation of data set 1 plotted in the local coordinate system (right) on a log colour scale. This shows an easy axis along local the z-direction which connects the centres of two adjacent triangles.

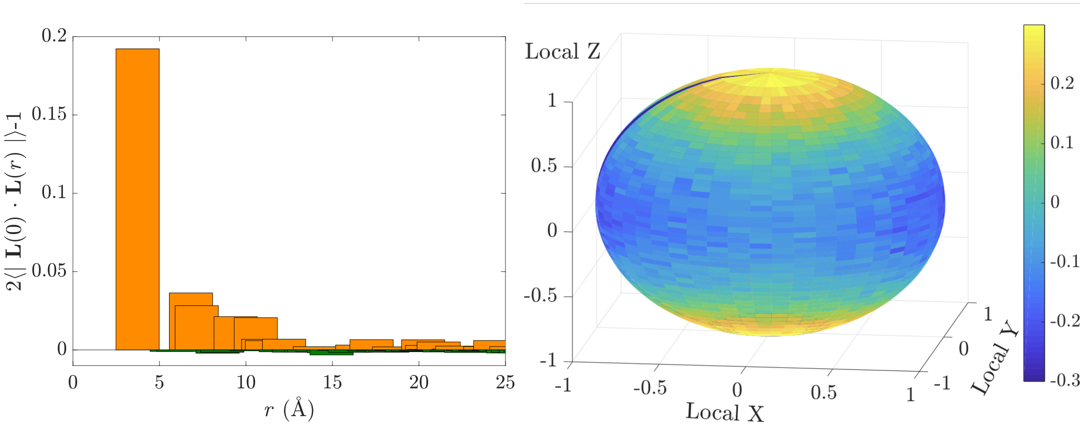

Figure 6.23: Left: Director correlations as a function of distance. Positive scalars (collinear director state) are plotted orange, negative scalars (orthogonal director state) are green. Directors form a collinear state and the correlation length is less than the distance across a 10-ion loop (11.210 Å). Right: Probability distribution of the directors in local coordinates defined in figures 6.1 and 6.22. The intensity is plotted on a logarithmic colour scale. Directors have an easy axis along local z-directions which is out-of-plane of the 10-ion-loop.

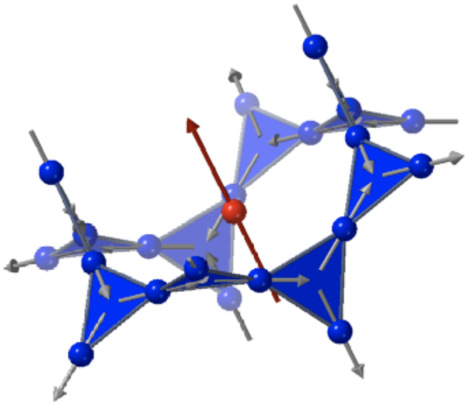

Figure 6.24: Example of a spin configuration on a single 10-ion loop in the hyperkagome lattice (in blue) where NN Ising spins along the local z direction couple FM (grey spins). The red ion from the opposite hyperkagome lattice at the centre of the 10-ion-loop mark the position of the director which also points along the local z direction.

6.4 Discussion

We have obtained 3 different data sets by probing YbGG with cold neutron scattering at two different instruments. While there are variations in the exact RMC simulation results, the simulations of all three data sets agree that spins have an easy axis along the local z axis connecting the centres of two corner-sharing triangles, and NN correlations are FM while there are AFM correlations across the 10-ion loops. Figure 6.24 shows an example of a spin configuration which follows this.

As such there are strong analogies to the spin ice compounds, described in section 5.1 which have a strong easy axis anisotropy connecting the centres of the tetrahedra and are well approximated by an Ising system with FM NN interactions. In spin ice compounds, this results in a correlated state which obeys the *ice rules* with two spins pointing *in* towards the centre of the tetrahedron and two spins pointing *out* of the tetrahedron [14], the two-in-two-out state. It is not possible to obtain a similar state in triangles since there is an odd number of spins, but we suggest the ground state presented in figure 6.24 where on average across all triangles in the system, 1.5 spins point in towards the centre of the triangles and 1.5 spins point out of the triangles. We term this the 1.5-in-1.5-out state.

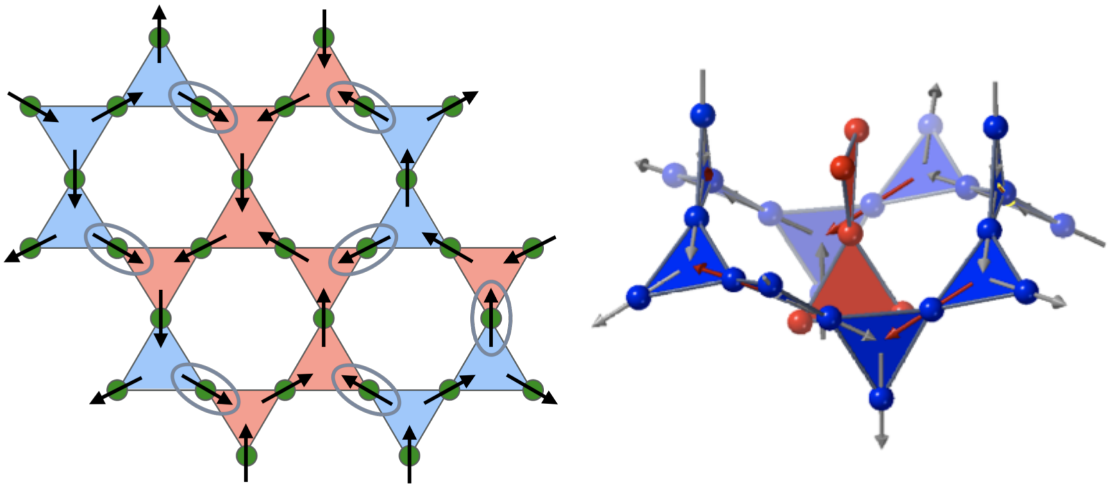

Figure 6.25: Left: 1.5-in-1.5-out state on a kagome lattice. 8 red triangles have 2-in-1-out spins and 8 blue triangles have 1-in-2-out spin configurations. 7 marked spins can flip without adding energy to the system. Right: E1.5-in-1.5-out state on a single 10-ion loop in YbGG. One spin in each triangle is marked red because it can flip without any energy cost (excluding edge-spins).

Figure 6.25(left) shows an example of a 1.5-in-1.5-out state on a 2D kagome lattice to enhance graphical clarity compared to the 3D hyperkagome lattice. Figure 6.25(left) contains 8 blue triangles with 1-in-2-out spin configurations and 8 red triangles with a 2-in-1-out spin configurations. Using the same terminology as for the excitations in spin ice compounds, the blue triangles are referred to as negative magnetic monopoles and red triangles are referred to as positive magnetic monopoles. The 7 marked spins in the figure can flip without adding energy to the system since this will simply translate the monopoles in the system which remains in a 1.5-in-1.5-out state thereby enabling substantial ground state fluctuations.

The same principle apply to YbGG as illustrated in figure 6.25(right) where spins on a single 10-ion-loop of the hyperkagome lattice form a 1.5-in-1.5-out state. All red spins in the figure can flip without any energy cost.

Figure 6.26 shows that it is possible to extend the analogy to spin ice further with propagation of magnetic monopoles. By flipping a series of 4 adjacent spins, two marked magnetic monopoles are separated in the kagome lattice very similarly to the propagation of magnetic monopoles in spin ice compounds described in section 5.1.

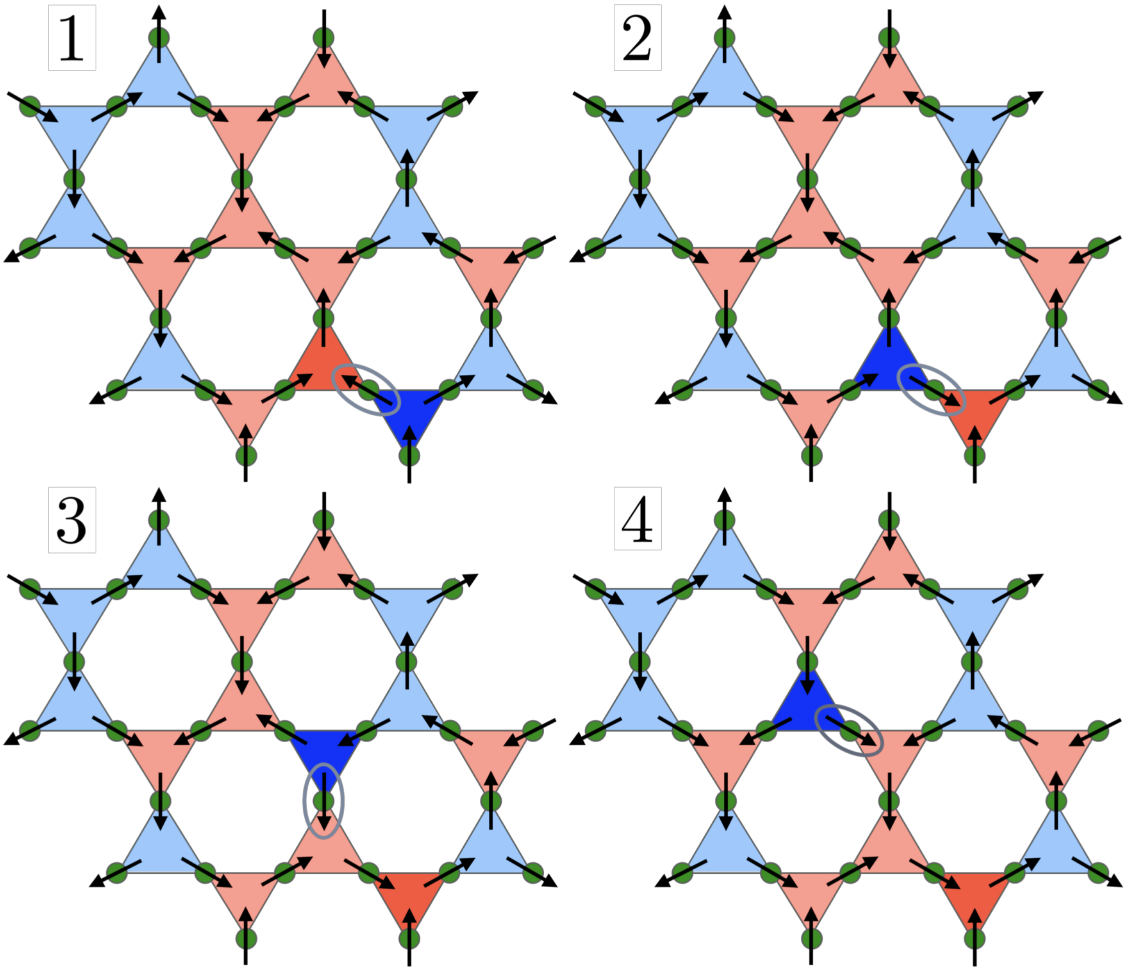

Figure 6.26: All four configurations above are ground state configurations, 1.5-in-1.5-out, where 8 triangles have spin configuration 2-in-1-out (red triangles) and 8 triangles have a 1-in-2-out spin configuration (blue triangles). Propagation of magnetic monopoles in the ground state on the kagome lattice are very similar to propagation of magnetic monopoles in the excitated state of spin ice (figure 5.2).

However, the anisotropy in YbGG is much weaker than in the classical spin ice compounds HTO and DTO, and the Ising model which is presented in figure 6.25 is therefore too simple. Indeed, classical Monte Carlo simulation of an Ising system is unable to reproduce all features observed in data sets 1-3 showing that a more complex Hamiltonian and possibly quantum effects are neeeded to describe YbGG.

Figure 6.27 shows the averaged probability distribution of the spins drawn on each site of a 10-ion loop, which is interpreted as the spin anisotropy. Figure 6.27(a) presents the anisotropy of GGG [56] which has been calculated based on the spin structure obtained by Paddison et al. from an RMC simulation of 6×6×6 unit cells. Figures 6.27(b)-(d) presents the anisotropy for YbGG in data sets 1-3. The anisotropy results which have been obtained with RMC simulations of YbGG are opposite to the results of GGG which a planar anisotropy in the local XY-plane while YbGG has an easy axis along the local Z direction. The physical origin of the observed anisotropy in YbGG is not currently understood. The diagonal elements of the crystal g-factor has been calculated by Pearson et al. as g = (2.84, 3.59, -3.72) in local coordinates [59] which would indicate a slight preference along the local z direction, but according to these calculations, the system is better approximated by an isotropic spin distribution. It should be noted that the Spinvert algorithm generally underestimates magnetic anisotropy [57], and the consistent easy axis along the local z direction for all three data sets therefore gives confidence in the easy axis. However, the crystal field calculations are able to describe well the susceptibility measurements and the crystal field energy levels, and it therefore seems highly interesting to explore this isotropic model further.

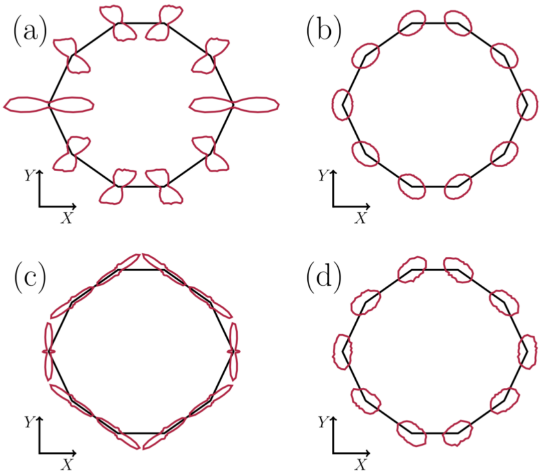

Figure 6.27: Probability distributions of the spin configurations obtained by RMC simulations. (a) shows the probability distribution of GGG which has been calculated based on the spin configuration obtained by Paddison et al. [56]. (b)-(c) shows the probability distributions obtained from RMC simulations of datasets 1-3 respectively.

Similarly, the correlations which have been obtained from the RMC simulations of YbGG and GGG are also distinctly different. The spin configuration obtained by Paddison et al. has been used to calculate $S^{\mathrm{calc}}_{\mathrm{GGG}}(\mathbf{Q})$ in the scattering plane that we used for the cold neutron scattering measurements of YbGG. Figure 6.28 compares $S^{\mathrm{calc}}_{\mathrm{GGG}}(\mathbf{Q})$ with the YbGG data $S_1(\mathbf{Q}, 0)$. The diffuse scattering features has no overlap which shows that the spin configuration obtained for GGG is not able to describe the neutron scattering measurements of YbGG. Additionally, the director state in GGG correlate long range despite the absence of long range spin correlations [56] which is not observed in YbGG.

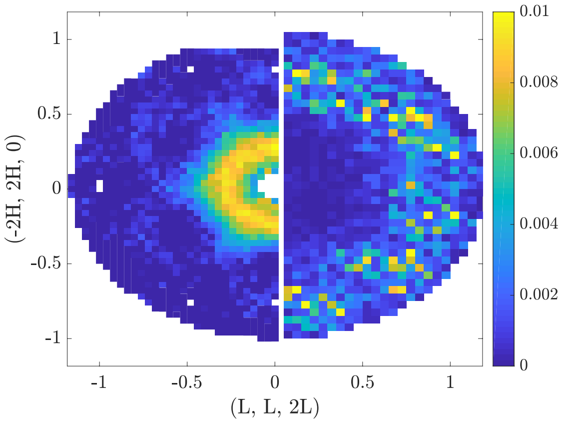

Figure 6.28: Comparison of $S_1(\mathbf{Q}, 0)$ for YbGG (left) and the calculated $S^{\mathrm{calc}}_{\mathrm{GGG}}(\mathbf{Q})$ based on the RMC simulation of GGG (right). There is no overlap between data for YbGG and simulations for GGG showing that the simulated spin configuration for GGG is unable to describe the observed features in YbGG.

Despite the differences in the structure of GGG and YbGG, the excitations seem remarkably similar. GGG has three dispersionless excitations at 0.04 meV, 0.12 meV and 0.58 meV respectively, where at least the second excitation has been assigned to the director dynamics [5]. It is therefore possible that a way to better understand the excitations in YbGG is to compare it to the excitations in GGG.

However, the elastic results show that the physics in these two isostructural systems is fundamentally different showing the importance of even small changes in the interatomic distances which alters the balance between different spin-spin interactions and the anisotropy.

6.5 Conclusion

We have measured the three lowest crystal field excitations in YbGG with thermal inelastic neutron scattering thereby confirming the crystal field calculations performed by Pearson et al. in 1967 [59]. We have used these calculations to determine the crystal field contribution to the magnetic susceptibility showing that a Hamiltonian without any exchange interactions is able to accurately reproduce the measured susceptiblity except at the very lowest temperatures, $T < 5$ K. A Curie-Weiss fit in this region yield $\Theta_{\mathrm{CW}} =$ -0.2(1) K showing AFM correlations.

We have probed the structure and dynamics of YbGG in its correlated, unordered phase for $0.1 \text{ K} < T < 0.6 \text{ K}$ with two different cold neutron scattering instruments. The three data sets probe different regions in $\mathbf{Q}$ and energy and have correspondingly different resolutions. With RMC simulations, we were able to reproduce all features in $S_1(\mathbf{Q}, 0)$ of data set 1, while we obtained qualitative agreement with $S_2(\mathbf{Q}, 0)$ and $S_3(\mathbf{Q})$. RMC simulation of all three data sets yield equivalent results on the averaged spin orientation showing an easy axis anisotropy along the local z direction connecting two adjacent triangles, and they also all obtain FM NN correlations and AFM correlations across the 10-ion loops. Finally, all three simulations find a short range collinear director state within the first unit cell. The correspondence between the results of RMC simulations of these three neutron scattering experiments which probe different regions in $\mathbf{Q}$ and use different methods to extract the magnetic contribution to $S(\mathbf{Q})$ motivates the credibility of these results.

Chapter 7

Summary

In this thesis, we have presented a neutron scattering and magnetic susceptibility study of the magnetically frustrated compound YbGG. We have measured the three lowest crystal field exciations with thermal neutron scattering, which allowed us to confirm the crystal field calculations that were performed by Pearson et al. in 1967 [59]. The results of these calculations, where exchange is neglected, were also able to correctly reproduce the measured magnetic susceptibility, which shows that the spin-spin interactions in YbGG are very weak compared to the crystal field interactions. We found θ_{CW} = -0.2(1) K showing AFM correlations.

We have also probed the magnetic structure of YbGG with polarised diffuse magnetic scattering and cold inelastic neutron scattering for the temperature regime 0.1 K < T < 0.6 K in the correlated, disordered phase of YbGG. RMC simulations of the data sets yielded equivalent results with antiferromagnetic couplings across the 10-ion loops and ferromagnetic couplings between nearest neighbour spins. All data and subsequent simulations also revealed an easy spin axis along the local z-axis connecting the centres of adjacent triangles. The total spin of each 10-ion loop, the director, displays short range collinear correlations within the first unit cell, unlike the director state in the isostructural compound GGG, which correlated long range despite the absence of long range correlations of the individual spins. The consistency of the YbGG RMC simulations shows the robusness of the results which are based on neutron scattering measurements with fundamentally different instruments and with different regions of reciprocal space probed.

The second part of the thesis involves the design, testing and calibration of a uniaxial pressure cell aimed at the study of magnetically frustrated compounds with diffuse neutron scattering. We have performed three different neutron scattering experiments at two different instruments with the cell. We here detected pressure induced changes which were only a few percent of the weak, diffuse neutron scattering signals at ambient pressure, showing that the cell background is sufficiently low and uniform to study correlated, but disordered materials. We were also able to perform neutron polarisation analysis and apply 32 kN with the cell, corresponding to 2 GPa on a 4.5 mm cylindrical sample. However, we have not been able to apply pressures above 800 MPa to any crystal samples, possibly due to the combination of the very hard WC10 anvils and a small uniaxial components when applying the pressure with the most up to date cell, cell D. We have therefore proposed cell E, where a more optimised application of pressure that is truly uniaxial should reduce the tension in the crystals during the force application. For pressures up to 350 MPa, it is possible to use the steel 316 seats in cell D, which absorbs some of the tension during force application. The cell is now ready to be directly used at many different instruments for elastic and inelastic neutron scattering and with polarisation analysis.

Index

Bibliography

[1] B. G. Wensley et al. "Experimental evidence for a frustrated energy landscape in a three-helix- bundle protein family". *Nature.* 463 (2010), p. 6858.

[2] C. Castellano et al. "Statistical physics of social dynamics". *Rev. Mod. Phys.* 81 (2009), p. 591.

[3] Heinz Maier-Leibnitz Zentrum et al. "DNS: Diffuse scattering neutron time-of-flight spectrometer." *Journal of large-scale research facilities* 1.A27 (2015). ISSN: 0168-9002. DOI: `http://dx.doi.org/10.17815/jlsrf-1-33`.

[4] Z. Guguchia et al. "Using uniaxial stress to probe the relationship between competing states in a cuprate with spin-stripe order". *Phys. Rev. Lett.* 125.097005 (2020).

[5] N. Ambrumenil, O. A. Petrenko, H. Mutka, and P. P. Deen. "Dispersionless Spin Waves and Underlying Field-Induced Magnetic Order in Gadolinium Gallium Garnet". *Physical Review Letters* 227203.JUNE (2015), pp. 1–5. DOI: `10.1103/PhysRevLett.114.227203`.

[6] Customer Technical Services Manager Andrew Lee. *HOW DO YOU HEAT TREAT COPPER BERYLLIUM PARTS?* `https://materion.com/about/new-at-materion/in-our-element-heat-treating-copper-beryllium-parts`. Accessed: August 30, 2021.

[7] R.I. Bewley, J.W. Taylor, and S.M. Bennington. "LET, a cold neutron multi-disk chopper spectrometer at ISIS". *Nuclear Instruments and Methods in Physics Research Section A: Accelerators, Spectrometers, Detectors and Associated Equipment* 637.1 (2011), pp. 128–134. ISSN: 0168-9002. DOI: `https://doi.org/10.1016/j.nima.2011.01.173`. URL: `https://www.sciencedirect.com/science/article/pii/S0168900211002750`.

[8] Tobias Biesner and Ece Uykur. "Pressure-Tuned Interactions in Frustrated Magnets : Pathway to Quantum Spin Liquids ?" *Crystals* 10.4 (2020), pp. 1–23. DOI: `10.3390/cryst10010004`.

[9] S. Blundell. *Magnetism in Condensed Matter.* 1st. Oxford Master Series in Condensed Matter Physics, Oxford University Press, 2001. ISBN: 978-0-19-850592-1.

[10] Steven T Bramwell and Michel J P Gingras. "Spin Ice State in Frustrated Magnetic Pyrochlore Materials". *Science* 294.November (2001), pp. 1495–1502.

[11] C. Broholm et al. "Quantum spin liquids". *Science* 367.6475 (2020). ISSN: 0036-8075. DOI: `10.1126/science.aay0668`. eprint: `https://science.sciencemag.org/`

`content/367/6475/eaay0668.full.pdf`. URL: `https://science.sciencemag.org/content/367/6475/eaay0668`.

[12] William H. Brumage, Chun C. Lin, and J. H. Van Vleck. “Magnetic Susceptibility and Crystalline Field Levels of Ytterbium Gallium Garnet”. *Physical Review* 132.2 (1963), pp. 608–610.

[13] R. A. Buchanan, K. A. Wickersheim, J. J. Pearson, and G. F. Herrmann. “Energy levels of Yb3+ in gallium and aluminum garnets. I. Spectra”. *Physical Review* 159.2 (1967), pp. 245–251. ISSN: 0031899X. DOI: `10.1103/PhysRev.159.245`.

[14] C. Castelnovo, R. Moessner, and S. L. Sondhi. “Magnetic monopoles in spin ice”. *Nature* 451.7174 (2008), pp. 42–45. DOI: `10.1038/nature06433`. arXiv: `0710.5515v2`.

[15] C Castelnovo, R Moessner, and S L Sondhi. “Spin Ice , Fractionalization , and Topological Order” (2012). DOI: `10.1146/annurev-conmatphys-020911-125058`.

[16] Robert J. Corruccini and John J. Gniewek. *Thermal Expansion of Technical Solids at Low Temperatures.* 1st. National Bureau of Standards Monograph 29, 1961.

[17] P. Dalmas de Réotier et al. “Absence of Magnetic Order in $Yb_3Ga_5O_{12}$: Relation between Phase Transition and Entropy in Geometrically Frustrated Materials”. *Phys. Rev. Lett.* 91 (16 Oct. 2003), p. 167201. DOI: `10.1103/PhysRevLett.91.167201`. URL: `https://link.aps.org/doi/10.1103/PhysRevLett.91.167201`.

[18] P Duthil. “Material Properties at Low Temperature”. *Proceedings of the CAS-CERN Accelerator School: Superconductivity for Accelerators.* Vol. 005. May 2013. 2014, pp. 77–95.

[19] R. Edberg et al. “Dipolar spin ice under uniaxial pressure”. *Physical Review B* 100.14 (2019), p. 144436. ISSN: 0031-899X. DOI: `10.1103/PhysRevB.100.144436`.

[20] R. Edberg et al. “Effects of uniaxial pressure on the spin ice $Ho_2Ti_2O_7$”. *Phys. Rev. B* 102 (18 Nov. 2020), p. 184408.

[21] G. Ehlers, A. A. Podlesnyak, and A. I. Kolesnikov. “The cold neutron chopper spectrometer at the Spallation Neutron Source—a review of the first 8 years of operation”. *Rev. Sci. Instrum.* 87 (2016), p. 093902.

[22] T. Fennell et al. “Field Induced Partial Order in the Spin-Ice Dysprosium Titanate”. *Applied Physics A* 74 (2002), pp. 889–891.

[23] T. Fennell et al. “Magnetic coulomb phase in the spin ice Ho2Ti2O7”. *Science* 326.October (2009), pp. 415–417. ISSN: 1095-9203. DOI: `10.1126/science.1177582`.

[24] T Fennell et al. “Wavevector and energy resolution of the polarized diffuse scattering spectrometer D7”. *Nuclear Inst. and Methods in Physics Research, A* 857.November 2016 (2017), pp. 24–30. ISSN: 0168-9002. DOI: `10.1016/j.nima.2017.03.024`. URL: `http://dx.doi.org/10.1016/j.nima.2017.03.024`.

[25] J. Filippi et al. “Magnetic properties of ytterbium gallium garnet between 44 mK and 4 K”. *J. Phys. C: Solid State Physics* 13 (1980), p. 1277.

[26] Jacob Fish and Ted Belytschko. *A First Course in Finite Elements.* 1st. Wiley, 2007.

[27] I. M. B. Fjellvagen et al. “Single crystal growth of pyrochlore titanate oxides (RE2Ti2O7) by optical zone melting for neutron and magnetic property studies”. *Unpublished Manuscript* (2022).

[28] Jason S (NIST center for neutron resarch) Gardner, University of Waterloo) Gingras, Michel J. P. (Department of Physics and Astronomy, and McMaster University)

Greedan, John E (Department of Chemistry and Brockhouse Institute for Materials Reseach. “Magnetic pyrochlore oxides”. *Reviews of Modern Physics* 82.March (2010), pp. 53–100. DOI: `10.1103/RevModPhys.82.53`.

[29] M. J. Gingras and P. A McClarty. “Quantum spin ice: A search for gapless quantum spin liquids in pyrochlore magnets”. *Reports on Progress in Physics* 77.55 (2014), p. 5.

[30] D.J. Griffiths. *Introduction to Quantum Mechanics*. 2nd, Pearson New International Edition. Pearson,

[31] Felix Groitl et al. “CAMEA—A novel multiplexing analyzer for neutron spectroscopy”. *Review of Scientific Instruments* 87.3 (2016), p. 035109. DOI: `10.1063/1.4943208`. eprint: `https://aip.scitation.org/doi/pdf/10.1063/1.4943208`. URL: `https://aip.scitation.org/doi/abs/10.1063/1.4943208`.

[32] Bianca Haberl et al. “Wide-angle diamond cell for neutron scattering”. *High Pressure Research* 37.4 (2017), pp. 495–506. ISSN: 14772299. DOI: `10.1080/08957959.2017.1390571`. URL: `https://doi.org/10.1080/08957959.2017.1390571`.

[33] Tian-heng Han et al. “Fractionalized excitations in the spin-liquid state of a kagome-lattice antiferromagnet”. *Nature* 492.7429 (2012), pp. 406–410. ISSN: 0028-0836. DOI: `10.1038/nature11659`. URL: `http://dx.doi.org/10.1038/nature11659`.

[34] Clifford W. Hicks, Shreenanda Ghosh, Mark E. Barber, and Hans-Henning Klauss. “Piezoelectric-Driven Uniaxial Stress Apparatus for Muon Spin Rotation”. *JPS Conference Proceedings* 21.011040 (2018), pp. 1–7. DOI: `10.7566/JPSCP.21.011040`.

[35] J. A. Hodges, P. Bonville, M. Rams, and K. Krolas. “Low temperature spin fluctuations in geometrically frustrated Yb3Ga5O12”. *Journal of Physics: Condensed Matter* 15 (2003), p. 4631.

[36] JKarl Hoffmann. *An Introduction to Measurements using Strain Gages*. 1st. Hottinger Baldwin Messtechnik GmbH, 1989.

[37] materials Hyperion and technology. *`http://www.allaboutcementedcarbide.com/what-is-cemented-carbide/thermal-properties/`*. June 2021.

[38] L. D. C. Jaubert and P. C. W. Holdsworth. “Signature of magnetic monopole and Dirac string dynamics in spin ice”. *Nature Physics* 5 (258 2009).

[39] J. Jensen and A.R. Mackintosh. *Rare Earth Magnetism - Structures and Excitations*. Ed. by J. et al. Birman. 1st. Clarendon Press, Oxford University Press, 1991. ISBN: 0-19-852027-1.

[40] David A. Keen and Andrew L. Goodwin. “The crystallography of correlated disorder”. *Nature* 521.7552 (2015), pp. 303–309. ISSN: 14764687. DOI: `10.1038/nature14453`.

[41] E Kermarrec et al. “Ground state selection under pressure in the quantum pyrochlore magnet Yb2Ti2O7”. *Nature Communications* 8.14810 (2017), pp. 6–10. DOI: `10.1038/ncomms14810`.

[42] M.G.a Kibble et al. “Low-background materials for high pressure cells used in inelastic neutron scattering experiments”. *Journal of Neutron Research* 21, no 3-4 (2019), pp. 105–116.

[43] H. Kimura et al. “Crystal growth and characterization of ytterbium garnet and holmium garnet using the Fz technique”. *Journal of Crystal Growth* 311 (2009), pp. 522–525. DOI: `10.1016/j.jcrysgro.2008.09.027`.

[44] Stefan Klotz. *Techniques in high pressure neutron scattering.* Taylor & Francis Group, 2013. ISBN: 9781439835630.

[45] Claudine Lacroix, Philippe Mendels, and Frédéric Mila. *Introduction to Frustrated Magnetism.* 1st ed. Springer Series in Solid State Physics, 2011. ISBN: 9783642105883. DOI: `10.1007`.

[46] Kim Lefmann. *Neutron Scattering - Theory, Instrumentation, and Simulation.* 1st ed. Notes for the NNSP summer school, found at `https://indico.nbi.ku.dk/event/1670/page/647-materials`, 2021.

[47] E. Lhotel et al. "Spin Dynamics of the Quantum Dipolar Magnet $Yb_3Ga_5O_{12}$ in an external field". *Phys. Rev. B* 104 (2 July 2021), p. 024427.

[48] Q. Li et al. "Two-dimensional superconducting fluctuations in stripe-ordered LBCO". *Phys. Rev. Lett.* 99.067001 (2007).

[49] Azo materials. *`https://www.azom.com/properties.asp`*. June 2021.

[50] I Mirebeau and I N Goncharenko. "Spin ice and spin liquid under pressure up to 8 . 6 GPa : A powder neutron diffraction study of R 2 Ti 2 O 7 (R = Tb , Ho)". *Physica B* 350 (2004), pp. 250–253. DOI: `10.1016/j.physb.2004.04.039`.

[51] I Mirebeau et al. "Pressure-induced crystallization of a spin liquid". *letters to nature* 420.November (2002).

[52] M. Mito et al. "Uniaxial pressure effects on spin-ice compound Dy2Ti2O7". *Journal of Magnetism and Magnetic Materials* 310.2, Part 2 (2007), e432–e434. ISSN: 0304-8853.

[53] J. Ollivier and J. M. Zanotti. "Diffusion inelastique de neutrons par temps de vol". *EDP Sciences* 10 (2010), pp. 379–4235.

[54] Jacques Ollivier, Hannu Mutka, and Luc Didier. "The New Cold Neutron Time-of-Flight Spectrometer IN5". *Neutron News* 21.2 (2010), pp. 22–25. DOI: `10.1080/10448631003757573`. eprint: `https://doi.org/10.1080/10448631003757573`. URL: `https://doi.org/10.1080/10448631003757573`.

[55] Joseph A. M. Paddison, J. Ross Stewart, and Andrew L. Goodwin. "Spinvert: A program for refinement of paramagnetic diffuse scattering data". *Journal of Physics: Condensed Matter* 25.454220 (2013). DOI: `10.1088/0953-8984/25/45/454220`.

[56] Joseph A M Paddison et al. "Hidden order in spin-liquid Gd 3 Ga 5 O 12". *Science* 350.6257 (2015), pp. 179–182.

[57] Joseph A.M. Paddison, J. Ross Stewart, and Andrew L. Goodwin. "Spinvert: A program for refinement of paramagnetic diffuse scattering data". *Journal of Physics Condensed Matter* 25.45 (2013). ISSN: 09538984. DOI: `10.1088/0953-8984/25/45/454220`. arXiv: `arXiv:1302.2949v1`.

[58] H. Pais and J.R. Stone. "Exploring the Nuclear Pasta Phase in Core-Collapse Supernova Matter". *Phys. Rev. Lett* 109 (2012), p. 151101.

[59] J. J. Pearson, G. F. Herrmann, K. A. Wickersheim, and R. A. Buchanan. "Energy Levels of Yb^{3+} in Gallium and Aluminum Garnets. II. Calculations". *Physical Review* 159 (1967), p. 2.

[60] L. Ø. Sandberg et al. "Uniaxial pressure induced changes in Ho2Ti2O7 measured with neutrons scattering". *Unpublished Manuscript* (2022).

[61] Lise Ø Sandberg et al. "Emergent magnetic behavior in the frustrated $Yb_3Ga_5O_{12}$ garnet". *Phys. Rev. B* 104 (6 Aug. 2021), p. 064425. DOI: `10.1103/PhysRevB.104.064425`. URL: `https://link.aps.org/doi/10.1103/PhysRevB.104.064425`.

[62] Lucile Savary and Leon Balents. "Quantum spin liquids: A review". *Reports on Progress in Physics* 80.016502 (2017). ISSN: 00344885. DOI: `10.1088/0034-4885/80/1/016502`. eprint: `1601.03742`.

[63] N. J. Simon, E. S. Drexler, and R. P. Reed. *Properties of Copper and Copper Alloys at Cryogenic Temperatures.* Nist Monograph 177, 1992.

[64] Yogesh Singh, Y. Tokiwa, J. Dong, and P. Gegenwart. "Spin liquid close to a quantum critical point in Na4Ir3O8". *Physical Review B* 88.22 (2013), p. 220413. ISSN: 1098-0121. DOI: `10.1103/PhysRevB.88.220413`. arXiv: `1312.3123`. URL: `https://link.aps.org/doi/10.1103/PhysRevB.88.220413`.

[65] G. L Squires. *Introduction to the Theory of Thermal Neutron Scattering.* 3rd ed. Cambridge University Press, 2012.

[66] National Institute of Standards and Technology. *https://www.ncnr.nist.gov/resources/n-lengths/*. Dec. 2021.

[67] National Institute of Standards and U.S. Department of Commerce Technology. *Compute Neutron Attenuation and Activation.* `https://www.ncnr.nist.gov/instruments/bt1/neutron.html`. Accessed: June 18, 2018.

[68] National Institute of Standards and U.S. Department of Commerce Technology. *Material Properties: Beryllium Copper.* `https://trc.nist.gov/cryogenics/materials/Beryllium%20Copper/BerylliumCopper_rev.htm`. Accessed: June 18, 2020.

[69] J. R. Stewart et al. "Disordered materials studied using neutron polarization analysis on the multi-detector spectrometer, D7". *J. Appl. Cryst.* 42 (2009), p. 69.

[70] J. M. Tranquada et al. "Evidence for stripe correlations of spins and holes in copper oxide superconductors". *Nature* 375.561 (1995).

[71] Kazunori Umeo et al. "Uniaxial-Pressure-Induced Release of Magnetic Frustration in a Triangular Lattice Antiferromagnet YbCuGe". *Metals* 11.30 (2021). DOI: `https://dx.doi.org/10.3390/met11010030`.

[72] X. R. Wang, X. C. Hu, and H. T. Wu. *Communications Physics* 4 (142 2021).

Appendix A

Publications and Manuscripts

A.1 Publication 1: Dipolar spin ice under uniaxial pressure

My contribution to the publication involves primarily the neutron scattering measurements with the pressure cell A. I designed, tested and calibrated the pressure cell for the neutron scattering beamtime at D7 at the Utgård facility at the European Spallation Source. In collaboration with Ingrid Marie Bakke Fjållvåg, I participated in the sample preparation, where HTO single crystals were made using the optical mirror furnace at the University of Lund as well as the crystal cutting and polishing. Finally, I performed the data analysis of the neutron scattering data, including the background simulations of the pressure cell, in collaboration with Morten Haubro, who did his master's thesis in the project.

Dipolar spin ice under uniaxial pressure

Edberg, R.; Sandberg, L. Orduk; Bakke, I. M. Bergh; Haubro, M. L.; Folkers, L. C.; Mangin-Thro, L.; Wildes, A.; Zaharko, O.; Guthrie, M.; Holmes, A. T.; Sorby, M. H.; Lefmann, K.; Deen, P. P.; Henelius, P.

Published in:
Physical Review B

DOI:
10.1103/PhysRevB.100.144436

Publication date:
2019

Document version
Publisher's PDF, also known as Version of record

Citation for published version (APA):
Edberg, R., Sandberg, L. O., Bakke, I. M. B., Haubro, M. L., Folkers, L. C., Mangin-Thro, L., Wildes, A., Zaharko, O., Guthrie, M., Holmes, A. T., Sorby, M. H., Lefmann, K., Deen, P. P., & Henelius, P. (2019). Dipolar spin ice under uniaxial pressure. *Physical Review B*, *100*(14), [144436]. https://doi.org/10.1103/PhysRevB.100.144436

Dipolar spin ice under uniaxial pressure

R. Edberg,[1] L. Ørduk Sandberg,[2] I. M. Bergh Bakke,[3] M. L. Haubro,[2] L. C. Folkers,[4] L. Mangin-Thro,[5] A. Wildes,[5]
O. Zaharko,[6] M. Guthrie,[7,8] A. T. Holmes,[7] M. H. Sørby,[9] K. Lefmann,[2] P. P. Deen,[2,7] and P. Henelius[1,10]
[1]*Physics Department, KTH Royal Institute of Technology, Stockholm, Sweden*
[2]*Nanoscience Center, Niels Bohr Institute, University of Copenhagen, Universitetsparken 5, 2100 Copenhagen Ø, Denmark*
[3]*Centre for Materials Science and Nanotechnology, University of Oslo, 0315, Oslo, Norway*
[4]*Department of Chemistry, University of Lund, Lund, Sweden*
[5]*Institut Laue-Langevin, 38042 Grenoble, France*
[6]*Laboratory for Neutron Scattering, Paul Scherrer Institute, 5232 Villigen PSI, Switzerland*
[7]*European Spallation Source ERIC, 22363 Lund, Sweden*
[8]*School of Physics and Astronomy and Centre for Science at Extreme Conditions, University of Edinburgh, Edinburgh, United Kingdom*
[9]*Department for Neutron Materials Characterization, Institute for Energy Technology, P.O. Box 40, 2027 Kjeller, Norway*
[10]*Faculty of Science and Engineering, Åbo Akademi University, Åbo, Finland*

(Received 20 May 2019; revised manuscript received 6 September 2019; published 25 October 2019)

The magnetically frustrated spin ice family of materials is host to numerous exotic phenomena such as magnetic monopole excitations and macroscopic residual entropy extending to low temperature. A finite-temperature ordering transition in the absence of applied fields has not been experimentally observed in the classical spin ice materials $Dy_2Ti_2O_7$ and $Ho_2Ti_2O_7$. Such a transition could be induced by the application of pressure, and in this work we consider the effects of uniaxial pressure on classical spin ice systems. Theoretically, we find that the pressure-induced ordering transition in $Dy_2Ti_2O_7$ is strongly affected by the dipolar interaction. We also report measurements of the neutron structure factor of $Ho_2Ti_2O_7$ under pressure and compare the experimental results to the predictions of our theoretical model.

DOI: 10.1103/PhysRevB.100.144436

I. INTRODUCTION

In a frustrated magnet a unique ground state can be difficult to reach since the primary interactions are obstructed by competition between interactions of similar strength or a special geometry of the lattice, leading to a strong ground-state degeneracy in the unperturbed case [1]. Therefore, an eventual low-temperature ordering transition and resolution of the third law of thermodynamics are often driven by weak, perturbative interactions whose effects are typically hidden in nonfrustrated systems. In recent years, the geometrically frustrated spin ice compounds have revealed many unusual phenomena such as magnetic monopole excitations [2], fractionalization of the magnetic moment [3], and a low-temperature Coulomb phase [4]. However, a low-temperature ordering transition below the Coulomb phase in the absence of applied fields has not been experimentally observed in the classical spin ice compounds $Dy_2Ti_2O_7$ (DTO) and $Ho_2Ti_2O_7$ (HTO) [5,6]. Theoretically, there are predictions for a dipolar-driven low-temperature transition in the 0.2 K temperature range [7], but experimentally, the measurements are challenging due to extremely slow relaxation effects [5], and the nature of such a transition is not known.

One way to increase the possible transition temperature into a more experimentally accessible range is to apply a suitable perturbation, such as pressure, to the system. Previous experimental studies detected a clear uniaxial pressure-induced signature in the susceptibility of DTO [8], while hydrostatic pressure has no noticeable effect on HTO [9]. A previous theoretical study predicted that uniaxial pressure should give rise to an unusual infinite order phase transition in DTO, with features of both continuous and discontinuous transitions, to a ferromagnetic state [10]. In this study, we include the long-range dipolar interaction in the theoretical model and find that it does not favor the ferromagnetic state. We also perform spin-polarized neutron scattering experiments on HTO under uniaxial pressure and compare the results to our theoretical predictions. While our model captures the qualitative features of the experiment, further measurements are needed in order to fully understand the effects of pressure on the low-temperature spin ice state in DTO and HTO.

II. MODEL, SIMULATION, AND EXPERIMENTAL METHODS

A. Model

Existing literature presents a large number of spin ice models, ranging from effective monopole models [2] and electrolyte theories [11] to microscopic models incorporating, for example, dipolar, exchange, and even hyperfine interactions [6,12,13]. Different models emphasize different aspects of the physical properties of spin ices. We aim to select the simplest model that captures the most relevant aspects of the pressure dependence of the system. In the previous theoretical study on the effects of pressure in the classical spin ice materials, a nearest-neighbor model was used [10]. Due to a self-screening of the long-range part of the dipolar interaction, this relatively simple model gives a surprisingly good description of classical spin ice behavior [12,14]. It can be analyzed analytically using a Husimi tree solution [15], and the low-temperature properties are similar to those of the monopole model [2]. However, to capture the experimental low-temperature behavior of DTO and HTO, dipolar interactions have proven to be important [12], and we therefore consider the dipolar spin ice model.

The Hamiltonian for normalized spins $\mathbf{S}_i$ residing on the sites $\mathbf{r}_i$ of the pyrochlore lattice with nearest-neighbor distance a is given by a nearest-neighbor antiferromagnetic exchange interaction J and a long-range dipolar interaction D,

$$\mathcal{H} = \sum_{\langle i,j\rangle} J(i,j)\,\mathbf{S}_i \cdot \mathbf{S}_j + Da^3 \sum_{i<j} \left(\frac{\mathbf{S}_i \cdot \mathbf{S}_j}{|\mathbf{r}_{ij}|^3} - 3\frac{(\mathbf{S}_i \cdot \mathbf{r}_{ij})(\mathbf{S}_j \cdot \mathbf{r}_{ij})}{|\mathbf{r}_{ij}|^5} \right). \quad (1)$$

Here, the angle brackets denote summation over nearest neighbors, and $\mathbf{r}_{ij} = \mathbf{r}_i - \mathbf{r}_j$. The antiferromagnetic interaction J is caused by oxygen-mediated superexchange between adjacent magnetic ions. Due to the strong crystal field, the spins are oriented along the local [111] axis connecting the center points of adjacent tetrahedra. To capture the detailed behavior of a number of physical properties for DTO, exchange interactions up to third-nearest neighbors have been determined [13]. For simplicity, we do not investigate the effects of pressure on weaker further neighbor interactions and truncate the exchange (but not the dipolar) interaction at the first-nearest neighbor. We therefore use as our starting point the so-called standard dipolar spin-ice model (s-DSM) with $J = 3.72$ K, $D = 1.41$ K [7] for DTO and $J = 1.56$ K, $D = 1.41$ K for HTO [16].

We model compression of the crystal with zero Poisson ratio, as suggested by experiment [8]. When atoms move closer, the wave function overlap and corresponding exchange parameters are expected to change. We make the assumption that $J(i,j) = J_\perp = J_{P=0}$ if the neighbors i and j are in a lattice plane perpendicular to the direction of applied pressure and $J(i,j) = J_{k\|}$ if they are not. $J_{P=0}$ is the ambient pressure value of the s-DSM model. k labels the six different directions of nearest-neighbor bonds, and we make no *a priori* assumptions on the magnitude of $J_{k\|}$. The dipolar interactions become stronger along the direction of compression, growing as $|\mathbf{r}_{ij}|^{-3}$, when distances decrease. Furthermore, we make the assumption that the spins continue to point towards the centers of the tetrahedra as the crystal deforms, altering the local [111] axis. This change in spin directions leads to a change in both exchange and dipolar interactions due to the dot products in Eq. (1).

Motivated by experiments [8], we model pressure applied along the [001], [111], and [110] directions. By symmetry, for the first two directions, it suffices to model the nearest-neighbor interactions with two parameters, $J_\perp$ and $J_\|$. For the [110] direction, however, the lower symmetry of the lattice requires us to use three different exchange parameters, $J_\perp$, $J_{1\|}$, and $J_{2\|}$. We illustrate these different exchange interactions for a single tetrahedron in Fig. 1 for the three respective directions of pressure. ($J_{(k)\|}$ need not be the same for the different directions of pressure.)

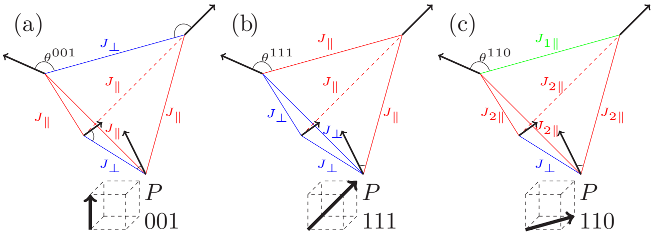

FIG. 1. Model of uniaxial pressure applied in the (a) [001], (b) [111], and (c) [110] directions. $J_\perp$ remains fixed, while $J_{(k)\|}$ vary with pressure. Colors indicate the different exchange interactions. The angle θ between the Ising axis and the side of the tetrahedron is altered to θ^{001}, θ^{111}, and θ^{110} when the crystal lattice is compressed in the respective direction.

Demagnetizing effects in susceptibility measurements can, under ambient pressure, be minimized by using needle-shaped samples. However, such samples are likely to break under pressure, and less elongated samples are used in practice. It is therefore important to consider the demagnetizing transformation

$$B_{\text{ext}} = B_{\text{int}} + NM, \quad (2)$$

which gives the relationship between the internal field B_{int}, the external field B_{ext}, the magnetization M, and the demagnetizing factor of the sample N. Note that N depends on the shape of the sample and therefore changes upon compression. We find that this effect cannot be ignored in an accurate description of the experiments [8]. Hence, the uniaxial pressure directly alters both microscopic properties, such as spin directions and interaction parameters, and macroscopic properties, such as the magnetization and shape of the sample.

In previous magnetization measurements, it was found that the signatures of pressure are largest when pressure is applied along the [001] direction [8]. Earlier theoretical work predicted a low-temperature transition into an ordered phase carrying net magnetization along this axis [10]. This motivates us to make an extended study of the zero-temperature phases for our model in the [001] direction to investigate the system at low temperature.

B. Simulation method and demagnetization corrections

Monte Carlo simulations using single spin flip and loop updates are used to investigate a number of different system sizes with periodic boundary conditions according to the Metropolis-Hastings algorithm. We use the 16-particle standard cubic unit cell [7]. All supercells used are cubic of size L^3, $L \in [1, \ldots, 8]$. Ewald summation is used to effectively account for the long-range conditionally convergent dipolar contributions [17]. The geometrical compression is introduced by an appropriate linear coordinate transformation depending on the direction of applied pressure. In particular, the Ewald summation is done using sheared lattice vectors for the reciprocal space contribution.

In order to account for the macroscopic boundary effects, demagnetization transformations are made by modeling the sample as a prolate ellipsoid. The major axes of the ellipsoid are given by the dimensions of the samples used in the experiment. For the DTO experiment [8], only the shape of the [001] and [110] crystals could be recovered: $1.77 \times 1.80 \times 1.61\ \mathrm{mm}^3$ ([001] pressure along the side of length 1.61 mm) and $1.28 \times 0.96 \times 1.63\ \mathrm{mm}^3$ ([110] pressure along the side of length 1.63 mm) [18]. These dimensions give $N_{001} = 0.319$ and $N_{110} = 0.426$, respectively, in the high-temperature limit [19], and we have not taken the temperature dependence of the demagnetization factor into account [20]. The sample dimensions are deformed in accordance with the microscopic compression of the lattice along the direction of pressure. The dimensions for the sample measured in the [111] direction were unavailable, and we assume the shape to be a perfect sphere with $N_{111} = 1/3$ under ambient pressure.

C. Experimental methods

Magnetic neutron diffraction experiments were performed at the Institut Laue-Langevin using the polarized diffuse scattering instrument, D7 [21,22]. Elastic neutron diffraction profiles with uniaxial polarization analysis (neutron polarization along the vertical axis) were measured for HTO under uniaxial pressure with an incident wavelength $\lambda = 4.86$ Å. Polarization analysis on D7 measures spin-flip and non-spin-flip contributions. In the limit of negligible background and nuclear spin incoherent scattering, the spin-flip scattering will have only the magnetic scattering given by Eq. (4). The data have been corrected for detector and polarization analyzer efficiencies using standard samples of vanadium and amorphous silica, respectively [21].

Uniaxial pressure was applied to HTO crystals using a Cu-Be anvil-type pressure cell optimized for uniaxial pressure (details of the cell will be published elsewhere [23]). Temperature control was achieved using a liquid-helium cryostat. The samples were cylindrical-shaped single crystals, $V = 10\ \mathrm{mm}^3$, cut from the larger image-furnace-grown crystals, with a surface alignment better than 0.1°. The pressure applied was determined via force gauge calibrations considering low-temperature changes to the cell with a maximum pressure of 2.2(0.5) GPa.

The crystals were synthesized using an image furnace located at the University of Lund with ambient oxygen conditions. Structural neutron diffraction measurements on ZEBRA of the Paul Scherrer Institute, Switzerland, showed an absence of structural diffuse scattering, which would have indicated oxygen defect clusters [24].

III. THEORETICAL AND EXPERIMENTAL RESULTS

A. Magnetization

The magnetization of DTO single crystals under applied uniaxial pressure and magnetic field was previously measured at $T = 1.7$ K [8]. The magnetic field ranged up to 3 T and was parallel to the axis of pressure. Measurements were performed with pressure along the [001], [111], and [110] directions with an alignment uncertainty [18] of less than 5°. We adjust the parameters of the proposed model, Eq. (1), to match the experimental data. The best match between experiment and model is shown in Fig. 2, and next, we describe the details of the modeling procedure.

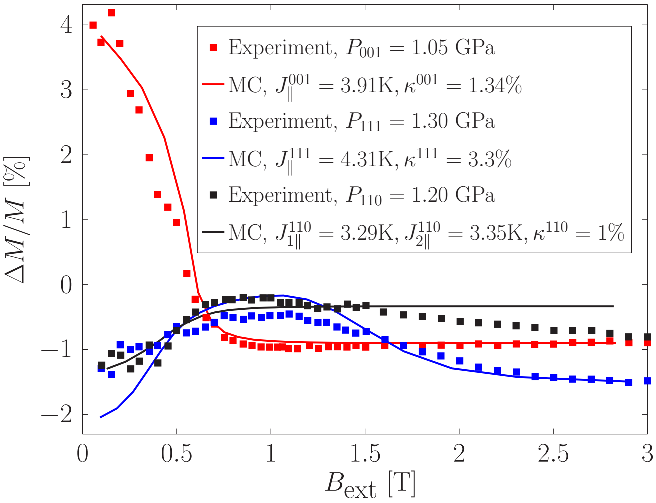

FIG. 2. Relative increase in the sample magnetization $\Delta M/M = (M_{P>0} - M_{P=0})/M_{P=0}$ when field and pressure are both applied in the [001], [111], and [110] directions at 1.7 K. The experimental result [8] (squares) and our fit by MC simulation for a system of 8192 spins (solid lines) are shown.

We assume that the magnetic moments retain their Ising symmetry under pressure and that a sufficiently strong field aligns the moments. For such a field, changes in the demagnetization factor or in the interaction energies will have no effect on the magnetization. The difference in saturation magnetization observed when applying pressure in different directions is purely due to lattice compression, which changes the angle of the local [111] axis. The components of the magnetic moments parallel to the direction of the applied field decrease, which reduces the saturation magnetization along the relevant direction. From the value of the saturation magnetization we can therefore determine the compression κ. We find that the crystals deform by $\kappa^{001} = 1.34\%$, $\kappa^{111} = 3.3\%$, and $\kappa^{110} = 1.0\%$ for the [001], [111], and [110] directions, respectively. This gives the demagnetization factors $N_{001}^{\kappa} = 0.322$, $N_{110}^{\kappa} = 0.433$, and $N_{111}^{\kappa} = 0.341$ under compression for the respective directions.

The data for the [001] direction appear saturated already at about 1 T, while we assume that the data for the [111] direction have saturated at 3 T. For the [110] direction the experimental data have not saturated at high field. We find this result peculiar since the configuration that minimizes the Zeeman energy can be reached without leaving the spin ice manifold for fields along [110] and [001], while that is not so for the [111] direction. We would expect that a stronger field is needed to create the necessary monopole excitations for full [111] saturation, but that is not reflected by the experiment. Due to this anomaly in the high-field behavior we take the value at 1.5 T, which would firmly saturate the crystal in the [001] direction, to be the saturation value for the [110] direction, resulting in a compression of 1%.

The difference in magnetization at low fields arise due to changes in the interactions between the moments. For example, with pressure in the [001] direction, an increased ferromagnetic interaction along the $J_{\parallel}$ bond leads to a lower energy for spin ice configurations with field-aligned spins.

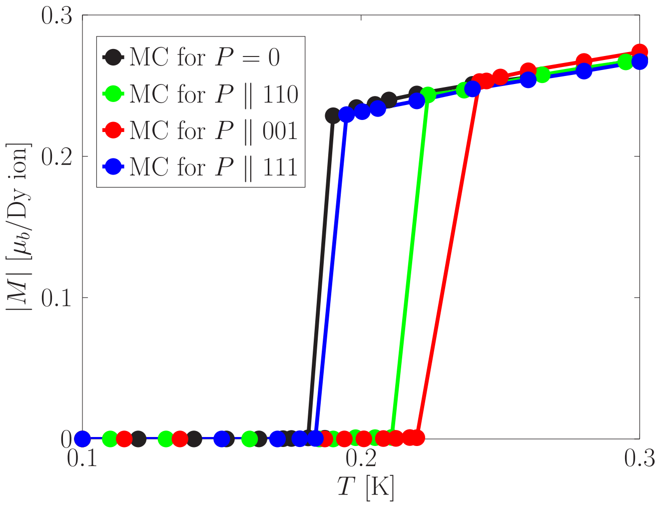

FIG. 3. Simulated values of magnetization plotted against temperature for 1024 spins. Ambient pressure (black) together with uniaxial pressure along [110] (1.20 GPa, green), [001] (1.05 GPa, red) and [111] (1.30 GPa, blue).

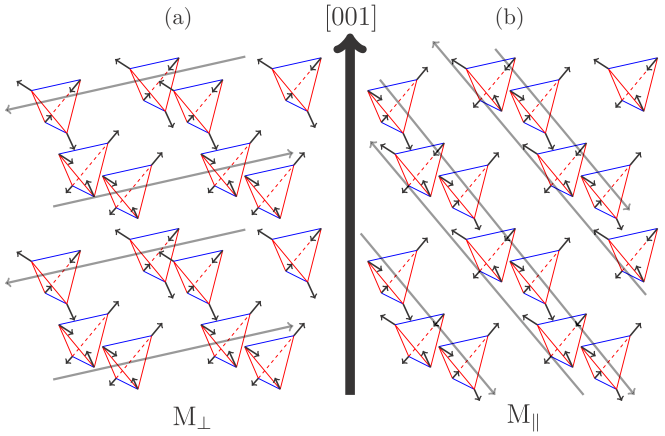

FIG. 4. The degeneracy is lifted under application of pressure. For the [001] direction, two submanifolds of ground states exist: (a) $M_\perp$ and (b) $M_\parallel$. Red and blue bonds correspond to $J_\parallel$ and $J_\perp$, respectively. Only up tetrahedrons are drawn for clarity. Gray lines indicate the directions of the spin chains.

This explains the relative increase in M at zero field. For the other directions, the decreasing magnetization can be explained by similar arguments.

With the compression and demagnetization factor fixed, the $J_\parallel$ exchange parameter is adjusted in order to give the best fit for the measured magnetization as a function of external field; these data are shown as solid lines in Fig. 2. It was found that for both the [001] and [111] directions, the $J_\parallel$ coupling increases from the original value of $J_\parallel = 3.72$ K. Our best estimate gives $J_\parallel^{001} = 3.91$ K and $J_\parallel^{111} = 4.31$ K. For the [110] direction, the parameters decrease, and it is the difference $J_{1\parallel}^{110} - J_{2\parallel}^{110}$ that determines the zero-field limit in magnetization change. Our best fit gives $J_{1\parallel}^{110} = 3.29$ K and $J_{2\parallel}^{110} = 3.35$ K. Assuming that the exchange parameters are independent of temperature we find that, for all directions, the ground state of our model is a dipolar spin chain state with zero net magnetization, which is also the expected ground state of the dipolar spin ice model under ambient pressure [6,7,25–27].

This is illustrated in Fig. 3, which shows how the finite-size absolute magnetization drops to zero in a first-order transition. The transition temperature increases with pressure, especially when pressure is applied in the [001] and [110] directions. The 12-fold degeneracy of the ground state is lifted due to the change in symmetry in the deformed unit cell. With pressure along [001], the ground-state manifold is split into two submanifolds, one with chains perpendicular to the [001] direction, $M_\perp$, and one with chains having a component along [001], $M_\parallel$ (see Fig. 4). Our fit to magnetic susceptibility data for DTO finds that the $M_\parallel$ state has the lowest energy of the two possible states.

B. Ground states for pressure along [001]

In Fig. 5, we illustrate schematically the ground states for our spin ice model, Eq. (1), when varying $J_\parallel$ and lattice compression for pressure applied in the [001] direction. We find that there are four possible ground states: the all-in, all-out state [antiferromagnetic (AFM), Fig. 5(a)], the spin chain states [$M_\perp$, $M_\parallel$, Figs. 5(b) and 5(c)], and the previously proposed ferromagnetic state [FM, Fig. 5(d)]. We introduce the critical values J_{c1}, J_{c2}, J_{c3} and $J_{c1}^\kappa, J_{c2}^\kappa, J_{c3}^\kappa$, denoting the phase boundaries without and with compression, respectively. For DTO without compression, the state boundaries are at $J_{c1} = 9.02$ K, $J_{c2} = 3.72$ K, $J_{c3} = 3.33$ K. For DTO at 1.05 GPa, inducing $\kappa^{001} = 1.34\%$ compression, we have $J_{c1}^\kappa = 9.21$ K, $J_{c2}^\kappa = 4.02$ K, $J_{c3}^\kappa = 3.64$ K.

In previous work [10], spin ice was modeled for pressure in the [001] direction with effective nearest-neighbor interactions, $\mathcal{H} = -\sum_{\langle i,j\rangle} J_{\text{eff}}(i,j)\,\mathbf{S}_i \cdot \mathbf{S}_j$ but without dipolar interactions and no lattice compression in the Hamiltonian. It was found by fitting to the experimental data that $J_{\parallel\text{eff}} > J_{\perp\text{eff}}$ and that this results in a ferromagnetic phase transition at low temperatures.

In this work, we find that with the inclusion of dipolar interactions the picture is more complicated since the $M_\parallel$ state will compete with the FM state. The outcome of this is that a larger difference between $J_{\parallel\text{eff}}$ and $J_{\perp\text{eff}}$ is needed for the ferromagnetic transition to occur. At the nearest-neighbor distance the interaction in the s-DSM model is $J_{\text{eff}} = 5D - J$, and we note that in order for J_{eff} to increase, J must decrease. We find that the ground state of the system is FM only when $J_{\parallel\text{eff}} > 5D - J_{c3} > 5D - J_\perp = J_{\perp\text{eff}}$, instead of immediately when $J_{\parallel\text{eff}} > J_{\perp\text{eff}}$. Furthermore, with the inclusion of lattice compression and the associated change in the local [111] axis, we find, when fitting to the magnetization measurements, that $J_\parallel$ increases as a function of pressure, rather than decreases. This change seemingly moves away from, rather than towards, the FM boundary, as illustrated in the left-hand side of Fig. 5. However, a further complication is that the critical value of the phase boundary J_{c3}^κ also increases with lattice compression (right-hand side of Fig. 5). So it may still be possible for the system to display the ferromagnetic transition, but this would require much higher pressure than what has been applied

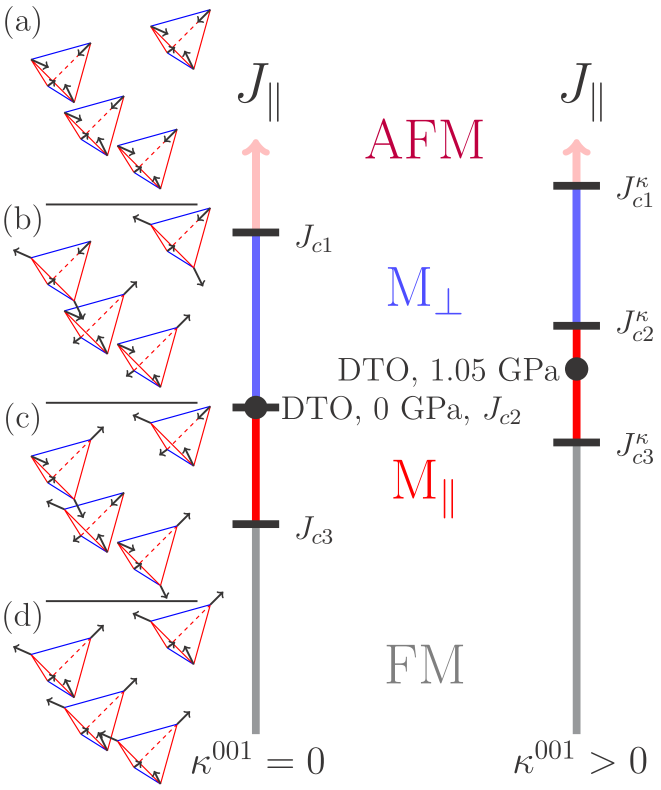

FIG. 5. Ground states of the model schematically plotted with varying $J_\parallel$ in the [001] direction. The values J_{c1}, J_{c2}, J_{c3} and $J^\kappa_{c1}, J^\kappa_{c2}, J^\kappa_{c3}$ denote the phase boundaries without and with compression, respectively. We plot instances of the ground states in the leftmost column for the 16-particle unit cell. Red and blue bonds correspond to $J_\parallel$ and $J_\perp$, respectively. Only up tetrahedrons are drawn for clarity.

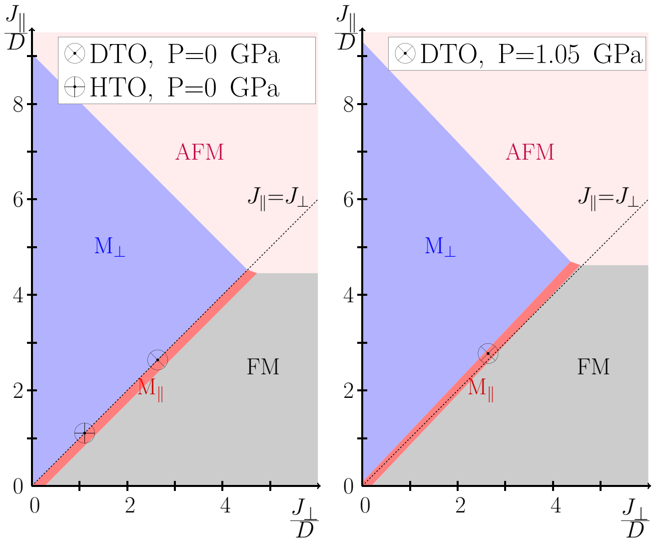

(a) $P \parallel [001]$, $\kappa^{001}=0$ (b) $P \parallel [001]$, $\kappa^{001}=1.34\%$

FIG. 6. Ground-state phase diagram for pressure along [001] in terms of normalized interactions J/D. Results are shown for both zero and 1.34% compression, the value suggested by the DTO magnetization data. Blue, light red, and gray regions represent the $M_\perp$, AFM, and FM states, respectively. The $M_\parallel$ region is very narrow and shown in orange close to the $J_\perp = J_\parallel$ line. The phase boundaries shift with compression, and $J_\parallel$ increases with pressure. We include also the ambient pressure value for HTO.

in the current measurements. By linear extrapolation, $J_\parallel$ for DTO would cross the zone boundary at 3.4GPa, and the FM transition would occur at low temperatures.

In Fig. 6 we show the general ground-state phase diagram as a function of normalized $J_\perp$ and $J_\parallel$ interactions. Figure 6(a) depicts the ground states of the system with no lattice compression. In this case $J_\parallel = J_\perp$ defines the boundary between the $M_\perp$ and $M_\parallel$ phases. When adding compression, the phase boundaries are shifted, which is illustrated as we plot the phase diagram for the experimentally relevant compression in Fig. 6(b). In particular, the $M_\parallel$ region moves, breaking the $M_\perp - M_\parallel$ degeneracy for $J_\parallel = J_\perp$ in favor of the $M_\parallel$ states. The overall behavior is the same, with an AFM ground state for large $J_\parallel$ and a FM ground state for small $J_\parallel$.

C. Prediction of neutron diffraction results for DTO

Neutron scattering is an ideal and unique tool to extract the spin-spin correlations in materials [28]. This enables a close comparison of experimental measurements and theoretically calculated correlations, a combination which often plays a crucial role in the understanding of magnetic materials at a microscopic level.

Using parameter values relevant for DTO, we sample the thermal average of the simulated spin-spin correlations and calculate the magnetic structure factor for neutron diffraction S_{mag} according to

$$S_{\text{mag}}(\mathbf{Q}) = \frac{[f(|\mathbf{Q}|)]^2}{N} \sum_{ij} \langle \mathbf{S}_i^\perp \cdot \mathbf{S}_j^\perp \rangle e^{i\mathbf{Q}\cdot\mathbf{r}_{ij}}, \tag{3}$$

where $\mathbf{Q}$ is the scattering wave vector, N is the number of spins in the simulation cell, $f(|\mathbf{Q}|)$ is the magnetic form factor, and the spin perpendicular component is given by $\mathbf{S}_i^\perp = \mathbf{S}_i - \mathbf{S}_i \cdot \mathbf{Q}/|\mathbf{Q}|$. We calculate also the structure factor for magnetic spin-flip scattering, relevant for experiments with neutron polarization analysis S_{SF} according to

$$S_{\text{SF}}(\mathbf{Q}) = \frac{[f(|\mathbf{Q}|)]^2}{N} \sum_{ij} \langle \mathbf{S}_i^\perp \cdot \mathbf{S}_j^\perp - (\mathbf{S}_i \cdot \mathbf{P})(\mathbf{S}_j \cdot \mathbf{P}) \rangle e^{i\mathbf{Q}\cdot\mathbf{r}_{ij}}, \tag{4}$$

where $\mathbf{P}$ is the normalized polarization direction of the incident neutron beam and $\mathbf{P} \perp \mathbf{Q}$ [29]. In our experiment, the neutron polarization direction is parallel to the direction of applied pressure, and we calculate the neutron scattering profiles for the plane in reciprocal space perpendicular to the direction of the applied pressure.

Based on the model parameters determined from the magnetization measurements in the previous section, our predictions for the relative increases in $S(\mathbf{Q})$, $\Delta S(\mathbf{q})/S(\mathbf{q}) = (S_{P>0}(\mathbf{q}) - S_{P=0}(\mathbf{q}))/S_{P=0}(\mathbf{q})$ at $T = 1.7$ K and pressures $P_{001} = 1.05$ GPa, $P_{110} = 1.20$ GPa, $P_{111} = 1.30$ GPa relevant for DTO are shown in Fig. 7. We find significant variations in the relative scattering intensities for the different scattering

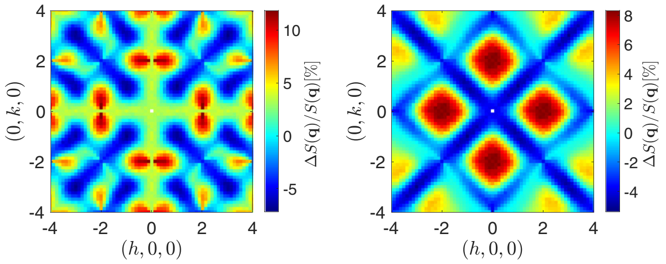

(a) [001] Magnetic. (b) [001] SF.

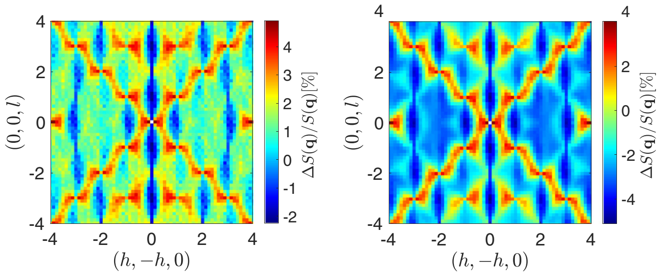

(c) [110] Magnetic. (d) [110] SF.

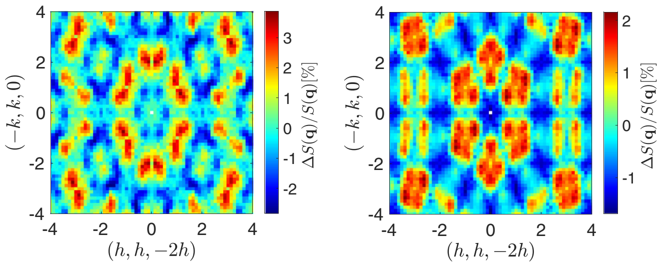

(e) [111] Magnetic. (f) [111] SF.

FIG. 7. Predictions for the relative difference in the total magnetic scattering and the spin-flip scattering by MC simulation on 8192 spins. Exchange parameters and lattice compression are taken from the fit to magnetization measurements on DTO (Fig. 2). In all cases, the reciprocal plane is perpendicular to the direction of pressure, and polarization is parallel to the direction of pressure. (a) and (b) pressure along [001] (1.05 GPa), (c) and (d) pressure along [110] (1.20 GPa), and (e) and (f) pressure along [111] (1.30 GPa), all at zero field and $T = 1.7$ K.

planes for both the magnetic and polarized spin-flip cross sections. The largest variation can be seen for pressure along the [001] direction with a relative increase of about 8% in the [001] spin-flip channel of the $(h, k, 0)$ plane, found for scattering vectors close to (2,0,0) and symmetry-related points in reciprocal space.

D. Neutron diffraction experiment on HTO

In order to make a close comparison with the theoretical predictions of Fig. 7 we would ideally like to perform neutron scattering measurements on DTO crystals. However, the high neutron absorption cross section of natural dysprosium, the cost of isotopically enriched samples, and the concurrent high probability of crystals cracking during the application of uniaxial pressure make these experiments inordinately expensive and challenging. Instead, we have chosen to perform neutron scattering measurements on crystals of HTO, which share many low-temperature properties with DTO [1].

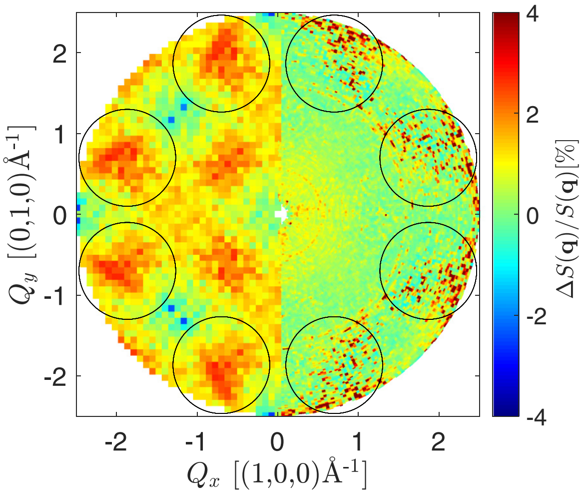

FIG. 8. Relative increases in the [001] spin-flip channel when pressure is applied along the [001] direction. Left: Estimate based on MC simulations of the model for 8192 spins ($J_\perp = 1.56$ K, $J_\parallel = 1.975$ K, $\kappa = 2.8\%$). Right: Experimental neutron scattering data after cell correction. Data are taken at 1.5 K and 2.2 GPa. The circles mark regions of increased intensity for high Q in the experimental data and are plotted in symmetry-equivalent places for the theoretical estimate.

Motivated by the theoretical results, uniaxial pressure was applied along the [001] crystalline axis with [001]-polarized neutrons used to probe the $(h, k, 0)$ plane. The axis perpendicular to the applied pressure is left unconstrained and therefore can give rise to the Poisson effect, in contrast to the previous magnetization measurements [8]. However, within the Q resolution of the instrument [30], no indicative change in the lattice parameters perpendicular to the pressure could be observed.

We construct a theoretical estimate of the change in scattering intensity. Since we do not know the pressure-dependent susceptibility or magnetization data for HTO, we are not able to make a detailed determination of the evolution of $J_\parallel$ and κ with pressure in HTO (in contrast to DTO). However, since the two materials are chemically similar, in order to make a rough estimate, we assume that the compression is linear in the applied pressure and that their compressibilities are identical. Using the fitted value for DTO ($\kappa = 1.34\%$ at 1.05 GPa) then gives a compression of $\kappa = 2.8\%$ for HTO at 2.2 GPa. The magnetic ions in HTO and DTO are significantly different, and it would be unreasonable to use the similarity argument also for the exchange interaction. Instead, we adjust the single parameter $J_\parallel$ for HTO to give the best possible match with experiment.

A comparison between the theoretical prediction and the experimental results for the relative increase in the magnetic structure factor under 2.2 GPa pressure is shown in Fig. 8. A fourfold rotational averaging, consistent with the crystalline symmetry, has been performed on the experimental data. The experimental data have been corrected for a strong background contribution from the pressure cell [23]. This background dominates the low angular region of reciprocal space, leaving this region rather poorly sampled.

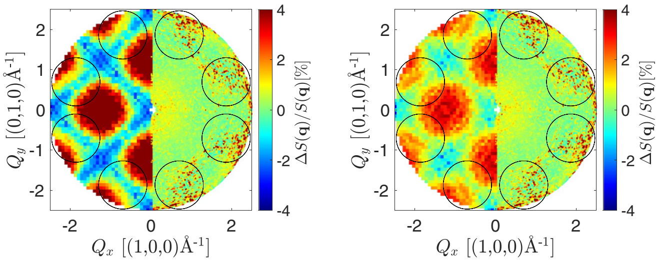

(a) $J_{\parallel} = 1.94$ K, $\kappa = 2.8\%$. (b) $J_{\parallel} = 1.96$ K, $\kappa = 2.8\%$.

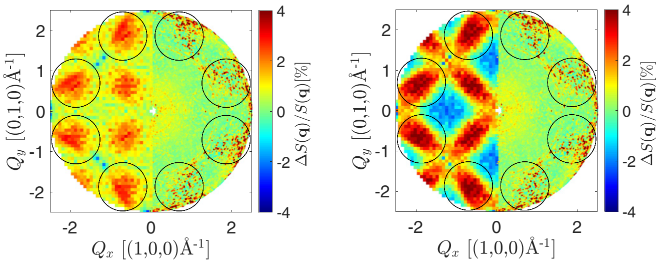

(c) $J_{\parallel} = 1.98$ K, $\kappa = 2.8\%$. (d) $J_{\parallel} = 2.00$ K, $\kappa = 2.8\%$.

FIG. 9. Evolution of theoretical predictions for the relative increases in the [001] spin-flip channel when pressure is applied along the [001] direction. Left: MC simulation of the model for 8192 spins with varying $J_{\parallel}$ and κ fixed. Right: Experimental data (constant) at $T = 1.5$ K, $P = 2.2$ GPa. We see that the cross/square pattern is inverted when we increase $J_{\parallel}$ from 1.94 to 2.00 K. The circles mark regions of increased intensity for high Q in the experimental data and are plotted in symmetry-equivalent places for the theoretical estimate.

There is a reasonable correspondence between the measurement and the theoretical prediction in the region corresponding to wave-vector transfers $Q > 1.5$ Å^{-1}, where the high-intensity regions are marked by circles. Further experimental activity will be required to improve the background from the pressure cell and reliably access the $Q < 1.5$ Å^{-1} region. In particular it is of interest to gather more statistics and to improve the construction and geometry of the cell to get a cleaner signal and better control of the pressure. The measurement of further crystallographic directions would also be of great value.

We note that the data from HTO have weaker features than those predicted for DTO [Fig. 7(b)]. This can be accounted for by the tuning of the $J_{\parallel}$ parameter. Both changes in κ and changes in $J_{\parallel}$ give rise to a cross/square pattern in the relative increases in the scattering, which are not prominent in the experimental data. The $J_{\parallel}$ parameter can be tuned such that these features are canceled to a large degree. We choose it to get a profile as similar to the experiment as possible. Figure 9 shows the evolution of the relative increases in the scattering (left panels) when varying $J_{\parallel}$, together with the experimental data (right panels). Note that the intensity in the cross/square pattern inverts as we increase $J_{\parallel}$ by only 2%, from 1.96 to 2.00 K.

We determine that the closest fit has $J_{\parallel} = 1.975$–1.98 K, about 27% larger than $J_{\perp}$, in contrast to $J_{\parallel}/J_{\perp} - 1 = 5\%$ seen for DTO. The fact that the experimental profile does not have a strong cross/square pattern implies, within our model, that the ground state of HTO lies close to the border between the $M_{\perp}$ and $M_{\parallel}$ states. This is because the inversion point of the cross/square pattern is at the border between the $M_{\parallel}$ and $M_{\perp}$ phases in the ground-state phase diagram (Fig. 6).

IV. DISCUSSION AND CONCLUSION

Using a dipolar spin ice model, we have accurately modeled the experimental changes in magnetization of DTO under the application of pressure in multiple crystalline directions. Using the model parameters derived from the magnetization measurements, we have calculated the correspondingly expected changes in neutron scattering cross section for DTO. Neutron scattering experiments were performed on HTO under applied pressure, and we found the response to be weaker than what we predicted for DTO. One possible reason for the difference is that HTO may be located at the boundary between two different chain states, as discussed in the previous section. Another is that the compressibility of HTO may be smaller than that of DTO and that the associated pressure-induced changes in the exchange parameters are also smaller. Furthermore, we have not considered changes to exchange parameters past the nearest neighbors, which certainly could influence the results [6,13]. In conclusion, we note that in order to determine which of these scenarios are relevant for HTO, more experiments are necessary. In particular magnetization measurements of HTO under pressure similar to those previously performed on DTO would be highly useful.

ACKNOWLEDGMENTS

We thank M. Mito and K. Matsuhira for useful discussions and sharing their data. The neutron scattering experiments were performed at the Paul Scherrer Institute and the Institute Laue-Langevin. The project was supported by Nordforsk through the program NNSP (Project No. 82248) and by the Danish Ministry for Science and Higher Education through the program DANSCATT.

---

[1] *Highly Frustrated Magnetism*, edited by C. Lacroix, P. Mendels, and F. Mila, Springer Series in Solid-State Sciences Vol. 164 (Springer, Heidelberg, New York, 2011).

[2] C. Castelnovo, R. Moessner, and S. L. Sondhi, Nature (London) **451**, 42 (2008).

[3] M. E. Brooks-Bartlett, S. T. Banks, L. D. C. Jaubert, A. Harman-Clarke, and P. C. W. Holdsworth, Phys. Rev. X **4**, 011007 (2014).

[4] C. L. Henley, Phys. Rev. B **71**, 014424 (2005).

[5] D. Pomaranski, L. R. Yaraskavitch, S. Meng, K. A. Ross, H. M. L. Noad, H. A. Dabkowska, B. D. Gaulin, and J. B. Kycia, Nat. Phys. **9**, 353 (2013).

[6] P. Henelius, T. Lin, M. Enjalran, Z. Hao, J. G. Rau, J. Altosaar, F. Flicker, T. Yavors'kii, and M. J. P. Gingras, Phys. Rev. B **93**, 024402 (2016).

[7] R. G. Melko and M. J. P. Gingras, J. Phys.: Condens. Matter **16**, R1277 (2004).
[8] M. Mito, S. Kuwabara, K. Matsuhira, H. Deguchi, S. Takagi, and Z. Hiroi, in *Proceedings of the 17th International Conference on Magnetism*, special issue of J. Magn. Magn. Mater. **310**, e432 (2007).
[9] I. Mirebeau and I. Goncharenko, J. Phys.: Condens. Matter **16**, S653 (2004).
[10] L. D. C. Jaubert, J. T. Chalker, P. C. W. Holdsworth, and R. Moessner, Phys. Rev. Lett. **105**, 087201 (2010).
[11] S. T. Bramwell, S. R. Giblin, S. Calder, R. Aldus, D. Prabhakaran, and T. Fennell, Nature (London) **461**, 956 (2009).
[12] B. C. den Hertog and M. J. P. Gingras, Phys. Rev. Lett. **84**, 3430 (2000).
[13] T. Yavors'kii, T. Fennell, M. J. P. Gingras, and S. T. Bramwell, Phys. Rev. Lett. **101**, 037204 (2008).
[14] S. V. Isakov, R. Moessner, and S. L. Sondhi, Phys. Rev. Lett. **95**, 217201 (2005).
[15] L. D. C. Jaubert, M. J. Harris, T. Fennell, R. G. Melko, S. T. Bramwell, and P. C. W. Holdsworth, Phys. Rev. X **3**, 011014 (2013).
[16] L. D. C. Jaubert and P. C. W. Holdsworth, J. Phys.: Condens. Matter **23**, 164222 (2011).
[17] D. Frenkel and B. Smit, *Understanding Molecular Simulation: From Algorithms to Applications*, 2nd edition, Computational Science Series (Academic Press, 2001), Vol. 1.
[18] M. Mito (private communication).
[19] J. A Osborn, Phys. Rev. **67**, 351 (1945).
[20] M. Twengström, L. Bovo, M. J. P. Gingras, S. T. Bramwell, and P. Henelius, Phys. Rev. Mater. **1**, 044406 (2017).
[21] J. R. Stewart, P. P. Deen, K. H. Andersen, H. Schober, J.-F. Barthélémy, J. M. Hillier, A. P. Murani, T. Hayes, and B. Lindenau, J. Appl. Crystallogr. **42**, 69 (2008).
[22] P. Deen, I. M. Bakke, R. Edberg, H. Fjellvåg, K. Leffmann, L. Ø. Sandberg, and A. Wildes, Institut Laue-Langevin, doi:10.5291/ILL-DATA.5-32-856, 2018.
[23] L. Ø. Sandberg, M. L. Haubro, M. A. Olsen, M. Guthrie, K. Lefmann, and P. P. Deen (unpublished).
[24] G. Sala, M. J. Gutmann, D. Prabhakaran, D. Pomaranski, C. Mitchelitis, J. B. Kycia, D. G. Porter, C. Castelnovo, and J. P. Goff, Nat. Mater. **13**, 488 (2014).
[25] R. G. Melko, B. C. den Hertog, and M. J. P. Gingras, Phys. Rev. Lett. **87**, 067203 (2001).
[26] R. A. Borzi, D. Slobinsky, and S. A. Grigera, Phys. Rev. Lett. **111**, 147204 (2013).
[27] P. A. McClarty, O. Sikora, R. Moessner, K. Penc, F. Pollmann, and N. Shannon, Phys. Rev. B **92**, 094418 (2015).
[28] W. Marshall and S. W. Lovesey, *Theory of Thermal Neutron Scattering: The Use of Neutrons for the Investigation of Condensed Matter* (Clarendon, Oxford, 1971).
[29] M. Blume, Phys. Rev. **130**, 1670 (1963).
[30] T. Fennell, L. Mangin-Thro, H. Mutka, G. Nilsen, and A. Wildes, Nucl. Instrum. Methods Phys. Res., Sect. A **857**, 24 (2017).

A.2 Publication 2: Effects of uniaxial pressure on the spin ice Ho2Ti2O7

My contribution to the publication involves primarily the neutron scattering measurements with the pressure cell C. I participated in the growth of the HTO single crystals which were grown in the mirror furnace at the University of Lund in collaboration with Ingrid Marie Bakke Fjällvåg. These crystals were used for both the neutron scattering measurements and the magnetization measurements. I was responsible for the design, testing and calibration of pressure cell C, including the load gauge, and I performed the test and analyses in collaboration with Morten Haubro who did his master's thesis in the project. I also did the analysis of the neutron scattering data in collaboration with Morten Haubro.

Effects of uniaxial pressure on the spin ice Ho2Ti2O7

Edberg, R.; Bakke, I. M. B.; Kondo, H.; Sandberg, L. Orduk; Haubro, M. L.; Guthrie, M.; Holmes, A. T.; Engqvist, J.; Wildes, A.; Matsuhira, K.; Lefmann, K.; Deen, P. P.; Mito, M.; Henelius, P.

Published in:
Physical Review B

DOI:
10.1103/PhysRevB.102.184408

Publication date:
2020

Document version
Publisher's PDF, also known as Version of record

Citation for published version (APA):
Edberg, R., Bakke, I. M. B., Kondo, H., Sandberg, L. O., Haubro, M. L., Guthrie, M., Holmes, A. T., Engqvist, J., Wildes, A., Matsuhira, K., Lefmann, K., Deen, P. P., Mito, M., & Henelius, P. (2020). Effects of uniaxial pressure on the spin ice $Ho_2Ti_2O_7$. *Physical Review B*, *102*(18), [184408]. https://doi.org/10.1103/PhysRevB.102.184408

PHYSICAL REVIEW B **102**, 184408 (2020)

Effects of uniaxial pressure on the spin ice $Ho_2Ti_2O_7$

R. Edberg,[1] I. M. B. Bakke,[2] H. Kondo,[3] L. Ørduk Sandberg,[4] M. L. Haubro,[4] M. Guthrie,[5,6] A. T. Holmes,[5]
J. Engqvist,[7] A. Wildes,[8] K. Matsuhira,[3] K. Lefmann,[4] P. P. Deen,[4,5] M. Mito,[3] and P. Henelius[1,9]
[1]*Department of Physics, KTH Royal Institute of Technology, SE-106 91 Stockholm, Sweden*
[2]*Centre for Materials Science and Nanotechnology, Department of Chemistry, University of Oslo, 0315 Oslo, Norway*
[3]*Faculty of Engineering, Kyushu Institute of Technology, Kitakyushu, Fukuoka 804-8550, Japan*
[4]*Niels Bohr Institute, University of Copenhagen, 2100 Copenhagen, Denmark*
[5]*European Spallation Source ERIC, 22363 Lund, Sweden*
[6]*School of Physics and Astronomy and Centre for Science at Extreme Conditions, University of Edinburgh,*
Edinburgh EH9 3FD, United Kingdom
[7]*Division of Solid Mechanics, Lund University, P.O. Box 118, SE-221 00 Lund, Sweden*
[8]*Institut Laue-Langevin, 38042 Grenoble, France*
[9]*Faculty of Science and Engineering, Åbo Akademi University, 20500 Åbo, Finland*

(Received 4 June 2020; revised 9 September 2020; accepted 21 October 2020; published 9 November 2020)

The spin ice materials $Ho_2Ti_2O_7$ and $Dy_2Ti_2O_7$ are experimental and theoretical exemplars of highly frustrated magnetic materials. However, the effects of applied uniaxial pressure are not well studied, and here we report magnetization measurements of $Ho_2Ti_2O_7$ under uniaxial pressure applied in the [001], [111], and [110] crystalline directions. The basic features are captured by an extension of the dipolar spin ice model. We find a good match between our model and measurements with pressures applied along two of the three directions, and we extend the framework to discuss the influence of crystal misalignment for the third direction. The parameters determined from the magnetization measurements reproduce neutron scattering measurements that we perform under uniaxial pressure applied along the [110] crystalline direction. In the detailed analysis, we include the recently verified susceptibility dependence of the demagnetizing factor. Our work demonstrates the application of a moderate applied pressure to modify the magnetic interaction parameters. The knowledge can be used to predict critical pressures needed to induce new phases and transitions in frustrated materials, and in the case of $Ho_2Ti_2O_7$ we expect a transition to a ferromagnetic ground state for uniaxial pressures above 3.3 GPa.

DOI: 10.1103/PhysRevB.102.184408

I. INTRODUCTION

Highly frustrated magnets display a rich variety of exotic ground states and excitations [1–4]. A primary reason for this diversity is that the physical properties of the system are frequently determined by a delicate balance of weaker interactions of similar strength. Following Anderson's original classification [5], there are two major classes of frustrated systems: one in which the lattice plays a dominant role in frustrating the system, and another where frustration arises due to competing interactions. Recently, it was realized that even in the first case, competing interactions may unexpectedly refrustrate the system, as was found for the spin ice materials $Ho_2Ti_2O_7$ (HTO) and $Dy_2Ti_2O_7$ (DTO) [6]. Therefore, it is of interest to find physical realizations of a wide variety of Hamiltonians, since even small alterations of the interactions may yield novel physical properties and phases.

To explore the vast parameter space of frustration, there is a constant drive to synthesize new and promising frustrated materials [1,7,8], each representing a unique set of interaction coefficients determined by, for example, crystal fields, ionic magnetic moments, interion distances, and atomic overlaps. A different approach to probing frustration is to alter the interactions of a given material. One way to do so is the application of external pressure, which alters the position and thereby also the dipolar interactions and atomic overlaps of the ions of the material. While there are many observations of novel states and phenomena induced by pressure [9–11], progress is hampered by a number of experimental challenges that are exacerbated when studying phenomena at cryogenic temperatures. On the theoretical side there are open questions, since it is not easy to predict the effects of external pressure on, for example, exchange interaction parameters.

In the present study, we apply uniaxial external pressure to increase the parameter space that we can explore using the parent material HTO. The physical properties of the multiaxial Ising materials HTO and DTO show a strong directional dependence on, for example, an applied magnetic field [12,13]. Therefore, we choose to use uniaxial pressure rather than

---

isotropic hydrostatic pressure in this study. Our starting point is relatively straightforward magnetization measurements to determine the evolution of the exchange parameters under pressure, and then we validate our results by comparing the derived model to neutron scattering experiments. In this study, we demonstrate the feasibility and limitations of describing the measurements of HTO under pressure using an effective model with a single pressure-dependent parameter. While our application of relatively low pressure did not induce any changes in the order of the material, it shows the feasibility of exploratory experimental studies using magnetization measurements. Such measurements can be used to determine the evolution of the model parameters and enable theoretical predictions of pressures necessary to alter the delicate balance of interactions in frustrated materials enough to cross phase boundaries and induce new phases.

Over the past 15 years, HTO and DTO have become model compounds for studying classically frustrated systems featuring residual ground-state entropy [14], topological magnetic monopole excitations [2], and slow low-temperature dynamics [15,16]. The theoretical description in terms of the dipolar spin ice model (DSM) [17–19] captures the experimental features at a quantitative level, and DTO and HTO are now some of the best characterized frustrated materials. This makes them an ideal starting point for a systematic exploration of the evolution of frustrated systems under pressure. In an earlier study, measurements of the pressure-induced changes in the magnetization of DTO were reported [20]. These results were first modeled theoretically using a nearest-neighbor exchange interaction model [21]. Recently, the effects of the dipolar interactions were included in the theory, and the measurements were modeled using a single parameter in the DSM [22]. Since DTO has a large neutron absorption cross section, neutron scattering measurements were performed on HTO, rather than DTO, but the observed changes in scattering intensity were modeled within the same framework.

One shortcoming of the previous study [22] was that magnetization measurements of HTO under pressure were missing, and it was not possible to connect the parameters determined from the evolution of the magnetization, measured for DTO, with the changes in the scattering intensity, determined for HTO [22]. In this study, we remedy the situation and report magnetization measurements on HTO, which we can use to independently determine the pressure-dependent parameter in the theory for HTO. Our main result is that the independent analysis of both the magnetization and the neutron scattering measurements lead to very similar values for the pressure-dependent parameter. We therefore verify the feasibility of our approach to use more straightforward magnetization measurements to determine the explicit evolution of model parameters to predict possible phase transitions before performing the more demanding neutron scattering experiments under pressure.

II. EXPERIMENTAL METHOD AND RESULTS

A. Magnetization measurements

High-quality samples are essential in high-pressure studies, and we synthesized HTO single crystals using the floating zone technique at the image furnace at Lund University. The crystals were grown from the bottom up with a growth rate of 3 mm/h. Visual inspection of the as-grown crystals revealed no color change along the growth direction as seen by others [23].

We ascertained the high quality of the single crystals using x-ray and neutron diffraction [24], and we will publish the details of the growth and resultant crystalline state elsewhere. To ensure an optimum shape for the application of uniaxial pressure, the single crystals were cut into cylinders of diameter 2.0 ± 0.05 mm and height 3.0 ± 0.05 mm. The crystals were cut with the major axis of the cylinders along the crystalline [001], [110], and [111] directions. The quality after cutting was asserted using x-ray diffraction. The crystalline direction of the major axis was ascertained after cutting the crystals. For each crystal, we applied uniaxial pressure and magnetic field along the cylinder major axis. We measured the magnetic moment at $p_{001} = p_{111} = 0,\ 1.0 \pm 0.2$, and 1.5 ± 0.3 GPa for the [001] and [111] crystalline direction, and at $p_{110} = 0,\ 0.5 \pm 0.1,\ 1.0 \pm 0.2$, and 1.5 ± 0.3 GPa for the [110] crystalline direction. We also measured the dc susceptibility at pressures $p_{001} = p_{111} = 0,\ 0.5 \pm 0.1,\ 1.0 \pm 0.2$, and 1.3 ± 0.2 GPa using a probing field of 0.01 T along the cylinder major axis.

Using an epoxy resin (Stycast 1266, Ablestick Japan Co., Ltd.), we placed the crystals into a piston- cylinder type of pressure cell (CR-PSC-KY05-1, Kyowa- Seisakusho Co., Ltd.), which can be inserted into a superconducting quantum interference device (SQUID) magnetometer (Quantum Design MPMS-XL). The combination of stycast and the above uniaxial pressure enables the Poisson effect to be excluded, and thus the shrinkage ratio in the direction perpendicular to the load can be ignored [25]. The quoted value of the pressure is at liquid helium temperature, after considering the thermal shrinkage. The pressure value at liquid helium temperature was estimated from the shift of the superconducting transition temperature of lead under applied pressure [26]. Due to the symmetric design of the upper and lower parts of the sample chamber, the magnetic background was negligible for the large magnetic signal of HTO. The measurements at different pressure were performed on the same respective crystal for each direction, and a maximum field of $H_{\text{ext}} = 7$ T was used.

B. Neutron scattering

Magnetic neutron diffraction experiments were performed at the Institut Laue-Langevin (ILL) using the polarized diffuse scattering instrument, D7 [27], with nominal incident wavelength $\lambda = 4.86 \pm 0.1$ Å. We recorded neutron diffraction profiles for HTO in the $(h, -h, l)$ scattering plane under uniaxial pressure along the [110] crystalline direction and with incident neutron polarization along the [110] crystalline direction. For this experimental study, we cut our synthesized HTO crystals into cylinders of diameter 3.0 ± 0.05 mm and height 2.0 ± 0.05 mm, still with the major axis along [110] but with a larger diameter and smaller height than the crystals used in the magnetization measurement. Pressure was applied using a CuBe anvil-type pressure cell with a CuBe window of minimal thickness of 2.5 mm for the entire scattering plane. Further details of the pressure cell are provided in

Appendix C, and a detailed overview of the pressure cell will be published elsewhere. The force was calibrated prior to the experiment using an *in situ* transducer for deviations experienced at cryogenic temperatures. The pressure was deduced from the force, allowing for some uncertainty via friction of the piston. We measured both the neutron spin-flip and non-spin-flip scattering as a function of the sample rotation about the major axis of the cylinder ([110] crystalline direction). The data were corrected for detector and polarization analyzer efficiencies using standard samples of vanadium and amorphous silica, respectively [27]. Background measurements were performed at 300 K with an Al sample, closely matched in dimensions to the HTO sample, to determine scattering from the pressure cell. The background was entirely symmetric in the sample holder rotation angle, and the rotation-averaged background at ambient pressure was subtracted from the measured signal.

C. Experimental results

Figures 1 and 2 show the measured magnetic moment and susceptibility at different pressures for the indicated directions. While the physics of spin ice in an applied field is a fascinating topic, with features such as chain ordered states [13], kagome ice [28], and Kasteleyn transitions [29], our aim is to focus on the effects of pressure. We see a change in the magnetic moment on the order of a few percent under the application of pressure. For the [001] measurement, Fig. 1(a), the magnetic moment is monotonically reduced for all fields when pressure is applied. For the [111] measurement, Fig. 1(b), the magnetic moment is reduced both in the high and the low field limits, but for an intermediate field around 1–2 T the magnetic moment increases as pressure is applied. For the [110] measurement, shown in Fig. 1(c), there is an overall decrease when pressure is applied, but the decrease is not monotonic at high fields, as it is for the other directions. There is also a large jump between the $p_{110} = 0$ measurement and the $p_{110} > 0$ measurements in the high- and low-field regions. We will discuss the implications of these features further in Sec. IV A.

Figure 2 shows the susceptibility, χ_{ext}, measured with field and pressure in the [001] and [111] crystalline directions. There is a noticeable change in the susceptibility when pressure is applied to the sample, but compared to the magnetic moments in Fig. 1, the effects are much less clear. For example, in our measurements using a small applied field of 0.01 T, the recorded change in the susceptibility is not generally monotonic with respect to the applied pressure.

Figure 3 shows the spin-flip neutron scattering structure factor, $S(\mathbf{Q})$, at ambient and at an applied pressure of 0.35 GPa at $T = 1.5$ K [30]. The well-established diffuse scattering map [31] shows some of the defining features of the spin ice phenomenology including regions of intensity at (0,0,3),(3/2,3/2,3/2), and equivalent wave vectors, separated by pinch points at, for example, (0,0,2) [32,33]. In this study, we focus on the effects of pressure on this scattering pattern. The noted pressure was applied at 300 K, and the subsequent pressure change as a result of thermal contraction could not be determined *in situ*. However, prior temperature-dependent calibration measurements of the pressure cell provide an indication that the noted pressure is approximately correct. A uniaxial pressure cell with *in situ* pressure determination for diffuse neutron scattering and polarization analysis is under development. In Figs. 3(a) and 3(b), the measurements are taken with two different samples, with equivalent sample

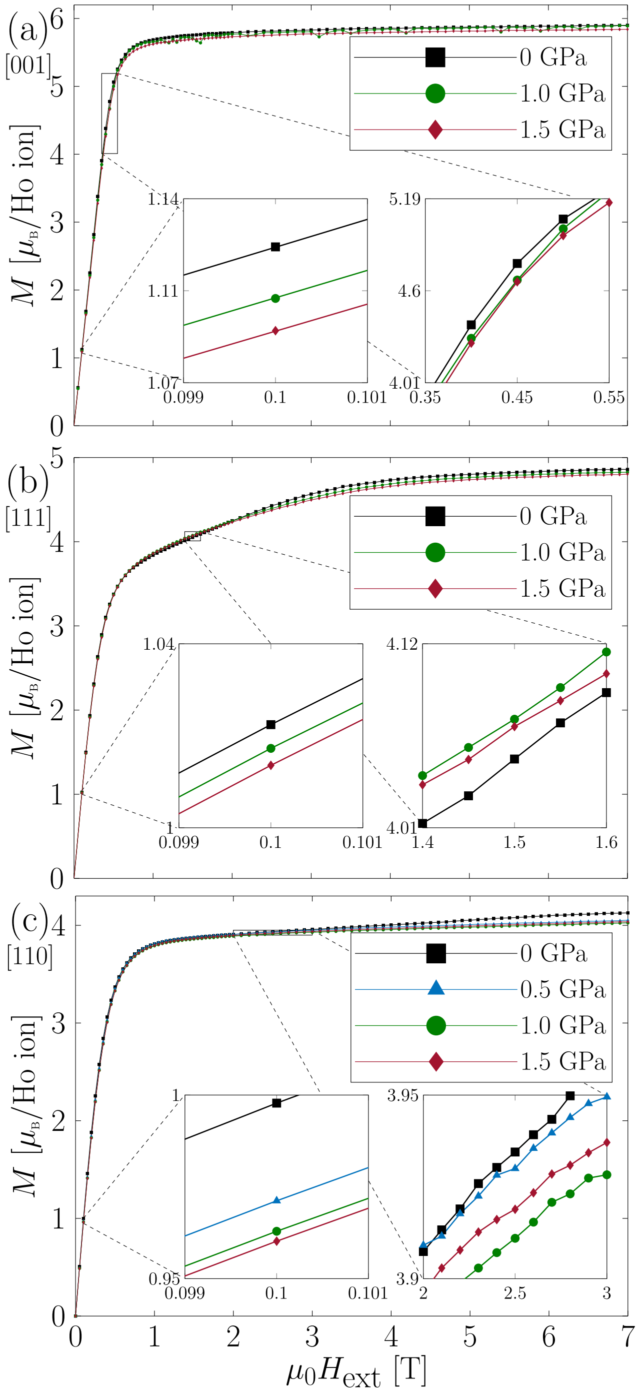

FIG. 1. Sample magnetic moment per holmium ion as a function of external magnetic field H_{ext}, without demagnetization corrections. Pressure and magnetic field along the (a) [001], (b) [111], and (c) [110] crystalline direction. The different curves indicate different pressure applied to the sample, all at sample temperature 1.83 K. The insets show the changes in magnetic moment at small and moderate field.

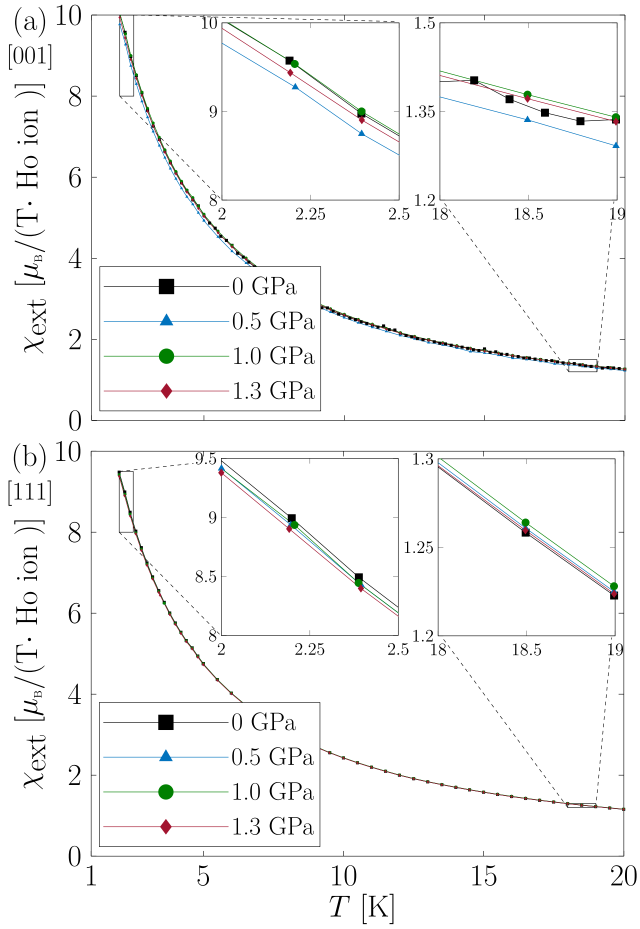

FIG. 2. Susceptibility per holmium ion as a function of temperature for field and pressure along the (a) [001] and (b) [111] crystalline directions. The field strength used to probe the susceptibility was 0.01 T. The insets show the change in susceptibility in the high- and low-temperature limit.

dimensions, as the first sample broke when pressure was applied. The samples were cut from the same single crystal. We note a change in the intensity of the diagonal satellite peaks ($h \approx \pm1.5, l \approx \pm1.5$) when pressure is applied. To better demonstrate these subtle changes, we have integrated the shaded regions over Q, see Fig. 3, and fitted a Gaussian curve to the integrated data. We find that the intensity of the diagonal satellite peaks increases by about 4% when pressure is applied, and we discuss this further in Sec. IV B.

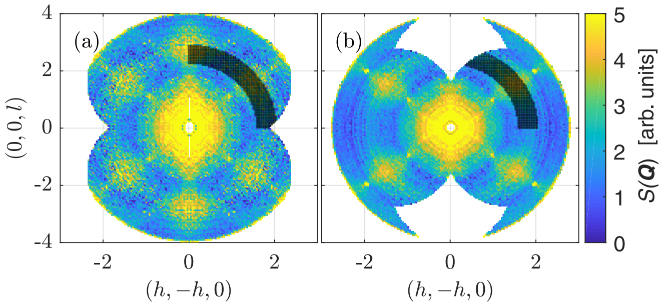

FIG. 3. [110] Spin-flip neutron scattering profile in the $(h, -h, l)$ plane at (a) 0 GPa and (b) 0.35 GPa [30]. The pressure is applied along the [110] crystalline direction, perpendicular to the scattering plane. The data displayed have been symmetrized according to the crystal symmetry. Both measurements were conducted at 1.5 K. The shaded area marks the region that we integrate and analyze further in Sec. IV B.

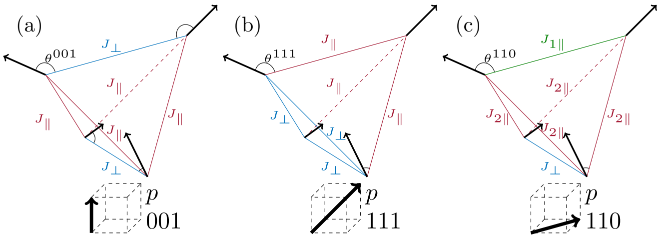

FIG. 4. Illustrations of the DSPM [22]. Pressure is applied along the (a) [001], (b) [111], and (c) [110] direction, and the colors indicate the different exchange interactions $J_\parallel$ (red), $J_{1\parallel}$ (green), $J_{2\parallel}$ (red), $J_\perp$ (blue). The angles of the Ising moments $\theta^{001}, \theta^{111}, \theta^{110}$ are assumed to change under application of pressure so that spins keep pointing toward the center of the compressed tetrahedron.

III. THEORETICAL MODELING

A. Model and simulation method

A theoretical model for the evolution of the interactions in classical spin ice under uniaxial pressure was proposed in an earlier investigation [22]. We adapt this model to the current measurements of HTO, and we refer to it as the dipolar spin ice pressure model (DSPM). The DSPM is an extension of the standard dipolar spin ice model (s-DSM) [34]. The Hamiltonian for the DSPM for classical unit Ising spins $\mathbf{S}_i$ on the pyrochlore lattice is defined as

$$\mathcal{H} = \sum_{\langle i,j\rangle} J(i,j)\,\mathbf{S}_i\cdot\mathbf{S}_j + Da^3\sum_{i<j}\left(\frac{\mathbf{S}_i\cdot\mathbf{S}_j}{|\mathbf{r}_{ij}|^3} - 3\frac{(\mathbf{S}_i\cdot\mathbf{r}_{ij})(\mathbf{S}_j\cdot\mathbf{r}_{ij})}{|\mathbf{r}_{ij}|^5}\right). \quad (1)$$

The strength of the dipolar interactions is taken to be $D = 1.41$ K [17]; a is the nearest-neighbor distance, $\mathbf{r}_i$ is the position of spin $\mathbf{S}_i$, and $\mathbf{r}_{ij} = \mathbf{r}_i - \mathbf{r}_j$. The angled brackets in the first sum denote summation over nearest neighbors. The antiferromagnetic nearest-neighbor interaction $J(i, j)$ is caused by oxygen-mediated superexchange. The value of J at ambient pressure is set to $J_{p=0} = 1.56$ K [31]. In the DSPM it is assumed that $J_\perp = J_{p=0} = 1.56$ K if the neighbors i and j are in a lattice plane perpendicular to the direction of applied pressure and $J(i, j) = J_\parallel$ if they are not ($J_{1\parallel}, J_{2\parallel}$ for pressure in the [110] direction, as there is less symmetry); see Fig. 4. The motivation for this assumption is that the distance between neighboring ions, and hence the exchange integral, will change when pressure is applied. Compression of the crystal is modeled with zero Poisson ratio, which is also the case in the current experimental setup for the measurements of the magnetic moment [25]. As the lattice is compressed, the local Ising axis of the spins is modeled to keep pointing toward the centers of the compressed tetrahedra. The dipolar interaction becomes stronger along the direction of compression, growing as $|\mathbf{r}_{ij}|^{-3}$ with decreasing distance. We define the lattice compression κ as the relative length contraction along the direction of pressure. At high fields, the saturated magnetic moment is dependent only on κ, due to the change in angles of the Ising moments. The high field saturated value of the magnetic moment therefore sets the lattice compression, and we use the low field data to determine exchange interactions.

At this point, a discussion of the crystal-field effects in HTO is necessary. The ionic state of the Ho^{3+} ion depends on the local electric fields of the surrounding ion. Shifting their position by applying pressure could affect the ionic ground state upon which our present analysis is based. Under ambient pressure, the electronic $^5I_8$ ground state of a single Ho^{3+} is lifted by the trigonal field of the surrounding oxygen atoms. Fitting the crystal field parameters to susceptibility and inelastic neutron measurements yields an almost pure $|J, M_J\rangle = |8, \pm 8\rangle$ non-Kramers ground-state doublet, with an excitation gap of more than 200 K, and an almost full magnetic moment of about $10\mu_B$ [35,36]. These are the two crucial points for our study. Although the ground-state doublet in HTO is not protected by Kramers' theorem, as it is for DTO, it is unlikely that the small shift in the ionic positions, which we induce by applying pressure, would significantly affect the nature of the ground-state doublet leading to our current Ising description. Considering a perturbation theory approach, it is not unlikely that the magnetic moment of the holmium ion could shift slightly due to crystal-field effects, since this is a first-order effect. However, the changes in the ground state itself are expected to be very small, since this second-order effect is suppressed by the very significant energy gap, and by the fact that the ground state has a very small overlap with states other than $|J, M_J\rangle = |8, \pm 8\rangle$. To completely rule out crystal-field effects would require a significant experimental and theoretical undertaking, but we believe the above perturbative argument to be strong enough to proceed with our analysis for HTO. We also note that pressure-induced changes in the crystal-field parameters in general can be expected to be more significant. For example, in the related compound $\mathrm{Tb_2Ti_2O_7}$ (TTO), the energy gap is ten times smaller than in HTO, and the admixture of the ground-state doublet is significant [37]. This also makes TTO an interesting case study for application of pressure, but the theoretical analysis would require a very different approach from the one presented here.

Monte Carlo (MC) simulations using the Metropolis-Hastings algorithm and single spin flip updates are used to investigate a number of different system sizes with periodic boundary conditions. Since the lowest temperature used in the experiment was 1.5 K, monopole excitations are still prevalent, and loop flips [38] are not needed. We use the 16-particle standard cubic unit cell. All supercells are cubic of size L^3 unit cells, $L \in [1, \ldots, 8]$. Ewald summation is used to effectively account for the long-range conditionally convergent dipolar contributions [39].

B. Theoretical misalignment effects

The DSPM describes the changes in the magnetic moment observed in measurements [20] of DTO under uniaxial pressure [22] quite well. When pressure and field are applied along the [001] or [111] crystalline directions, the model works particularly well. However, when pressure and field are applied in the [110] crystalline direction for DTO, anomalous behavior is observed that cannot be explained by the DSPM [20,22], since the pressure-induced change in the magnetic moment does not saturate at high fields [20,22].

In this study, we attempt to explain this previously noted discrepancy for the measurement in the [110] crystalline direction, and we speculate that it can be an experimental artefact due to misalignment of the crystal. Next, we outline a brief discussion of what effects might be expected from crystal misalignment.

When measuring the magnetic moment of a single crystal under uniaxial pressure, there are three quantities that need to be aligned: the crystalline direction, the direction of the uniaxial pressure, and the direction of the magnetic field.

To investigate the influence of misalignment, we consider the possibility that the crystalline direction matches the direction of pressure perfectly, and that the magnetic field is misaligned with respect to the direction of pressure. This assumption minimizes the number of new parameters introduced to the theoretical model, and we believe that it still captures the essential effects of misalignment. In the experiment, on the other hand, we may expect the misalignment between the crystal direction and the applied pressure to be more significant. Since the crystal is surrounded by more compressible stycast, it is also possible that this misalignment may change during a series of compressions. See Appendix A for further discussion.

Misalignment has particularly strong effects when the measurement is conducted with pressure along the [110] direction [40]. This is because half of the spins in the material have a local Ising axis perpendicular to the [110] direction, so that at high fields, already a small misalignment will strongly affect the dynamics of these. We therefore adjust the applied field so that it is misaligned by an angle $\delta\varphi$ with respect to the [110] direction and remains perpendicular to [001], as this is the simplest way for the field to couple to the previously unaffected spins. Figure 5 illustrates the scenario. The magnetic moment is measured along the direction of the field, and when the field is misaligned we start to observe the dynamics of the previously perpendicular spins. This is not the case when we measure along the [001] and [111] crystalline directions, since in that case all spins already have a large component along the field. Hence we expect that the high-field behavior will be less affected by misalignment for measurements in the [001] and [111] crystalline directions. Our simulations confirm that this is indeed the case. The saturation fields for the pressure-induced changes in magnetic moment in the [001] and [111] measurements are not affected by misalignment, in contrast to the [110] direction. The effects of misalignment in the [110] direction are presented in Sec. IV A, and the key result is then shown in Fig. 7(c).

C. Demagnetizing corrections

To account for the macroscopic boundary effects, we perform a demagnetizing transformation. The samples used were cylindrical with an aspect ratio of $\gamma \equiv \frac{\text{height}}{\text{diameter}} = 1.50 \pm 0.05$ at ambient pressure. However, as the sample is compressed, the aspect ratio decreases. By fitting κ to the change in

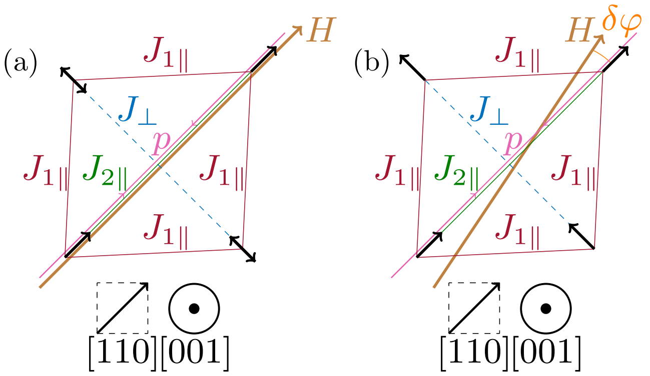

FIG. 5. View along [001] of a single tetrahedron with pressure along [110]. (a) Perfect alignment. (b) Field misalignment perpendicular to [001]. We assume that the misalignment angle $\delta\varphi$ can vary with application of pressure. For a field in this direction there are two degenerate ground states for perfect alignment [double-headed arrows in (a)], and only one ground state when the field is misaligned (b). We denote the misalignment at ambient and applied pressure by $\delta\varphi^0$ and $\delta\varphi^p$, respectively.

saturated magnetic moment, we determine γ. An important aspect, often overlooked, is that the demagnetization factor N is a function of both γ and the internal volume susceptibility $\chi^V_{\rm int}$, $N = N(\gamma, \chi^V_{\rm int})$, as has been recently calculated and verified [41,42]. In high-susceptibility materials ($\chi_{\rm int} > 1$), such as HTO, the susceptibility dependence of N is very significant, and we include it in the analysis. We perform a demagnetization transformation according to

$$H_{\rm ext} = H_{\rm int} + N(\gamma, \chi^V_{\rm int})M^V,$$

$$\chi^V_{\rm ext} = \frac{\chi^V_{\rm int}}{1 + N(\gamma, \chi^V_{\rm int})\chi^V_{\rm int}}, \tag{2}$$

where the intensive quantities M^V and χ^V are the magnetization and volume susceptibility, respectively. It is important to differentiate these from the external extensive quantities $M = M^V V(\gamma(p))$ and $\chi_{\rm ext} = \chi^V_{\rm ext} V(\gamma(p))$, measured in the experiment. The Monte Carlo calculations, performed using periodic Ewald boundary conditions, yield internal quantities.

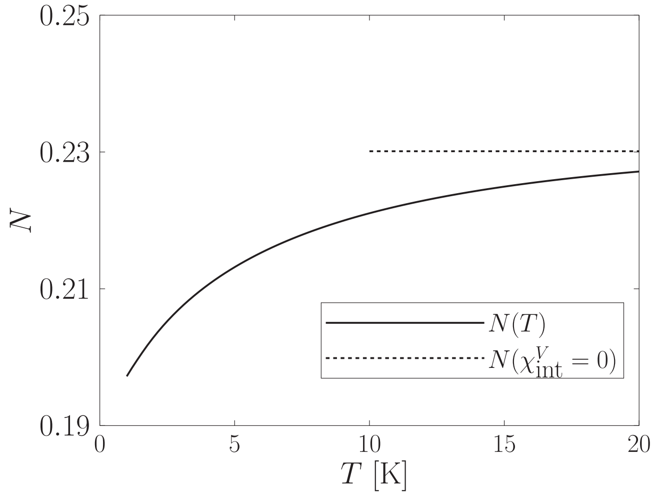

FIG. 6. Demagnetizing factor N as a function of T at zero field for a HTO cylinder of aspect ratio $\gamma = 1.5$.

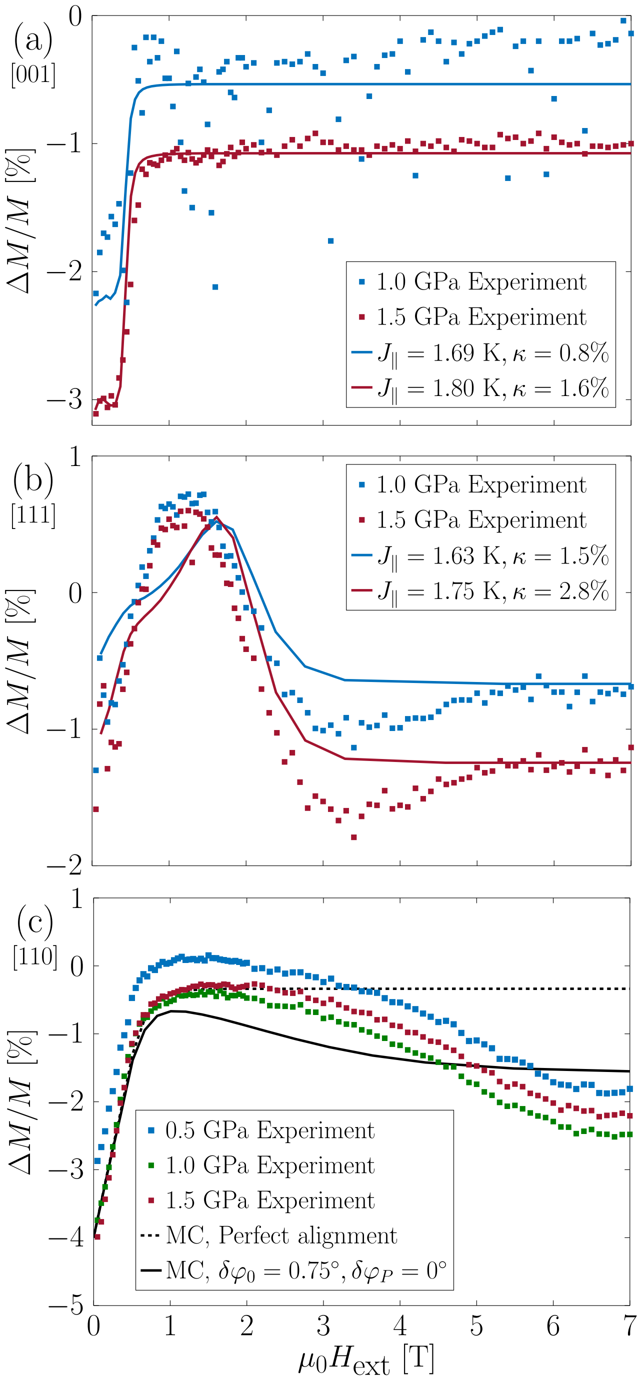

FIG. 7. Relative change in sample magnetic moment, $\Delta M/M = (M^p - M^0)/M^0$, as a function of magnetic field at sample temperature 1.83 K. The pressure and field are along the (a) [001], (b) [111], and (c) [110] crystalline direction. MC results are drawn as solid lines and performed on cubic systems of 8192 particles, $L = 8$. For the [110] measurement (c) we show the model prediction for $J_{1\|} = J_{2\|} = 1.2$ K, $\kappa = 1\%$ both for perfect alignment (dashed line) and for a small misalignment when pressure was applied (solid line).

Since the susceptibility of classical spin ice is isotropic, the susceptibility dependence of N calculated in Ref. [41] can be used for HTO, as demonstrated in Ref. [42]. Using the tabulated values of $N(\gamma, \chi^V_{\text{int}})$, we perform an interpolation using cubic splines [41]. As an example, we show the temperature dependence of N for an HTO cylinder of aspect ratio $\gamma = 1.5$ in Fig. 6, where we use the experimentally measured intrinsic susceptibility for HTO [43] at zero field to determine the temperature dependence.

D. Calculation of susceptibility

For the susceptibility measurements, we define the relative change in the susceptibility with respect to the applied pressure as $\Delta\chi_{\text{ext}}/\chi_{\text{ext}} \equiv (\chi^p_{\text{ext}} - \chi^0_{\text{ext}})\chi^0_{\text{ext}}$. We measured the relative change $\Delta\chi_{\text{ext}}/\chi_{\text{ext}}$ as a function of temperature. This quantity is highly sensitive to changes in J and κ, and in order to gain some physical insight, we consider the high-temperature limit, $T \to \infty$. In this noninteracting limit, the relative change depends only on κ. For the crystalline directions along which measurements were performed, we find that

$$\begin{aligned} \lim_{T\to\infty} \frac{\Delta\chi^{111}_{\text{ext}}}{\chi^{111}_{\text{ext}}} &= \frac{9\,(1-\kappa)^2}{4\,(1-\kappa)^2+32} - \frac{1}{4}, \\ \lim_{T\to\infty} \frac{\Delta\chi^{001}_{\text{ext}}}{\chi^{001}_{\text{ext}}} &= \frac{3(1-\kappa)^2}{2+(1-\kappa)^2} - 1, \end{aligned} \tag{3}$$

where the superscripts denote the crystalline direction of pressure and field.

From these formulas, we see that in both directions, the susceptibility at high temperature is reduced under application of pressure. This is a purely geometrical effect stemming from the fact that the Ising moments tilt away from the axis of pressure when the lattice is compressed.

E. Calculation of magnetic structure factor

We calculate theoretical predictions for the spin-flip magnetic structure factor according to

$$\begin{aligned} S(\mathbf{Q}) = &\frac{[f(|\mathbf{Q}|)]^2}{\mathcal{N}} \\ &\times \sum_{ij} \big\langle \mathbf{S}^\perp_i \cdot \mathbf{S}^\perp_j - (\mathbf{S}_i \cdot \mathbf{P})(\mathbf{S}_j \cdot \mathbf{P}) \big\rangle e^{i\mathbf{Q}\cdot\mathbf{r}_{ij}}, \end{aligned} \tag{4}$$

where the scattering wave vector is denoted by $\mathbf{Q}$, and the normalized polarization vector of the incident neutron beam is given by $\mathbf{P} \perp \mathbf{Q}$. The component of the spin perpendicular to the wave vector is defined as $\mathbf{S}^\perp_i = \mathbf{S}_i - \mathbf{S}_i \cdot \mathbf{Q}/|\mathbf{Q}|^2\mathbf{Q}$. $\mathcal{N}$ is the number of particles in the supercell, and $f(|\mathbf{Q}|)$ is the magnetic form factor for Ho^{3+}. The angled brackets $\langle \cdots \rangle$ denote the thermal average, which is calculated using the MC method.

IV. ANALYSIS AND DISCUSSION

A. Magnetization and susceptibility

In Fig. 7 we show the relative change in sample magnetic moment, $\Delta M/M = (M^p - M^0)/M^0$, as a function of applied magnetic field. The solid lines show the best theoretical fit for the different directions of pressure and field. For the [001] and [111] measurements, shown in Figs. 7(a) and 7(b), κ has been set so that the change in calculated saturation magnetic moment agrees with that of the experiment. With this constraint, there is only one free parameter, $J_\parallel$, which we determine from the best fit for each case. We find that for the [001] and [111] measurements, $J_\parallel$ increases monotonically with pressure. The change in $J_\parallel$ is similar in both directions, and the model accommodates the basic features in the experimental data: the upturn at 1.5 T in the [111] measurement as well as the drop at 0.5 T in the [001] direction, upon decreasing field. For the [001] measurement, we have excellent agreement between theory and experiment. We note that the observed decrease in the magnetic moment for HTO at low fields is in contrast with measurements made on DTO, where an increase of $\Delta M/M = 4\%$ was observed [20]. Although $J_\parallel$ and κ increase similarly for both materials, the ratio J/D is smaller for HTO, and the effects of the dipolar interactions dominate, leading to a decrease in the magnetic moment. In the [111] direction, the experimentally observed minimum centered at $\mu_0 H_{\text{ext}} = 3.5$ T is not accounted for in the model, and the shape of the maximum around 1.8 T differs, but the model captures the qualitative experimental features. Furthermore, in all measurements, the change in magnetic moment is strongly dependent on the field. This is due to a competition between different effects. At large fields the moment is saturated, and since spins tilt away from the direction of pressure, it decreases. At low fields, the thermal fluctuations determine the magnetic moment. In the case of HTO, the magnetization decreases when pressure is applied, while for DTO in the [001] direction the preference for a ferromagnetic ground state is indicated by an upturn in the magnetization.

Figure 7(c) shows the change in magnetic moment for the [110] measurement. We note that the change has hardly saturated as a function of field. Seemingly, we need a field of about 7 T to saturate the change in the [110] direction, higher than the 5.5 T needed for the [111] direction. This feature is not possible to reproduce in the DSPM in which the field needed for [111] saturation is higher than that needed for [110] saturation, since the saturated [111] state requires that we break the two-in two-out ground state of spin ice [44].

As discussed in Sec. III B, we speculate that the high-field unsaturated behavior can be due to misalignment of the crystal, since measurements are particularly sensitive in the [110] direction. In Fig. 7(c) we illustrate the influence of misalignment. We first fit a curve with $\kappa = 1\%$ as an estimate of the compression based on the other directions at 1 GPa (0.8% and 1.5% for [001] and [111], respectively). In the DSPM, the change in magnetic moment will saturate at about 1 T (same order of magnitude as in the [001] case) regardless of the parameters used. For simplicity we assume that $J_{1\parallel} = J_{2\parallel} = J_\parallel$, which gives a rough value of $J_\parallel = 1.2$ K when we fit this single parameter to match the sub 1 T experimental results. This DSPM fit is shown as the dashed line in Fig. 7(c). For all fields above 1 T, the DSPM gives a constant saturated change in magnetic moment dependent only on κ. Clearly this is not what we see in the experiment, where the change keeps varying up to fields of about 7 T.

If we introduce crystal misalignment according to Sec. III B, we can partially reproduce the high-field trend observed in the measurement. Within this framework, we have

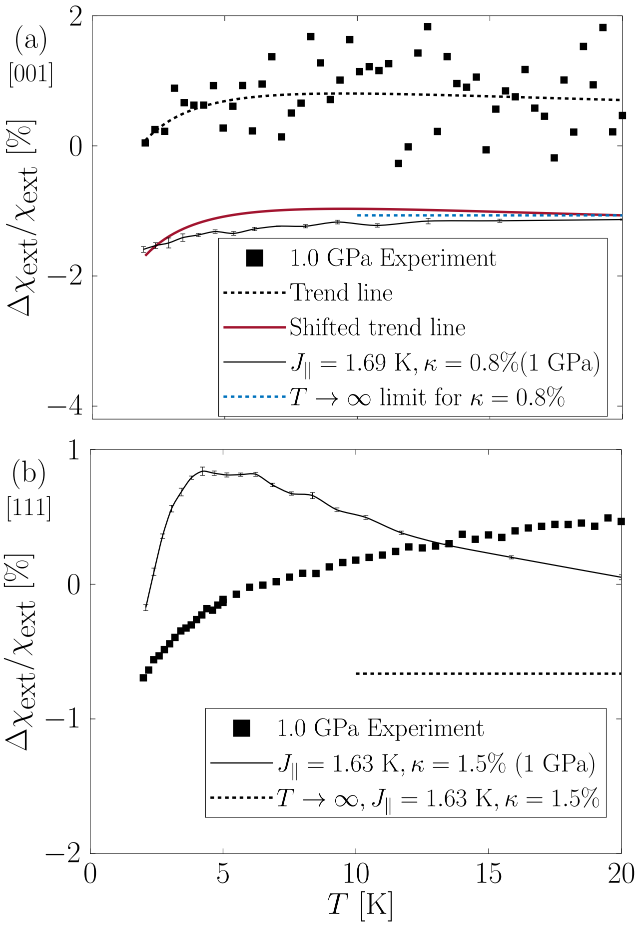

FIG. 8. Relative change in external susceptibility for pressure and field along (a) [001] and (b) [111], both for probing an external field of strength 0.01 T. Solid lines show the theoretical MC prediction from the parameters fitted from the magnetic moment measurements at 1.0 GPa. Dashed lines indicate the $T \to \infty$ analytical limiting value, Eq. (3). MC simulation for 2000 particles, $L = 5$.

two additional parameters $\delta\varphi^0$, $\delta\varphi^p$ as discussed in Sec. III B for the misalignment of H with respect to the [110] direction, at zero (0) and applied pressure (p), respectively. To get a decrease in magnetic moment when pressure is applied, we find it necessary that the field couples more strongly to the perpendicular spins in the reference measurement. Hence, to keep the model as simple as possible, we set $\delta\varphi^p = 0^\circ$. We then adjust $\delta\varphi^0$ in order to fit the experimental curve above 1 T. We find that $\delta\varphi^0 = 0.75^\circ$ gives the best fit. We do not get the exact same features as those observed, but we do demonstrate that the decrease in magnetization above 1 T could be due to misalignment. For further discussion of more elaborate misalignment models under pressure, we refer to Appendix A.

Finally, we use our obtained values of $J_\parallel$ and κ to predict the change in susceptibility as a function of temperature. In Fig. 8 we show the measured relative change in external susceptibility plotted against temperature for an applied pressure of 1 GPa. The theoretical predictions are shown for the values derived from the 1.0 GPa [001] and [111] magnetic moment fits, Figs. 7(a) and 7(b), respectively. In contrast with the measurements of the magnetic moment, the susceptibility measurements are more challenging due to the low field used and a higher sensitivity to uncertainties in the demagnetizing factors.

Due to the fluctuations in the [001] measurement, Fig. 8(a), we include a trend line by fitting rational polynomials to the susceptibility. The qualitative curve shape is the same for both theory and experiment, but they differ by an overall shift along the vertical axis. At the lowest temperature $T = 1.83$ K we expect that the relative change in susceptibility should coincide with the $H_{\mathrm{ext}} \to 0$ limit in the relative change in the magnetic moment, Fig. 7(a), which for 1 GPa is -2%. There is therefore a discrepancy between the two experimental measurements. From theory we also expect that the susceptibility should be reduced at high temperature when pressure is applied; see Eq. (3). Since the susceptibility measurements in Fig. 2 were nonmonotonic in pressure, we suspect a systematic error in the experimental data, and we note that if we shift the susceptibility measurement performed under pressure by -2%, the data match the theoretical prediction as well as the magnetization measurement performed at $T = 1.83$ K.

For the [111] direction there is a more significant mismatch between theory and experiment. In particular, theory would predict a maximum in $\Delta\chi/\chi$ near 5 K, which is not present in the experiment. We would also expect from theory that the relative change should saturate to a lower value. Indeed, with the assumption of Ising spins it directly follows from Eq. (3) that $\Delta\chi/\chi$ must reach a negative value at high temperature. The discrepancy is most likely due to insufficient accuracy in the present susceptibility measurements.

B. Neutron scattering

The parameters extrapolated from the measurements of the magnetic moment can be used to compute the thermal spin-spin correlation function and hence the magnetic structure factor, Eq. (4), within the DSPM. For pressure along the [001] crystalline axis, theoretical and experimental results match well, see Fig. 7(a), and we use the parameters from this fit to predict the [001] spin-flip structure factor under pressure. The resulting change in $S(\mathbf{Q})$, $\Delta S(\mathbf{Q})/S(\mathbf{Q}) \equiv [S(\mathbf{Q})_p - S(\mathbf{Q})_0]/S(\mathbf{Q})_0$, is shown in the left half of Fig. 9, simulated at $T = 1.5$ K and $p = 1.5$ GPa. In the right half we show the change in the experimental [45] scattering at $p = 2.2$ GPa and $T = 1.5$ K measured in previous work [22]. In the outer region we see eight patches of increased intensity that have been marked and coincide with the theory prediction. In the inner region there are two regions of increased intensity not seen in the experiment, but we note, as mentioned in previous work, that the experimentally measured signal was poorly sampled at wave vectors shorter than 1.5 Å^{-1} due to windows in the scattering plane of the previous CuBe pressure cell [22] used in that neutron scattering experiment.

A key result of this study is therefore that the scattering profile calculated from the parameters obtained from the fit to the magnetic moment, Fig. 7(a), matches the best profile that can be obtained by freely adjusting $J_\parallel$ to the experimental neutron data, as was done in the previous study [22]. Furthermore, we use the DSPM to calculate the spin-flip structure factor in the $(h, -h, l)$ plane with pressure along [110], shown in Fig. 3. We take the parameters fitted to the

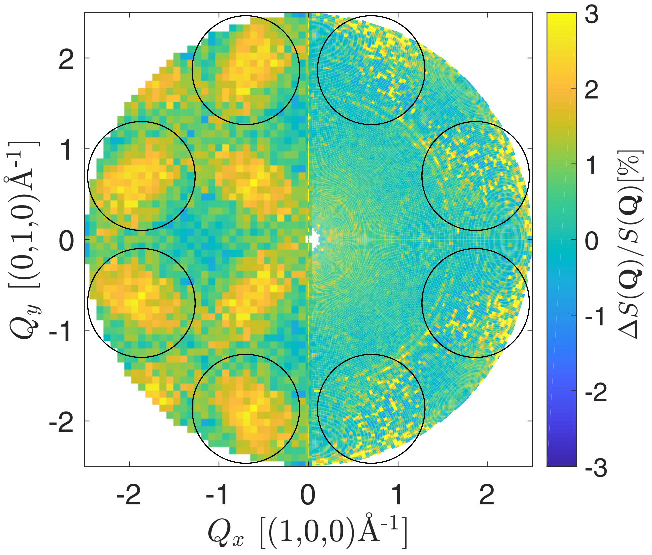

FIG. 9. Left: Relative change in the [001] spin-flip neutron scattering profile predicted from parameters found in the measurement of the magnetic moment, Fig. 7, at 1.5 GPa along [001] and 1.5 K ($J_\parallel = 1.80$, $\kappa = 1.6\%$). Right: Relative change in experimental [001] spin-flip neutron scattering data [22,45] for HTO at 2.2 GPa pressure along [001], 1.5 K. Circles mark regions of increased intensity and are plotted at symmetry-equivalent regions in the theoretical prediction. In previous investigations [22], the DSPM parameters were estimated based directly on this experimental scattering profile. The current measurements of the magnetic moment show consistency with this estimate.

magnetic moment, Fig. 7(c), and calculate $S(\mathbf{Q})$ from Eq. (4). To better show the changes in scattering intensity, we integrate the signal around one of the satellite peaks as shown by the shaded region in Fig. 3. In Fig. 10 we see Gaussian fits to the experimental [30] data (solid lines). The theoretical estimate from the fit to the magnetic moment ($J_\parallel = 1.2$ K, $\kappa = 1\%$) is shown together with the theoretical prediction at zero pressure (dashed lines). Although the experimental error bars, set by the neutron exposure time, are of the same order as the observed increase under applied pressure, we note that the theory captures the increased peak intensity of about 4%, and we conclude that the model describes the observed phenomena both for magnetization and neutron scattering measurements in several crystalline directions.

C. Evolution of the model parameters

Using the straightforward magnetization measurements, we can obtain the model parameter dependence on pressure. In Fig. 11 we depict the pressure dependence of $J_\parallel$ and κ in all three direction. We include the current data points at pressures of 1.0 GPa and $p = 1.5$ GPa, as well as the result of the previous neutron study at an applied pressure of 2.2 GPa [22]. The three data points along [001] show a near-linear dependence on pressure. Analyzing the phase diagram using a combination of MC and a direct comparison of the state energies [22], we find that all three points lie on a curve in the ($J_\parallel$, κ)-space for which the exchange interaction evolves so as to cancel the changes in the dipolar dynamics originating from lattice compression, and the system is on the border between two different types of dipolar chain [34] ground states [22]. This suggests that the ground state will remain a dipolar chain state under application of uniaxial pressure along the [001] direction. This result contrasts the predictions for DTO, where at sufficiently high pressure a ferromagnetic ground state is expected [21,22].

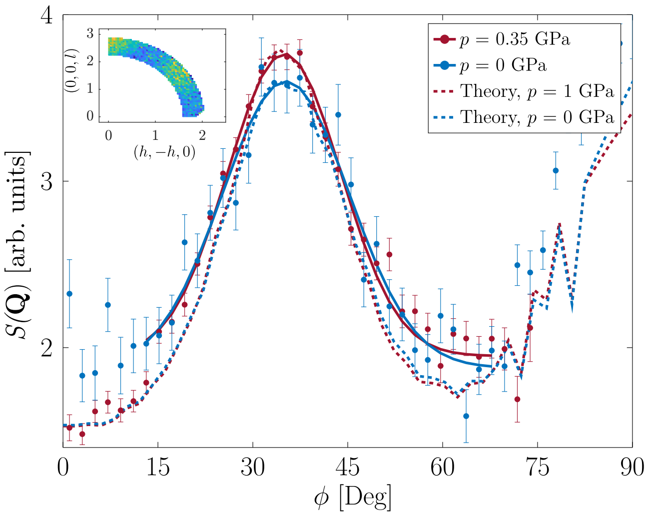

FIG. 10. [110] spin-flip $S(\mathbf{Q})$ line-cut average over $2.22 < Q < 2.87$ (reduced units) for polar angle $\phi = 0^\circ \rightarrow 90^\circ$ in the neutron scattering data (shaded area in Fig. 3) [30]. Gaussian fit to the experimental data (solid). Theoretical prediction at 0 and 1.0 GPa uniaxial pressure for the parameters found in the measurements of the magnetic moment, $J_\parallel = 1.2$ K, $\kappa = 1\%$, Fig. 7(c) (dashed). MC simulation for 8192 particles $L = 8$.

To extrapolate our results to higher pressure, we use linear extrapolations for the parameters in the [111] and [110] directions:

$$\begin{aligned} J_\parallel &= J_\parallel^{p=0} + (J_\parallel^{p^*} - J_\parallel^{p=0})p, \\ \kappa_\parallel &= \kappa^{p=0} + (\kappa^{p^*} - \kappa^{p=0})p. \end{aligned} \tag{5}$$

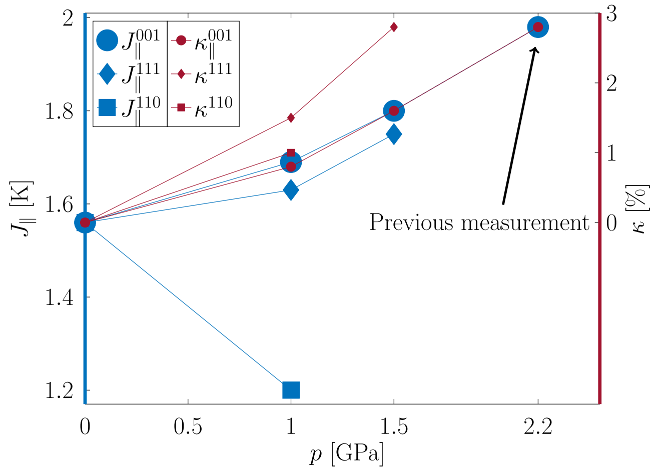

FIG. 11. Evolution of the model parameter $J_\parallel$ and crystal compression κ under applied uniaxial pressure along the [001] crystalline axis.

TABLE I. Summary of the fitted and estimated DSPM parameters found in this work. p_c is the critical pressure above which a linear extrapolation predicts a ferromagnetic [21] ground state. We estimate the error to be less than 5% of the fitted parameter value. However, for the [110] direction this might be as much as 20% due to misalignment having more prominent effects.

	$p = 0\,\text{GPa}$	$p = 1\,\text{GPa}$		$p = 1.5\,\text{GPa}$		
Direction	J (K)	$J_\parallel$ (K)	κ (%)	$J_\parallel$ (K)	κ (%)	p_c (GPa)
[001]	1.56	1.69	0.8	1.80	1.6	
[111]	1.56	1.63	1.5	1.75	2.8	>4
[110]	1.56	1.2	1			3.3

For κ this is motivated by Hooke's law, while the true pressure dependence on $J_\parallel$ may deviate from our linear model, but we proceed with p^* as the highest measured pressure for the respective direction.

For the [111] direction, we find that the dipolar chain ground state is stable up to pressures of at least 4 GPa. In the [110] direction, on the other hand, we find a transition to the previously mentioned ferromagnetic state at a critical pressure of 3.3 GPa. In DTO this state is expected when applying pressure in excess of 3.4 GPa in the [001] direction [21,22]. We therefore conclude that further uniaxial high-pressure studies should be conducted either on DTO in the [001] direction, or on HTO in the [110] direction. At such high pressures, the crystals are likely to break. However, using techniques like submerging the crystals in epoxy resin, as we did in this study, or using some other type of support material, we believe that such experiments can be realized. We summarize the fitted and estimated parameter values in Table I.

V. CONCLUSIONS

We have performed measurements of the field-induced magnetic moment, magnetic susceptibility, and neutron structure factor of HTO under applied uniaxial pressure. Through extensive MC calculations we demonstrate that a dipolar spin ice model, with a pressure-tuned nearest-neighbor interaction, is able to capture the most essential features of the measurements of HTO. The framework is extended to include effects of misalignment, and we have found that misalignment can, to some extent, describe the anomalous effects observed in the magnetic moment for the [110] direction in both HTO and DTO.

The T-dependent pressure-induced changes in the susceptibility turn out to be a more sensitive quantity to both measure and model than the field-induced magnetic moment. The low field used experimentally results in a weak signal that is easily overshadowed. Theoretically, the susceptibility of spin ice has proven to be a sensitive function of the intrinsic competing interactions [46], and the measurements are sensitive to sample shape [42], with the optimal sample size probably spherical. To perform susceptibility measurements on a spherical sample under pressure is highly challenging, and we therefore have to contend with our present results. Still, the qualitative curve shape for the susceptibility in the [001] direction is captured rather well by our model, but there are significant discrepancies in the [111] measurement.

Our main result is that the model parameters derived from the measurement of the magnetization also capture the most salient features of the pressure-induced change in the neutron scattering structure factor. That the same model describes both bulk properties and spin-spin correlation functions lends credibility to the theory. Therefore, we hope that using relatively straightforward magnetization measurements to determine the pressure dependence of interaction parameters can prove useful also when it comes to other classes of frustrated materials. Increased theoretical predictive power supporting demanding neutron experiments under high pressure would benefit many investigators in the field. With new, and more intense, neutron sources under construction, we expect this to be a research topic of increasing importance in the near future.

ACKNOWLEDGMENTS

We thank Steven Bramwell for insightful discussions. The neutron scattering experiments were performed at the Paul Scherrer Institute and the Institute Laue-Langevin. We thank the sample environment group of the ILL for preparatory help and access to facilities. The simulations were performed on resources provided by the Swedish National Infrastructure for Computing (SNIC) at the Center for High Performance Computing (PDC) at the Royal Institute of Technology (KTH). The project was supported by Nordforsk through the program NNSP (Project No. 82248) and by the Danish Agency for Research and Innovation through DANSCATT.

APPENDIX A: MISALIGNMENT

The main text discusses the influence of misalignment of the applied field. Of even greater importance is probably a misalignment of the crystalline axis with respect to the applied pressure and field. Our basic analysis for the magnetization measurements suggests that the [001] and [111] directions are not sensitive to a slight misalignment. The [110] direction, on the other hand, is much more sensitive due to the large subset of spins that are perpendicular to the field under perfect alignment. We suspect that this result holds also in more elaborate models of crystalline axis misalignment. A more general description than provided in the main text introduces up to six independent exchange parameters since there are six different types of nearest-neighbor bonds in a tetrahedron. Figure 12 illustrates the two different kinds of misalignment. The field misalignment depicted in Fig. 12(a) was discussed in the main text. In this case, there are only three distinct exchange couplings ($J_\perp, J_{1\parallel}, J_{2\parallel}$) due to the symmetry of the tetrahedron. In the case of misalignment of the crystalline axis, the $J_{2\parallel}$ couplings will no longer be equal. Figure 12(b) illustrates a case in which all six distances between different corners of the compressed tetrahedron are different. To reduce the number of free parameters, we could linearize the distance dependence of $J, J = J_{p=0} + K(r_0 - r)$, where r_0 is the unperturbed distance and K is a free parameter. This would give the same number of free parameters as in the basic model presented in the main text. However, J does not necessarily depend on the distance between the ions in the same way for all nearest-neighbor bonds. Therefore, we contend with the model of the main text, and we believe that it demonstrates sufficiently that the

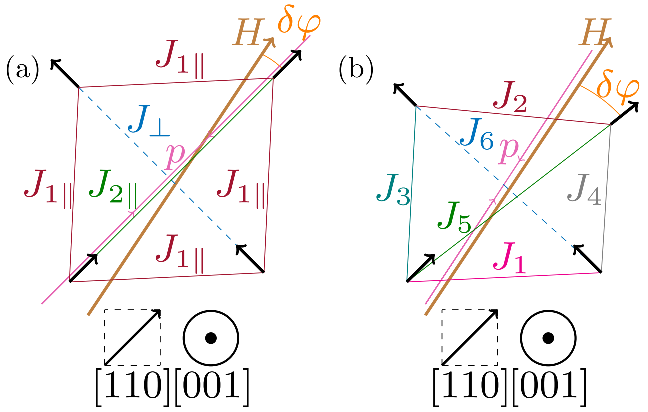

FIG. 12. Misalignment. (a) Field misalignment, discussed in the main text. (b) Crystalline axis misalignment. The view is along the [001] direction in both cases. More symmetries are broken in (b) as the tetrahedron is compressed along the p axis.

features above 1 T in the [110] relative change in magnetic moment can be an artefact due to misalignment.

APPENDIX B: CRYSTALS

The crystal quality is particularly important when working with external pressure. The crystals must withstand high pressure without cracking, and due to the demagnetizing effects it is important that the crystals are cut with accuracy. Figure 13(a) shows a picture of one of the crystals used in the magnetization experiment. The crystals have been aligned to the uniaxial pressure axis. However, as the crystals were submerged in stycast, which is much softer than HTO, a small shift in the alignment may arise as pressure is applied due to plastic deformation.

In the neutron scattering experiment for the larger 3-mm-diam crystals, the nuclear Bragg peaks observed on D7 are consistent with the alignment. However, the instrumental parameters of D7—incident beam size, divergence, and detection resolution—do not provide a very accurate determination of the absolute alignment. The nature of the neutron scattering experiment also prevents the use of stycast to mitigate against the Poisson expansion. To include such expansion of the sample in the simulation would introduce additional unknown model parameters, which from these few measurements is hard to determine. We therefore chose not to include this effect, and we find that this approximation still provides a valid prediction for the neutron scattering intensity. However, we mention that the physics that can be reached by including this effect can also be reached by allowing $J_\perp$ to vary, and it will not introduce any new effects, apart from having more free parameters allowing for an easier fit to data.


(a) (b)

FIG. 13. (a) One of the HTO crystals (ø 2 mm) used for the magnetization measurement. The picture shows the accuracy of the cutting procedure. (b) One of the crystals used in the neutron scattering experiment (ø 3 mm), placed on top of the steel anvil that was used for applying uniaxial pressure.

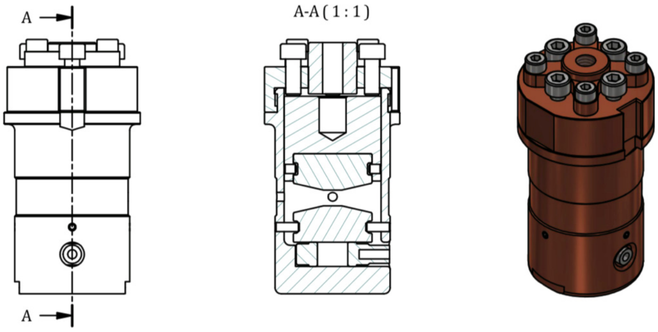

FIG. 14. Engineering drawings and overview of the uniaxial pressure cell.

APPENDIX C: UNIAXIAL PRESSURE CELL

The neutron scattering uniaxial pressure cell has been developed to enable neutron scattering experiments in the cold energy spectra range, $2 \lesssim \lambda \lesssim 20$ Å, for diffuse magnetic scattering profiles, inclusive of weak inelastic scattering features, with polarization analysis. The uniaxial pressure cell should be able to provide pressures up to 2 GPa at cryogenic temperatures. As such, the requirements include a scattering window that covers a wide angular range with a very clean background profile and a nonmagnetic cell that enables polarization analysis. These requirements place stringent restrictions on the materials for the manufacturing of the cell, and they lead us to focus on the optimization of an anvil-type cell. An engineering overview of the cell employed during the D7 experiment is shown in Fig. 14. The main body is manufactured out of CuBe with nonmagnetic stainless-steel anvils. Force is applied at room temperature and recalibrated using a calibration profile developed within our team. Pressure is deduced from the known contact area. The calibration profiles are not perfect and may lead to some uncertainty in the exact pressure applied at the lowest temperatures. Complete details of the cell will be published elsewhere, and a uniaxial pressure cell with *in situ* pressure determination is under development ensuring we maintain the aforementioned parameters.

[1] *Highly Frustrated Magnetism*, edited by C. Lacroix, P. Mendels, and F. Mila, Springer Series in Solid-State Sciences Vol. 164 (Springer, Berlin, 2011).

[2] C. Castelnovo, R. Moessner, and S. L. Sondhi, Nature (London) **451**, 42 (2008).

[3] M. E. Brooks-Bartlett, S. T. Banks, L. D. C. Jaubert, A. Harman-Clarke, and P. C. W. Holdsworth, Phys. Rev. X **4**, 011007 (2014).

[4] C. L. Henley, Phys. Rev. B **71**, 014424 (2005).

[5] P. W. Anderson, Science **235**, 1196 (1987).

[6] P. Henelius, T. Lin, M. Enjalran, Z. Hao, J. G. Rau, J. Altosaar, F. Flicker, T. Yavors'kii, and M. J. P. Gingras, Phys. Rev. B **93**, 024402 (2016).

[7] C. R. Wiebe and A. M. Hallas, APL Mater. **3**, 041519 (2015).

[8] T. Biesner and E. Uykur, Crystals **10**, 4 (2020).

[9] I. Mirebeau, I. N. Goncharenko, P. Cadavez-Peres, S. T. Bramwell, M. J. P. Gingras, and J. S. Gardner, Nature (London) **420**, 54 (2002).

[10] H.-J. Kim, C. R. S. Haines, C. Liu, S. H. Chun, K. H. Kim, H. T. Yi, S.-W. Cheong, and S. S. Saxena, Low Temp. Phys. **43**, 901 (2017).

[11] S. A. Zvyagin, D. Graf, T. Sakurai, S. Kimura, H. Nojiri, J. Wosnitza, H. Ohta, T. Ono, and H. Tanaka, Nat. Commun. **10**, 1064 (2019).

[12] S. V. Isakov, K. S. Raman, R. Moessner, and S. L. Sondhi, Phys. Rev. B **70**, 104418 (2004).

[13] T. Fennell, O. A. Petrenko, B. Fåk, J. S. Gardner, S. T. Bramwell, and B. Ouladdiaf, Phys. Rev. B **72**, 224411 (2005).

[14] A. P. Ramirez, A. Hayashi, R. J. Cava, R. Siddharthan, and B. S. Shastry, Nature (London) **399**, 333 (1999).

[15] L. D. C. Jaubert and P. C. W. Holdsworth, Nat. Phys. **5**, 258 (2009).

[16] H. M. Revell, L. R. Yaraskavitch, J. D. Mason, K. A. Ross, H. M. L. Noad, H. A. Dabkowska, B. D. Gaulin, P. Henelius, and J. B. Kycia, Nat. Phys. **9**, 34 (2013).

[17] B. C. den Hertog and M. J. P. Gingras, Phys. Rev. Lett. **84**, 3430 (2000).

[18] R. Siddharthan, B. S. Shastry, A. P. Ramirez, A. Hayashi, R. J. Cava, and S. Rosenkranz, Phys. Rev. Lett. **83**, 1854 (1999).

[19] T. Yavors'kii, T. Fennell, M. J. P. Gingras, and S. T. Bramwell, Phys. Rev. Lett. **101**, 037204 (2008).

[20] M. Mito, S. Kuwabara, K. Matsuhira, H. Deguchi, S. Takagi, and Z. Hiroi, J. Magn. Magn. Mater. **310**, e432 (2007), proceedings of the 17th International Conference on Magnetism.

[21] L. D. C. Jaubert, J. T. Chalker, P. C. W. Holdsworth, and R. Moessner, Phys. Rev. Lett. **105**, 087201 (2010).

[22] R. Edberg, L. Ørduk Sandberg, I. M. B. Bakke, M. L. Haubro, L. C. Folkers, L. Mangin-Thro, A. Wildes, O. Zaharko, M. Guthrie, A. T. Holmes, M. H. Sørby, K. Lefmann, P. P. Deen, and P. Henelius, Phys. Rev. B **100**, 144436 (2019).

[23] A. Ghasemi, A. Scheie, J. Kindervater, and S. Koohpayeh, J. Cryst. Growth **500**, 38 (2018).

[24] P. P. Deen, I. M. B. Bakke, T. Hansen, M. Haubro, K. Lefmann, and L. Ørduk Sandberg, Institut Laue-Langevin (2019), doi: 10.5291/ILL-DATA.5-41-1008.

[25] F. Guo, K. Murata, A. Oda, Y. Mizuno, and H. Yoshino, J. Phys. Soc. Jpn. **69**, 2164 (2000).

[26] M. Mito, J. Phys. Soc. Jpn. **76**, 182 (2007).

[27] J. R. Stewart, P. P. Deen, K. H. Andersen, H. Schober, J.-F. Barthélémy, J. M. Hillier, A. P. Murani, T. Hayes, and B. Lindenau, J. Appl. Crystallogr. **42**, 69 (2008).

[28] R. Higashinaka, H. Fukazawa, and Y. Maeno, Phys. Rev. B **68**, 014415 (2003).

[29] T. Fennell, S. T. Bramwell, D. F. McMorrow, P. Manuel, and A. R. Wildes, Nat. Phys. **3**, 566 (2007).

[30] P. Deen, I. M. Bakke, R. Edberg, M. Haubro, K. Leffmann, D. M. Vasiukov, and A. Wildes, ILL (2019), doi: 10.5291/ILL-DATA.DIR-185.

[31] S. T. Bramwell, M. J. Harris, B. C. den Hertog, M. J. P. Gingras, J. S. Gardner, D. F. McMorrow, A. R. Wildes, A. L. Cornelius, J. D. M. Champion, R. G. Melko, and T. Fennell, Phys. Rev. Lett. **87**, 047205 (2001).

[32] T. Fennell, P. P. Deen, A. R. Wildes, K. Schmalzl, D. Prabhakaran, A. T. Boothroyd, R. J. Aldus, D. F. McMorrow, and S. T. Bramwell, Science **326**, 415 (2009).

[33] M. Twengström, P. Henelius, and S. T. Bramwell, Phys. Rev. Res. **2**, 013305 (2020).

[34] R. G. Melko and M. J. P. Gingras, J. Phys.: Condens. Matter **16**, R1277 (2004).

[35] Y. M. Jana and D. Ghosh, Phys. Rev. B **61**, 9657 (2000).

[36] S. Rosenkranz, A. P. Ramirez, A. Hayashi, R. J. Cava, R. Siddharthan, and B. S. Shastry, J. Appl. Phys. **87**, 5914 (2000).

[37] A. J. Princep, H. C. Walker, D. T. Adroja, D. Prabhakaran, and A. T. Boothroyd, Phys. Rev. B **91**, 224430 (2015).

[38] R. G. Melko, B. C. den Hertog, and M. J. P. Gingras, Phys. Rev. Lett. **87**, 067203 (2001).

[39] D. Frenkel and B. Smit, *Understanding Molecular Simulation: From Algorithms to Applications*, Computational Science (Elsevier Science, Amsterdam, 2001).

[40] H. Fukazawa, R. G. Melko, R. Higashinaka, Y. Maeno, and M. J. P. Gingras, Phys. Rev. B **65**, 054410 (2002).

[41] D.-X. Chen, E. Pardo, and A. Sanchez, J. Magn. Magn. Mater. **306**, 135 (2006).

[42] M. Twengström, L. Bovo, M. J. P. Gingras, S. T. Bramwell, and P. Henelius, Phys. Rev. Mater. **1**, 044406 (2017).

[43] L. Bovo, L. D. C. Jaubert, P. C. W. Holdsworth, and S. T. Bramwell, J. Phys.: Condens. Matter **25**, 386002 (2013).

[44] M. J. Harris, S. T. Bramwell, D. F. McMorrow, T. Zeiske, and K. W. Godfrey, Phys. Rev. Lett. **79**, 2554 (1997).

[45] P. Deen, I. M. Bakke, R. Edberg, H. Fjellvåg, K. Leffmann, L. Ø. Sandberg, and A. Wildes, ILL (2018), doi: 10.5291/ILL-DATA.5-32-856.

[46] L. Bovo, M. Twengström, O. A. Petrenko, T. Fennell, M. J. P. Gingras, S. T. Bramwell, and P. Henelius, Nat. Commun. **9**, 1999 (2018).

A.3 Publication 3: Emergent magnetic behaviour in the frustrated Yb3Ga5O12 garnet.

I played a central role in the two different neutron scattering beamtimes with sample preparation and alignment, participation in the beamtimes and the initial data analysis. For the CNCS beamtime, this includes extraction of the diffuse scattering signals in the elastic line, INS1 and INS2 for the measurements at the CNCS instrument as described in the thesis. For the D7 experiment, it includes extraction of the magnetic, nuclear and spin incoherent scattering profiles.

I have taken part in the RMC simulations and prepared the data for the simulations, but the final RMC simulations that are presented in the publication were performed by Richard Edberg. The interpretations and analyses of the RMC simulation results with anisotropy and correlations of the individual spins and director state in local coordinates were made in a collaboration between Richard Edberg and myself. I have written the first draft of the manuscript except appendices on the RMC refinement technique and the MC simulations which were written by Richard Edberg.

Emergent magnetic behavior in the frustrated Yb3Ga5O12 garnet

Sandberg, Lise Ørduk; Edberg, Richard; Bakke, Ingrid Marie Berg; Pedersen, Kasper S.; Hatnean, Monica Ciomaga; Balakrishnan, Geetha; Mangin-Thro, Lucile; Wildes, Andrew; Fåk, B.; Ehlers, Georg

Total number of authors:
14

Published in:
Physical Review B

Link to article, DOI:
10.1103/PhysRevB.104.064425

Publication date:
2021

Document Version
Publisher's PDF, also known as Version of record

Citation (APA):
Sandberg, L. Ø., Edberg, R., Bakke, I. M. B., Pedersen, K. S., Hatnean, M. C., Balakrishnan, G., Mangin-Thro, L., Wildes, A., Fåk, B., Ehlers, G., Sala, G., Henelius, P., Lefmann, K., & Deen, P. P. (2021). Emergent magnetic behavior in the frustrated $Yb_3Ga_5O_{12}$ garnet. *Physical Review B*, *104*(6), [064425]. https://doi.org/10.1103/PhysRevB.104.064425

PHYSICAL REVIEW B **104**, 064425 (2021)

Emergent magnetic behavior in the frustrated $Yb_3Ga_5O_{12}$ garnet

Lise Ørduk Sandberg,[1] Richard Edberg,[2] Ingrid-Marie Berg Bakke,[3] Kasper S. Pedersen,[4] Monica Ciomaga Hatnean,[5]
Geetha Balakrishnan,[5] Lucile Mangin-Thro,[6] Andrew Wildes,[6] B. Fåk,[6] Georg Ehlers,[7] Gabriele Sala,[7]
Patrik Henelius,[2,8] Kim Lefmann,[1] and Pascale P. Deen[1,9,*]
[1]*Nanoscience Center, Niels Bohr Institute, University of Copenhagen, Universitetsparken 5, DK-2100 Copenhagen Ø, Denmark*
[2]*Physics Department, KTH Royal Institute of Technology, Sweden*
[3]*University of Oslo, Centre for Materials Science and Nanotechnology, NO-0315 Oslo, Norway*
[4]*Department of Chemistry, Technical University of Denmark, DK-2800 Kgs. Lyngby, Denmark*
[5]*Department of Physics, University of Warwick, Coventry CV4 7AL, United Kingdom*
[6]*Institut Laue-Langevin, 71 Avenue des Martyrs, CS 20156, 38042 Grenoble Cedex 9, France*
[7]*Neutron Technologies Division, Oak Ridge National Laboratory, Oak Ridge, Tennessee 37831-6466, USA*
[8]*Faculty of Science and Engineering, Åbo Akademi University, Åbo, Finland*
[9]*European Spallation Source ERIC, 22363 Lund, Sweden*

(Received 25 May 2020; revised 30 April 2021; accepted 13 July 2021; published 13 August 2021)

We report neutron scattering, magnetic susceptibility and Monte Carlo theoretical analysis to verify the short-range nature of the magnetic structure and spin-spin correlations in a $Yb_3Ga_5O_{12}$ single crystal. The quantum spin state of Yb^{3+} in $Yb_3Ga_5O_{12}$ is verified. The quantum spins organize into a short-ranged emergent director state for $T < 0.6$ K derived from anisotropy and near-neighbor exchange. We derive the magnitude of the near-neighbor exchange interactions $0.6 < J_1 < 0.7$ K, $J_2 = 0.12$ K and the magnitude of the dipolar exchange interaction, D, in the range $0.18 < D < 0.21$ K. Certain aspects of the broad experimental dataset can be modeled using a J_1D model with ferromagnetic near-neighbor spin-spin correlations while other aspects of the data can be accurately reproduced using a J_1J_2D model with antiferromagnetic near-neighbor spin-spin correlation. As such, although we do not quantify all the relevant exchange interactions, we nevertheless provide a strong basis for the understanding of the complex Hamiltonian required to fully describe the magnetic state of $Yb_3Ga_5O_{12}$.

DOI: 10.1103/PhysRevB.104.064425

I. INTRODUCTION

In recent years, emergent behavior has been observed in three-dimensional (3D) geometrically frustrated compounds, due to the interplay between spin-spin interactions and anisotropy. In spin-ice compounds $Ho_2Ti_2O_7$ (HTO) and $Dy_2Ti_2O_7$ (DTO), with magnetic rare-earth ions placed on the 3D pyrochlore lattice, a strongly correlated ground state is observed with remarkable excitations that can be modeled as magnetic monopoles. This new physics is derived from a combination of ferromagnetic (FM) nearest-neighbor (NN) spin-spin interactions and a strong local Ising anisotropy along the central axes of each tetrahedron [1–4].

A second emergent state, which has recently come to light, is the long-range multipolar director state found in the 3D hyperkagome structure $Gd_3Ga_5O_{12}$ (GGG) [5]. In GGG, the Gd^{3+} ions are positioned on two interpenetrating hyperkagome lattices, shown in Fig. 1. Despite the absence of long-range correlations of the individual spins, an emergent long-range hidden order known as a director state has been determined. The director state is derived from the collective spins on a 10-ion loop and is defined as

$$\mathbf{L}(\mathbf{rc}) = \frac{1}{10}\sum_n \cos(n\pi)\mathbf{S}_n(\mathbf{r}), \tag{1}$$

where $\mathbf{S}_n(\mathbf{r})$ are unit-length spins on the ten-ion loop with the center in **rc**. The director state was found to display long-range correlations in GGG and governs both the magnetic structure [5] and magnetic dynamics [6] into the high-field regime. The director state is derived from anisotropy and near-neighbor exchange. Gd^{3+} ions display a nominal zero orbital angular momentum $L = 0$ and thus no strong anisotropy due to spin-orbit coupling. However, the spins in GGG are highly anisotropic in the local XY-plane, defined in Fig. 1. This anisotropy could be derived from the dipole exchange interaction, and, along with antiferromagnetic (AFM) near-neighbor (NN) interactions, it is essential for the formation of the director state. Furthermore, as the temperature is reduced below $T < 0.175$ K, GGG enters a spin slush state, a coexistence of longer-range, solidlike and shorter-range, liquidlike correlations [7], which has theoretically been shown to require the inclusion of the very-long-range nature of the dipolar interactions [8] and interhyperkagome exchange.

The director and spin slush states in GGG can be contrasted with the unusual long-range magnetic structures observed in the isostructural compounds $Tb_3Gd_5O_{12}$ (TGG)

---

[*] Corresponding author: pascale.deen@ess.eu

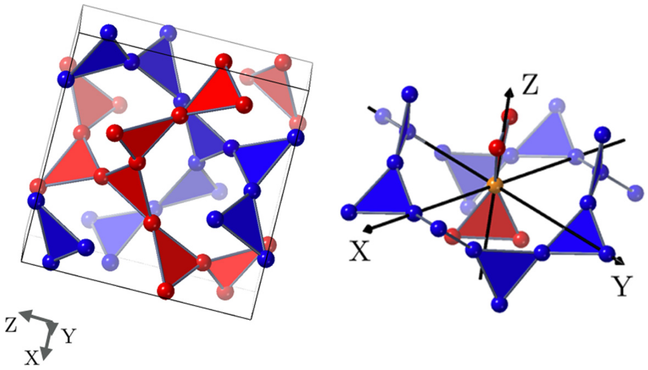

FIG. 1. Left: 24 Yb^{3+} ions in a unit cell of YbGG. Blue and red atoms are Yb ions of the two interpenetrating hyperkagome lattices, respectively. Triangle surfaces between neighboring Yb ions are colored. Right: Local coordinate system of the central orange ion, which is located in the center of the blue 10-ion loop.

and $\mathrm{Er_3Al_5O_{12}}$ (ErAG) [9,10] for $T \leqslant T_{\mathrm{N}} = 0.25$ and 0.8 K, respectively. Both compounds reveal strong local anisotropy resulting in an ordered multiaxis AFM ground state. The ground state in both compounds has been ascribed to the interaction between local anisotropy and long-range dipolar interactions. The effect of dipolar interactions on Ising spins on the garnet lattice has been investigated by Monte Carlo simulations revealing a variety of distinct phases, with the phase diagram strongly affected by the cutoff length of the long-range interactions [11].

The diverse states of matter observed in these 3D compounds depend on the perturbative effect of the anisotropy on the exchange interactions as the rare-earth ions are exchanged in the hyperkagome structure. As such, we now study $\mathrm{Yb_3Ga_5O_{12}}$ (YbGG). Significant spin-orbit interaction from the ground level $^2F_{7/2}$ of the Yb^{3+} ions provides strong anisotropy. The YbGG room-temperature unit-cell lattice parameter, $a = 12.204(4)$ Å, smaller than GGG ($a = 12.385$ Å), ErGG ($a = 12.265$ Å) [10], and TbGG ($a = 12.352$ Å) [9], will affect the dipole exchange interaction. YbGG also presents the possibility to study quantum effects via the effective $S = 1/2$ state due to the effect of the crystal field that acts on the Yb^{3+} $^2F_{7/2}$ state to leave a ground-state Kramers doublet, well isolated from a series of excited Kramers doublets [12]. It is widely expected that quantum effects on a 3D frustrated lattice could lead to novel states of matter, including a quantum spin liquid state, topological order, and quantum entanglement [13].

Previously, heat capacity and magnetic susceptibility measurements on YbGG revealed a λ transition at 0.054 K in addition to a broad peak centered at 0.18 K that extends to 0.6 K [14]. The energy scale of the interactions, extracted by a Curie-Weiss fit, yields $\theta_{\mathrm{CW}} = 0.045(5)$ K, showing dominant FM interactions [14]. The λ transition was assigned to an ordered magnetic state, however this is not confirmed by muon spin resonance and Mössbauer spectroscopy from which a disordered moment has been determined down to 0.036 K [15,16]. The broad peak centered at 0.18 K resembles the specific heat anomaly in GGG indicative of the correlated director state [5].

Here, single-crystal studies on YbGG are presented. We have employed neutron scattering techniques, magnetic susceptibility, and Monte Carlo theoretical analysis to verify the short-range nature of the magnetic structure and spin-spin correlations in YbGG.

II. METHOD

A. Experimental method

A single crystal of YbGG was grown using the floating-zone method in an $\mathrm{Ar} + \mathrm{O_2}$ gas atmosphere at a growth rate of 10 mm/h [17] (see Fig. 15). X-ray Laue diffraction was used to determine the quality of the crystal and to align the samples used for the magnetic properties measurements.

Susceptibility measurements were performed for $1.8 < T < 300$ K at the Technical University of Denmark on a 0.29 g YbGG single crystal using the VSM and AC-MSII options on a Quantum Design Dynacool PPMS. Cold and thermal inelastic neutron spectroscopy and polarized neutron diffraction have been performed on a 1.9 g YbGG single crystal to access the spin-spin correlations and crystal-field levels [18].

Cold neutron spectroscopy was performed at the time-of-flight cold neutron chopper spectrometer (CNCS) at the Spallation Neutron Source, Oak Ridge National Laboratory [19]. Measurements were performed at 0.05 K with incident neutron energies $E_{\mathrm{i}} = 1.55$ and 3.32 meV. The energy resolutions, obtained via the incoherent scattering of a vanadium sample, are $\Delta E_i = 0.0371(5)$ and 0.109(2) meV, respectively, while the Q-resolutions were significantly narrower than the observed features [19]. The scattering plane comprises $(-H, H, 0)$ and $(L, L, 2L)$ with the sample rotated through 180° using 2° steps in order to access a complete rotational plane.

Polarized neutron diffraction was performed using the diffuse scattering spectrometer D7 at the Institut Laue-Langevin (ILL), Grenoble [20], with $E_{\mathrm{i}} = 8.11$ meV and a sample temperature of 0.05 K [21]. D7 provides an energy-integrated measurement. The scattering plane again is comprised of $(-H, H, 0)$ and $(L, L, 2L)$ with the sample rotating through 180° using 1° steps. D7 also provides a Q-resolution that is significantly narrower than the observed features [22]. Calibration for detector and polarization efficiency have been performed using vanadium and quartz, respectively. An empty can measurement at 50 K provides a background subtraction for non-sample-dependent scattering.

The experimental temperature determined on CNCS and D7 was stable and experimentally determined to be 0.05 K, yet the long-range order expected below the λ transition of 0.054 K was not observed. Rare-earth garnet compounds display very low thermal conductivity, particularly at low temperatures. In addition, it is possible that a poor thermal contact between the sample and the thermal bath leads to higher temperatures than provided by thermometry. The specific-heat measurements indicate a short-ranged broad feature for $T < 0.6$ K preceding the λ transition. We believe both the D7 and CNCS datasets probe the short-ranged ordered regime, $0.07 < T < 0.6$ K, since the correlation lengths of the magnetic scattering are short ranged; see Sec. III B.

Thermal inelastic neutron scattering measurements have been performed at the ILL to access the crystal-field levels. We employed the thermal time-of-flight spectrometer, IN4, with an incident energy $E_\mathrm{i} = 113$ meV at a temperature of 1.5 K. Measurements were performed for three different sample orientations with no observed angular dependence [23]. YbGG crystal-field parameters were extracted using the combined data.

B. Analysis method

We have modeled the elastic neutron scattering profiles using the reverse Monte Carlo (RMC) SPINVERT refinement program [24]. The algorithm employs simulated annealing to determine real-space correlations from the neutron scattering data. We simulate cubic supercells with side $L \in [1, 8]$ unit cells, corresponding to a maximum number of $24 \times 8^3 = 12\,288$ spins. To obtain good statistical accuracy, we performed up to 400 refinements and employed an average of these to derive the final correlations. To aid visualization, we employed an interpolation technique frequently used in the SPINVERT program package, *windowed-sinc filtering* [24]. The interpolation allows us to calculate $S(\mathbf{Q})$ at a wave-vector transfer that is not periodic in the supercell [24].

The RMC simulations yield information on the spin correlations, but not on the magnitude of the interactions. To obtain information on the interaction strengths, we have performed Monte Carlo (MC) simulations of an Ising system, with each magnetic site in one of two spin states, with nearest-, next-to-nearest, and long-range dipolar interactions. The crude Ising approximation is motivated on two fronts: (i) The heat capacity measured by Filippi *et al.* [14] shows a qualitative resemblance to that of a long-range dipolar Ising model [11]. (ii) The resultant correlations from the RMC (SPINVERT) algorithm suggest that there is an easy axis along the local z-direction. We have optimized the interaction parameters in the MC simulation to match the experimentally observed heat capacity. From the interactions, we have computed $S(\mathbf{Q})$ scattering profiles to see how they compare with the experimentally observed scattering profile, $S(\mathbf{Q})$. We employed Ewald summation to handle the conditionally convergent dipolar sum.

III. EXPERIMENTAL RESULTS

A. Susceptibility

Susceptibility measurements are presented in Fig. 2 with data taken for $2 < T < 5$ K in the main figure, and $2 < T < 300$ K in the inset figure. Measurements have been performed in an applied magnetic field of 0.1 T. The crystal-field parameters are strong, and consequently only the ground-state doublet is occupied at the lowest temperatures, $T \leqslant 5$ K. In fact, the susceptibility for $T \geqslant 5$ K is well reproduced by crystal-field calculations, neglecting exchange interaction. In these calculations, we use the Stevens parameters as obtained by Pearson *et al.* [12] and verified from our IN4 experiment. Data and model are shown in the inset of Fig. 2 and Fig. 13 with the energy diagram of the determined crystal field level excitations provided in Fig. 14.

The effects of the exchange interaction on the susceptibility become prominent for temperatures below 5 K, when the crystal-field levels no longer dominate. Figure 2 shows a linear fit to the inverse magnetic susceptibility for $T \leqslant 5$ K. A Curie-Weiss temperature $\theta_\mathrm{CW} = -0.2(1)$ K is extracted, indicative of weak AFM interactions. This result is in contrast to the FM interactions determined by Filippi *et al.* [14].

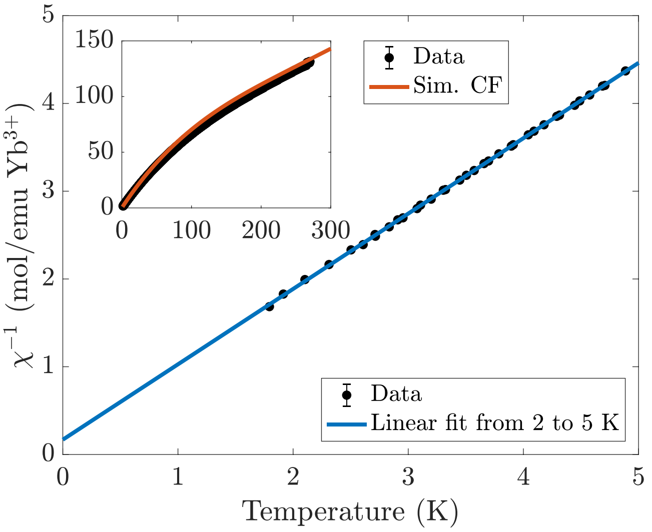

FIG. 2. Inverse susceptibility from PPMS measurements of single-crystal YbGG and a linear fit for $T \leqslant 5$ K yields $\theta_\mathrm{CW} = -0.2(1)$ K. The inset shows the entire inverse susceptibility curve from 2 to 300 K along with the simulated crystal-field contribution as discussed in the text. Error bars are contained within the plotted linewidth.

B. Neutron scattering

1. Thermal neutron spectroscopy

In YbGG, the Yb^{3+} ion is surrounded by eight nearest-neighbor oxygen ions and therefore experiences a dodecahedral local environment and an orthorhombic site point symmetry. The relevant crystal-field levels in YbGG can be most accurately determined via inelastic neutron scattering. Figure 3 presents inelastic neutron scattering data with an incident neutron energy $E_\mathrm{i} = 113$ meV. As expected, three crystal-field excitations are located at energies $E_1 = 63.8(2)$ meV, $E_2 = 74(1)$ meV, and $E_3 = 77(2)$ meV, respectively. The two upper excitations are not fully resolved, with the highest excitation appearing as a shoulder on the second excitation. All three excitations are dispersionless and follow the Yb^{+3} form factor, expected for the single ion effect of a crystal-field excitation. The excitation energies closely match previous experimental [25] and theoretical [12] results, see Appendix A, Table I. Based on these results, we confirm the isolated Γ_7 doublet ground state of the Yb^{3+} spins in YbGG with corresponding g-factors $gx = 2.84$, $gy = 3.59$, and $gz = -3.72$. YbGG is therefore an effective spin $S = 1/2$ system at low temperatures $T \leqslant 5$ K. The crystal-field analysis is further described in Appendix A.

2. Cold neutron spectroscopy

The magnetic energy scales in YbGG are in the mK regime and thus accessible via cold neutron scattering. Figure 4(a) presents the magnetic contribution to the elastic scattering

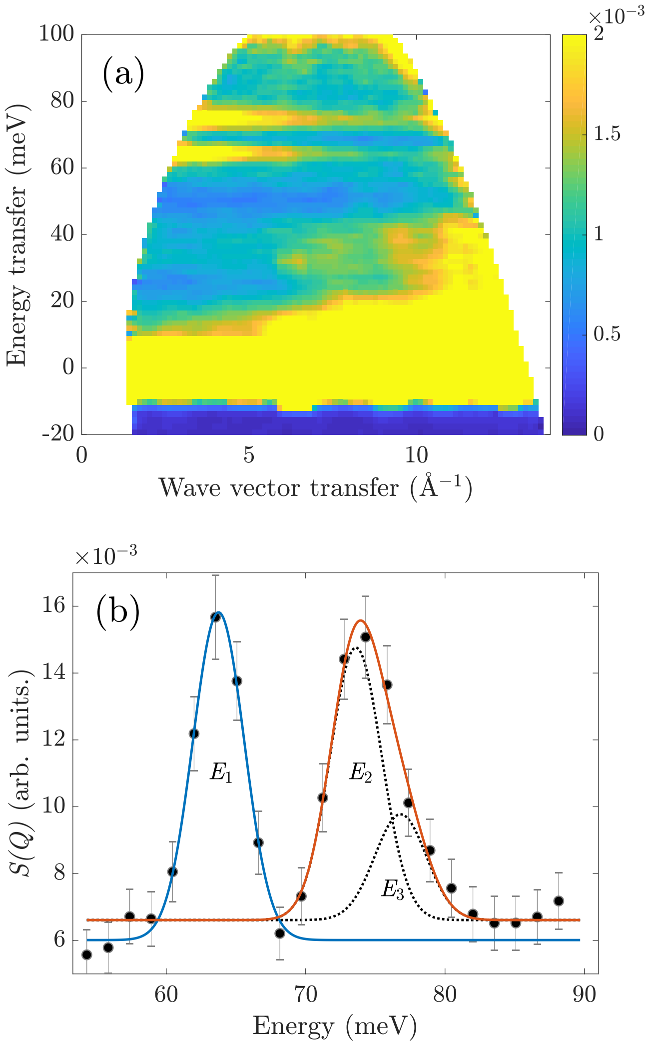

FIG. 3. $S(\mathbf{Q}, \omega)$ of the crystal-field excitations in YbGG showing the excitations well separated from the ground-state doublet. The color bar represents neutron scattering intensity. (b) Integrated data for $4 \leqslant Q \leqslant 5$ Å^{-1}. The two upper excitations ($E2, E3$) are resolved using a double Gaussian line shape.

profile measured at CNCS with incoming neutron energy $E_\mathrm{i} = 1.55$ meV, accessing a low-Q region. The elastic magnetic scattering profile, $S_\mathrm{magff}(\mathbf{Q})$, is extracted from the scattering within the instrumental energy resolution with a background subtraction of equivalent scattering at 13 K, in the paramagnetic regime. In comparison, Fig. 4(b) presents the magnetic contribution measured on D7, $S_\mathrm{mag}(\mathbf{Q})$, of the energy-integrated measurements with $E_\mathrm{i} = 8.11$ meV and thus provides a wider $\mathbf{Q}$ range. The magnetic signal is extracted using XYZ polarization analysis [20] from the spin-flip channel. $S_\mathrm{magff}(\mathbf{Q})$ can therefore be considered as a static contribution. Figure 4(c) shows the relative regions of reciprocal space accessed by the CNCS and D7 datasets and their overlap. The Q range and Q resolution accessed in the experiments vary significantly due to the different incident wavelength. The CNCS dataset, Fig. 4(a), extends across $0.1 < (2H, 2H, 0) \sim 1$ and $0.13 < (L, L, 2L) \sim 1$. In contrast, the D7 dataset extends across $0.3 < (2H, 2H, 0) < 3$ and $0.2 < (L, L, 2L) < 3$. Of course, the relative $\mathbf{Q}$ resolutions also vary significantly affecting boundary conditions and smoothing features in the D7 data that are distinct in the CNCS data. Both datasets show distinct, non-resolution-limited, short-ranged correlated scattering, the

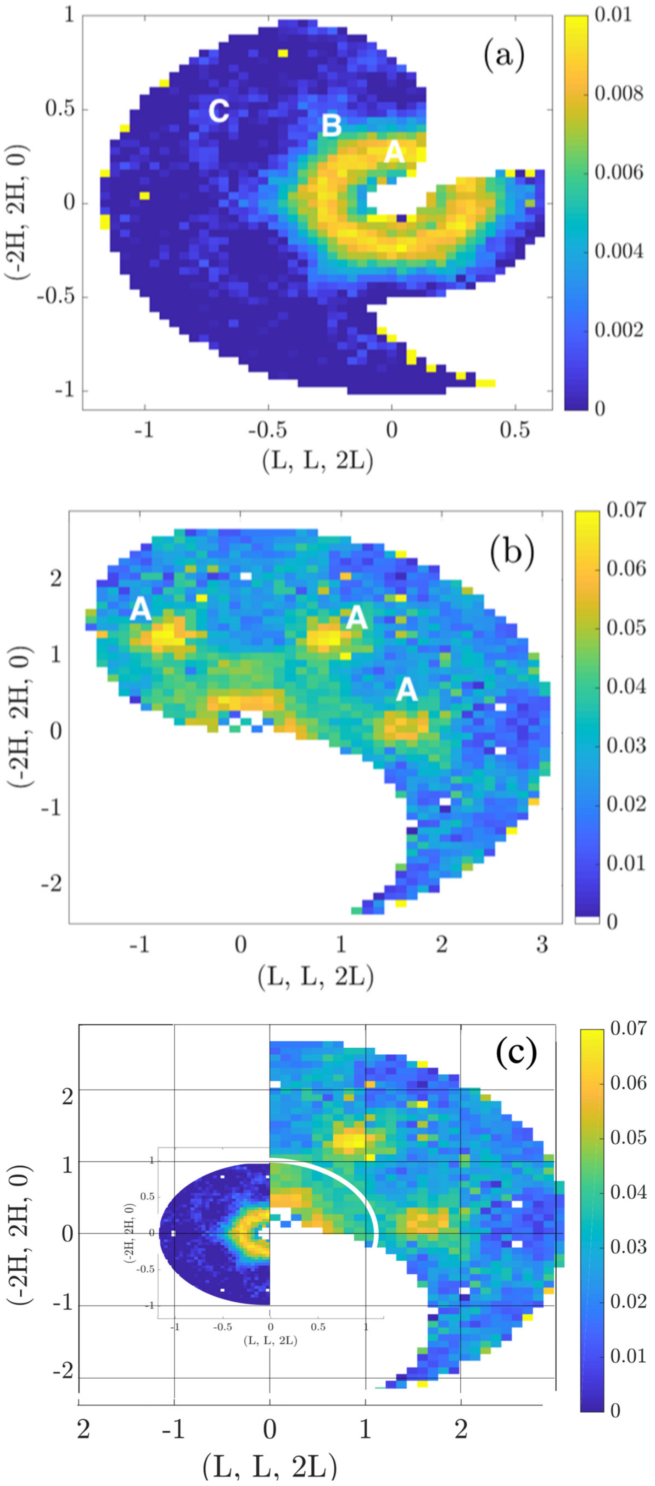

FIG. 4. (a) $S_\mathrm{magff}(\mathbf{Q})$, $E_\mathrm{i} = 1.55$ meV, derived from a high-temperature subtraction. (b) $S_\mathrm{mag}(\mathbf{Q})$, $E_\mathrm{i} = 8.11$ meV. We estimate the sample temperature to be $0.1 < T < 0.2$ K. (c) Relative regions of reciprocal space probed in $S_\mathrm{magff}(\mathbf{Q})$, $E_\mathrm{i} = 1.55$ meV (CNCS) (a) and $S_\mathrm{mag}(\mathbf{Q})$, $E_\mathrm{i} = 8.11$ meV (D7) (b).

Q dependence of which does not follow the magnetic form factor of Yb^{3+}. Indeed, the scattering is correlated with a sixfold symmetry, consistent with the crystalline structure. The short-ranged nature of the magnetic structure factors measured, consistent with the broad feature in the specific-heat data, provides confidence that a sample temperature of $0.1 < T < 0.6$ K was reached. Figure 4(a), with the highest Q resolution, shows clearly a hexagon feature for $|Q| \leqslant 0.63$ Å^{-1}, marked **A**. The reduced intensity for the lowest **Q**, $|Q| \to 0$ Å^{-1}, indicates that these correlations are AFM. A fit to the data with a simple Gaussian line shape, see Appendix C, shows a peak in intensity at $|Q| = 0.30(3)$ Å^{-1} corresponding to a lattice spacing $d = 2\pi/Q = 20(2)$ Å, and a correlation length of 12(2) Å, as determined from the peak full width at half-maximum (FWHM). Weak circular features extend from the edges of the hexagon, **B** → **C**. The low **Q** hexagon feature is also visible in the D7 data but is limited due to reduced **Q** resolution and detection boundaries. The higher **Q** D7 data show three distinct diffuse peaks [Fig. 4(b)], **A**, centered at $|Q| = 1.95(8)$ Å^{-1}, corresponding to a lattice spacing of $d = 3.2(1)$ Å, with a correlation length of 4(0.6) Å. These peaks, **A**, also follow the sixfold symmetry of the crystalline structure. In a simplistic manner, considering the Q positions and correlation lengths, one could assign the low Q hexagonal feature to a looped structure encompassing 10 ions extending throughout the unit cell while the higher Q features are derived from near-neighbor exchange.

IV. DATA MODELING

A. Reverse Monte Carlo

We have performed RMC simulations on $S_{\mathrm{magff}}(\mathbf{Q})$ and $S_{\mathrm{mag}}(\mathbf{Q})$. It is, however, not possible to directly minimize the 2D $S(\mathbf{Q})$ of the single-crystal results, since the RMC simulations leave all points in **Q** outside the $(-2H, 2H, 0)$, $(L, L, 2L)$ scattering plane unconstrained and can thus lead to errors. In this work, we have mitigated the possibility of erroneous minimization with three approaches. First, comparing data from several experiments with various incident energies and thus energy and **Q** resolution. Second, creating an isotropic scattering distribution from the measured 2D $S(\mathbf{Q})$ through integration of all points with similar $|Q|$, which we shall term powder diffraction pattern $S(Q)$ (see Fig. 5), and deriving a single-crystal pattern, $S(\mathbf{Q})$, from the RMC spin configuration obtained. Third, we use the average of 400 RMC minimizations to obtain good statistics on the spin correlations. We accept that the data presented are only an approximation of the true correlations. By testing several extrapolation techniques in addition to extracting RMC from various datasets with different incident energies and averaging across 400 RMC minimizations, we believe that the results are stable and that some variation in the assumed extrapolation will not affect the fundamental structure of the solution. The exact procedure is outlined in Appendix D.

Figure 5 compares the result of the RMC simulation with the $S(Q)$ powder diffraction pattern from CNCS, $S_{\mathrm{magff}}(Q)$ (a) and D7, $S_{\mathrm{mag}}(Q)$ (b). Figure 5(a) shows an excellent reproduction of powder data for all Q. In contrast, the reproduction of the D7 powder diffraction pattern in Fig. 5(b) provides reasonable agreement only for $Q \leqslant 0.8$ Å^{-1}. For higher Q, the RMC model shows similar features, but with discrepancies in the intensities. We do not simultaneously minimize the CNCS and D7 datasets since this would introduce an additional parameter representing the importance of each dataset and the various regions of reciprocal space. Our approach is minimalistic and shows the extreme cases when minimizing to the respective datasets.

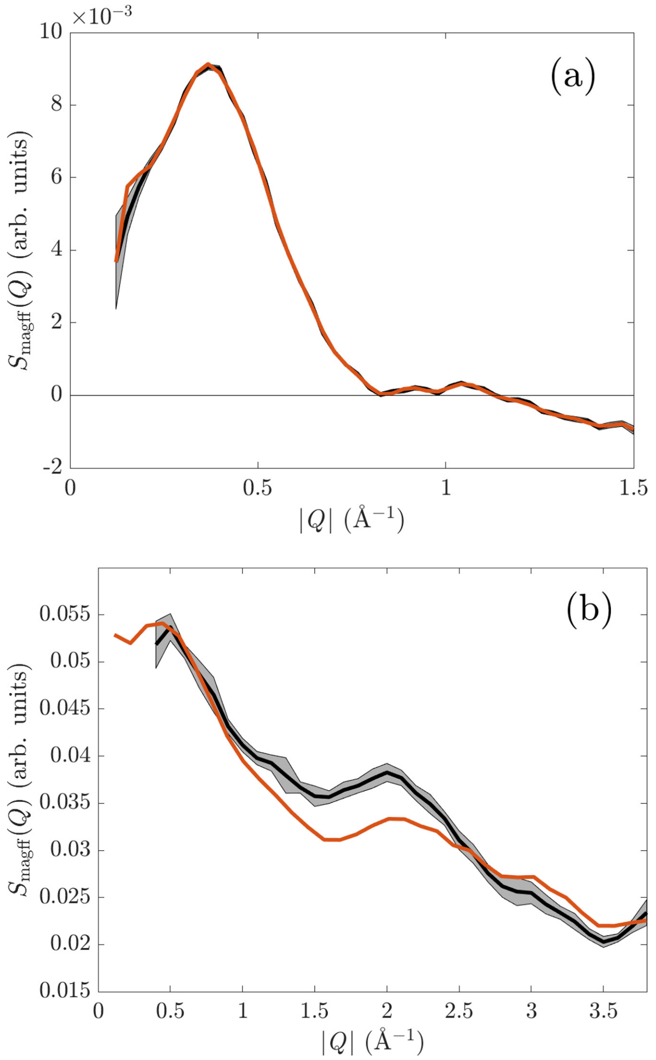

FIG. 5. Comparison of $S(Q)$ RMC simulation (red) and powder averaged data (black). (a) Powder averaged CNCS data and RMC $S(Q)$ simulation. (b) Powder averaged D7 data and RMC $S(Q)$ simulation.

The spin structure derived from the RMC $S(Q)$ powder refinement is used to recalculate the 2D magnetic scattering profiles, $S_{\mathrm{magff}}(\mathbf{Q})$ or $S_{\mathrm{mag}}(\mathbf{Q})$, and subsequently compared to experimental data; see Fig. 6 for CNCS $S_{\mathrm{magff}}(\mathbf{Q})$ data (a) and D7 $S_{\mathrm{mag}}(\mathbf{Q})$ data (b). The RMC $S_{\mathrm{magff}}(\mathbf{Q})$ of the CNCS data contains the correct crystal symmetry and accurately reproduces all of the main features at the correct **Q** positions, including the low-Q hexagon and the higher-Q features extending from the sides of the hexagon. In contrast, the comparison in Fig. 6(b), of the D7 data and the corresponding RMC $S_{\mathrm{mag}}(\mathbf{Q})$, is much less accurate. Although the main features are reproduced, the broad Q features are slightly offset.

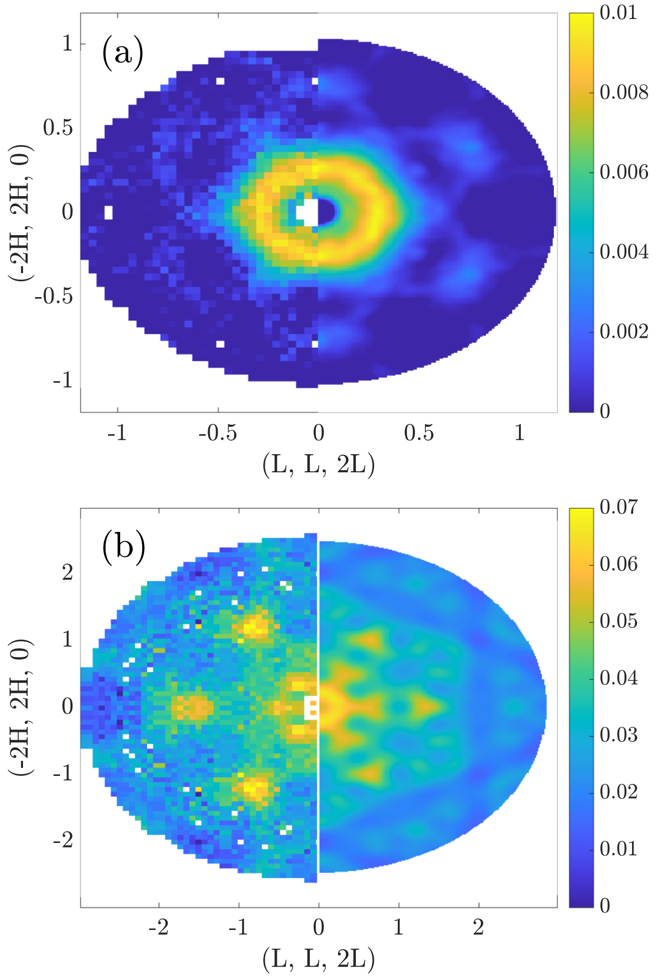

FIG. 6. Comparison of experimental data and RMC fit (left and right, respectively). (a) CNCS $S_{\mathrm{magff}}(\mathbf{Q})$, (b) D7 $S_{\mathrm{mag}}(\mathbf{Q})$. The color bar represents scattering intensity.

There are several subtle differences between the CNCS and D7 neutron scattering intensities that may give rise to the difference in accuracies. The CNCS magnetic scattering intensity, $S_{\mathrm{magff}}(\mathbf{Q})$, is obtained via the subtraction of high-temperature scattering from base temperature scattering. The high-temperature scattering provides an intense magnetic form factor, and $S_{\mathrm{magff}}(\mathbf{Q})$ can result in negative intensities. This is considered in the RMC. D7 magnetic scattering, $S_{\mathrm{mag}}(\mathbf{Q})$, is extracted using XYZ polarization. The determination of $S_{\mathrm{mag}}(\mathbf{Q})$ in this manner assumes that the net moment of the compound is zero, as is the case for paramagnetic systems or powdered antiferromagnet compounds. A ferromagnetic signal would induce some depolarization of the scattered polarization. Using this equation for the case of a single crystal makes an implicit assumption that there is a net zero averaged moment with no symmetry breaking such that the magnetic cross section is isotropic with magnetic components of equal magnitude projected along the three orthogonal directions. We made these assumption since (a) we did not observe any depolarization of the scattered beam, (b) only short-range order was observed, and (c) we had prior knowledge of the director state, which provides an isotropic spin distribution to a first approximation. However, the incoherent scattering signal, expected to be homogeneous in $\mathbf{Q}$, contains weak hexagonal features reminiscent of the magnetic signal that affect only the peak intensities of $S_{\mathrm{mag}}(\mathbf{Q})$. RMC optimizes directly to $S(Q)$ and is sensitive to such relative changes. We suggest that these small variations give rise to the differences observed between the CNCS and D7 RMC, and they are the reason for the poorer simulations of the D7 data. Nevertheless, the resultant D7 RMC spin structure is consistent with that determined from the CNCS RMC and provides confidence in our results.

To interpret the RMC results, the spin distributions and correlations are investigated. In the following, only CNCS RMC simulations are presented, but despite the less perfect correspondence between RMC results and D7 data, there is strong equivalence between the spin distributions and correlations obtained from the RMC derived spin structure of all datasets; see Appendix D. The resultant D7 RMC spin structure is consistent with that determined from the CNCS RMC, and distinctly different from the spin structure determined for GGG; see Fig. 20. The similarities between the spin structures extracted from different experiments with very different Q ranges and resolutions provide confidence in our results. Figure 7(a) presents the spin probability distribution, derived from RMC, in the local coordinate system showing an easy axis along the local z-direction, the axis that connects the centers of two adjacent triangles within the crystal structure; see Fig. 1 (right). Figure 7(b) presents the average spin-spin correlations $\langle \mathbf{S}(0) \cdot \mathbf{S}(r) \rangle$ as a function of spin-spin distance. NN correlations are on average positive and thus FM with an average angle of 73° between neighboring spins. This is in contrast to the AFM NN correlations and strong planar anisotropy in the local XY plane observed for GGG [5]. Figure 7(b) further shows that spins in YbGG are correlated AFM across the loop, consistent with FM NN correlations, and they correspond to the spatial scales extracted from the low-Q hexagon, Fig. 4(a). This final spin structure results in a director state. We find that the local easy axis of the directors is along the local z-direction [see Fig. 8(a)], directly equivalent to the director state found in GGG. The director state is further supported by the magnetic excitations observed in the extended CNCS dataset; see Fig. 23. Three dispersionless low-lying excitations are observed at 0.06, 0.1, and 0.7 meV entirely consistent with dispersionless excitations observed in GGG and assigned to the director state [6,26]. Detailed analysis of the excitation spectra will be published elsewhere.

We next investigate the correlations between the directors, $\mathbf{L}$, Eq. (1). The radial correlation function of the directors, $g_L = 2\langle \hat{\mathbf{L}}(0) \cdot \hat{\mathbf{L}}(r) \rangle - 1$, is equal to -1 if, on average, the loop directors are orthogonal to each other and to $+1$ if collinear. Figure 8(b) shows the radial correlation function and reveals a predominantly collinear director state within the first unit cell, 12.2 Å. However, unlike the long-range correlated state of GGG, the directors in YbGG correlate weakly beyond the first unit cell.

The resultant spin configuration and director state in YbGG are presented in Fig. 9, which shows FM correlated NN spins along the local easy axes as well as the resultant director of the loop.

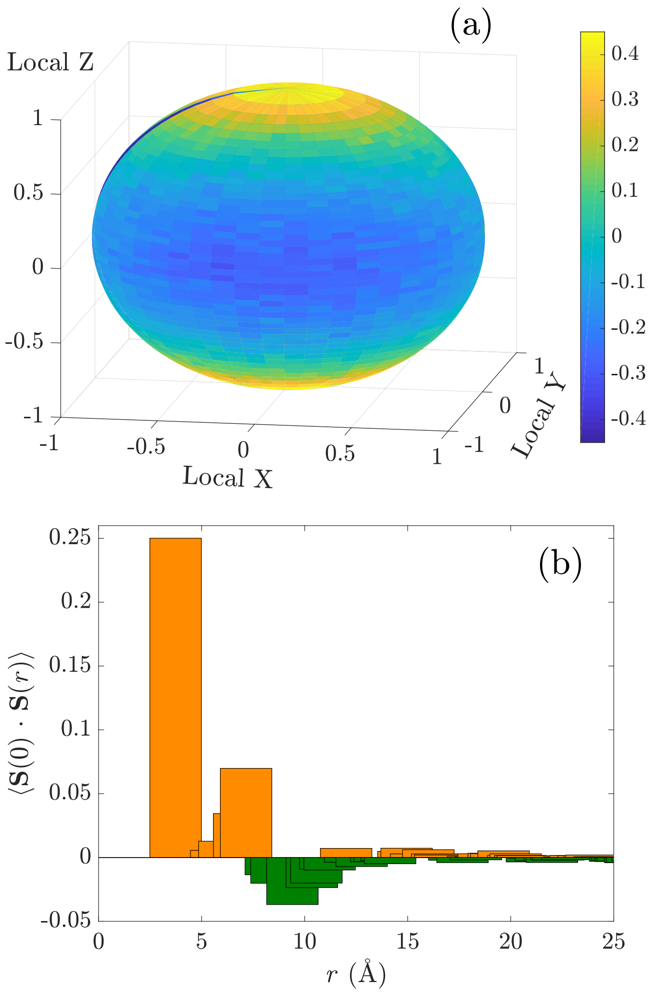

FIG. 7. (a) Stereographic projection of the spin distribution in the local coordinate system with a log color scale. The spins show an easy axis along the local z-direction. (b) Radial dependence of $\langle \mathbf{S}(0)\cdot\mathbf{S}(r)\rangle$. Positive scalars orange, negative scalars green.

B. Monte Carlo

To gain a further grasp of the absolute energy scale of the spin-spin couplings in YbGG, we have investigated classical Heisenberg and Ising models with anisotropy along the local z-direction motivated by the RMC results. In Appendix E we present a short discussion of an anisotropic Heisenberg model. In the current text, we present an Ising model optimized for the heat-capacity measured in experiment [14]; see Fig. 10(a). We use the term “Ising model” to indicate that the spins have two states, pointing along the local z-direction either into or out of the triangles; see Fig. 9. The resultant exchange parameters are used to recalculate S($\mathbf{Q}$), and these are compared to the experimental $S_{\text{mag}}(\mathbf{Q})$, Fig. 10(b). We compare to $S_{\text{mag}}(\mathbf{Q})$ from D7 due to the extended $\mathbf{Q}$ range provided in this dataset. In GGG the relevant Hamiltonian in the director phase includes the NN exchange J_1, the next-nearest-neighbor (NNN) exchange J_2, and the dipolar interaction D, with interhyperkagome coupling J_3 only relevant at lower temperatures to drive the spin slush state [8]. As such, the relevant Hamiltonian for

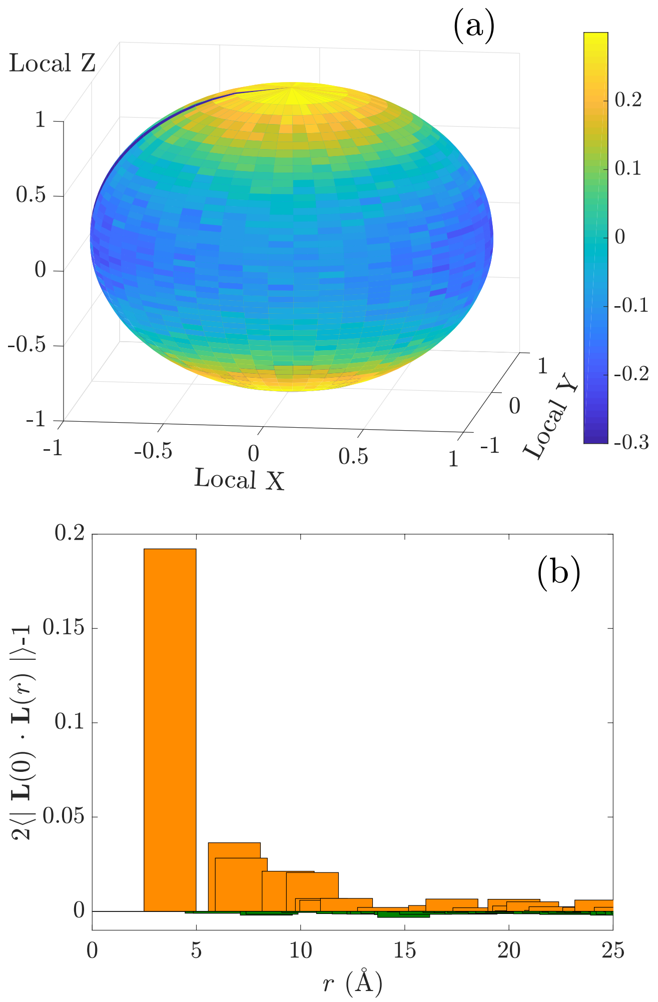

FIG. 8. (a) Stereographic projection of the director distribution in the local coordinate system with a log color scale. (b) Radial correlation function of the directors. Positive scalars are plotted in orange, negative scalars are plotted in green.

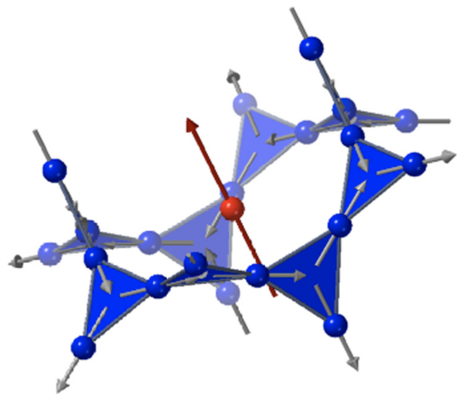

FIG. 9. A 10-spin-loop together with a single ion from the opposite hyperkagome lattice (central, red). The blue spheres depict Yb^{3+} ions, while the red sphere can be considered as the net average magnetic moment of the 10-ion loop, the director. Local spin distributions peak along the local z-direction (gray arrows), which connects the centers of adjacent triangles. The local spin structure is presented with spins point along the easy axis. The director distribution (red arrow) peaks along the local z-direction.

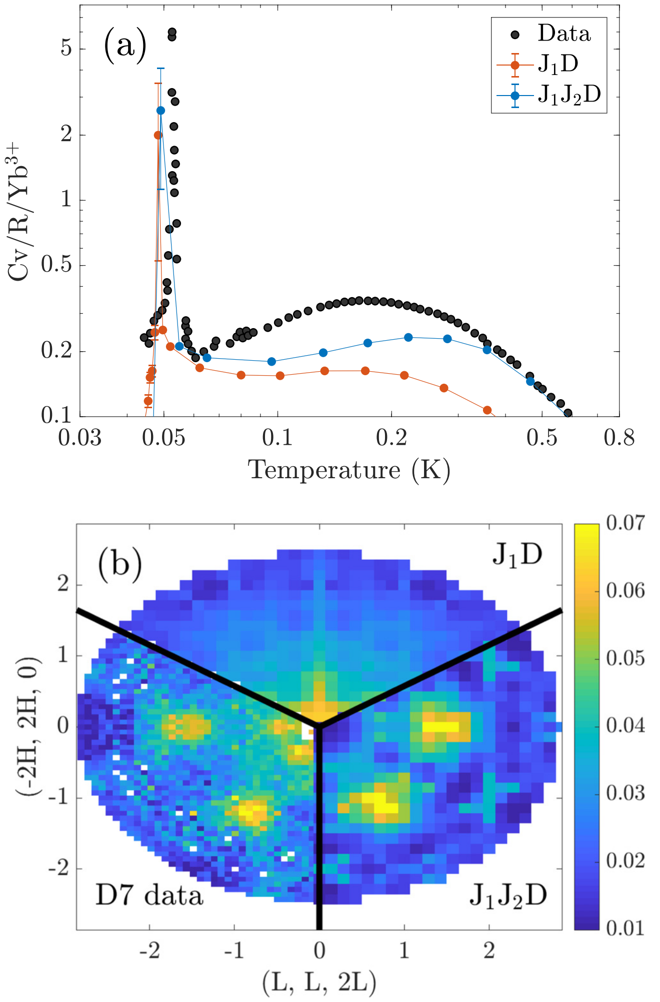

FIG. 10. (a) Heat-capacity data [14] with simulated heat capacity for the J_1D and J_1J_2D models. (b) Simulated $S(\mathbf{Q})$, $T = 0.2$ K, for the J_1D model and the J_1J_2D model with $S_{\rm mag}(\mathbf{Q})$. The color bar represents $S(\mathbf{Q})$.

YbGG in the director state is

$$\mathcal{H} = J_1 \sum_{\langle i,j \rangle} \mathbf{S}_i \cdot \mathbf{S}_j + J_2 \sum_{\langle\langle i,j \rangle\rangle} \mathbf{S}_i \cdot \mathbf{S}_j + Da^3 \sum_{i<j} \left(\frac{\mathbf{S}_i \cdot \mathbf{S}_j}{|\mathbf{r}_{ij}|^3} - 3\frac{(\mathbf{S}_i \cdot \mathbf{r}_{ij})(\mathbf{S}_j \cdot \mathbf{r}_{ij})}{|\mathbf{r}_{ij}|^5} \right). \quad (2)$$

Here, a is the nearest-neighbor distance, $\mathbf{r}_i$ is the position of the classical Ising spin $\mathbf{S}_i$ oriented along the local z-direction, and $\mathbf{r}_{ij} = \mathbf{r}_i - \mathbf{r}_j$. $\langle \cdot \rangle$ and $\langle\langle \cdot \rangle\rangle$ denote summation over NN and NNN, respectively.

Two distinct models are simulated. First, we simulate a spin structure with J_1 and D only, a J_1D model. Second, we add J_2 in a J_1J_2D model. In principle, the dipolar interaction strength can be calculated explicitly from the magnetic moment μ and inter-atomic distances, $D = \frac{\mu_0\mu^2}{4\pi a} = 0.24$ K for $\mu = 4.3$ Bohr magnetons [27]. However, the magnetic moment of Yb^{3+} is strongly affected by the crystal field, which motivates varying the strength of the dipolar interaction in addition to the exchange interactions. The resultant magnetic moment derived within the J_1D model is $\mu = 4.19$ Bohr magnetons and $\mu = 3.88$ Bohr magnetons for the J_1J_2D model.

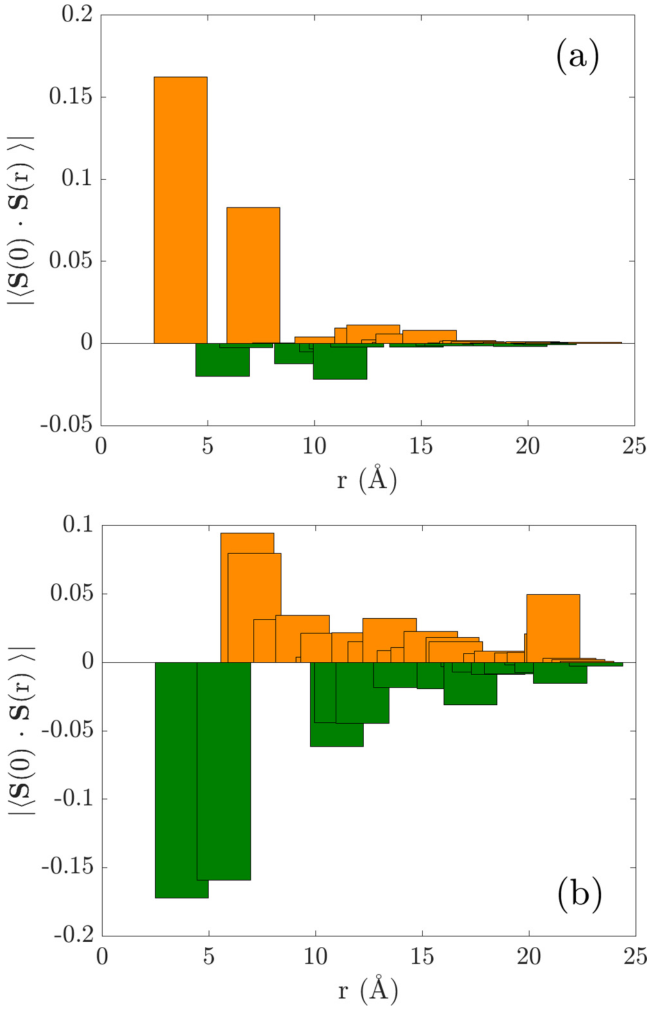

FIG. 11. Correlation functions for MC simulations. (a) J_1D model, (b) J_1J_2D model. Positive scalars are colored orange and negative scalars are colored green.

Figure 10(a) shows the resultant heat capacities for the two models with optimized parameters $J_1 = 0.6$ K, $D = 0.21$ K for the J_1D model, and $J_1 = 0.72$ K, $J_2 = 0.12$ K, and $D = 0.18$ K for the J_1J_2D model. The λ transition is well described by both models, and would correspond to long-range ordering due to dipolar interactions if YbGG was an Ising system [11]. Both models reproduce the broad specific-heat anomaly, albeit with an overall suppression. The J_1J_2D model has better agreement with data above the λ transition, and above 0.4 K the model coincides with data.

Figure 10(b) compares $S_{\rm mag}(\mathbf{Q})$ and the resultant $S(\mathbf{Q})$ for the J_1D and J_1J_2D models. Both models provide features that are consistent with the data. The low-$\mathbf{Q}$ region is well reproduced by the J_1D model, while this is not captured by the J_1J_2D model. In contrast, the diffuse peaks at higher $\mathbf{Q}$ are reproduced by the J_1J_2D model. These peaks do not appear in the J_1D model.

Figure 11 presents the radial dependence of the spin-spin correlations for (a) the J_1D model and (b) the J_1J_2D model.

Interestingly, the J_1D model provides FM NN correlations, while the correlations across the loop are negative, and thus AFM. Correlations are not significant beyond the unit-cell distance. The J_1J_2D model has AFM NN correlations, with FM correlations across the 10-ion loop. In the J_1J_2D model, the correlations remain significant for distances up to 25 Å.

V. DISCUSSION

We have studied the magnetically short-range-ordered state in YbGG, $0.1 < T < 0.6$ K. We have revisited the crystal-field excitations using inelastic neutron scattering, and we show that for $T \leqslant 5$ K the Yb^{3+} ions can be considered with an effective $S = 1/2$ ion as spin-spin interactions dominate. In this description, we obtain a negative Curie-Weiss temperature of $-0.2(1)$ K indicative of AFM interactions. Previous susceptibility measurements by Filippi *et al.* [14] in the low-temperature regime yielded a positive Curie-Weiss temperature of $+0.045(5)$ K indicative of FM interactions. Although these present inconsistent results, all susceptibility measurements agree that the spin-spin interactions are in the mK range and several orders of magnitude smaller than the crystal-field energies.

The magnetic scattering profiles are determined in different manners from two different experiments: (i) via neutron polarization analysis $S_{\mathrm{mag}}(\mathbf{Q})$, and (ii) via a high-temperature paramagnetic subtraction, $S_{\mathrm{magff}}(\mathbf{Q})$. These two techniques provide different scattering profiles with PA providing an absolute magnetic scattering profile and the high-temperature subtraction oversubtracting the form-factor contribution of the paramagnetic scattering. The datasets vary in $\mathbf{Q}$ and energy resolutions. We compare the energy-resolved and energy-integrated datasets directly since the static components of these datasets dominate. $S_{\mathrm{mag}}(\mathbf{Q})$ and $S_{\mathrm{magff}}(\mathbf{Q})$ present short-range correlated scattering with correlation lengths varying from near-neighbor correlations to 20 Å thereby providing confidence that we are probing the magnetically short-range-ordered regime.

We have performed RMC simulations to extract the spin configurations from each dataset considering the difference in $S_{\mathrm{mag}}(\mathbf{Q})$ and $S_{\mathrm{magff}}(\mathbf{Q})$. The RMC simulations, for three distinct datasets, provide spin configurations that are rather similar to each other but very distinct from the spin distribution found in the isostructural compound GGG.

We compare the distribution of the azimuthal angle of the spins within a 10-ion loop, and we find that, for YbGG, each spin is peaked along the tangent of the loop, along the local z-direction, and with FM near-neighbor correlations. In contrast, the spin structure for GGG provides a distribution perpendicular to the 10-ion loop. It is unclear what the origin of the significant anisotropy in YbGG along the local z-direction might be. Pearson *et al.* [12] calculated the diagonal elements of the crystal-field g-factors and found these to be $g = (2.84, 3.59, -3.72)$, thus showing a slightly larger contribution along the local z-direction, but not significant enough to provide strong anisotropy.

Extracting the spin structure across the 10-ion loop provides a director state with an easy axis along the local z-direction, comparable to the easy axis of the director state in GGG. The resultant director state of the 10-ion loop is also, similar to GGG, strongly anisotropic, but unlike GGG it is not long-range-ordered.

We have studied a J_1D and J_1J_2D model using MC simulations for specific-heat data and determined a range for the exchange interactions, J_1, J_2, and D. Both models providing convincing reproductions for the heat-capacity data reproducing the short-range-ordered feature for $0.06 < T < 0.6$ K and the long-range λ transition around 0.05 K. In GGG the relative J_1/D value is $J_1/D = 0.107/0.0457\ \mathrm{K} = 2.34$, while our MC simulations for YbGG yield $2.86\ (0.6/0.21\ \mathrm{K}) < J_1/D < 3.88\ (0.72/0.18\ \mathrm{K})$.

The exchange interactions determined by MC are used to recalculate $S_{\mathrm{mag}}(\mathbf{Q})$ using the relevant Hamiltonian for the J_1D and J_1J_2D models. The resultant scattering patterns are comparable, in part, to the experimental data. However, our data and models provide no unique interpretation of the complete dataset. The J_1D model, with ferromagnetic near-neighbor spin-spin correlations, captures the low-$\mathbf{Q}$ neutron scattering data while the J_1J_2D, with antiferromagnetic near-neighbor spin-spin correlation, closely captures the data at higher $\mathbf{Q}$. A more complex Hamiltonian is required to fully describe the magnetic state of YbGG, and this will be the focus of further studies.

VI. CONCLUSION

In conclusion, we have probed the enigmatic magnetic state of YbGG and have been able to deduce the magnetic correlations using a combination of RMC and MC to describe heat capacity and neutron scattering results. We derive the magnitude of the near-neighbor exchange interactions $0.6 < J_1 < 0.7$ K, $J_2 = 0.12$ K, and the magnitude of the dipolar exchange interaction, D, in the range $0.18 < D < 0.21$ K. Magnetic correlations develop below 0.6 K, in line with a broad feature in the specific-heat data. Through RMC simulations we find a spin structure consistent with a director state, similar to that found in GGG for $T < 1$ K with an associated broad feature in the specific heat. However, in YbGG, the director correlations are short-ranged. The broad dataset cannot be fully described within the current, rather basic, model, but it provides an avenue for further studies. We welcome further elaborate insight.

ACKNOWLEDGMENTS

L.S., R.E., and I.M.B.B. were funded by Nordforsk through the NNSP project. This project was further supported by the Danish Agency for Science and Innovation though DANSCATT and Interreg. The work at the University of Warwick was funded by EPSRC, UK through Grant No. EP/T005963/1. This research used resources of the Spallation Neutron Source, a DOE Office of Science User Facility operated by Oak Ridge National Laboratory. We thank ILL and SNS for providing the facilities to perform the neutron scattering experiments. The authors would like to thank J. Jensen for valuable discussions.

This manuscript has been authored by UT-Battelle, LLC under Contract No. DE-AC05-00OR22725 with the US Department of Energy. The U.S. Government retains and the publisher, by accepting the article for publication,

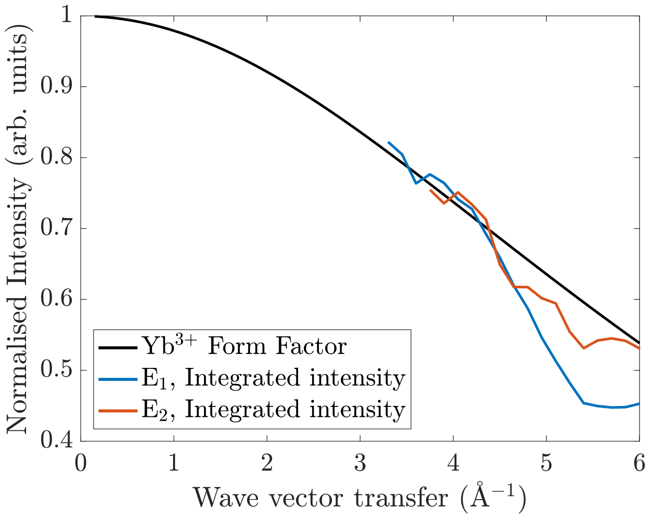

FIG. 12. The integrated intensities of E_1 and E_2 from the IN4 measurements show good qualitative agreement with the calculated form factor of Yb^{3+}.

acknowledges that the U.S. Government retains a nonexclusive, paid-up, irrevocable, worldwide license to publish or reproduce the published form of this manuscript, or allow others to do so, for U.S. Government purposes. The Department of Energy will provide public access to these results of federally sponsored research in accordance with the DOE Public Access Plan [29].

APPENDIX A: CRYSTAL FIELD

The inelastic neutron scattering results from IN4 (see Figs. 3 and 12) confirmed that YbGG has very strong crystal-field levels and verified the excitation energies of the crystal-field levels determined experimentally by Buchanan *et al.* [25] and theoretically by Pearson *et al.* [12]. In the calculations, a crystal-field Hamiltonian,

$$\mathcal{H}_{\mathrm{CF}} = \sum_i \sum_{lm} A_{lm} \langle r^l \rangle \alpha_l \left(\frac{2l+1}{4\pi} \right)^{1/2} \tilde{O}_l^m(J) \tag{A1}$$

$$= \sum_i \sum_{lm} B_l^m O_l^m(J), \tag{A2}$$

was optimized. Here, $\tilde{O}_l^m(J)$ are the Racah operators, which transform like spherical harmonics, while $O_l^m(J)$ are the Stevens operators, which transform like tesseral harmonics. α_l is the Stevens factor, which depends on the form of the electronic charge cloud of the single ion, A_{lm} is the effective charge distribution of the surrounding ions projected into the Y_l^m-basis, and B_l^m are the Stevens parameters. Since both α_l and $\langle r^l \rangle$ are well-defined from the system, there is direct correspondence between the A_{lm} parameters and the B_l^m parameters.

Yb^{3+} is a rare-earth ion with $4f$ electrons as the outer shell. Consequently, $l \leqslant 7$, but in order to obey time-reversal symmetry, only even l and m are allowed, and the crystal symmetry excludes negative m. Consequently, there are nine Stevens parameters with $l = 2$, 4, and 6, and $m \leqslant l$. Pearson *et al.* [12] calculated the Stevens parameters using a point charge model approximation and later fitted the obtained parameters to experimental data of near-infrared spectroscopy and susceptibility measurements [25]. Table I shows the resulting Stevens parameters, which have been calculated based on the A_{lm} parameters presented by Pearson *et al.*

TABLE I. Stevens parameters obtained from Refs. [12,25].

	Stevens parameters (meV) [12]
B_{20}	−0.267
B_{22}	1.097
B_{40}	0.0368
B_{42}	−0.0459
B_{44}	−0.1291
B_{60}	0.000870
B_{62}	−0.008205
B_{64}	0.01460
B_{66}	−0.004138

The susceptibility has been simulated using the McPhase program with the Stevens parameters listed in Table I, using the values determined by Buchanan and Pearson [12,25], see Fig. 13, without including any spin-spin interactions, such as exchange or dipolar interactions. Consequently, the simulated susceptibility, which is presented in Fig. 13, only contains the crystal-field contribution to the susceptibility. The experimental data are well reproduced. It is thus possible to describe the susceptibility using only the crystal-field considerations in the high-temperature regime where the crystal-field splitting, see Fig. 14, is several orders of magnitude larger than the spin-spin interactions found from θ_{CW}.

APPENDIX B: CRYSTAL

A single crystal of YbGG has been grown using the floating zone method in Ar + O$_2$ gas mixture at a growth rate of 10 mm/h [17]. The results achieved thus far indicate that the crystal's quality and size are suitable for magnetic frustration studies using neutron diffraction (see Fig. 15). Synthesizing

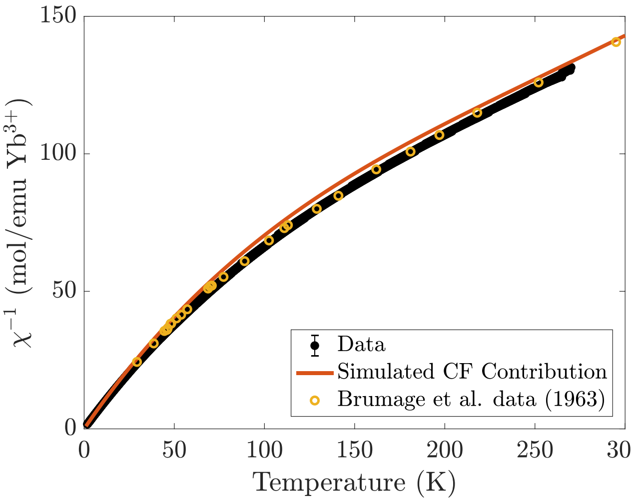

FIG. 13. Temperature dependent magnetic susceptibility with the simulated crystal field contribution as simulated in this work and by Brummage *et al.* [28].

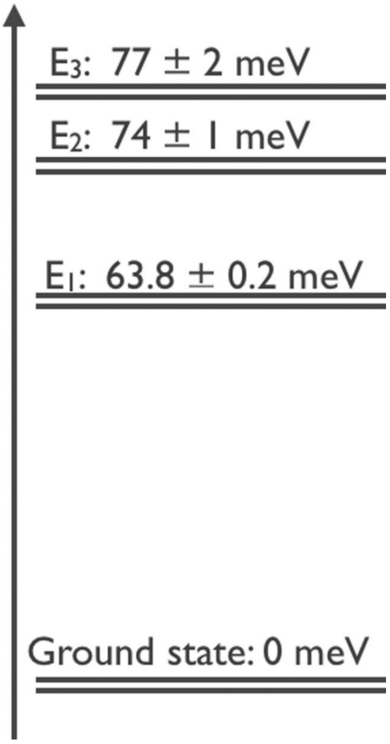

FIG. 14. Energy diagram of crystal-field levels obtained from inelastic neutron scattering measurements on IN4.

crystals with an adequate volume for neutron scattering is complex due to the weak scattering cross sections and thus the requirement for large (cm^3) single crystals. As such, the growth of a large single crystal is a success. X-ray Laue diffraction after growth determined sample crystallinity and orientation. Future work will include a detailed analysis of the effects of stoichiometry, vacancies, and site mixing on the magnetic behavior of YbGG garnets.

FIG. 15. Crystal used for neutron scattering experiments and susceptibility measurements.

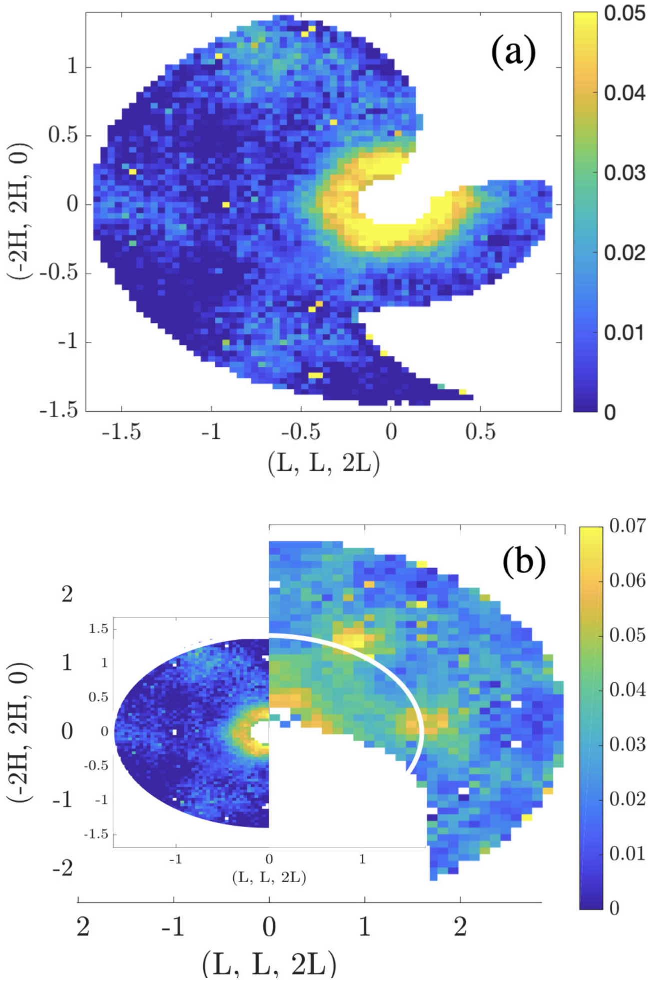

FIG. 16. (a) Magnetic contribution to $S(Q, E = 0)$, measured at CNCS with $E_\mathrm{i} = 3.32$ meV. (b) The relative reciprocal space accessed for the CNCS, the $E_\mathrm{i} = 3.32$ meV dataset, and the D7 dataset.

APPENDIX C: ELASTIC NEUTRON SCATTERING DATA AND LINECUTS

This Appendix contains elastic 2D data along with Gaussian fits of linecuts through the elastic neutron scattering data to quantify the observed diffuse features. Figure 16 shows the 2D $S(\mathbf{Q}, E = 0)$ data obtained from the CNCS measurements with $E_\mathrm{i} = 3.32$ meV. Figure 16 contains only the magnetic contribution derived by subtracting a 13 K dataset from a 0.05 K dataset. The signal-to-noise ratio in the data is lower than the two other elastic neutron scattering datasets presented in the main text.

This is supported by the data in Fig. 17, which show various linecuts from the two-dimensional neutron scattering data together with Gaussian fits (fit parameters are shown in Table II).

Figure 17(a) shows a Gaussian fit to a linecut through the CNSC data with $E_\mathrm{i} = 1.55$ meV, where $(-2H\ 2H\ 0) = (0\ 0\ 0)$. Low-Q hexagon peaks are seen at $|Q| = 0.30 \pm 0.03$ Å^{-1}, corresponding to an equivalent magnetic lattice spacing of $d = 20 \pm 2$ Å. The correlation length, obtained by FWHM $= 0.41 \pm 0.07$ Å^{-1}, becomes 12 ± 2 Å.

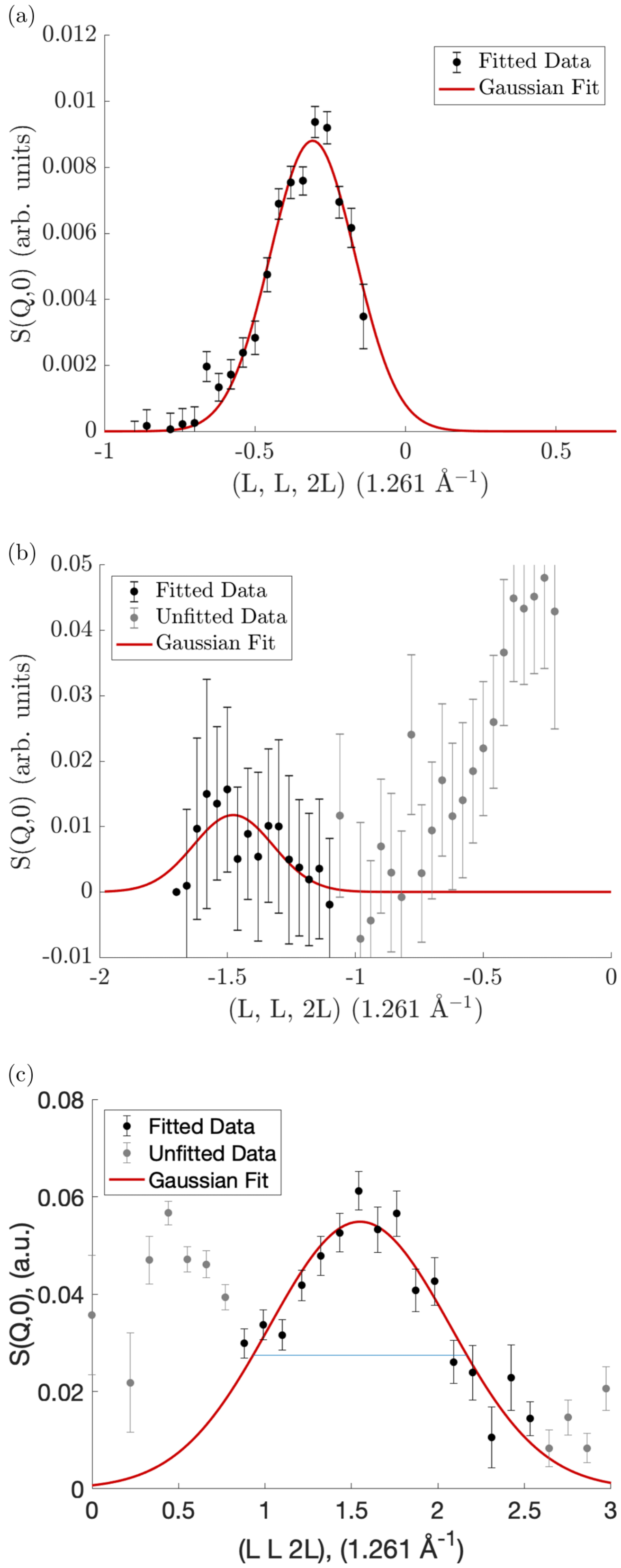

FIG. 17. Linecuts from the two-dimensional neutron scattering data together with Gaussian fits. (a) CNCS data, $E_\mathrm{i} = 1.55$ meV. (b) CNCS data, $E_\mathrm{i} = 3.32$ meV. (c) D7 data, $E_\mathrm{i} = 8.11$ meV. Fit parameters are presented in Table II.

TABLE II. Fit parameters of the three Gaussian fits in Fig. 17.

$E_\mathrm{i} = 1.55$ meV	
Gaussian peak position	0.30 ± 0.03 Å^{-1}
Distance (from peak pos)	20 ± 2 Å
FWHM	0.52 ± 0.09 Å^{-1}
Correlation length (from FWHM)	12 ± 2 Å
$E_\mathrm{i} = 3.32$ meV	
Gaussian peak position	1.86 ± 0.09 Å^{-1}
Distance (from peak pos)	3.4 ± 0.2 Å
FWHM	0.55 ± 0.25 Å^{-1}
Correlation length (from FWHM)	11.5 ± 5.2 Å
$E_\mathrm{i} = 8.11$ meV	
Gaussian peak position	1.95 ± 0.08 Å^{-1}
Distance (from peak pos)	3.2 ± 0.1 Å
FWHM	1.6 ± 0.2 Å^{-1}
Correlation length (from FWHM)	4.0 ± 0.6 Å

Figure 17(b) shows a Gaussian fit to a linecut through the CNCS data with $E_\mathrm{i} = 3.32$ meV, where $(-2H\ 2H\ 0) = (0\ 0\ 0)$. The Gaussian peak position is $|Q| = -1.86 \pm 0.09$ Å^{-1}, giving an equivalent lattice spacing of $d = 3.4 \pm 0.2$ Å. The FWHM is 0.43 ± 0.20 Å^{-1}, giving a correlation length of 12 ± 5 Å.

Figure 17(c) shows a Gaussian fit to a linecut in the D7 data, where $(-2H\ 2H\ 0) = (0.1\ 0.1\ 0)$. The Gaussian peak position is 3.14 ± 0.13 Å^{-1}, giving an equivalent lattice spacing of $d = 2.0 \pm 0.1$ Å. The FWHM is 1.89 ± 0.29 Å^{-1}, giving a correlation length of 2.6 ± 0.4 Å.

APPENDIX D: RMC REFINEMENTS

1. Method and additional data

We follow the procedure of the SPINVERT refinement program [24] and use a Monte Carlo technique to find classical Heisenberg spin configurations that can reproduce the experimentally observed scattering pattern. In theory, the spin-spin correlations $\langle \mathbf{S}_i^\perp \cdot \mathbf{S}_j^\perp \rangle$ are uniquely related to the magnetic scattering intensity. For clarity, in this Appendix we shall use $(\frac{d\sigma}{d\Omega})$ for the experimental signal and S for the theoretically calculated signal from a single configuration. Assuming that we can describe the observed scattering with a static Heisenberg spin configuration, we are interested in the set of M equations,

$$\left\{ \left(\frac{d\sigma}{d\Omega} \right)(\mathbf{Q}_k) = S\big(\{\mathbf{S}_i\}_{i=1}^N, \mathbf{Q}_k\big) \right\}_{k=1}^M,$$
$$S \equiv \frac{C[f(|\mathbf{Q}|)]^2}{N} \sum_{i,j} \langle \mathbf{S}_i^\perp \cdot \mathbf{S}_j^\perp \rangle e^{i\mathbf{Q}\cdot\mathbf{r}_{ij}}, \tag{D1}$$

which relates a spin configuration $\{\mathbf{S}_i\}_{i=1}^N$ of N spins to the scattering intensity. k is a labeling index for all allowed $\{\mathbf{Q}_k\}_{k=1}^M \subset \mathbb{R}^3$ points. Ideally, the refinement method uses knowledge of the experimental left-hand side of this system of equations to compute $\{\mathbf{S}_i\}_i^N$. In particular, we use single spin flips in simulated annealing to minimize the residual,

$$\chi^2 \equiv \sum_k \left[\left(\frac{d\sigma}{d\Omega} \right)(\mathbf{Q}_k) - S\big(\{\mathbf{S}_i\}_{i=1}^N, \mathbf{Q}_k\big) \right]^2. \tag{D2}$$

The experiment only gives information about **Q**-points in the $(-2H, 2H, 0)$, $(L, L, 2L)$ plane, and in the following we shall discuss what can be deduced about the underlying configurations. We find that refining a solution only to the plane where the data were taken ends up overfitting scattering intensities at unconstrained **Q**-points outside the plane, giving unphysical results. We made several attempts to compensate for this, such as adding mirrors of the plane in different directions allowed by the crystal symmetries, to try to capture more of **Q**-space. However, this was not enough to resolve the issue. We conclude that with an underconstrained set of equations, we will always overfit in the simulated annealing, and we do not find physical solutions that are continuous and respect the crystal symmetries.

Hence, we investigate possible ways of fully constraining the set of equations given the data. We need to postulate a scattering intensity for every **Q**-point in order to avoid over-fitting. Since we do not have information about scattering intensities outside the measured plane, our attempt will be to extrapolate from the data the scattering intensities outside the plane to achieve a refinement result that agrees with the measured data and is continuous in the rest of **Q**-space. Naturally, we cannot assume to get a correct description of the spin configurations if we do not have access to the full diffraction pattern. Hence, we accept that the data presented are only an approximation of the true correlations. However, by testing several extrapolation techniques in addition to extracting RMC from various datasets with different incident energies and averaging across 400 RMC minimizations, we believe that the results are stable and that some variation in the assumed extrapolation will not affect the fundamental structure of the solution.

To construct a three-dimensional dataset for the scattering intensity, we make the assumption that the scattering has the same directional average for a given $Q = |\mathbf{Q}|$ in the experimentally measured plane as it has over all directions. The open source available SPINVERT program [24] is built for refining scattering data from powder samples by transforming Eq. (D1) into a powder average that depend only on Q, Eq. (D6). We term the calculated powder average $S(Q)$ [as opposed to $S(\mathbf{Q})$] for which we minimize the residual against the constructed powder average $(\frac{d\sigma}{d\Omega})(Q)$, named the *powder diffraction pattern* in the main text, and defined as

$$\left(\frac{d\sigma}{d\Omega}\right)(Q) \equiv \frac{1}{\mathcal{M}(Q)} \sum_{||\mathbf{Q}_k|-Q|<t} \left(\frac{d\sigma}{d\Omega}\right)(\mathbf{Q}_k), \tag{D3}$$

where $\mathcal{M}(Q)$ is the number of **Q**-points in the experiment of magnitude $Q \pm t$. We choose the tolerance t so that features can still be resolved and that good statistics are obtained. For the D7 data, we have the magnetic signal, denoted by the subscript "mag," from the experiment and we directly minimize the residual

$$\chi^2_{\text{mag}} \equiv \sum_k \left(\left(\frac{d\sigma}{d\Omega}\right)_{\text{mag}} (Q_k) - S_{\text{mag}}\big(\{\mathbf{S}_i\}_{i=1}^N, Q_k\big)\right)^2. \tag{D4}$$

For the CNCS data, we obtain the magnetic signal as the subtraction of the 13 K paramagnetic signal from the 0.05 K signal. We use the subscript "magff" to indicate this and minimize the residual

$$\chi^2_{\text{magff}} \equiv \sum_k \left(\left(\frac{d\sigma}{d\Omega}\right)_{\text{magff}} (Q_k) - S_{\text{magff}}\big(\{\mathbf{S}_i\}_{i=1}^N, Q_k\big)\right)^2. \tag{D5}$$

$S_{\text{mag}}(Q)$ and $S_{\text{magff}}(Q)$ are given by

$$\begin{aligned} S_{\text{magff}}(Q) &= sC[\mu F(Q)]^2 \frac{1}{N} \sum_{i,j} \Bigg[A_{ij} \frac{\sin Qr_{ij}}{Qr_{ij}} \\ &\quad + B_{ij} \left(\frac{\sin Qr_{ij}}{(Qr_{ij})^3} - \frac{\cos Qr_{ij}}{(Qr_{ij})^2} \right) \Bigg], \\ S_{\text{mag}}(Q) &= S_{\text{magff}}(Q) + \frac{2sC}{3N}[\mu F(Q)]^2, \end{aligned} \tag{D6}$$

where

$$\begin{aligned} A_{ij} &= \mathbf{S}_i \cdot \mathbf{S}_j - (\mathbf{S}_i \cdot \hat{\mathbf{r}}_{ij})(\mathbf{S}_j \cdot \hat{\mathbf{r}}_{ij}), \\ B_{ij} &= 3(\mathbf{S}_i \cdot \hat{\mathbf{r}}_{ij})(\mathbf{S}_j \cdot \hat{\mathbf{r}}_{ij}) - \mathbf{S}_i \cdot \mathbf{S}_j. \end{aligned} \tag{D7}$$

$F(Q)$ is the magnetic form factor of Yb^{3+}, μ is the effective dipole moment of Yb^{3+}, and $C = 0.072\,65$ barn is a physical constant. N is the number of particles in the refinement supercell, and s is an overall dimensionless scale factor, which relates neutron counts to the differential cross section. Due to the complexity of determining this scale factor, we choose to probe the solution space for all values of s. The resulting refinement will depend in a nontrivial way on s, and from the subset of configurations that minimize the residual of Eq. (D4) or Eq. (D5) we determine the best fit from the residual of Eq. (D2), where the directional dependence is included. From this definition of the best fit, we take the average of 400 minimizations to obtain the RMC fits presented in the main text. Here, we also present the RMC fit to the secondary CNCS dataset, Fig. 18.

In Fig. 19 we show the RMC spin-spin and director-director correlation functions for the D7 and CNCS $E_{\text{i}} = 3.32$ meV datasets, which we left out in the main text. We see that the average product between nearest-neighbor spins is positive, just as in the main text.

Figure 20 shows the distribution of the azimuthal angle of the members in the loop in the coordinate system presented in Fig. 1. We see that for YbGG, Figs. 20(b)–20(d), each spin is peaked along the tangent of the loop (local z-direction). This differs from the GGG refinements [5], where the distribution is peaked for angles perpendicular to the loop, Fig. 20(a).

The looped spin structure derived from the CNCS 3.32 meV dataset is more anisotropic than the D7 and the CNCS 1.55 meV datasets. It is estimated that this arises from a poorly sampled dataset, particularly for the medium to higher Q regions. Unlike the D7 and CNCS 1.55 meV datasets, the CNCS 3.32 meV dataset does not have clearly defined features. The spin structure derived from this dataset is therefore less reliable.

2. Notes on the D7 polarization

We have presented D7 data and corresponding simulations. The resultant spin-spin correlations and angular distribution show equivalence to those in the CNCS data, but the RMC

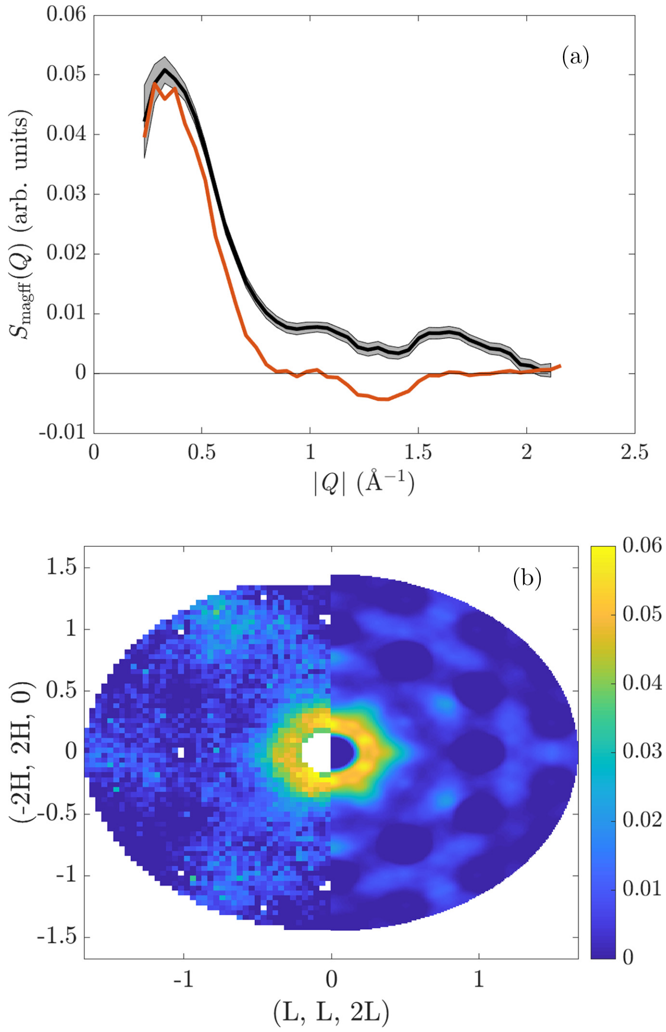

FIG. 18. (a) The constructed powder average from the CNCS, $E_{\mathrm{i}} = 3.32$ meV dataset $(\frac{d\sigma}{d\Omega})_{\mathrm{magff}}(Q)$ (black), together with the RMC fit $S_{\mathrm{magff}}(Q)$ (red). (b) The CNCS, $E_{\mathrm{i}} = 3.32$ meV dataset (left) together with the RMC average $S_{\mathrm{magff}}(\mathbf{Q})$ over 400 configurations (right).

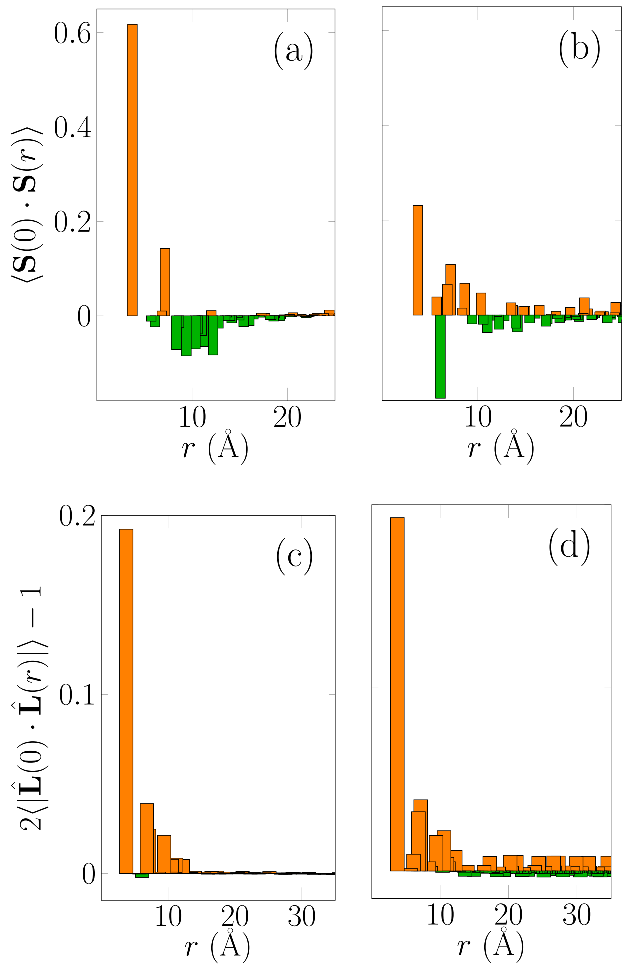

FIG. 19. Spin-spin correlation function and director-director correlation function from the RMC refinements of the other datasets. Parts (a) and (b) show the spin-spin correlations for the CNCS $E_{\mathrm{i}} = 3.32$ MeV and D7 refinements, respectively. Parts (c) and (d) show the director-director correlation function, $\langle |\hat{\mathbf{L}}(0) \cdot \hat{\mathbf{L}}(r)| \rangle - 1$. $[g_L(r)]$ for CNCS $E_{\mathrm{i}} = 3.32$ meV and the D7 data, respectively.

fit is less convincing. There are several subtle differences between the CNCS and D7 neutron scattering intensities that may give rise to this. The CNCS magnetic scattering intensity, which we term $S_{\mathrm{magff}}(Q)$, is obtained via the subtraction of a high-temperature scattering from base temperature scattering. The high-temperature scattering provides the intense magnetic form factor, and $S_{\mathrm{magff}}(Q)$ can result in negative intensities. This is considered in the RMC. D7 magnetic scattering, $S_{\mathrm{mag}}(\mathbf{Q})$, is extracted using XYZ polarization analysis with the following equation:

$$S_{\mathrm{mag}}(\mathbf{Q}) = 2(I_{x,x'} + I_{y,y'} - 2I_{z,z'})^{\mathrm{sf}}, \tag{D8}$$

in which $I_{x,x'}$ is the neutron y spin-flip scattering with the incident and scattered neutron polarization along a Cartesian x direction, and y, z denote the orthogonal directions [20]. The resultant spin-incoherent scattering is determined via

$$I_{\mathrm{SI}} = \tfrac{3}{2}(-I_{x,x'} - I_{y,y'} + 3I_{z,z'}). \tag{D9}$$

The determination of $S_{\mathrm{mag}}(\mathbf{Q})$ in this manner assumes that the net moment of the compound is zero, as is the case for paramagnetic systems or powdered antiferromagnet compounds and is thus employed for powder samples. A ferromagnetic signal would induce significant depolarization of the scattered polarization. Using this equation for the case of a single crystal makes an implicit assumption that there is a net zero averaged moment with no symmetry breaking such that the magnetic cross section is isotropic with magnetic components of equal magnitude projected along the three orthogonal directions. We made these assumption since we did not observe any depolarization of the scattered beam; only short-range order was observed, and prior knowledge of the director state, which provides an isotropic spin distribution, to a first approximation. Nevertheless I_{SI}, expected to be homogeneous in $\mathbf{Q}$, contains weak hexagonal features reminiscent of the magnetic signal. The peak positions of the spin-incoherent signal are equivalent to the magnetic diffuse peaks in Fig. 4(b), and thus only peak intensities are affected while no shift of the peaks is observed. RMC optimizes directly to $S(Q)$ and is sensitive to

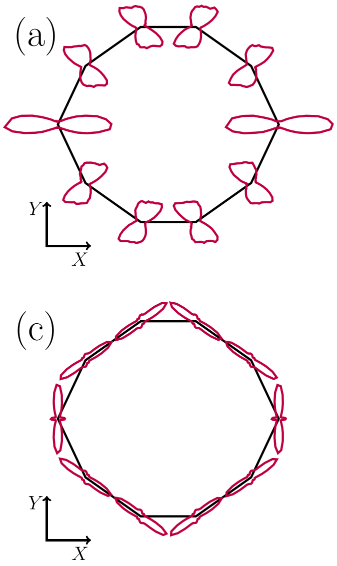

FIG. 20. Probability distribution of the azimuthal angle for each spin in the coordinate frame of a 10-spin loop viewed from above. Panel (a) shows the distribution from earlier GGG refinements [5]. Panels (b)–(d) show the distributions from the CNCS $E_\mathrm{i} = 1.55$ meV, $E_\mathrm{i} = 3.32$ meV, and D7 refinements, respectively. The distance from spin to the surrounding contour is proportional to the probability for the spin to have the associated azimuthal angle.

such relative changes. We suggest that these small variations give rise to the differences observed between the CNCS and D7 RMC, and they are the reason for the poorer simulations of the data. Nevertheless, the resultant D7 RMC spin structure is consistent with that determined from the CNCS RMC and provides confidence in our results.

APPENDIX E: A FEW NOTES ON THE HAMILTONIAN

1. Heisenberg model with anisotropy

The RMC method of the previous Appendix suggests that spins have a preference to point along the tangential direction of the 10-spin loop. In particular, the distribution is peaked along the direction connecting the center points of two adjacent triangles, the local z-direction. Inspired by this result, we propose a nearest-neighbor classical Heisenberg Hamiltonian with an energy penalty for spins pointing away from the axis direction,

$$\mathcal{H} = J \sum_{\langle i,j \rangle} \mathbf{S}_i \cdot \mathbf{S}_j + F \sum_i |\mathbf{S}_i - \mathbf{S}_{i\parallel}|^2, \qquad \text{(E1)}$$

where $\mathbf{S}_{i\parallel}$ is the spin component along the local tangent axis (local z-direction), and J is the strength of the nearest-neighbor exchange interaction. In this simple Hamiltonian, $F > 0$ models a classical easy-axis crystal-field anisotropy, and in the limit of large F, we obtain an Ising model. With the Metropolis-Hastings algorithm, we calculate a thermal average of the structure factor Eq. (D1) and tune the parameters J and F to make the scattering pattern agree with the experimental data. Our best fit is shown in Fig. 21(b). In Fig. 21(a) we also show the residual, χ^2, Eq. (D2), with respect to the CNCS $E_\mathrm{i} = 3.32$ meV scattering signal. Experimental data

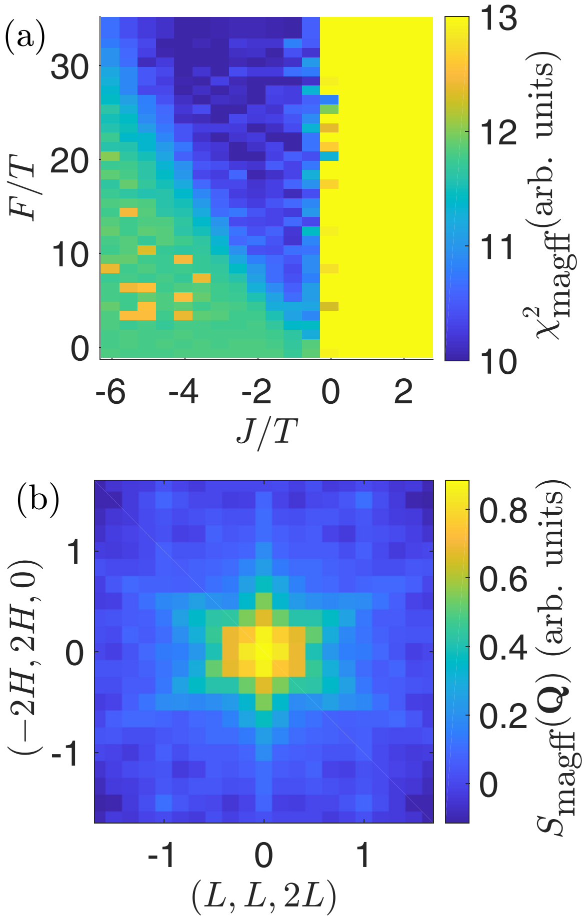

FIG. 21. (a) Least-squares fit for the temperature reduced signal χ^2_magff, Eq. (D2). We vary J/T and F/T and calculate the residual for a system of 648 ($L = 3$) particles. The CNCS $E_\mathrm{i} = 3.32$ meV data are used as a reference. (b) Scattering profile for the best fit in this model. Here $J/T = -3$, $F/T = 32$ [best fit in (a)] is shown for a system of 5184 particles ($L = 6$).

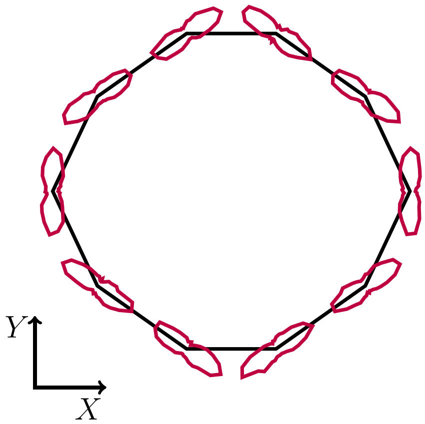

FIG. 22. Characteristic probability distribution of the azimuthal angle for each spin in the coordinate frame of a 10-spin loop viewed from above in the anisotropic Heisenberg model. Distance from spin to the surrounding contour is proportional to the probability for the spin to have the associated azimuthal angle.

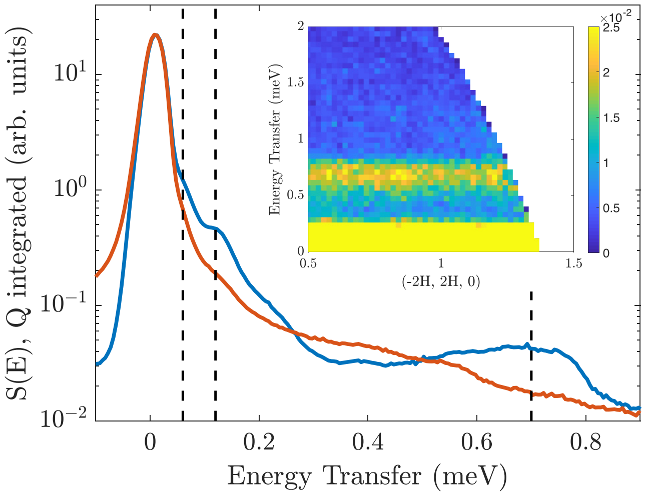

FIG. 23. (a) $S(E)$, $E_i = 1.55$ meV, three excitations (vertical dashed lines) are observed for the nominal temperature of 50 mK which are absent at 13 K. (b) Cut in data with $E_i = 3.22$ meV, along $(L, L, 2L)$, with $L = 0.23$, clearly showing the dispersionless nature of the highest magnetic excitation.

were binned to wave vectors periodic in the supercell. We show the error as a function of J/T and F/T for 648 particles ($L = 3$). We see that negative $J < 0$ (FM NN interactions) gives the best fit to the data. This is also in agreement with the SPINVERT refinement, which found a positive value for the nearest-neighbor spin correlations presented in the main text. From the parameter sweep, we see also that χ^2 is minimized for large F. In this limit we get an Ising model, which further motivates the crude Ising assumption of the main text. We conclude by showing the characteristic spin distribution for the anisotropic Heisenberg model, Fig. 22.

APPENDIX F: EXCITATIONS

Magnetic excitations have been identified within the CNCS dataset. Three low-lying dispersionless excitations are observed at 0.06, 0.12, and 0.7 meV at 0.05 K (see Fig. 23), but they are absent at 13 K. The inset of Fig. 23 shows a cut in CNCS data with incoming energy 3.32 meV with $(L, L, 2L)$, $L = 0.23$, clearly showing the dispersionless nature of the highest magnetic excitation. A detailed analysis of these data will be published elsewhere.

[1] J. S. Gardner, M. J. P. Gingras, and J. E. Greedan, Rev. Mod. Phys. **82**, 53 (2010).

[2] T. Fennell, P. P. Deen, A. R. Wildes, K. Schmalzl, D. Prabhakaran, A. T. Boothroyd, R. J. Aldus, D. F. McMorrow, and S. T. Bramwell, Science **326**, 415 (2009).

[3] D. J. P. Morris, D. A. Tennant, S. A. Grigera, B. Klemke, C. Castelnovo, R. Moessner, C. Czternasty, M. Meissner, K. C. Rule, J.-U. Hoffmann, K. Kiefer, S. Gerischer, D. Slobinsky, and R. S. Perry, Science **326**, 411 (2009).

[4] C. Castelnovo, R. Moessner, and S. L. Sondhi, Annu. Rev. Condens. Matter Phys. **3**, 35 (2012).

[5] J. A. M. Paddison, H. Jacobsen, O. A. Petrenko, M. T. Fernández-Díaz, P. P. Deen, and A. L. Goodwin, Science **350**, 6257 (2015).

[6] N. d'Ambrumenil, O. A. Petrenko, H. Mutka, and P. P. Deen, Phys. Rev. Lett. **114**, 227203 (2015).

[7] O. A. Petrenko, C. Ritter, M. Yethiraj, and D. McK Paul, Phys. Rev. Lett. **80**, 4570 (1998).

[8] J. G. Rau and M. J. P. Gingras, Nat. Commun. **7**, 12234 (2016).

[9] R. Wawrzyńczak, B. Tomasello, P. Manuel, D. Khalyavin, M. D. Le, T. Guidi, A. Cervellino, T. Ziman, M. Boehm, G. J. Nilsen, and T. Fennell, Phys. Rev. B **100**, 094442 (2019).

[10] Y. Cai, M. N. Wilson, J. Beare, C. Lygouras, G. Thomas, D. R. Yahne, K. Ross, K. M. Taddei, G. Sala, H. A. Dabkowska, A. A. Aczel, and G. M. Luke, Phys. Rev. B **100**, 184415 (2019).

[11] T. Yoshioka, A. Koga, and N. Kawakami, J. Phys. Soc. Jpn. **73**, 1805 (2004).

[12] J. J. Pearson, G. F. Herrmann, K. A. Wickersheim, and R. A. Buchanan, Phys. Rev. **159**, 251 (1967).

[13] C. Broholm, R. J. Cava, S. A. Kivelson, D. G. Nocera, M. R. Norman, and T. Senthil, Science **367**, eaay0668 (2020).

[14] J. Filippi, C. Lasjaunias, B. Hebral, J. Rossat-Mignod, and F. Tcheou, J. Phys. C **13**, 1277 (1980).

[15] P. Dalmas de Réotier, A. Yaouanc, P. C. M. Gubbens, C. T. Kaiser, C. Baines, and P. J. C. King, Phys. Rev. Lett. **91**, 167201 (2003).

[16] J. A. Hodges, P. Bonville, M. Rams, and K. Krolas, J. Phys.: Condens. Matter **15**, 4631 (2003).

[17] H. Kimura, R. Tanahashi, K. Maiwa, R. Morinaga, and T. J. Sato, J. Cryst. Growth **311**, 522 (2009).

[18] G. L. Squires, *Introduction to the Theory of Thermal Neutron Scattering* (Cambridge University Press, Cambridge, 1978).

[19] G. Ehlers, A. A. Podlesnyak, and A. I. Kolesnikov, Rev. Sci. Instrum. **87**, 093902 (2016).

[20] J. R. Stewart, P. P. Deen, K. H. Andersen, H. Schober, J.-F. Barthélémy, J. M. Hillier, A. P. Murani, T. Hayes, and B. Lindenau, J. Appl. Cryst. **42**, 69 (2009).

[21] P. P. Deen, M. Haubro, L. Ørduk-Sandberg, R. Edberg, I. M. B. Bakke, K. Lefmann, A. Wildes, and L. Mangin-Thro, https://doi.ill.fr/10.5291/ILL-DATA.5-53-274.

[22] T. Fennell, L. Mangin-Thro, H. Mutka, G. J. Nilsen, and A. R. Wildes, Nucl. Instrum. Methods Phys. Res. A **857**, 24 (2017).

[23] https://doi.ill.fr/10.5291/ILL-DATA.INTER-433.

[24] J. A. M. Paddison, J. Ross Stewart, and A. L. Goodwin, J. Phys.: Condens. Matter **25**, 454220 (2013).

[25] R. A. Buchanan, K. A. Wickersheim, J. J. Pearson, and G. F. Herrmann, Phys. Rev. **159**, 245 (1967).

[26] P. P. Deen, O. A. Petrenko, G. Balakrishnan, B. D. Rainford, C. Ritter, L. Capogna, H. Mutka, and T. Fennell, Phys. Rev. B **82**, 174408 (2010).

[27] Radio chemistry society, lanthanides and actinides, https://www.radiochemistry.org/periodictable/la_series/L8.html, accessed: 2020-04-22.

[28] W. H. Brumage, C. C. Lin, and J. H. Van Vleck, Phys. Rev. **132**, 608 (1963).

[29] http://energy.gov/downloads/doe-public-access-plan.

A.4 Manuscript 1: Design, calibration, and performance of a uniaxial pressure cell for neutron scattering studies of quantum magnetism.

I have designed, tested and calibrated the pressure cell and the load gauge for all four iterations of the cell with the help of many collaborators most importantly Morten Haubro, Jan Oechsle and Alexander Holmes. I have analysed the neutron scattering data from the neutron scattering beamtimes with cell A and cell C and participated in the sample preparation for these beamtimes. I have written the first draft of the manuscript.

Design, calibration, and performance of a uniaxial pressure cell for neutron scattering studies of quantum magnetism.

L. Ø. Sandberg,[1] M. L. Haubro,[1,2] M. E. Kamminga,[1] K. M. L. Krighaar,[1] R. Edberg,[3] I. M. B. Fjellvåg,[4] M. Guthrie,[5,6] A. T. Holmes,[5] L. Mangin-Thro,[7] A. Wildes,[7] M. Boehm,[7] J. Oechsle,[8] K.-E. Nielsen,[8] D. W. Wistisen,[8] K. Theodor,[1] P. Henelius,[3,9] K. Lefmann,[1] and P. P. Deen[1,10]
1) *Nanoscience Center, Niels Bohr Institute, University of Copenhagen, Universitetsparken 5, DK-2100 Copenhagen Ø, Denmark*
2) *Department of Physics, Technical University of Denmark, 2800 Kongens Lyngby, Denmark*
3) *Physics Department, KTH Royal Institute of Technology, Sweden*
4) *University of Oslo, Centre for Materials Science and Nanotechnology, NO-0315, Oslo, Norway*
5) *European Spallation Source ERIC, 22363 Lund, Sweden*
6) *University of Edinburgh, School of Physics and Astronomy and Centre for Science at Extreme Conditions*
7) *Institut Laue-Langevin, 71 Avenue des Martyrs, CS 20156, 38042 Grenoble Cedex 9, France*
8) *Niels Bohr Institute, University of Copenhagen, Universitetsparken 5, DK-2100 Copenhagen Ø, Denmark*
9) *Faculty of Science and Engineering, Åbo Akademi University, Åbo, Finland*
10) *European Spallation Source ERIC, Partikelgatan 224 84 Lund Sweden*

(Dated: January 2, 2022)

An article usually includes an abstract, a concise summary of the work covered at length in the main body of the article. It is used for secondary publications and for information retrieval purposes.

I. INTRODUCTION

Uniaxial pressure allows for an asymmetric distortion of the lattice which makes it possible to drive the system into highly unconventional states of matter. In recent years, hydrostatic pressure has become a standard sample environment in many neutron facilities, while the ability to apply uniaxial pressure remains technically challenging. Pressure is particularly interesting within the field of frustrated magnetism since it perturbs the balance between the different interactions: exchange interactions, dipolar interaction and crystal field anisotropy effects, which vary with the interatomic distance changed through the application of uniaxial pressure. In this study we focus on the application of uniaxial pressure to quantum materials as found in the scientific fields of frustrated magnetism[1].

Crystalline impurities exert a chemical pressure on the crystal. Indeed, crystal impurities such as oxygen vacancies[2] and stuffing (excess magnetic ions)[3] in frustrated pyrochlore spin ice compounds have shown to have large consequences on the nature of both structure and dynamics. Application of an external pressure offers an opportunity to study the effects of pressure in a more controlled way compared to chemical pressure where the exact amount and position of the impurities are difficult to control. Indeed, Biesner et al. recently suggested that pressure offers a convenient way of tuning compounds in order to find quantum spin liquids and tuned quantum phase transitions[4]. Hydrostatic pressures has been used to study the quantum spin liquid candidates $Tb_2Ti_2O_7$[5] and $Yb_2Ti_2O_7$[6] and clarify the strong impact of even small levels of impurities on the ground state and dynamics of the compounds due to the chemical pressure caused by the impurities.

Hydrostatic pressure tunes all bond lengths symmetrically while uniaxial pressure breaks the symmetry of the crystal thereby enabling the creation of new unconventional states of matter. This was recently described by Umeo et al.[7] who were able to increase or decrease the ordering temperature of the geometrically frustrated compound YbCuGe through the application of uniaxial pressure along different crystallographic directions. In contrast, the application of hydrostatic pressure did not affect the ordering temperature. The compound was studied with magnetisation and specific heat measurements. Similarly, Mirebeau et al. saw no pressure induced order when applying hydrostatic pressure up to 6 GPa to the classical spin ice compound $Ho_2Ti_2O_7$ (HTO)[8]. However, even low uniaxial pressures around 0.35 GPa do induce changes in HTO[1],[9].

Uniaxial pressure is available for μSR[10] and X-ray diffraction[11], but until now it has remained challenging for diffuse and inelastic neutron scattering. The type of neutron scattering experiment that we target are diffuse neutron scattering and cold inelastic neutron scattering experiments, which are characterized by broad, weak scattering close to the background. Through the use of neutron polarisation analysis one can separate the nuclear scattering, accessed only in the non spin flip scattering, and the magnetic scattering which is observed in both the non spin flip and spin flip scattering[12]. A typical experimental set up is shown in figure 1 using D7 as the example instrument. Figure 1(top) shows an incident divergent neutron beam impinging onto a pressure cell with neutrons scattering vertically into a detector. The scattering is limited vertically due to absorbing surfaces on regions of the pressure cell that may scatter, thus limiting spurious background effects. The top view shows the same incident divergent beam impinging onto the pressure cell and scattering into a broad horizontal angular range. It is important to note the broad detector coverage ($-10^\circ \leq 2\theta \leq 155^\circ$ for D7) required to provide a broad overview of reciprocal space.

According to Bragg's law, there is direct relation between

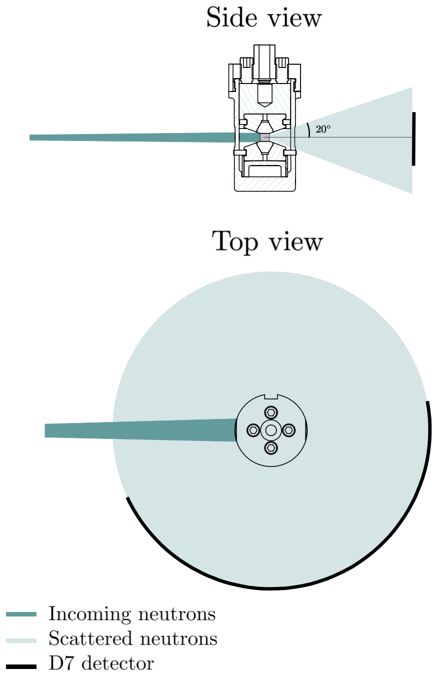

Figure 1. Sketched scattering from a sample in the pressure cell. A divergent incoming neutron beam scatter from the cell and sample. Top: the cell allows ± 20 degrees vertical scattering. Bottom: the cell allows ± 180 degrees horizontal scattering. The sketched detectors have the angular coverage of the D7 instrument at the ILL (-10 degrees, +155 degrees) horizontal, ± 10 degrees vertical scattering. Note that the sample-to-detector distances are not drawn to scale.

the scattering angle, 2θ and the reciprocal lattice vector, $\mathbf{Q}$,

$$2\mathbf{k}\sin(\theta) = \mathbf{Q}. \tag{1}$$

Here, $\mathbf{k}$ is the wave vector which describes the neutron momentum. For neutron scattering experiments on single crystal samples, the scattering profile which provide information on the spin-spin-correlations varies in different directions of $\mathbf{Q}$, and the cell and sample are therefore rotated along a vertical rotation axis in order to measure all areas in the scattering plane which is spanned by 2 of the 3 unit vectors in $\mathbf{Q}$. (Ref Andrew Boothroyd) Such a device requires the following experimental aims to be met:

E1 Apply highest possible uniaxial pressure to single crystal samples.

E2 Reach cryogenic temperatures at the sample position ($T < 50$ mK)

E3 Enable diffuse neutron diffraction from the pressurized sample.

E4 Enable inelastic neutron scattering from the pressurized sample.

E5 Ensure that the incident neutron spin is not depolarised to enable neutron polarisation analysis studies.

The experimental requirement E1 is driven by scientific interests that reveal phase changes for uniaxial pressure application. Clearly this aim is limited by the strength of the crystals studied which is ultimately limited by the strength of the crystal bonds. In reality, however, it is typically limited by the amount of impurities and the mosacity of the crystal, as well as the ability to polish two surfaces of the crystal to obtain planar and parallel surfaces.

The experimental requirement E2 is motivated by the low lying excitations of many frustrated compounds, often below 1 meV (ref), which can only be studied with cold neutrons at low temperatures. Furthermore, the states of matter which are studied here will typically only occur at cryogenic temperatures, typically in the mK range, and consequently the cell has to conduct heat even at these temperatures in order to cool the system within a reasonable time frame.

Experimental aim E3: In a correlated, but disordered phase, the magnetic neutron scattering signatures are weak, broad and diffuse[13],[14]. The width of the diffuse signals requires large opening angles of the cell preferably both within and outside the scattering plane, and it requires a uniform background. Furthermore, the weak interaction between neutrons and matter makes large samples particularly important in these studies. However, large samples are challenging in pressure studies since it involves large forces which the cell must be able to accommodate.

Experimental aim E4: Pressure is expected to affect not only the structure, but also the dynamics, which can be studied with inelastic neutron scattering. The intensity of inelastic neutron scattering signals are orders of magnitude smaller than the elastic line. Consequently, large samples and a uniform background is also important in order to meet experimental aim E4.

Experimental aim E5 is motivated by the wish to separate magnetic from nuclear contributions in order to better resolve small pressure induced changes in the magnetic spin-spin correlations. This is possible with neutron polarisation analysis (PA). However, PA requires that there are no magnetic contributions in the sample environment since any net ferromagnetic parts will interact with the neutrons and depolarise the neutron state making it impossible to use the technique[15].

The unconventional states of matter described above are typically studied with diffuse neutron scattering instruments and with cold inelastic neutron spectrometers, and instruments such as D7[12], IN5[16], CNCS[17], AMATERAS[18] LET[19], DNS[20] and CAMEA[21] are kept in mind. Currently, uniaxial pressure cells have strong limitations on the sample size and non-uniform cell background signals,[22],[23] resulting in poor signal during diffuse neutron experiments. The challenges also include measuring the applied force and avoiding indentation of the cell materials especially at the sample contact area where the pressure is particularly large. However, with the pressure cell described in this article, it is possible to meet all of the experimental challenges mentioned and measure the applied pressure in-situ.

II. DESIGN AND CALIBRATION METHODS

In order to meet the experimental aims defined in the previous section, we have defined the following system requirements:

S1 Keep 2 GPa uniaxial pressure constant within 5 % at the sample position during 24 hours. (experimental aim E1, E3, E4)

S2 Allow broad scattering range of at least 180 degrees horizontal and ± 20 degrees vertical scattering. (experimental aim E3)

S3 Measure the applied force at cryogenic temperatures with less than 10 % error. (experimental aim E1, E2).

S4 Obtain uniform and low background from the cell (experimental aim E3, E4).

S5 Use materials that are thermally conducting even at cryogenic temperatures in order to cool the cell to cryogenic temperatures in less than 24 h. (experimental aims E3, E4 and E5).

S6 Use only materials that are non-magnetic (experimental aim E5).

S7 Accommodate mm-size samples (experimental aim E3, E4).

S8 Obtain a cell with a maximum diameter of 45 mm so it fits into cryostats of common neutron scattering instruments (E4, E5).

S9 Use only materials that have low neutron activation (experimental aims E3, E4).

How these system requirements are met is described in the next sections that describes the cell design, the choice of materials and the load gauge design.

A. Cell design and materials

The design of the cell has been an iterative process where three cells have been designed, constructed and tested. This chapter is a description of the design and materials in the final version, cell C. The two first cells, cell A and cell B, are described and discussed in section IV.

1. Cell design

The cell design is originally based on the principles of a diamond anvil cell (DAC) (REF), which creates pressure through the use of two opposing diamond anvils with a sample that is compressed in between. A DAC is typically used to apply hydrostatic pressure through the use of a gasket but in this case we modify a DAC to apply uniaxial pressure. Figure 2 shows all parts of the pressure cell in exploded view. Part 1: top screws are used to apply the force. They are M8 pinol screws in order to fit them within the size specifications in system requirement S8. Part 2: The lid is screwed onto to the cell cage (part 9) and the top screws are screwed through the lid in order to apply the force to the lid and piston (part 3). The cell is mounted on the cryostat by screwing the lid onto an M6 screw. Part 3: The piston transfers the force from the top screws to the upper seat. Part 4: There are two identical seats in the cell, the upper and the lower seat. The seats transfer the force to the anvils and reduce the horizontal stress in the anvils as described later in this section. Part 5: sample position. Part 6: the anvils transfer the force to the sample. The highest pressure in the cell for a given applied force is obtained between the anvils and the sample. Part 7: the cage of the load gauge. Four strain gauges are connected in a Wheatstone bridge and glued onto the back of the lid of the load gauge cage along with a thermometer, see section II B for a detailed description of the load gauge. Part 8: a spacer which is used to align the load gauge and lower seat. The load gauge wire exit through a groove in the spacer. Part 9: the cell cage contains all the above parts. The load gauge wire exit through a hole in the cell cage.

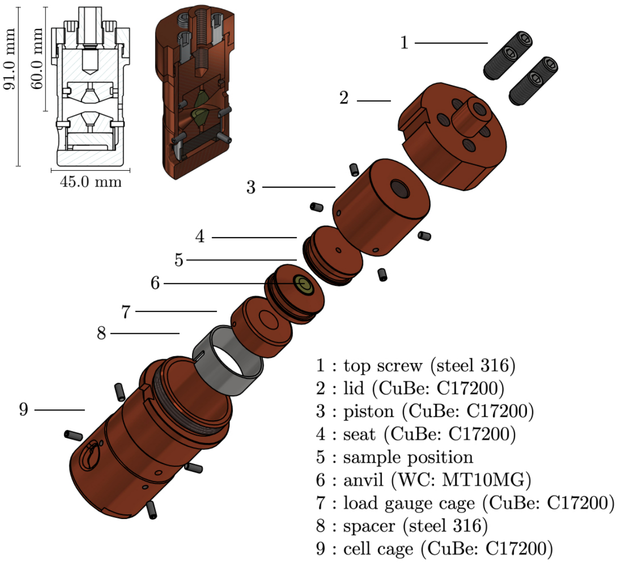

Figure 2. Cell design in exploded view and transparent sideview. Parts are numbered in exploded view and materials are described in parenthesis.

The cell needs a broad scattering range both horizontally and vertically in order to meet system requirement S2. Many diamond anvil cells have large windows to reduce the cell background according to system requirement S4 (ref: SNS with large windows from approx. 2018/2019). However, variations in the scattering profile between window regions that are empty and regions that contain cell wall are more significant than the weak diffuse scattering profiles, rendering a cell with windows impossible to use for these systems. The effect of windows is discussed in section IV A. System requirement S4 is therefore met more efficiently with a cell without

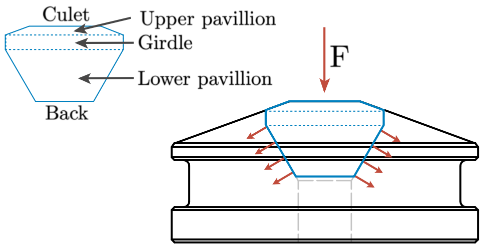

Figure 3. Drawing of the principle of the anvil and seat design. The force which is applied to the culet is transferred from the side of the lower pavillion to the seat. The lower pavillion and girdle are confined within the seats to reduce the horizontal stress in the anvils. The naming convention of the different parts of the anvil from a diamond anvil cell is illustrated in the upper left corner.

windows which results in a uniform cell background. The absence of windows increases the cross section area of the cell cage which enables a thinning of the cell walls from 3 mm to 2 mm around the sample position. The cell cage has two small pin holes at the sample position with a 90 degrees relative angle to optically check the crystal alignment before the neutron experiment. Figure 1 shows that the cell allows $\pm$ 20 degrees vertical scattering and $\pm$180 degrees horizontal scattering which is well above the angular coverage of the detectors at D7[12] both horizontally and vertically and and above the specifications in system requirement S2.

Figure 3 describes the principles of the seats and conical anvils (part 4 and 6 respectively in figure 2) while also describing the names of the different parts of the anvils. The highest pressure in the cell occurs between the culet of the anvil and the sample. Accordingly, the anvils are made from tungsten carbide which is very hard, which reduces the risk of indentation, but it is also brittle, which increases the risk of breaking the anvils, see section II A 2. The contact area between the side of the lower pavillion and the seat is larger than the culet area, which reduces the pressure on the seat in order to prevent deformations. Furthermore, the lower pavillion and the girdle of the anvil are confined within the seat, which reduces the horizontal tension in the anvils and prevents it from breaking.

The neutron beam has a divergence, and both incoming and especially the scattered neutron beam will therefore hit not only the sample, but also the cell. In order to reduce the background from these scattering events (system requirement S4), the seats (part 4 in figure 2) and the cage (part 9 in figure 2) outside the beam position are covered in cadmium (Cd) which is a strong absorber of cold neutrons. Besides a background reduction, Cd will also reduce the neutron activation of the cell in compliance with system requirement S9, see section II A 2 for a further discussion of neutron activation of the cell.

Figure 4 shows the Cd covered cage of cell B. The cage and piston of cell B and the final cell C are identical and the experiments performed on cell B presented in this section would provide similar information to what one would gain from experiments on cell C.

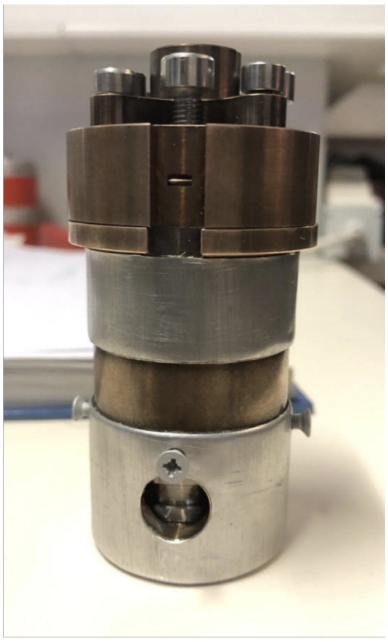

Figure 4. Photo of cell B. The cell cage is covered in Cd outside the beam position. The hole in the cell cage allows the load gauge wires to exit the cell. The wires are transferred through a groove in the lid to the sample stick.

2. *Materials*

Pressure cells that are used for X-ray diffraction or μSR studies typically contain μm size samples, and the forces in the pressure cell are correspondingly smaller. However, system requirement S7 requires mm size samples and all materials in the cell thereby experience pressures on the order hundreds of MPa in order meet the 2 GPa at the sample, as specified in system requirement S1. Furthermore, the cell materials have to be non-magnetic according to system requirement S6, conduct heat even at cryogenic temperatures (system requirement S5), and they should have low neutron activation in order to reuse the cell after the experiment (system requirement S9).

Figure 2 shows that apart from the spacer, anvils and screws, all parts of the cell are made from beryllium copper C17200 (CuBe), which consist of 1.8-2 % Be, 0.2-0.6 % Co+Ni, while the remaining part is Cu. It has a yield strength of 1240 MPa[24]. Yield strength is the highest possible pressure which can be applied to a material before it deforms plastically (REF).

The highest possible sample diameter which is accomodated by the cell is 6 mm for which a force of 57 kN will provide a pressure of 2 GPa. The remaining parts of the cell have a larger cross section area and are therefore exposed to a lower pressure than the sample and the anvils (part 10 and 6 in figure 2). For instance, the cell wall at the sample position is exposed to a pressure of 208 MPa at an applied force of 57 kN, which is well below the yield strength of CuBe, and thus fulfills scientific aim S1. However, typical samples will have a diameter close to 4 mm, in which case 25 kN is required in order to obtain 2 GPa at the sample position and the testing and calibration of the cell, which are presented in the following sections, have therefore been performed with this force in mind. CuBe is non-magnetic and has a thermal conductivity of 108 W/mK at 300 K and 1.40 W/mK at 3 K,[25], which makes it possible to cool to cryogenic temperatures and thus fulfill scientific requirement S5. The exact amount of Co in CuBe is important with regards to neutron activation. If the cell is active, it is not allowed to remove it from the neutron facility and use in another experiment. After 5 days of beamtime at D7 at the ILL, it would take 37.8 years before the cell had less than $5 \cdot 10^{-4} \mu$Ci at the worst case scenario with 0.6 % Co in the cell without any Cd coverage. However, we were able to retrieve the cell within weeks after a 5 day experiment at D7 in October 2019 due to the Cd coverage of the cell cage.

The anvils (part 6 in figure 2) are made from cemented tungsten carbide MT10MG (WC10), which consists of 10 % Co, 45 % W and 45 % C, which is one of the hardest materials that exists. It has typical yield strengths between 3347 and 6833 MPa[26] and it will therefore not indent within scientific aim S1. Tungsten carbide is very brittle, and the typical issue if a large force is applied to it is therefore not indentation, but cracks due to tensions in the material. The yield strength is typically not provided and instead WC10 is described by its hardness, which is 1610 HV. This is a measure of the level of plastic deformation of a material during application of a large force with a sharp object. WC10 was chosen because it has a large transverse rupture strength of 4 GPa and a high fracture toughness k_{1c} of 11.0, see data sheet in appendix. The anvils and seats are designed to support the sides of the anvils and thereby reduce the horizontal stress in the anvils as discussed in section II A 1.

10 % Co is used as a binder in WC10 which is an issue in regards to system requirement S9. The lifetime of Co-59 is 5.3 years, and any neutron activation above the safety limit will therefore make it difficult to retrieve the anvils within a reasonable time frame. It is not possible to cover the culets of the anvils with Cd, and some activation is therefore expected. We will therefore expect to produce several pairs of anvils and seats and store them at the facility while they are active. The room temperature conductivity of wolfram carbides like WC10 with microstructure grain size is approximately 50 W/mK,[27], which is better than many metals such as steel 316 that has a thermal conductivity of 15 W/mK at room temperature, see datasheet in appendix. We can thus expect good thermal contact with the sample in compliance with system requirement S5.

The spacer (part 8 in figure 2) and the screws (part 1) are made from steel 316 and are non-magnetic. It has a yield strength of 200 MPa and a hardness of 225 HV, see datasheet in appendix.

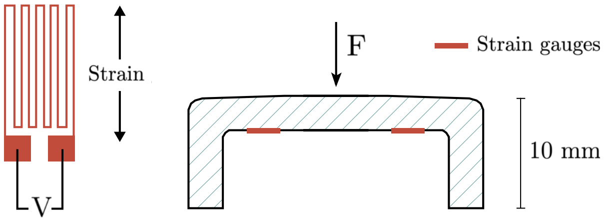

Figure 5. Schematics of a strain gauge (left) and the load gauge design (right). The resistance in a strain gauge changes due to strain along the axis specified in the figure. The load gauge consist of a CuBe cylinder with a slightly conical lid here seen in a side view, with four commercially available strain gauges placed in a Wheatstone bridge (figure 6). The strain gauges respond to the deformation of the CuBe cage which occurs when a force is applied. More details on the load gauge is found in figures 7 and 8.

B. Load gauge design

The change in pressure on the sample upon cooling is determined by the relative ratios of the thermal contractions of CuBe, steel 316, WC10 and the sample. The anvils are confined within the CuBe seats extending up to 0.7 mm from the sample and the dominating contribution to the change in pressure upon cooling is thus the relative thermal contraction of the sample, steel 316 and the CuBe. It is thus not possible to precalibrate the changes in sample pressure during cooling for any sample, and a load gauge which can measure the force in-situ has therefore been designed and calibrated according to system requirement S3.

The principle of the load gauge is illustrated in figure 5. The load gauge cage is a hollow cylinder with a slightly conical lid. When a force is applied to the centre of the lid, it will deform elastically, which causes a deformation of four strain gauges that are glued onto the back of the load gauge lid. A strain gauge is a resistor whose resistance varies depending on its deformation, the strain, due to a stress which is applied to it[28]. The change in resistance is positive or negative depending on the sign of the strain (compression or elongation). Figure 5 shows that strain gauges are sensitive to strain along the length of the wires as specified by the arrows, while it is almost insensitive to strains perpendicular to this axis.

The load gauge consists of four strain gauges connected in a Wheatstone bridge as illustrated schematically in figure 6. An excitation voltage, V_e, is applied between the points B and C in the bridge, and an output voltage, V_0, is measured between points A and D in the bridge. If the bridge is balanced so 2 strain gauges are stretched and 2 strain gauges are compressed, the 4 strain gauge resistors fulfil the requirement

$$\frac{R_1}{R_2} = \frac{R_3}{R_4} \qquad (2)$$

with the surface relaxed, and the output voltage is zero in that case. Any small deviation from the equilibrium state will induce a change in the output voltage, reflecting the surface strain caused by the applied force. An advantage of the

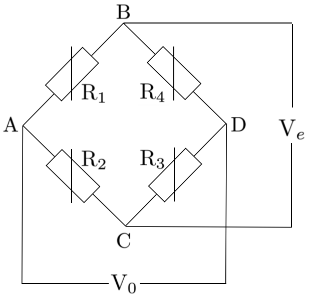

Figure 6. Wheatstone bridge circuit. The circuit consists of 4 variable resistors (R_1 to R_4). An excitation voltage, V_e is applied between the points C and B in the bridge, and the output voltage V_0 is measured.

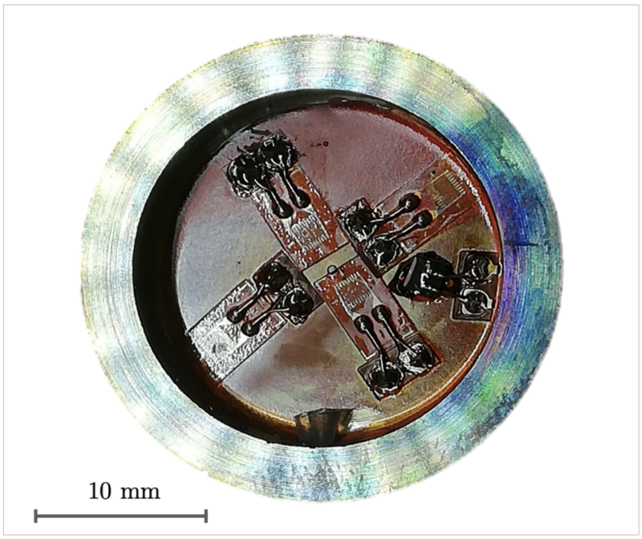

Figure 7. Photo inside the load gauge where the four strain gauges and the PT100 thermometer have been glued onto the CuBe cage lid. Photo taken before wires have been soldered.

Wheatstone bridge is that it reduces the sensitivity of non-centered force application and resistance effects in the wires compared to measurements with a single strain gauge. If two of the four strain gauges in a Wheatstone bridge experience a compression while the remaining two experience an elongation, the obtained signal is enhanced by a factor of four compared to the signal from a single strain gauge and it increases the temperature stability of the bridge.

Figure 7 shows a photo of the inside of the load gauge lid where four CFLA-1-350 strain gauges are attached with adhesive type C-1 from Tokyo Measuring Instruments Lab. The strain gauges are calibrated for relative strain up to 0.1 % and for temperatures down to 4 K. We estimate that mK temperatures can be accommodated once 4 K has been reached. The figure also shows a thermometer of the type PT100 that has been attached to the load gauge lid. The thermometer is calibrated down to 74 K and was used during the calibration, but it will not be used during cryogenic neutron scattering experiments.

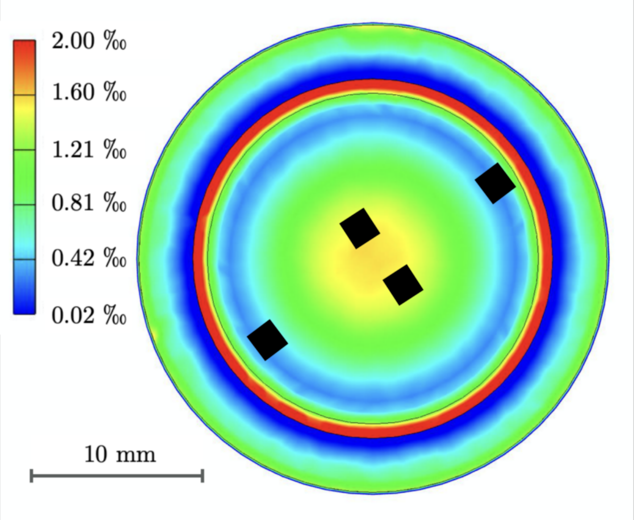

Figure 8. Finite element analysis of the lid of the load gauge cage for a 25 kN load. The strain active area of the strain gauges are marked in dark grey.

The position of the 4 strain gauges in figure 7 has been decided based on the finite element analysis (FEA) that is presented in figure 8. FEA is a numerical calculation of the relative strain during an applied force[29]. The calculations are based on a 25 kN load which is required to obtain 2 GPa pressure on a 4 mm diameter sample.

Figure 8 shows that the load gauge cage only has positive strain and it is therefore not possible to place 2 strain gauges in an area with negative strain and two strain gauges in an area with positive strain. Two strain gauges are placed near the edge where the relative strain is very small. These two strain gauges therefore mostly contributes to an adjustment for non-vertical components of the applied force and for differences in the resistances in the wires. The other two strain gauges are attached near the center and they experience relative strain changes slightly above the specified 0.1 %. However, force has been applied to the load gauge many times during the tests which are presented in section II C, and no systematic changes are observed upon pressurization. We therefore conclude that the adhesive and strain gauges are not damaged by force applications of this magnitude.

C. Load gauge calibration

The load gauge has been calibrated for forces up to 22 kN at 300 K, at 195 K (cooled with dry ice), at 125 K (cooled with liquid nitrogen while heating) and at 80 K (cooled with liquid nitrogen). At all temperatures, the force was applied externally with a calibrated force press.

According to system requirement S3, the intention is to measure the force at cryogenic temperatures and we would therefore like to calibrate the load gauge at lower temperatures. However, it requires a complicated experimental setup to control the applied force at very low temperatures. The

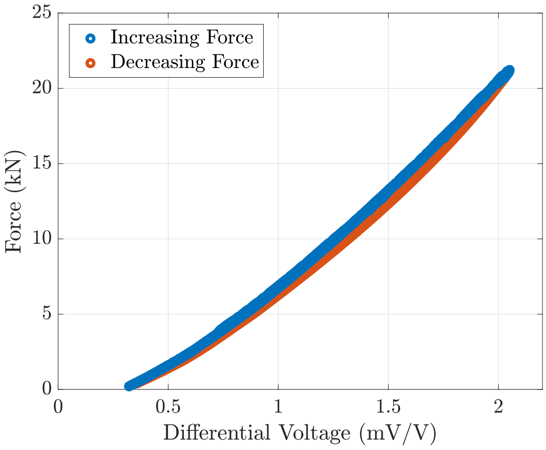

Figure 9. A single room temperature calibration (data set 6), where the force has been increased to 22 kN and reduced to 0 kN 3 times. The data has been separated into increasing and decreasing force which shows a significant hysteresis.

thermal contraction of the cell materials is minimal below liquid nitrogen temperatures,[30],[31], and the pressure is thus not expected to change significantly for lower temperatures. The 80 K calibration curve will be used as an estimate for the pressure even at cryogenic temperatures. All calibrations have been performed with an external force press which is calibrated with a commercial reference load gauge LC929. Despite the Wheatstone bridge circuit, the load gauge is sensitive to non-vertical components of the force. This is believed to be caused by a tilt of one of the strain gauges as shown in figure 7. In order to reduce the effects caused by non-vertical force components, the load gauge was in the cell during the calibrations.

The room temperature calibration was repeated 6 times and the cell was disassembled between each calibration. In each calibration, the force was increased to 22 kN 3 times, the limit of the commercial load gauge LC929 which was used during the calibration. We do not foresee any difficulties reaching 25 kN which is the requirement to obtain 2 GPa on a 4 mm diameter sample.

First we consider the effect on increasing and decreasing force. Figure 9 shows a single data set (data set 6), which shows a hysteresis between increasing and decreasing force. Consequently, the calibration curves have been separated into increasing and decreasing force and the data has been treated independently. The curves presented here are the increasing force curves, since these are the curves that are relevant when force is applied to the cell prior to an experiment.

Figure 10 shows the calibration curves for increasing force for all 6 assemblies which we term data sets. The independent variable in the experiment was the force, but during a neutron scattering experiment, the relative voltage is read off and converted into a force. In order to use the calibration curves most conveniently during a neutron scattering experiment, the curves in this section are plotted with the force along the y-axis. There are 3 data sets (data set 1-3) before cooling, 2 data sets between cooling with dry ice and cooling with liquid nitrogen (data set 4-5) and 1 data set after cooling with liquid nitrogen (data set 6). Figure 10 shows that there are no systematic changes in the calibration curves upon cooling and stress testing which shows the reproducibility and robustness of the load gauge. We therefore combine all 6 data sets and take the error on the calibration curve from the variation in the force curve, mostly derived from different cell assemblies, see inset. In the following, we term this the calibration error.

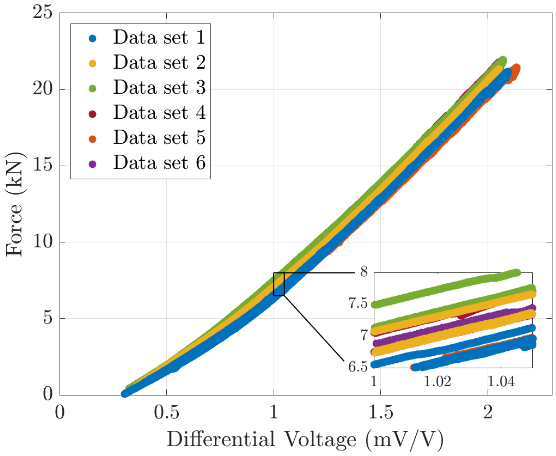

Figure 10. Differential voltage to force calibration curves for increasing force. The cell was assembled 6 times at room temperature (6 data sets) in order to create a calibration curve, and the force was increased to 22 kN 3 times within each data set. The inset contains a zoom which shows that variations between data sets are larger than variations within each data set.

Figure 11 shows the combined data of all 6 data sets along with a 3rd degree polynomial fit. Furthermore, the inset figure in the upper right left corner of figure 11 shows the relative residual differences between fit and data,

$$dF_{\mathrm{rel}} = \frac{F_{\mathrm{fit}} - F_{\mathrm{data}}}{F_{\mathrm{data}}}, \tag{3}$$

which are interpreted as the error on the calibration curve. It is below 5 % for forces above 15 kN as specified in system requirement S1. The main contribution to this error is variations between each cell assembly which is clearly seen in the zoom-inset of figure 10.

We now describe the calibrations at low temperatures, which were performed with the experimental setup that is presented in figure 12. Similarly to the room temperature calibrations, the load gauge is inside the cell to minimize horizontal components of the force. The cell is in a container which is filled with either liquid nitrogen or dry ice. The reference load gauge LC929 is calibrated down to 263 K, and the force was therefore transferred from the press to the cell through a steel rod to thermally disconnect the cell and press. Furthermore, the container was covered with an insulating lid in order to reduce evaporation of dry ice and liquid nitrogen, and in order to prevent cooling of the press. A PT100 thermometer was attached to the reference load gauge, and the temperature was always above 273 K. We estimate an error of 5 K due to the

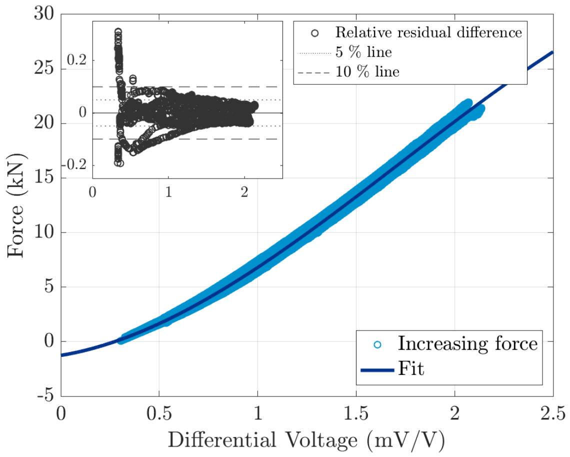

Figure 11. Room temperature force calibration of the load gauge for increasing force. A third degree polynomial has been fitted, fit parameters in table I. The relative residual difference is shown in the inset figure, where lines mark 5 % and 10 % relative residual difference.

difference of the temperature of the cell in liquid nitrogen and the thermometer readout.

During the calibration at 125 K, the cell was partly covered by liquid nitrogen. The discrepancy between liquid nitrogen cooling and evaporation, meant that the cell temperature increased by 3 K whilst calibrating. The last cold calibration at 195 K was done with the cell covered in dry ice. The system was allowed 4 hours to thermally stabilise due to the poor thermal contact between dry ice and the cell. The temperature was stable during the calibration within ΔT = ±-0.5 K.

Figure 13 shows the three cold calibration curves in addition to the room temperature calibration curve. The room temperature curve shows a larger deviation due to the accumulation of 6 data sets which we do not show for the other temperatures. All four calibration curves have been fitted to third degree polynomials with fit parameters listed in table I.

The two curves at 125 K and 80 K almost coincide which supports the assumption that the applied pressure will not change significantly at cryogenic temperatures compared to 80 K. All four calibration curves almost coincide at low applied forces, and the main difference is thus seen at large forces.

	a	*b*	*c*	*d*
300 K	-1.214(73)	6.29(27)	2.98(30)	-1.261(95)
195 K	-0.399(3)	3.887(11)	5.739(11)	-1.788(3)
125 K	-1.795(10)	7.976(32)	4.221(31)	-1.308(9)
80 K	-1.005(11)	5.213(35)	6.772(34)	-1.740(10)

Table I. Fit parameters of third degree polynomial fit ($ax^3 + bx^2 + cx + d$) to load gauge calibration data presented in figures 11 and 13.

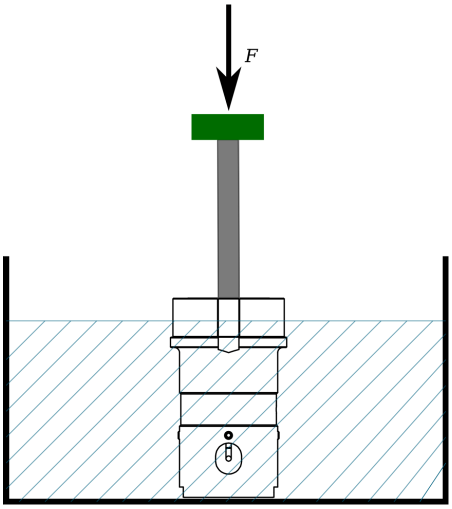

Figure 12. Experimental setup used to calibrate the load gauge at low temperatures. The load gauge, inside the pressure cell, was placed in an isolated container filled with liquid nitrogen or dry ice. Pressure was applied from a hydraulic force press through a stainless steel spacer rod once the load gauge temperature was stable. The rod was used to thermally disconnect the cell from the calibrated reference load gauge LC929 (green square).

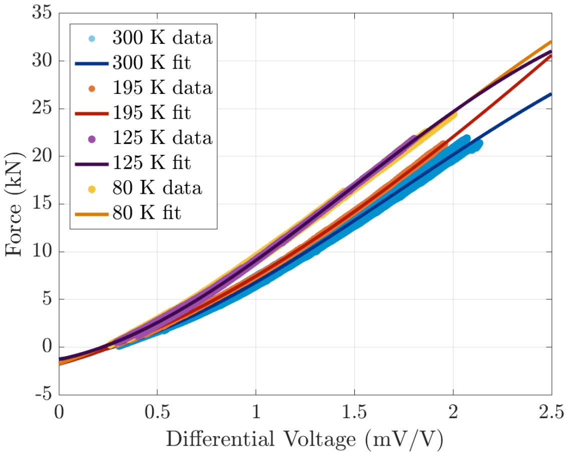

Figure 13. Force calibrations at 300 K, 195 K, 125 K and 80 K. Data from each temperature has been fitted to a third degree polynomial. Fit parameters are presented in table I. Calibration curves of 80 K and 125 K coincide. The 300 K curve consists of 6 data sets while the remaining temperatures consists of 1 data set each.

We do not calibrate the load gauge below liquid nitrogen temperatures, but we investigate the load gauge response at temperatures down to 26 K in a closed cycle refrigerator (CCR). This was done for the unloaded load gauge inside the cell.

Figure 14 shows the differential voltage output when the temperature is varied from 300 K to 26 K and back to 300 K twice. The error on the differential voltage is found from the standard deviation of the room temperature calibrations without applied load. The dominant contribution to this error is the cell assembly, while the statistical deviations during a calibration within the same cell assembly are insignificant in com-

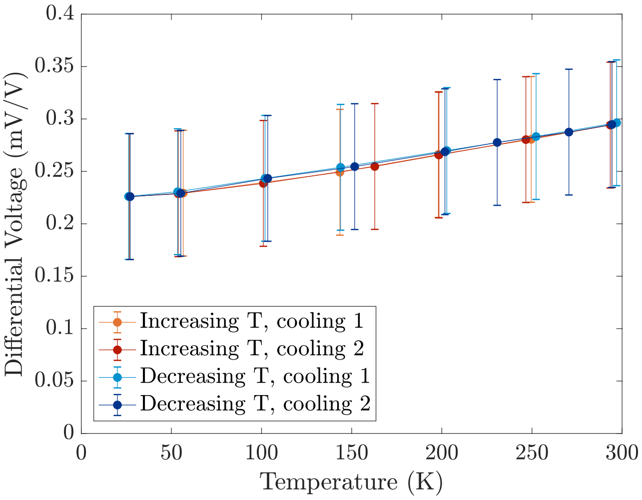

Figure 14. Differential voltage as a function of temperature, measured for the unloaded load gauge in a CCR cryocooler. Blue curves are decreasing temperature and orange/red curves are increasing temperature. The plotted errors are the calibration errors which are found from the room temperature calibrations. The cell was not disassembled between the two coolings which are presented here.

parison. The errors in figure 14 represent the errors of the cell assembly and they are therefore very large in comparison to signal variations. The load gauge response curve in figure 14 flattens as the temperature is decreased below 80 K, but it is not completely constant, which will introduce a small systematic error when using the 80 K calibration curve. The total change in signal between 300 K and 26 K is 0.07 mV/V which is 3.5 % of the room temperature signal at 22 kN. The measurement thus supports the results in figure 13 which show a very weak temperature dependence at low forces.

Figure 14 shows that there is a small hysteresis in the system, but it is of the order 0.002 mV/V which is 3 orders of magnitude less than the room temperature load gauge readout at 22 kN. The signal recovers once the load gauge returns to room temperature which shows the temperature robustness and stability of the load gauge.

III. TESTS RESULTS

In order to test the stability of the cell, it was left at room temperature with an initial load force of 12.6 kN for almost 60 hours, sufficient time for an inelastic neutron scattering experiment to be performed. The result is presented in figure 15. The applied force corresponds to 2 GPa pressure on a 2.8 mm diameter sample at room temperature. Figure 28 shows that during 60 hours, the force drops from 12.60 kN to 12.45 kN which is 1% of the initially applied force and less than the calibration error. It is also well within system requirement S1.

Figure 16 shows the temperature dependence of the drift for temperatures between 300 K and 250 K in 10 K steps. The differential voltage readout of the load gauge is converted to force with the room temperature calibration curve for all

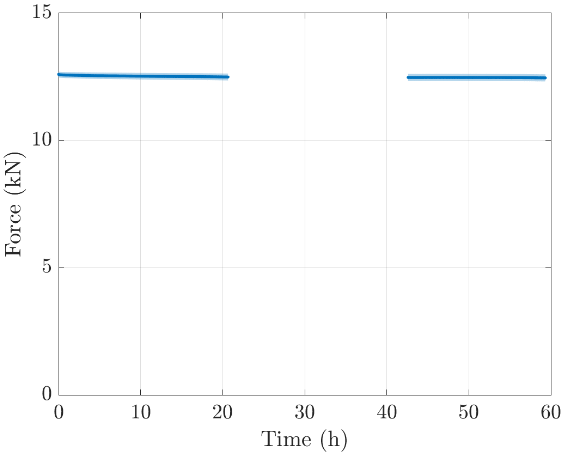

Figure 15. Room temperature stability test of the cell with a initially applied force of 12.6 kN applied. The force was measured during the following almost 60 hours. After approximately 21 hours, the data files were overwritten and not logged properly. This error was only corrected 21.5 hours later which is the reason for the missing data points in that time interval. The force decreases from 12.60 kN to 12.48 kN in 60 hours, which is less than 1% of the initially applied force.

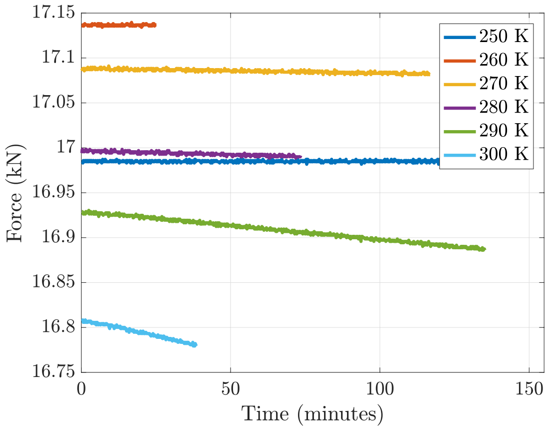

Figure 16. Stability tests of cell B performed at 10 K intervals from 300 K to 250 K. The room temperature calibration error is approximately 0.18 kN for these forces, see figure (see figure 11).

6 measurements. The force reduction is linear, and the slope decreases during a reduction of the temperature. Figure 17 show the slope of linear fits to each measurement as a function of temperature along with an exponential fit:

$$\text{slope} = A \exp\left(\frac{T}{T_0}\right), \tag{4}$$

with T_0 = 9.3 K. This shows that the force relaxation is thermally activated, possibly due to differing thermal contraction rates of the various materials in the cell, specifically steel 316 and CuBe thereby increasing friction between the top screws and the lid.

In order to simulate the pressure and temperature conditions

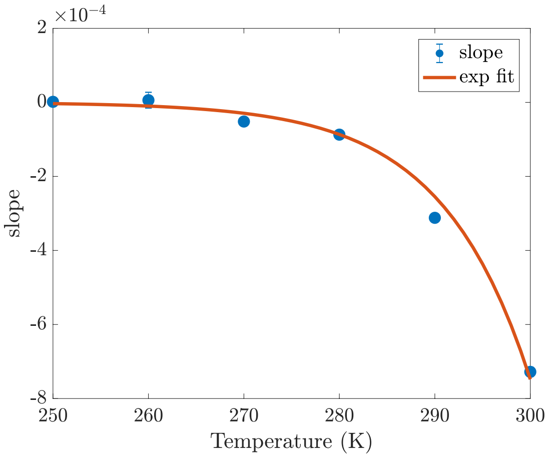

Figure 17. The slope of linear fits to the stability curves of figure 16. An exponential as defined in equation 4 has been fitted to the slope which is close to zero for 250 K.

of a neutron experiment, cell B was cooled with three different forces applied at room temperature. Figure 18 shows 6 curves: 3 for decreasing temperature (light colours) and 3 for increasing temperature (dark colours). The differential voltage readout of the load gauge is converted to force with the calibration curves in figure 13 which is nearest in temperature. Below 150 K, the force is stable, which is in compliance with the expectation that most materials contract very little below 100 K.

There is very little hysteresis between cooling and heating for all three applied forces, and the curves coincide except for the room temperature point in cooling 3, where there is a small discrepancy. The shape of the curves is similar, and it reflects the relative thermal coefficients of the materials in the cell. During this experiment, the steel seats of cell B (see section IV) were used, and the shape of the curves is thus primarily caused by the ratio between the thermal contraction of steel 316 and that of CuBe. During a neutron scattering experiment, the dominant contribution to the change in force is the relative ratio between CuBe and the sample, and it is therefore not possible to create an estimate of the shape of the curve, except for the expectation that it is likely to stabilise for temperatures below approximately 100 K.

Finally, figure 19 shows that the cooling of cell B from 300 K to 26 K lasted less than 30 hours with many intermediate steps in order to measure the differential voltage readout that has been used in figure 18. Cell C contains the same materials as cell B except for the WC10 anvils, which is used due to its hardness, but is also beneficial for cooling since it conducts heat better than steel 316. Figure 19 shows that the cell materials are sufficiently conducting to make it realistic to cool the cell to cryogenic temperatures in less than 24 hours in compliance with system requirement S5.

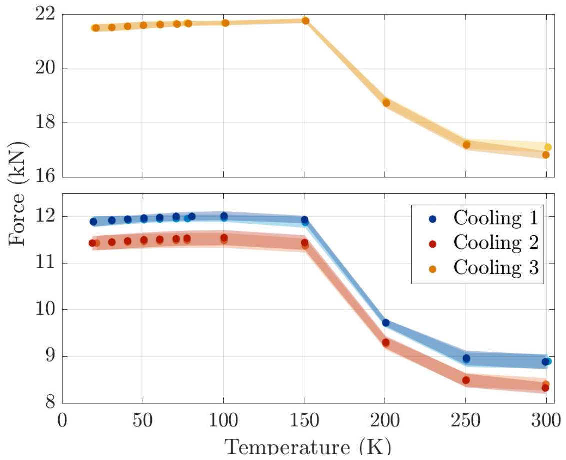

Figure 18. 3 different forces were applied to the cell (yellow, blue and red curves respectively). The cell was cooled to 26 K (light colours) and heated back to room temperature (dark colours) for all three forces. The hysteresis between heating and cooling is lower than the error.

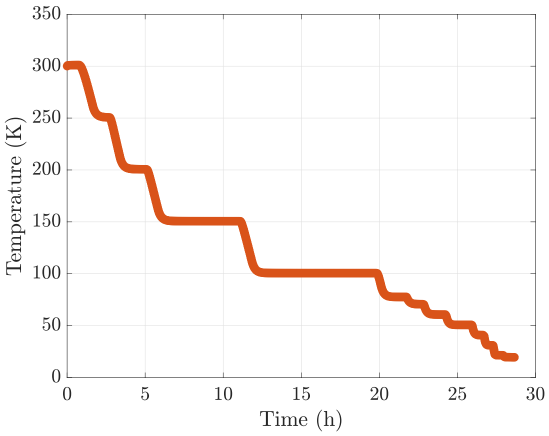

Figure 19. Temperature curve during cooling 1 of cell B. The entire cooling from 300 K to 26 K takes less than 30 hours with steps during the cooling to measure the differential voltage readout in thermal equilibrium.

IV. NEUTRON SCATTERING RESULTS AND DISCUSSION

As previously described, the cell development has been an iterative process. We here describe the results of the two first attempts, cell A and cell B, as well as the final optimised cell C.

A. Cell A

Figure 20 shows the drawings of the first cell constructed, cell A. The differences between cell A and cell B are:

- Cell A has large windows considered optimal for broad

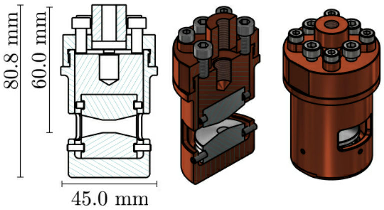

Figure 20. Drawings of cell A. Left: transparent technical drawing with outer dimensions and dimensions from top mounting to sample position. Center: a cut through the assembled cell. Right: the assembled cell.

diffuse scattering

- Force is applied externally to cell A and the external force readout is used as a pressure gauge.

The original intention was to apply the force with an external force press and cell A therefore has no load gauge. Furthermore, the lid is divided into two parts. The lower part contains a hole at the center and screw holes for four M5 top screws with a fine thread. The top screws have been polished flat at the tip where it transfers the force to the piston, to increase the surface area. Once the force is applied with the external press, the top screws are tightened to maintain the force, and the external press is released. Finally, a mounting lid which has an M6 hole is attached to the lower lid with 4 screws and these screws are thereby not exposed to large forces. Another difference between cell A and cell C is the windows in cell A. Cell A was made with 2 windows of 70 degrees opening angles each. However, this reduces the area in the cell cage around the sample position, and the walls of the cell cage are therefore 1 mm thicker compared to the walls at the sample position in cell C.

Cell A was tested at D7 at the ILL in 2018 with a similar experimental setup that is described in section II A 1. Figure 21 shows a photo of the cell, before the experiment. The cell cage is covered in Cd outside the beam position, and the seats are covered in Cd except at the culets of the seats. The figure also shows a crystal of the spin ice compound $Ho_2Ti_2O_7$ (HTO) which is placed between the seats. Measurements were performed at 1.5 K on HTO with the force applied along the crystalline c-axis.

The resulting neutron scattering intensity is presented in figure 22 and it shows the intensity on a colour scale along the two components of **Q** which are perpendicular to the applied force. The characteristic profile of HTO with diffuse scattering and pinch points is clearly observed for high Q above 1.5 Å^{-132}. However, for low Q, the intensity is not symmetric in all four quadrants as expected due to the cubic crystal symmetry. Instead, there is a high intensity area marked by the line L_2 and a low intensity area marked by the line L_1.

Figure 21. Cell A which has two large windows. Seats and the cell is covered in Cd outside the beam position. A cylindrical HTO sample is placed between the seats.

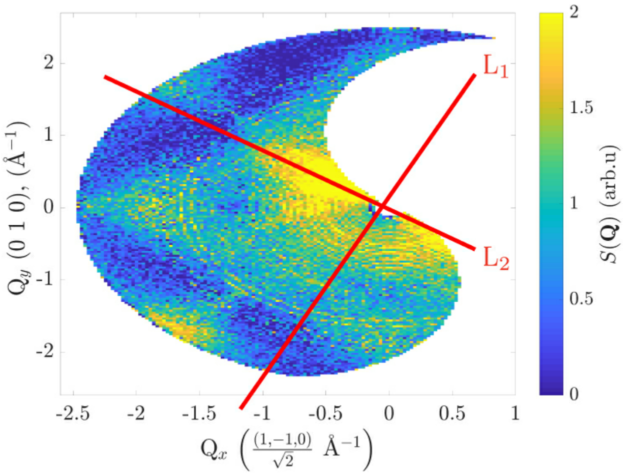

Figure 22. Measurement of HTO in cell A at 1.5 K. The background signal from the cell absorption marked by the red lines is stronger than the signal from HTO. The pressure induced changes are few percent of the intensity of the observed diffuse profiles.

The low Q features that are observed in figure 22 are also seen in figure 23 which is a measurement of the paramagnetic signal at 50 K. At this temperature, all spins in HTO are uncorrelated, and the expected profile from the crystal is the form factor decay of Ho^{3+} which decays homogeneously with Q and is rotationally symmetric. The observation of the low Q features in the paramagnetic signal shows that the features do not originate from the sample, but from the cell itself.

Figure 24 shows a simulation of a non-divergence neutron beam interacting with a point scatterer at the center of the cell and being attenuated through the cell walls. A form factor decay of HTO has been included in order to better compare with the paramagnetic signal in figure 23. A comparison of figures 23 and 24 shows remarkably good agreement despite the simplicity of the model. The low Q signal is thus dominated by background features which are caused by absorption in the cell walls. The pressure induced signals are typically only a few percent of the diffuse signal, and they are thereby difficult to resolve with the background of cell A. It is clear that these background contributions would not impede a neu-

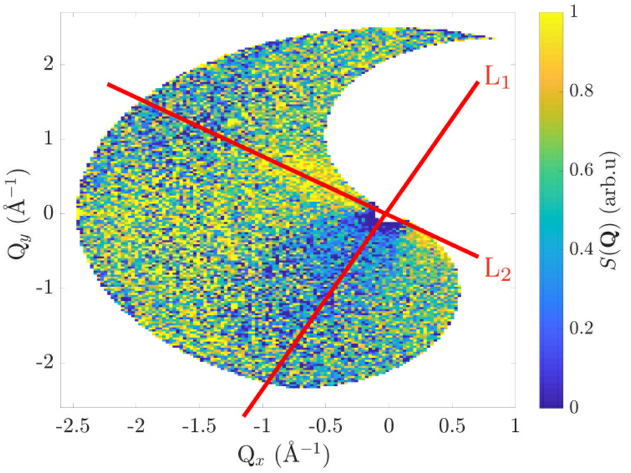

Figure 23. Neutron measurement of HTO in cell A at 50 K. The signal is measured in the paramagnetic regime of the sample where it has no features except the rotationally symmetric form factor decay. The regions of varying intensity marked by the two red lines L$_1$ and L$_2$ are an attenuation effect due to neutron absorption in the cell walls.

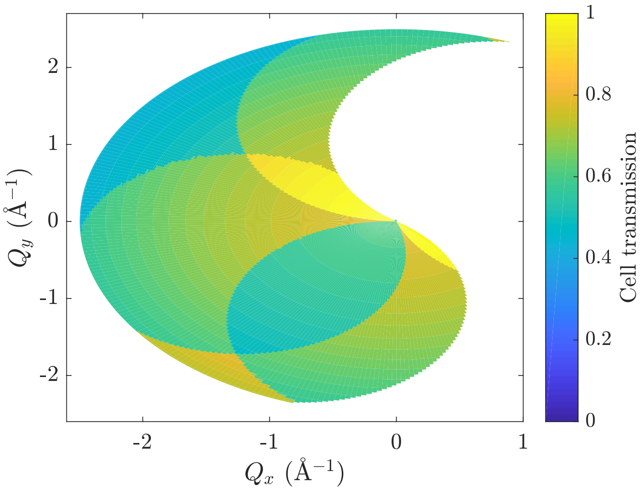

Figure 24. Simple simulation of the effect of the pressure cell windows. The attenuation caused by the cell walls lead to this very distinct pattern with regions of three levels of attenuation. These correspond to the neutron beam not being attenuated or once or twice.

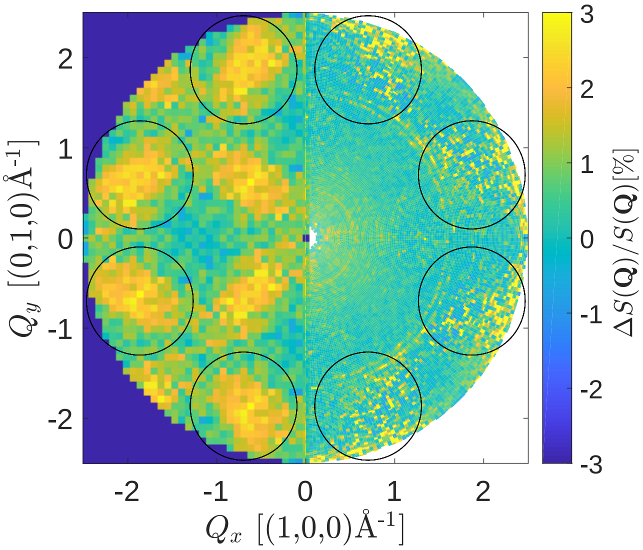

Figure 25. Comparison between MC simulations (left) and neutron data (right). Black circles mark regions with agreement between data and MC simulation. Figure from[1] .

tron scattering measurement of a well defined Bragg peak or dispersion curve but hampers the measurements of weak scattering profiles that we target.

The data is figure 22 has been normalised with the cell background simulation in figure 24 to further extract information. It is not possible to use the paramagnetic results from figure 23 directly because the noise is larger than the diffuse features in figure 22. It therefore introduces too much noise to the 1.5 K data in order to extract the spin ice pattern. Figure 25 shows the relative difference in the data profiles for ambient and pressurized data, which is defined as

$$\frac{\Delta S(\mathbf{Q})}{S(\mathbf{Q})} = \frac{S_{P>0} - S_{P=0}}{S_{P=0}}, \tag{5}$$

along with a Monte Carlo (MC) simulation of the expected signal. The background subtraction and the MC simulation are further described in ref.[1]. While there is agreement between data and simulation in the marked high Q regions, the data in the low Q regions are not convincing making it impossible to draw any firm conclusions regarding the low Q signal. This is especially unfortunate, since the interesting long-range correlations would appear most clearly at the lowest Q-values and because the form factor decay reduces the intensity of magnetic neutron scattering at higher Q. This is the reason why many relevant instruments have coverage on both the negative and positive detector banks at low Q for improved statistics in this range. All of the above of course indicates that cell A is not suitable for these measurements since we are not able to access the low Q regions.

To overcome the poor data access at low Q, we have completely removed the windows in later iterations of the cell and instead thinned the cell walls around the sample position. The cell walls in cell A are 3 mm thick, and with a linear attenuation coefficient for CuBe of $\mu_{BeCu} = 0.086$ mm^{-1}, the intensity is reduced by 40 %. The walls in cell B and cell C without windows are 2 mm thick around the sample position, which reduces the signal by 30 % in these cells. The experimental counting time is thereby increased, but with the high flux that will soon be available at the European Spallation Source, this will no longer be an essential hindrance, and it is therefore more important to optimise the signal to uniform noise.

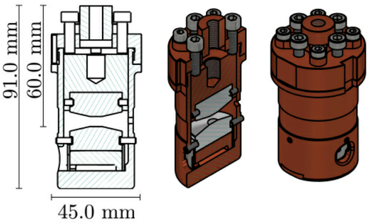

Figure 26. Drawings of cell B. Left: transparent technical drawing with outer dimensions and dimensions from top mounting to sample position. Center: a cut through the assembled cell. Right: the assembled cell.

B. Cell B

Figure 26 shows the drawings of the second iteration of the cell, cell B. The upgrade from cell A to cell B contains:

- Design, construction and calibration of a load gauge which can operate at cryogenic temperatures.
- Removal of windows and a thinning of the cell cage walls around the sample position.

With the removal of the windows, the cage of cell B is identical to the cage in cell C which was described in section II A 1. Without windows, the cross section area of the cell cage is increased, which motivated a reduction of the wall thickness at the sample position compared to cell A. Another successful part of the upgrade from cell A to cell B was the introduction of a load gauge that is identical to the load gauge in cell C and which was described in section II B.

In cell B, the force is applied in the same way as in cell A with M5 screws or with an external press through the hole in the lower lid. However, with the load gauge, it is possible to measure the applied force before and after the release of the external press. When the externally applied force is released, the force drops by a factor of 8-10 despite application of additional force with the top screws. Such a significant pressure loss means that we cannot measure, the crystal near the limit before it breaks, but the interesting research often happens near this limit. It is also possible to apply almost uniaxial force with the top screws directly by using a torque wrench and by cross-tightening the cross in small steps. There is no deformation of the screw thread, but the tip of the screws did indent during pressure tests which motivated the usage of M8 pinol screws in the final cell. The pinol screws were necessary because there is no room for the screw heads within the limitations of the cell size in system requirement S8.

Cell B is not able to meet system requirement S1 because the force is applied via steel 316 seats without anvils. Such a design resulted in indentation issues which motivated the development of separate anvils and seats. However, in scientific cases where pressures up to 200-300 MPa are desired, the steel seats can be used since they fit in cell C. The fact that steel 316 can deform is an advantage since it can compensate for small unparallellities in the sample which reduces the stress in the sample and thereby reduces the risk of breaking the sample.

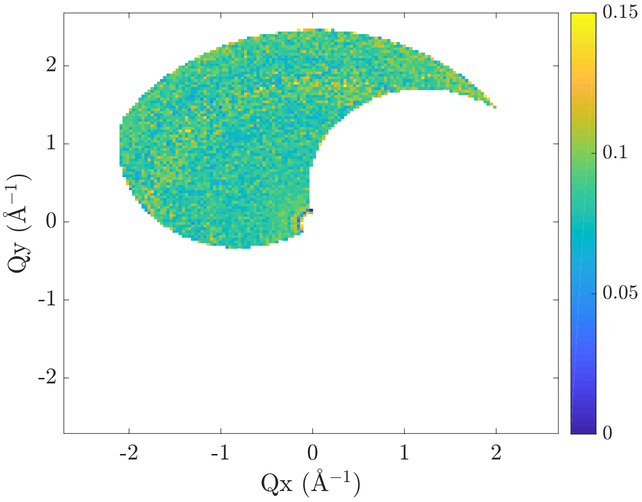

Figure 27. Spin flip neutron scattering background measurement of cell B from D7 (ILL) with an Al sample at room temperature. The intensity is plotted on a colour scale as a function of the two components of **Q** in the scattering plane. The cell signal is very uniform with sample rotation. The rings reflect variations in detector efficiencies (and maybe also a powder ring?).

A room temperature background neutron scattering measurement of the cell with an aluminum nut at the sample position was taken at the D7 instrument. Figure 27 shows the resulting intensity for variations as a function of the two **Q**-components in the scattering plane. The scattering profiles are uniform with sample rotation in compliance with system requirement S4. The rings reflect slight variation in detector and polarisation efficiencies. The powder rings for both Al and CuBe are outside the presented scattering range[24],

During the experiment, the neutron scattering profile of pressurized HTO at 1.5 K was measured, the result of which will be published elsewhere. However, due to the limitations of the seats and screws, the experiment was performed with approximately 0.35 GPa pressure instead of 2 GPa. This is above the yield strength of the steel 316 seats, and the seats therefore indented. However, the force was maintained, and it was possible to complete the measurements, but in order to reuse the seats and to fulfill system requirement S1, the seats were modified to the design in cell C which is specified in section II A 1. The sample cracked vertically during force application, but it stayed in the correct position between the seats and the cracked parts of the sample became coaligned crystals.

In order to test the stability of the cell, it was left at room temperature with an initial load force of 8.2 kN for 30 hours. This corresponds to 2 GPa pressure on a 2.3 mm diameter sample at room temperature. Figure 28 shows that during 30 hours, the cell loses 0.21 kN or 2.5 % of the initially applied force, which is less than the calibration error. It is also well within system requirement S1.

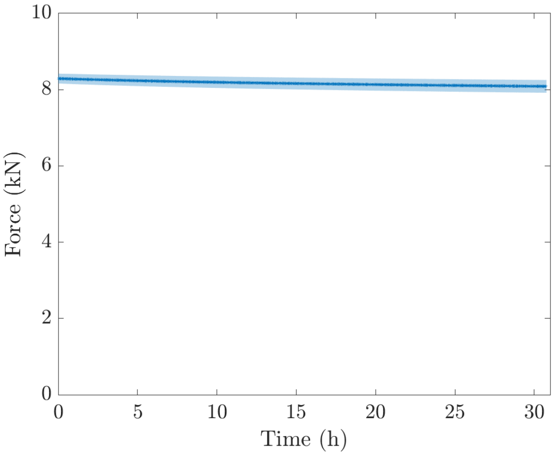

Figure 28. Measured load force as a function of time at room temperature in cell B. During 30 hours, the force decreases by 0.21 kN which corresponds to 2.5 % of the initially applied force. This is less than the calibration error.

C. Cell C: Final cell

With cell C, we meet system requirement S1 with a constant pressure of 2 GPa pressure for 60 hours within 1 % as shown in figure 15. Figure 1 shows that the cell allows 360 degrees horizontal scattering and ± 20 degrees vertical scattering, thereby exceeding the scattering ranges that were specified in system requirement S2. As described in the introduction, the most obvious neutron instruments to utilize this cell are D7, IN5, CNCS, AMATERAS, DNS, LET, and CAMEA. The vertical scattering range of the cell exceeds the vertical scattering ranges of all of these instruments - except LET that allows ±30 degrees vertical scattering. If there is a future demand for even larger vertical scattering angle coverage, it is possible to replace the current seats with new seats with a steeper angle since the current seats have a large safety margin based on the material specifications of WC10 and CuBe.

A load gauge has been designed, constructed and calibrated according to the specifications in system requirement S3. Figure 13 shows that we can use the calibration curve for liquid nitrogen to estimate the force even at cryogenic temperatures as discussed in section II B. The largest contribution to the uncertainty is termed the calibration error and it origins from the cell assembly. This error has been found based on the room temperature calibrations in figure 11 and is less than 5 % for forces above 20 kN.

Figure 27 shows that the neutron scattering background of cell B is symmetric under sample rotation as specified in system requirement S4. The rotationally symmetric design without windows that was used in cell B has also been used in the final cell C, and we therefore expect a rotationally symmetric background of cell C. A large cell background requires large counting times in order to obtain a reasonable statistics, and it is therefore the intention that the cell will be used at the new high intensity neutron sources such as the European Spallation Source.

Figure 19 shows that we were able to cool the cell from 300 K to 26 K in less than 30 hours with many intermediate steps to allow the cell temperature to stabilise before a differential voltage was measured. We therefore conclude that we have used materials in the cell that are sufficiently thermally conducting to cool the cell in less than 24 hours during a neutron scattering experiment as defined in system requirement S5.

With cell C, it is possible to accommodate samples which are up to 6 mm in diameter and up to 8 mm high, and the materials in the cell are all non-magnetic as specified in system requirements S7 and S6 respectively. As specified in figure 2, the outer cell dimensions do not exceed 45 mm, so it fits inside the most commonly used cryostats for neutron scattering experiments as specified in system requirement S8. System requirement S9 regarding neutron activation is met for all parts of the cell except for the WC10 anvils which are expected to be difficult to retrieve from the facilities upon a neutron scattering experiment, especially at high flux instruments, due to the long decay time of Co. We therefore expect to construct several pairs of anvils and seats and store them at the facilities.

The main challenge with the use of cell C is the sample preparation, since single crystal samples with low mosaicity must be polished to have 2 planar and parallel surfaces to prevent breakage. Furthermore, if the samples are not perfectly cylindrical, the uniaxial pressure cell create tension in the crystal which also increase the risk of breaking the crystal. If only low forces are required (up to 200 MPa), it is possible to use the steel seats from cell B. These are softer than the WC anvils, and they can indent slightly in order to compensate for small non-parallellities in the sample or during force application.

We used Cell C for an experiment at the ThALES triple-axis instrument in 2021[33]. We aimed for a modest pressure of 30 MPa on a single crystal sample of the cuprate superconductor $(La,Ba)_2CuO_4$ to study the effect of uniaxial pressure on the weak, incommensurate magnetic signal, denoted as stripes[34]. The scientific results of this experiment will be published elsewhere[35].

In the ThALES experiment, we prepared the sample as a cylinder of 5.0 mm diameter and 3.9 mm height and used a custom-made polishing setup to create smooth and parallel surfaces. We tested the pressure cell by performing a couple of test experiments with the load screws and W-seats on similar $(La,Ba)_2CuO_4$ samples, while measuring the pressure with the strain gauge. In the first test, the crystal broke upon applying 200 MPa pressure, while in the second test, the crystal broke while quench-cooling in liquid N_2 after being pressurised up to around 30 MPa. For the neutron experiment, we therefore chose to revert to the slightly softer steel seats, as we only needed a very modest pressure. Additionally, we loaded the pressure extremely slowly, as shown in figure 29. We subsequently cooled the cell with sample to 2 K with a rather slow rate of around 0.5 K/min. The total cool time to 2 K was about 8 hours, again confirming that we easily reach the system requirement S5. In the experiment, the crystal suffered no damage and the pressure maintained well. The measurement without pressure was performed with the crystal mounted in

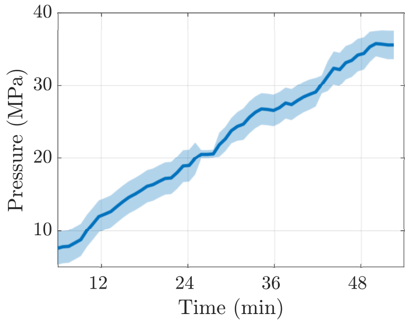

Figure 29. Real-time visualization of the applied pressure at room temperature when manually loading cell C for the ThALES neutron experiment[35]. A pressure difference of around 30 MPa was obtained.

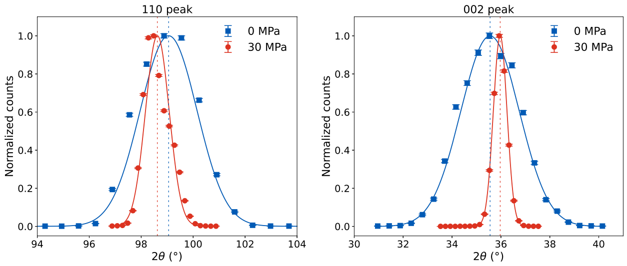

Figure 30. Alignment scans of (left) the (110) and (right) the (002) Bragg peaks. The data is normalized for easy comparison. Data taken using $k_i = 1.55$ Å^{-1}. With collimation of 40' for the pressurized data.

cell C, to keep the background comparable. The weight of the piston (∼ 180 g) was used to keep the crystal in place. As shown in figure 29, a pressure offset of roughly 6 MPa was present at room temperature and this corresponded to an offset of roughly 2 MPa at base temperature. Note that the relative error margins are relatively large at such small pressures.

Notably, we first measured the magnetic stripes without pressure, before repeating the measurement with pressure. As a result, we applied the pressure after 3 days in the massive neutron flux of ThALES. Therefore, the cell needed to deactivate for roughly 12 hours before the activation level had fallen to below 100 μSv/hour, needed to safely apply the pressure manually.

Unfortunately, two wires to the pressure gauge broke during the sample exchange of the ThALES experiment, so we could not measure the pressure at base temperature during the neutron experiment. However, 10 days after the experiment, where the cell had been standing at room temperature, the wires were re-soldered and the pressure reading was 18 MPa. The cell was then cooled in the cryostat, again by 0.5 K/hour, and the pressure reading was 15 MPa. This shows that the cell stays under pressure for an extended time period, even at room temperature. The pressure decay rate is around 5% of the total pressure per day, which is somewhat higher than that value of 2% per day seen from the high-pressure tests in figure 28. However, the small difference in pressure between room temperature and base temperature, of comparable size to the offset observed without pressure as stated above, allowed us to determine the pressure during the experiment and we are confident that the pressure was close to 30 MPa during the ThALES experiment.

Additionally, the lattice parameters were changed significantly upon applying pressure. The parameters (in tetragonal settings) changed from $a = b = 3.7679(5)$ Å and $c = 13.2764(6)$ Å to $a_p = b_p = 3.7802(2)$ Å and $c_p = 13.1287(6)$ Å. In figure 30, we show the alignment scans of the (110) and (002) Bragg peaks of the crystal. To observe the weak stripe signal, we needed to use 40' collimation on both incoming and outgoing beam, which reduced the background by a factor 100 (CHECK).

D. Possibilities beyond Cell C

In Cell C, the force is applied with 4 screws, which is intrinsically non-uniaxial. An even amount of force is ensured with a torque wrench, and diagonal tightening of the screws. However, non-unaxial components to the force are unavoidable while the force is applied which might cause jamming of the piston if too much force is applied at a time and it causes tension in the crystal. A more user friendly design only has a single top screw which applies the force, but this requires a torque of approximately 75 Nm in order to apply a force of 22 kN. For this reason, gearing might be necessary in order to apply it in a controlled way. Furthermore, it is important that the anvil does not rotate when the screw is rotated, because this will increase the tension in the sample, which could cause it to break. These two challenges makes the design with a single top screw significantly more complex, and the simpler 4-screw design presented here is therefore preferred.

V. CONCLUSION

We have designed, tested and calibrated a pressure cell aimed for diffuse neutron scattering and inelastic neutron scattering for the study of strongly correlated magnetic systems. We have performed several successful neutron scattering experiments at the diffuse scattering instrument D7 at the ILL showing that the cell does indeed comply with the system requirements. An experiment on the triple-axis spectrometer ThALES further shows that the cell performs well also on this type of instrument, that our in-situ pressure monitoring device works, and that a massive neutron flux does not lead to excessive activation of the cell.

ACKNOWLEDGMENTS

We thank the ILL for providing beam time for the the neutron scattering measurements on D7 and ThALES, which were also supported by the Danish Agency for Innovation and Research through DANSCATT, grant number 7129-00003B.

LØS, IMBB, and RE were supported by Nordforsk through the Nordforsk project 82248 "Magnetic Frustration Under Pressure". MLH was supported by a student grant from the Siemens Foundation. MEK was supported by MSCA-IF Horizon 2020, grant number 838926.

....

Appendix A: Appendixes

Appendix B: Drawings of all parts of the cell

Appendix C: Drawings of the Load Gauge and additional photos

REFERENCES

[1] R. Edberg, L. Ø. Sandberg, I. M. B. Bakke, M. L. Haubro, L. C. Folkers, A. Wildes, O. Zaharko, M. Guthrie, A. T. Holmes, M. H. Sørby, K. Lefmann, P. P. Deen, and P. Henelius, "Dipolar spin ice under uniaxial pressure," Physical Review B **100**, 144436 (2019).

[2] G. Sala, M. J. Gutmann, D. Prabhakaran, D. Pomaranski, C. Mitchelitis, J. B. Kycia, D. G. Porter, C. Castelnovo, and J. P. Goff, "Vacancy defects and monopole dynamics in oxygen-deficient pyrochlores," Nature Materials **13**, 488–493 (2014).

[3] K. A. Ross, T. Proffen, H. A. Dabkowska, J. A. Quilliam, L. R. Yaraskavitch, J. B. Kycia, and B. D. Gaulin, "Lightly stuffed pyrochlore structure of single-crystalline $yb_2ti_2o_7$ grown by the optical floating zone technique," Phys. Rev. B **86**, 174424 (2012).

[4] T. Biesner and E. Uykur, "Pressure-Tuned Interactions in Frustrated Magnets : Pathway to Quantum Spin Liquids ?" Crystals **10**, 1–23 (2020).

[5] I. Mirebeau, I. N. Goncharenko, P. Cadavez-Peres, S. T. Bramwell, M. J. P. Gingras, and J. S. Gardner, "Pressure-induced crystallization of a spin liquid," letters to nature **420** (2002).

[6] E. Kermarrec, J. Gaudet, K. Fritsch, R. Khasanov, Z. Guguchia, C. Ritter, K. A. Ross, H. A. Dabkowska, and B. D. Gaulin, "Ground state selection under pressure in the quantum pyrochlore magnet Yb2Ti2O7," Nature Communications **8**, 6–10 (2017).

[7] K. Umeo, D. Watanabe, K. Araki, K. Katoh, and T. Takabatake, "Uniaxial-Pressure-Induced Release of Magnetic Frustration in a Triangular Lattice Antiferromagnet YbCuGe," Metals **11** (2021), https://dx.doi.org/10.3390/met11010030.

[8] I. Mirebeau and I. N. Goncharenko, "Spin ice and spin liquid under pressure up to 8.6 GPa : A powder neutron diffraction study of $R_2Ti_2O_7$ (R = Tb , Ho)," Physica B **350**, 250–253 (2004).

[9] R. Edberg, I. M. B. Bakke, H. Kondo, L. O. Sandberg, M. L. Haubro, M. Guthrie, A. T. Holmes, J. Engqvist, A. Wildes, K. Matsuhira, K. Lefmann, P. P. Deen, M. Mito, and P. Henelius, "Effects of uniaxial pressure on the spin ice $Ho_2Ti_2O_7$," Phys. Rev. B **102**, 184408 (2020).

[10] A. Molak, M. Koralewski, G. Saunders, and W. Juszczykj, "Effects of uniaxial pressure on the ferroelectric phase transition in pb5ge3o11:ba crystals," Acta Physica Polonica A.

[11] T. Nakajima, Y. Iguchi, H. Tamatsukuri, S. Mitsuda, Y. Yamasaki, and H. Nakao, "Uniaxial pressure effects on magnetic and crystal structural phase transitions in a frustrated magnet cufe1-xgaxo2 (x=0.035)," Photon Factory Activity Report, 2012 **30** (2013).

[12] J. R. Stewart, P. P. Deen, K. H. Andersen, H. Schober, J.-F. Barthélémy, J. M. Hillier, A. P. Murani, T. Hayes, and B. Lindenau, "Disordered materials studied using neutron polarization analysis on the multi-detector spectrometer, D7," J. Appl. Cryst. **42**, 69 (2009).

[13] J. A. M. Paddison, H. Jacobsen, O. A. Petrenko, M. T. Fernández-Díaz, P. P. Deen, and A. L. Goodwin, "Hidden order in spin-liquid Gd_3Ga_5O12," Science **350**, 179–182 (2015).

[14] L. Ø. Sandberg, R. Edberg, I.-M. B. Bakke, K. S. Pedersen, M. C. Hatnean, G. Balakrishnan, L. Mangin-Thro, A. Wildes, B. Fåk, G. Ehlers, G. Sala, P. Henelius, K. Lefmann, and P. P. Deen, "Emergent magnetic behavior in the frustrated $Yb_3Ga_5O_{12}$ garnet," Phys. Rev. B **104**, 064425 (2021).

[15] T. Fennell, L. Mangin-Thro, H. Mutka, G. J. Nilsen, and A. R. Wildes, "Wavevector and energy resolution of the polarized diffuse scattering spectrometer D7," Nuclear Inst. and Methods in Physics Research, A **857**, 24–30 (2017).

[16] J. Ollivier, H. Mutka, and L. Didier, "The new cold neutron time-of-flight spectrometer in5," Neutron News **21**, 22–25 (2010), https://doi.org/10.1080/10448631003757573.

[17] G. Ehlers, A. A. Podlesnyak, and A. I. Kolesnikov, "The cold neutron chopper spectrometer at the Spallation Neutron Source—a review of the first 8 years of operation," Rev. Sci. Instrum. **87**, 093902 (2016).

[18] K. Nakajima, S. Ohira-Kawamura, T. Ktxucm, M. Nakamura, R. Kajimoto, Y. Inamura, N. Takahashi, K. Atzawa, K. Suzuya, and K. Shibata, "AMATERAS : A Cold-Neutron Disk Chopper Spectrometer," J. Phys. Soc. Jpn. **80**, SB028 (2011).

[19] R. Bewley, J. Taylor, and S. Bennington., "Let, a cold neutron multi-disk chopper spectrometer at isis," Nuclear Instruments and Methods in Physics Research Section A: Accelerators, Spectrometers, Detectors and Associated Equipment **637**, 128–134 (2011).

[20] Y. Xu, K. Nemkovskiy, and S. Demirdis, "DNS: Diffuse scattering neutron time-of-flight spectrometer," Journal of large-scale research facilities **1** (2015), http://dx.doi.org/10.17815/jlsrf-1-33.

[21] F. Groitl, D. Graf, J. O. Birk, M. Markó, M. Bartkowiak, U. Filges, C. Niedermayer, C. Rüegg, and H. M. Rønnow, "Camea—a novel multiplexing analyzer for neutron spectroscopy," Review of Scientific Instruments **87**, 035109 (2016), https://aip.scitation.org/doi/pdf/10.1063/1.4943208.

[22] C. W. Hicks, S. Ghosh, M. E. Barber, and H.-H. Klauss, "Piezoelectric-Driven Uniaxial Stress Apparatus for Muon Spin Rotation," JPS Conference Proceedings **21**, 1–7 (2018).

[23] B. Haberl, S. Dissanayake, F. Ye, L. L. Daemen, Y. Cheng, C. W. Li, A. J. Ramirez-Cuesta, M. Matsuda, J. J. Molaison, and R. Boehler, "Wide-angle diamond cell for neutron scattering," High Pressure Research **37**, 495–506 (2017).

[24] M. Kibble, V. Laliena, C. Goodway, E. Lelièvre-Berna, K. Kamenev, S. Klotz, and O. Kirichek, "Low-background materials for high pressure cells used in inelastic neutron scattering experiments," Journal of Neutron Research **21, no 3-4**, 105–116 (2019).

[25] N. J. Simon, E. S. Drexler, and R. P. Reed, *Properties of Copper and Copper Alloys at Cryogenic Temperatures* (Nist Monograph 177, 1992).

[26] A. materials, "`https://www.azom.com/properties.asp`," (visited June 2021).

[27] m. Hyperion and technology, "`http://www.allaboutcementedcarbide.com/what-is-cemented-carbide/thermal-properties/`," (visited June 2021).

[28] K. Hoffmann, *An introduktion to Measurements using Strain Gages* (Hottinger Baldwin Messtechnik Gmbh, Darmstadt, 1989).

[29] J. Fish and T. Belytschko, *A First Course in Finite Elements*, 1st ed. (Wiley, 2007).

[30] P. Duthil, "Material Properties at Low Temperature," in *Proceedings of the CAS-CERN Accelerator School: Superconductivity for Accelerators*, Vol. 005 (2014) pp. 77–95.

[31] N. I. of Standards and U. D. o. C. Technology, "Material properties: Beryllium copper," `https://trc.nist.gov/cryogenics/materials/Beryllium\%20Copper/BerylliumCopper_rev.htm`, accessed: June 18, 2020.

[32] C. Castelnovo, R. Moessner, and S. L. Sondhi, "Spin Ice, Fractionalization, and Topological Order," Annual Review of Condensed Matter Physics **3** (2012), 10.1146/annurev-conmatphys-020911-125058.

[33] ILL, doi:10.5291/ILL-DATA.5-41-1159.

[34] J. M. Tranquada, B. J. Sternlieb, J. D. Axe, Y. Nakamura, and S. Uchida, "Evidence for stripe correlations of spins and holes in copper oxide superconductors," Nature **375**, 561–563 (1995).

[35] M. E. Kamminga, K. L. M. Krighaar, A. T. Rømer, L. Ø. Sandberg, P. P. Deen, M. Boehm, G. Gu, J. M. Tranquada, and K. Lefmann, "Evolution of magnetic stripes under uniaxial pressure in $La_{1.885}Ba_{0.115}CuO_4$ studied by neutron scattering," in preparation (2021).

A.5 Manuscript 2: Single crystal growth of pyrochlore titanate oxides (RE2Ti2O7) by optical zone melting for neutron and magnetic property studies

I have participated in design and execution of the pressing and sintering of the crystal powder rods and the crystal growth of the $Ho_2Ti_2O_7$(HTO) crystals in the mirror furnace in Lund. The initial design of the HTO sample growth was chosen based on studies on other compounds that I performed in collaboration with Laura Folkers at the University of Lund. I also participated in the initial sample characterization with X-ray and neutron Laue diffraction in collaboration with Ingrid Marie Bakke Fjällvågen.

Single crystal growth of pyrochlore titanate oxides ($RE_2Ti_2O_7$) by optical zone melting for neutron and magnetic property studies

I. M. Bakke Fjellvåg,[*,†] M. L. Haubro,[‡] L. Ørduk Sandberg,[‡] R. Edberg,[¶] K. Lefmann,[‡] P. Henelius,[¶,§] T. Hansen,[‖] O. R. Fabelo Rosa,[‖] B. C. Hauback,[⊥] and P. P. Deen[#,@]

†*Center for Materials Science and Nanotechnology (SMN), University of Oslo, Oslo, Norway*

‡*Nanoscience Center, Niels Bohr Institute, University of Copenhagen, Copenhagen, Denmark*

¶*Physics Department, KTH Royal Institute of Technology, Stockholm, Sweden*

§*Faculty of Science and Engineering, Åbo Akademi University, Åbo, Finland*

‖*Institut Laue-Langevin, Grenobe, France*

⊥*Institute for Energy Technology (IFE), Kjeller, Norway*

#*Niels Bohr Institute, University of Copenhagen, Copenhagen, Denmark*

@*European Spallation Source ERIC, 22363 Lund, Sweden*

E-mail: i.m.b.fjellvag@smn.uio.no

Abstract

We demonstrate the suitability of the floating zone technique for growth of stoichiometric pyrochlore $RE_2Ti_2O_7$ single crystals of high quality, a technique that has previously been reported to be unsuitable. We focus our synthesis on $Ho_2Ti_2O_7$ and $Yb_2Ti_2O_7$.

For these, the floating zone technique provides crystals with a hue consistent with expected electronic state and oxygen stoichiometry.

The quality and structural state of precursors and obtained single crystals have been ascertained by x-ray and neutron scattering investigations. We claim that a step with synthesis of high quality stoichiometric powders is a key component for subsequently producing stoichiometric single crystals. In order to aid future growth of pure and chemically modified crystals, we provide a detailed outline of synthesis route and growth parameters.

Our neutron based studies reveal that although we have at hand high quality single crystals, we observe structural deviations connected with the 8a oxygen sites in terms of unexplained features along the strong crystal field directions. This is of importance since the physics of the spin ice compounds are often defined by their crystal field states. This work complements and refines earlier studies with a strong focus on oxygen sites.

Introduction

Any gained insight to materials is strongly dependent on the quality of the powders and single crystals experimentally probed. Impurities or deviations in stoichiometry will in most cases alter the resultant physical properties of the system. This is a particular problem for probes that require large samples of which neutron scattering is one. Neutrons interact weakly with matter which is advantageous since the resultant scattering profile, the double partial partial differential cross section, is proportional to the dynamic structure factor S($\mathbf{Q}$, ω), dependant on the wavevector transfer between sample and neutrons, $\mathbf{Q}$, and the neutron energy transfer between sample and neutrons, ω, respectively, can be theoretically determined via the Born approximation. The subsequent data analysis enables for instance the direct determination of phonon force constants and magnetic exchange interactions in materials and provides means to understand material properties. As such, neutron scattering is a very important tool, however, it suffers from being interaction and flux limited. Hence, large samples (1 cm^3) are necessary. Large crystals, in excess of mm^3, are difficult to grow and prone to imperfections. This is well recognised in the field of frustrated magnetism and is a challenge in the study and characterisation of novel states of matter.[1] In the current work we outline a procedure to synthesise high quality single crystals of the archetypal frustrated magnet $Ho_2Ti_2O_7$, a rare-earth pyrochlore type oxide. We provide a detailed, step-by-step explanation starting with synthesis and characterisation of an initial powder sample, follwed by characterisation of an optimum single crystal using neutron diffraction at D9, ILL. Particular emphasis is placed on achieving control on oxygen stoichiometry which is important for the physical properties of these materials.

Geometrically frustrated materials such as spin ice materials, $RE_2Ti_2O_7$ (RE = rare earth), represent an excellent playground for novel states of matter like spin ice, spin liquids, and spin glasses.[2–4]Spin ice materials follow the ”spin ice rules” first described by Bernal and Fowler,[5] and adopted by Pauling[6] to describe the mismatch between the crystal structure and hydrogen bonding that occurs in water ice, H_2O, from which the name ”spin ice” is derived.[6]

The crystal structure adopted by rare-earth pyrochlore oxides is a model system for a geometrically frustrated compound. In this case, all pairwise magnetic interactions cannot be satisfied simultaneously, giving rise to multiple degenerate ground states at a microscopic level. This leads to zero-point (residual) entropy for the spin-ice materials,[2,7] .

For this type of systems, even small deviations from the ideal composition, in the form of impurities, intrinsic magnetic defects or non-stoichiometry may have a strong impact on the physics of the materials in the form of enhanced electronic contribution to heat capacity, glassy behaviour from defect spins, extra diffusion pathways or altered malleability.[1] It is helpful to consider the thermodynamics of the binary constituents. For instance, in the case of $Ho_2Ti_2O_7$, it is relevant to question the redox properties and possibility of oxygen vacancies in the Ti-based atomic arrangement. Hence, insight to and controlling oxygen vacancies that may alter the intrinsic properties of these materials, is critical for theoretical and experimental research. As such it is paramount that such aspects are properly evaluated for single crystals in neutron and magnetic property studies.

There are numerous reports of single crystal growth of pyrochlore oxides using flux, optical floating-zone, travelling solvent floating-zone and Czochralski methods.[8–11] An extensively used synthesis method for large single crystals of rare-earth titanates is the floating zone method. With moderate efforts single crystals can easily be grown.[12] This provides a facile route for larger single crystals that are a necessity for neutron scattering studies. Interestingly, there are quite contradictory reports concerning the color of the crystals obtained from single crystal growth by the floating zone technique, with the color ranging from clear orange to black for $Ho_2Ti_2O_7$ and from light brown to red for $Yb_2Ti_2O_7$.[13–18] A change in color signifies a change in electronic structure, either at the local or the bulk level and may point towards unexpected impurities or defects, for instance undesired deviations in cation or anion stoichiometry.

Ghasemi et al. and Arpino et al. considered the floating zone technique as unsuitable for several pyrochlore oxides,[11,16] claiming that these materials melt incongruently and that non-stoichiometric crystal could emerge from the flux growth. This thereby questions earlier reports on successful growth of $RE_2Ti_2O_7$ (RE = Ho, Yb) with the floating zone technique.

Through extensive work on pyrochlores, Trump et al. observed small deviations from the ideal atomic arrangment in $Yb_2Ti_2O_7$ and $A_2B_2O_7$ (A = Pr, La,; B = Zr).[19] Through the use of neutron and X-ray PDF (pair distribution function) methods they probed the local structure and observed displacements from the Fd-3m ideal Wyckoff sites, in the range of 0.004 - 0.015 nm in $Yb_2Ti_2O_7$ and $Pr_2Zr_2O_7$ consistent with a β-cristobalite distortion. They further observed a broad, non-symmetric peak in ^{91}Zr nuclear quadrupole resonance on $Pr_2Zr_2O_7$ and argued that this is due to variations in next-nearest neighbor distances. They suggested that the displacements could be caused by A/B cation size mismatch and may occur for a wide range of pyrochlore materials.

In this work we find that the floating zone technique is highly suitable for the growth of high-quality $Ho_2Ti_2O_7$ single crystals, in agreement with earlier work.[13,20] We outline a procedure to help ensure optimal crystal growth, expectedly of general value. We suggest that the technique can be equally well applied to related rare-earth pyrochlore oxides and document this by the growth of $Yb_2Ti_2O_7$ crystals. The starting reactants and $Ho_2Ti_2O_7$ products are benchmarked by extensive structural characterisation using x-ray and neutron diffraction, and broad Q-range single neutron diffraction measurements, with due attention on parameters like oxygen atomic positions and product stoichiometry. We propose that the color of the crystal will in many cases be a good indicator of stoichiometry and sample quality.

Based on our experience we argue that poor synthesis of the precursor powder is a likely origin of difficulties encountered when synthesising single crystals with the floating zone technique. In order to achieve correct stoichiometry of the crystal, it is vital to have a a high quality powder with full control on cations and oxygen content. This specifies a path to stoichiometric single crystal growth of rare-earth titanates. We demonstrate universality of the growth method by reporting results from a test growth of $Yb_2Ti_2O_7$ single crystal.

Crystal structure

The crystal structure of pyrochlore oxides with general formula $A_2B_2O_7$, space group Fd-3m, can be derived from the MX_2 fluorite type structure of CaF_2, Figure 1 by a 2 x 2 x 2 doubling of the unit cell. The tetrahedral 8c anion sites of the fluorite structure, split into 8a, 8b and 48f sites when moving to the pyrochlore structure (Z = 8). In the pyrochlore structure, the 8b sites are systemtically empty and the oxygen 48f sites take a lower local symmetry, see Table 2 and 1, and Figure 1 a) and b). The A and B cations are ordered on the Ca-sites, and their coordination changes from cubes (in CaF2) owing to the systematic O-vacancies and O-displacements.

The structure for rare-earth titanate pyrochlores can be visualized as two intertwining sublattices of corner sharing tetrahedra, one consisting of rare-earth elements and titanium, respectively. Localised magnetic moments positioned at the cations in the corners of the tetrahedra provide the origin of the geometric magnetic frustrations observed in several RE-based compounds adopting this structure.[21] For certain element combinations, there exists pyrochlore variants with either ordered or disordered oxygen vacancies.

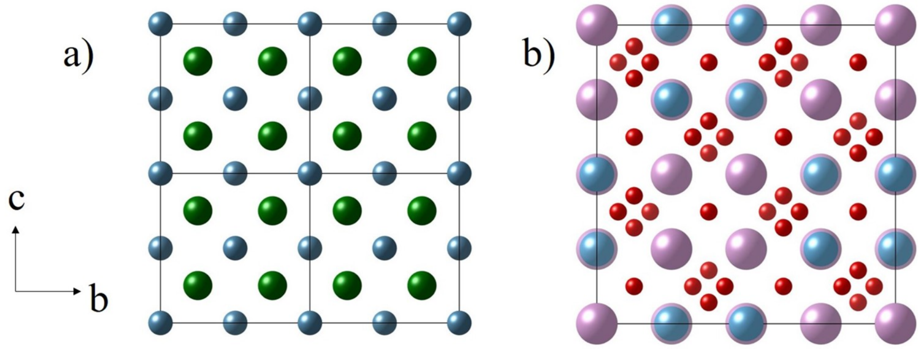

Figure 1: Crystal structure of a) 2x2x2 super-cell of CaF_2, Ca^{2+} in blue and F^- in green, space group Fm-3m and b) $Ho_2Ti_2O_7$, Ho^{3+} in pink, Ti^{4+} in blue and O^{2-} in red, space group Fd-3m. Structures drawn with the visualization program VESTA.[22]

Table 1: Wyckoff sites for space group Fm-3m (225) and corresponding atoms for CaF_2.

Wyckoff site	x	y	z	atom at site
4a	0	0	0	Ca
8c	1/4	1/4	1/4	F

Table 2: Wyckoff sites for space group Fd-3m (227) origin choice 2 with corresponding atoms, and x parameter for Wyckoff site 48f in parenthesis, for $Ho_2Ti_2O_7$

Wyckoff site	x	y	z	atom at site
8a	1/8	1/8	1/8	O
8b	3/8	3/8	3/8	not occupied
16c	0	0	0	Ho
16d	1/2	1/2	1/2	Ti
48f	x(0.4286)	1/8	1/8	O

Experimental

Powder synthesis

Powders with nominal composition $Ho_2Ti_2O_7$ were synthesized from stoichiometric amounts of the starting materials Ho_2O_3 (Sigma-Aldrich purity: $\geq$ 99.9%) and Ti-isopropanol (Sigma-Aldrich purity: 99.999%) in batches of 4 – 12 g. The molar content of cations in the starting reactant were assured by gravimetric analysis. Prior to the synthesis, an aqueous (Type II water) holmium solution was prepared to ensure liquid (atomic) mixing of the reactants during synthesis.

The synthesis is based on a modified Pechini method[23] using an excess of citric acid monohydrate (Sigma-Aldrich purity: $\geq$ 99.5%) as complexing agent. Ti(IV) isopropoxide was dissolved in an excess of molten citric acid. The temperature was lowered to approximately 100 °C and the aqueous solution of Ho_2O_3 was added to the transparent solution. The solution was left under rigorous magnetic stirring until the formation of a gel, then transferred to a porcelain crucible and dried at 180 °C overnight (16 hours). Upon drying we obtained a dark brown powder that in turn was calcined at 450 °C for 20 h. This resulted in a pink powder, which was ground in a mortar and pressed into pellets. Finally, annealing at 1350

°C for 50 h in air resulted in a pale pink powder.

The wet-chemical synthesis approach provides a homogeneous mix at the atomic level, and as such, a shorter diffusion path for cations and anions upon crystallization and growth. A lower temperature during heat treatment gives better control and tuning possibilities of the products. The treatment at high temperature could possibly be a reason for the presence of Ti^{3+} in the as-grown $Ho_2Ti_2O_7$ crystals of Ghasemi et al,[11] however, we were unable to spot any deviation in stoichiometry at these conditions for our powder samples

Single crystal growth

Crystal growth was performed using the floating zone technique. The $Ho_2Ti_2O_7$ powder was well ground with mortar and pestle for several minutes before it was funneled into a latex balloon. We added a piece of cotton above the powder to limit powder losses during evacuation of the balloon using a vacuum pump (RM-001, Crystal Systems Corporation). We pressed the powder into rods with an approximate diameter of 5 mm and 7 cm length using a hydrostatic water pressure of 70 MPa for 30 minutes. These were thereafter sintered for 15 hours at 1350 °C in air to give dense, sturdy rods.

We sintered the rods using a vertical furnace with a rotational lifter (model VEF-1800-BR from Crystal Systems Corporation). Subsequent inspection of a rod showed that it was evenly sintered through the entire rod. An uneven sintering, for instance due to a temperature gradient in the furnace, may easily result in a density variance along the rod direction. This could affect heat transfer and melting behaviour of the rod and could cause the molten zone to collapse during the growth as the zone suddenly increases, or decreases, in size. Again, this was not observed.

For our initial studies we experienced difficulties during the sample rod preparation due to a starting powder that was too coarse. This caused the powder to be insufficiently tacky, causing the rod to break into small pieces when we tried to remove it from the balloon. No improvement was gained on leaving the coarse powder under pressure for several hours. However, grinding the sample into a finer powder gave rods that were much less brittle and sufficiently robust for the growth experiments.[24]

An optical mirror furnace, with four 1000 W halogen lamps (FZ-T-10000-H-VPO-series from Crystal Systems Corporation), was used for the crystal growth. The feed rod was hung with a platinum wire. The feed and seed rods were rotated clockwise and anti-clockwise, respectively, at a speed of 20 rpm and the lamp stage moved upwards at 3 mm/h.[25]

We observed that the highest quality single crystals did not develop facets during the growth. Based on our experience, we note that the crystals that developed facets during growth consisted of multiple crystallites and were thus unsuitable for neutron experiments. An example of a crystal showing facets is shown in Figure 2a.

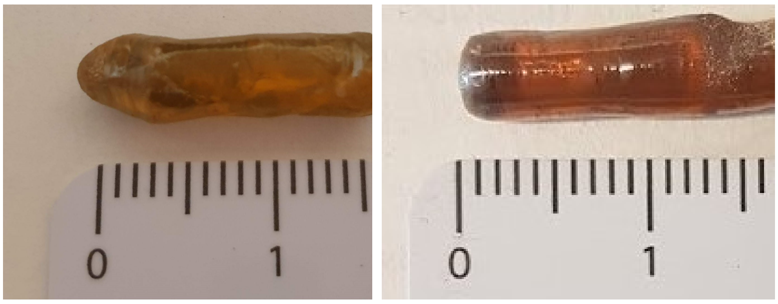

(a) (b)

Figure 2: a) Example of as-grown $Ho_2Ti_2O_7$ that developed facets during the growth. b)High quality as-grown $Ho_2Ti_2O_7$ with no visible facets. Scale is in cm.

The color of a material is intimately connected to its electronic state.[26] For rare earth cations, effects caused by differences in crystal field are typically negligible. However, impurities of certain d-cations into the structure could possibly trigger color changes. On the other hand, changes in the occupancy of the oxygen sites may have a significant effect. In this case, a charge compensation must occur to keep the neutrality of the compound. For rare-earth titanates this means a partial reduction of Ti^{4+} to Ti^{3+} which in most cases results in a black hue as well-known from TiO_2.[27] This is usually observed for such oxide crystals grown in protective N_2atmosphere. However, for Czochralski grown crystals of $Gd_2Ti_2O_{7-\delta}$ and also for $Ho_2Ti_2O_7$ the opposite situation i reported, i.e. oxygen deficiency gives a lighter color.[10]

The resultant high quality crystals, example shown in Figure 2b, had a homogeneous clear orange color with no visible sign of a black hue which could indicate small amounts of Ti(III), as reported by Ghasemi et al.[11] As an initial test of the oxygen stoichiometry a small piece of the as-grown crystal was heat treated in an oxygen rich atmosphere for 48 hours at 1000 °C. After the heat treatment, the color was compared to that of the as-grown crystal. No color change was visible, indicating no change in the electronic state of the sample.

This intimate connection between electronic state and color makes visual inspection of the crystal a simple way of assessing the crystal growth and the oxygen stoichiometry. It is indeed helpful in the case when neutron diffraction data are not easily at hand, and where magnetic property studies, as well as X-ray diffraction data are not sufficient to affirm the presence of small amounts of oxygen vacancies in a compound consisting of both light and heavy elements.[28]

Structural characterisation

Characterisation of synthesized $Ho_2Ti_2O_7$ powders by powder X-ray diffraction (PXRD) were performed on a Bruker D8 instrument with Cu monochromatized $K_{1,\alpha}$ radiation in Bragg-Brentano geometry.Ppowder neutron diffraction (PND) data were collected at 12 K using the PUS instrument at IFE, Kjeller, and a Displex cooling unit, $\lambda = 1.55440$ Å. The PXRD and PND data were refined using the Rietveld refinement software Topas.[29]

Single crystal neutron diffraction data were measured at the D9 instrument at ILL, Grenoble.[30]The single crystal specimen was cylindrical with 3 mm diameter and 2 mm height to limit multiple scattering effects. Data were collected at 30 K with a wavelength of 0.5021 Å. We measured at 30 K to minimise thermal fluctuation while remaining in an uncorrelated magnetic regime.[2] During the data collection we measured approximately 1600 peaks providing an effective number of 330 independent reflections. We refined the single crystal data using the FULLPROF software package.[31]

Results and discussion

Powder X-ray and neutron diffraction

Our XRD analysis shows a phase pure sample of $Ho_2Ti_2O_7$, goodness-of-fit (GOF) = 1.467, space group Fm-3d, see Figure 3. The broad hump in the background visible from $15° \leq 2\theta \leq 25°$ originates from the instrument.

The PND data were likewise very well fitted, see Table 2 for atomic cordinates. in the Rietveld refinement particular emphasis was put on the oxygen sites to evaluate any possible deviation from the stoichiometric composition. The refinement of the occupation number for the oxygen Wyckoff sites 8a and 48f gave a partial occupation of 100.7(7)% and 95(4)%. The obtained good fit with $R_{wp} = 5.026$, is shown in Figure 4.Hence, based on the PND data we conclude that the sample is stoichiometric within uncertainty of the experiment, however, error bars are significant.

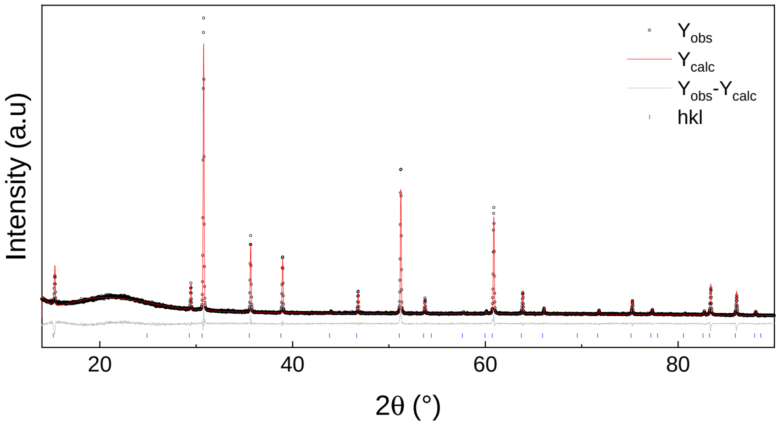

Figure 3: Rietveld refinement of powder X-ray diffraction data of $Ho_2Ti_2O_7$ measured with Cu K_1 radiation $\lambda = 1.5406$ Å

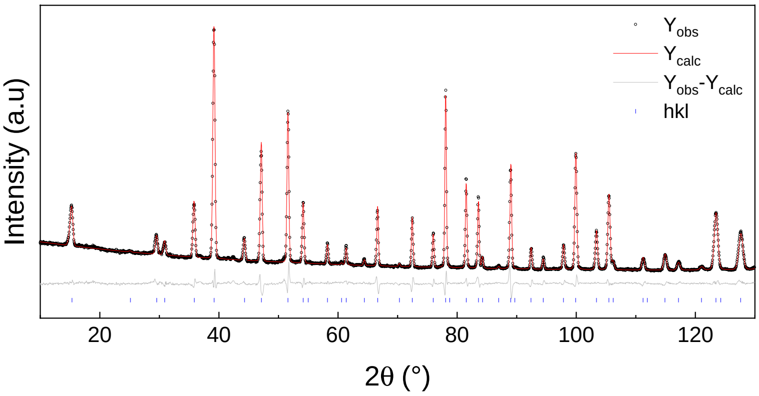

Figure 4: Rietveld refinement of powder neutron diffraction data of $Ho_2Ti_2O_7$ measured at 12 K and $\lambda = 1.55440$ Å on PUS at IFE.

Single crystal diffraction

We confirmed the correct symmetry of the single crystal by X-ray Laue diffraction data obtained on a home-built instrument, shown in Figure 5, with well defined single diffraction spots in full agreement with space group Fd-3m.

The refinement of the single crystal diffraction data from D9 gave a good fit for the stoichiometric model of $Ho_2Ti_2O_7$ $R_F = 3.747$, Table 3 and Figure 6. The possibility of oxygen non-stoichiometry was evaluated by refining occupation numbers of the 8a and 48f Wyckoff

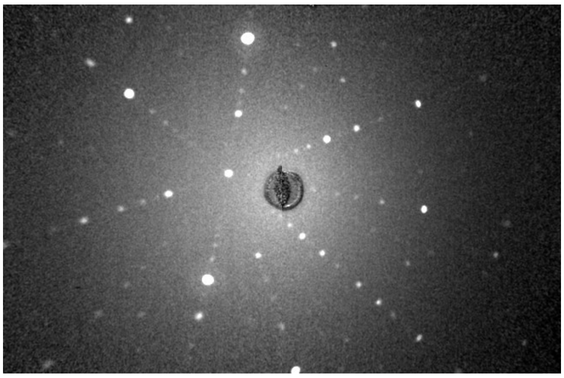

Figure 5: Laue diffraction of as-grown $Ho_2Ti_2O_7$ sample by floating zone technique

sites, as well by defining a specific level for non-stoichiometry. Deviation from the stoichiometric composition gave a significantly poorer fit, for example $R_F = 4.338$ for $Ho_2Ti_2O_{7-x}$ with x = 0.1.

Table 3: Crystal structure and refinement of single crystal diffraction data for $Ho_2Ti_2O_7$ measured on D9, ILL at 30 K with $\lambda = 0.5021$ Å[30]

Empirical formula	$Ho_2Ti_2O_7$
Instrument	D9, ILL
Temperature	30.0(1) K
Wavelength	0.5021 Å
Crystal structure	Cubic
Space group	*Fd-3m* (origin choice 2)
Unit cell dimensions	$a = 10.10$ Å[32]
Sample size	$2\pi \times 1.5^2 \times 2$ mm^3
Index ranges	$2 \leq h \leq 10$, $1 \leq k \leq 17$, $0 \leq l \leq 9$
Reflections collected	1600
Independent reflections	330
R_{F^2}-factor[a]	3.053
R_{F^2w}-factor[b]	4.940
χ^2 (intensity)[c]	5.060

In order to better evaluate the possibility of oxygen vacancies we have visualized the positive Fourier difference between the experimental data and our crystal structure refinement, see Figure 7a. Possible deviation from the ideal positions in the crystal structure is visualized

---

[0a]

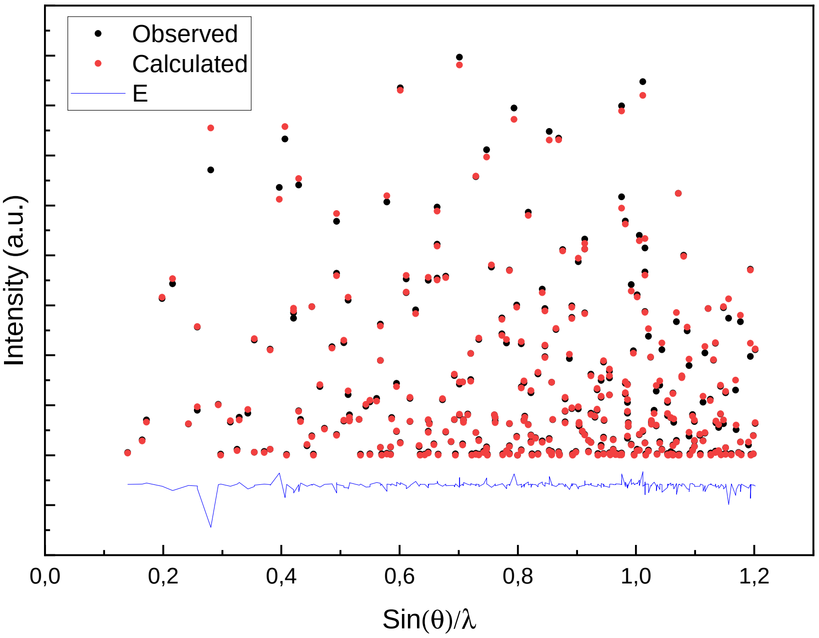

Figure 6: Visualisation of the refinement of single crystal diffraction data. $Ho_2Ti_2O_7$ measured on D9, ILL at 30 K with $\lambda = 0.5$ Å.[30] Observed, calculated and difference in intensities in black, red and blue.

by the scattering length density isosurfaces in yellow. These show a positive difference, indicating excess scattering length density (SLD), in proximity to the two oxygen sites, Wyckoff sites 8a and 48f.

The features in the isosurfaces, as well as in the atomic arrangement, are related by a center of inversion at the fluorite 8c Wyckoff site (3/8, 3/8, 3/8), see Figure 7a. The isosurfaces show an elongated feature along the face diagonals outwards from the oxygen 8a site. These elongations run along the crystal field directions shown in Figure 7b, with an extension less than a quarter of the Ho-O distance, approximately 0.55 Å. The spin ice behaviour is strongly dependent on the crystal field directions and, as such, any variation of the oxygen atoms along these direction are of significance.

The isosurfaces shows a disparity of the neutron scattering intensities relative to those for an ideal $Ho_2Ti_2O_7$. The disparity could be due to aspects of oxygen vacancies or substitutes, twinning of the crystal, a surface effect or dynamic effects relating to the oxygen sites.

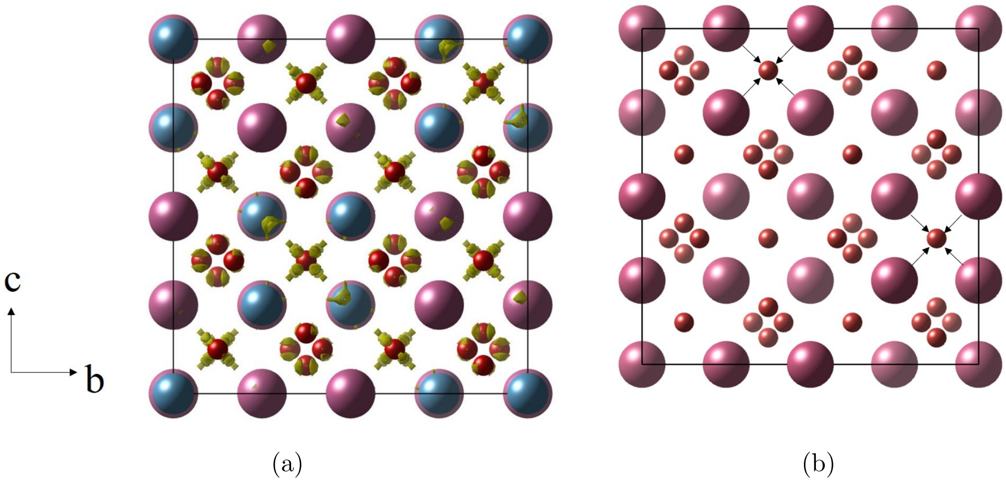

(a) (b)

Figure 7: a) Crystal structure of $Ho_2Ti_2O_7$, space group Fd-3m; holmium in pink, titanium in blue and oxygen in red. The positive Fourier difference from our refinement is shown as yellow isosurfaces. b) Crystal structure of $Ho_2Ti_2O_7$, crystal field direction given by black arrows.

The isosurfaces correspond to a disparity of the neutron scattering intensities to the ideal neutron scattering profile of $Ho_2Ti_2O_7$. The disparity could be due to oxygen vacancies (or substitutes), twinning of the crystal, a surface effect or dynamic effects relating to the oxygen sites.

To address the possibility of oxygen vacancies or substitutes, we note that any vacancies will lower the SLD, rather than give the observed enhancement. In a series of refinements we added an oxygen atom to our refinement at this site to account for the extra scattering length density. However the refinement gave an occupation of ≤ 0.1 % and no improvement in the overall fit to the data.

If the origin of the isosurfaces is due to twinning of the crystal, then certain Bragg peaks would have a non-resolution limited lineshape or peak splitting. We have no indication of this from our single crystal diffraction experiment on D9. We also considered the possibility that isosurfaces originate from dangling bonds at the surface of the crystal. However we discount this possibility due to the relative ratio of surface to bulk atoms, approximately 1 to 1.5 million, a resolution that the D9 experiment is not sensitive to.

Finally, a dynamic effect could not be distinguished within the time frame of a neutron scattering experiment. This leaves us to question whether our observation originates from the degenerate ground state of the structure. Trump et al.[19] report a static displacement from the Fd-3m Wyckoff sites through the use of HAADF STEM, arguing that dynamic displacements would not show due to the long timescale of the measurement. The same can be said for our experiment. Neutron diffraction measurements have a timescale in the order of minutes and we would therefore expect to see the average position from dynamic motions with a nano- to picosecond timescale.

Test growth of $Yb_2Ti_2O_7$

A test growth of $Yb_2Ti_2O_7$ using the floating zone technique and the optimised synthesis approach described earlier gave a transparent, colorless single crystal, Figure 8, indicating the ideal composition. Note the different sections of the figure where: a) is the poly-crystalline interface between the sintered seed rod and the single crystal, b) is the transparent colorless single crystal, and c) is a poly-crystalline section due to quenching when the seed and feed rod were separated at the end of the growth.

Our results stand in contrast to the findings of Arpino et al. who reports a dark red color[16] when attempting to grow $Yb_2Ti_2O_7$ with the floating zone technique, the pale brown color reported by Li et al.,[15] and the black color reported by Li et al.[14] This span of different colors can not be obtained with one electronic state for the Yb- and for the Ti-cations.[26] It therefore stands to reason that it is impossible for all these reported single crystals to possess the ideal composition $Yb_2Ti_2O_7$.

Arpino et al. were able to solve the color issue of the crystals by making use of a eutectic composition in the molten zone, also known as the travelling solvent floating zone technique, to obtain colorless single crystals like the one we obtained in our growth study. As $Yb_2Ti_2O_7$ is a congruently melting compound, this extra step via the eutectic composition should not be necessary.

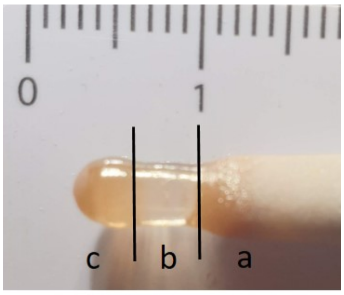

Figure 8: Test growth of a $Yb_2Ti_2O_7$ sample by floating zone technique; a) the poly-crystalline interface between the sintered seed rod and the single crystal, b) the transparent colorless single crystal, and c) a poly-crystalline section due to quenching when the seed and feed rod were separated at the end of the growth.

Conclusion

We have shown the suitability of the floating zone technique for synthesis of stoichiometric $Ho_2Ti_2O_7$ single crystals of high quality. The additional test growth of $Yb_2Ti_2O_7$ indicates that the floating zone technique is suitable for growth of related $RE_2Ti_2O_7$ (RE = rare earth) compounds, in agreement with earlier practice.[13,20] The absence of a dark hue in our as-grown crystals shows that such a feature is not an intrinsic effect of the growth method utilized in this work. This is in contrast to the conclusions reached by Ghaseemi et al.[11]

Other origins need to be explored to explain the vast range of colors, and electronic states, observed for $RE_2Ti_2O_7$ compounds.

We have ascertained that an initial step of powder synthesis might be a key component in producing stoichiometric single crystals. In literature, the synthesis route of single crystals are often not described in full detail, which can be problematic when a small deviation from the expected composition can have a large impact on the measured properties. In this work we provide a clear synthesis route from powder to finished single crystal, for which the quality has been studied with neutron diffraction. Though we have high quality crystals we nevertheless observe a deviation in the Fourier maps for the 8a oxygen sites along the strong crystal field directions. This work complements and refines the results provided by Trump et al. on related compounds with a strong focus on the oxygen sites.

Acknowledgement

This work was supported by NordForsk through the NNSP program, project number 82248.

Supporting Information Available

References

(1) Chamorro, J. R.; McQueen, T. M.; Tran, T. T. Chemistry of Quantum Spin Liquids. *Chemical Reviews* **2021**, *121*, 2898–2934, PMID: 33156611.

(2) Bramwell, S. T.; Gingras, M. J. P. Spin Ice State in Frustrated Magnetic Pyrochlore Materials. *Science* **2001**, *294*, 1495–1501.

(3) Canals, B.; Lacroix, C. Pyrochlore Antiferromagnet: A Three-Dimensional Quantum Spin Liquid. *Phys. Rev. Lett.* **1998**, *80*, 2933–2936.

(4) Booth, C. H.; Gardner, J. S.; Kwei, G. H.; Heffner, R. H.; Bridges, F.; Subramanian, M. A. Local lattice disorder in the geometrically frustrated spin-glass pyrochlore $Y_2Mo_2O_7$. *Phys. Rev. B* **2000**, *62*, R755–R758.

(5) Bernal, J. D.; Fowler, R. H. A Theory of Water and Ionic Solution, with Particular Reference to Hydrogen and Hydroxyl Ions. *The Journal of Chemical Physics* **1933**, *1*, 515–548.

(6) Pauling, L. The Structure and Entropy of Ice and of Other Crystals with Some Randomness of Atomic Arrangement. *Journal of the American Chemical Society* **1935**, *57*, 2680–2684.

(7) Gardner, J. S.; Gingras, M. J. P.; Greedan, J. E. Magnetic pyrochlore oxides. *Rev. Mod. Phys.* **2010**, *82*, 53–107.

(8) Anand, V.; Islam, A.; Samartzis, A.; Xu, J.; Casati, N.; Lake, B. Optimization of single crystal growth of candidate quantum spin-ice Pr2Hf2O7 by optical floating-zone method. *Journal of Crystal Growth* **2018**, *498*, 124 – 129.

(9) Prabhakaran, D.; Wang, S.; Boothroyd, A. Crystal growth of pyrochlore rare-earth stannates. *Journal of Crystal Growth* **2017**, *468*, 335 – 339, The 18th International Conference on Crystal Growth and Epitaxy (ICCGE-18).

(10) Guo, F.; Zhang, W.; Ruan, M.; Kang, J.; Chen, J. Czochralski growth of Gd2Ti2O7 single crystals. *Journal of Crystal Growth* **2014**, *402*, 94 – 98.

(11) Ghasemi, A.; Scheie, A.; Kindervater, J.; Koohpayeh, S. The pyrochlore Ho2Ti2O7: Synthesis, crystal growth, and stoichiometry. *Journal of Crystal Growth* **2018**, *500*, 38 – 43.

(12) Koohpayeh, S.; Fort, D.; Abell, J. The optical floating zone technique: A review of

experimental procedures with special reference to oxides. *Progress in Crystal Growth and Characterization of Materials* **2008**, *54*, 121–137.

(13) Balakrishnan, G.; Petrenko, O. A.; Lees, M. R.; Paul, D. M. Single crystal growth of rare earth titanate pyrochlores. *Journal of Physics: Condensed Matter* **1998**, *10*, L723–L725.

(14) Li, Q.; Xu, L.; Fan, C.; Zhang, F.; Lv, Y.; Ni, B.; Zhao, Z.; Sun, X. Single crystal growth of the pyrochlores R2Ti2O7 (R=rare earth) by the optical floating-zone method. *Journal of Crystal Growth* **2013**, *377*, 96 – 100.

(15) Li, S. J.; Che, H. L.; Wu, J. C.; Zhao, X.; Sun, X. F. Low temperature specific heat of Yb2Ti2O7 single crystals. *AIP Advances* **2018**, *8*, 055705.

(16) Arpino, K. E.; Trump, B. A.; Scheie, A. O.; McQueen, T. M.; Koohpayeh, S. M. Impact of stoichiometry of $Yb_2Ti_2O_7$ on its physical properties. *Phys. Rev. B* **2017**, *95*, 094407.

(17) Prabhakaran, D.; Boothroyd, A. Crystal growth of spin-ice pyrochlores by the floating-zone method. *Journal of Crystal Growth* **2011**, *318*, 1053 – 1056, The 16th International Conference on Crystal Growth (ICCG16)/The 14th International Conference on Vapor Growth and Epitaxy (ICVGE14).

(18) Gardner, J.; Gaulin, B.; Paul, D. Single crystal growth by the floating-zone method of a geometrically frustrated pyrochlore antiferromagnet, Tb2Ti2O7. *Journal of Crystal Growth* **1998**, *191*, 740 – 745.

(19) Trump, B. A.; Koohpayeh, S. M.; Livi, K. J. T.; Wen, K. E., J. J. Arpino; Ramasse, Q. M.; Brydson, R.; Feygenson, M.; Takeda, H.; Takigawa, M.; Kimura, K.; Nakatsuji, S.; Broholm, C. L.; McQueen, T. M. Universal geometric frustration in pyrochlores. *Nature Communications* **2018**, *9*, 2619.

(20) Mostaed, A.; Balakrishnan, G.; Lees, M. R.; Yasui, Y.; Chang, L.-J.; Beanland, R. Atomic structure study of the pyrochlore $Yb_2Ti_2O_7$ and its relationship with low-temperature magnetic order. *Phys. Rev. B* **2017**, *95*, 094431.

(21) Snyder, J.; Slusky, J.; Cava, R.; Schiffer, P. How 'spin ice' freezes. *Nature* **2001**, *413*, 48–51.

(22) Momma, K.; Izumi, F. *VESTA3* for three-dimensional visualization of crystal, volumetric and morphology data. *Journal of Applied Crystallography* **2011**, *44*, 1272–1276.

(23) Sunde, T. O. L.; Grande, T.; Einarsrud, M.-A. In *Handbook of Sol-Gel Science and Technology*; Klein, L., Aparicio, M., Jitianu, A., Eds.; Springer International Publishing: Cham, 2016; pp 1–30.

(24) Balakrishnan, G. personal communication, 2019.

(25) Rudolph, P., Ed. *Handbook of Crystal Growth (Second Edition)*, second edition ed.; Handbook of Crystal Growth; Elsevier: Boston, 2015; pp 281–329.

(26) Tilley, R. J. *Colour and the Optical Properties of Materials*, 3rd ed.; Wiley: Hoboken, USA, 2020.

(27) Chen, X.; Liu, L.; Huang, F. Black titanium dioxide (TiO2) nanomaterials. *Chem. Soc. Rev.* **2015**, *44*, 1861–1885.

(28) West, A. R. *Solid State Chemistry and its Applications*, 2nd ed.; Wiley: West Sussex, UK, 2014.

(29) Coelho, A. A. *TOPAS* and *TOPAS-Academic*: an optimization program integrating computer algebra and crystallographic objects written in C++. *Journal of Applied Crystallography* **2018**, *51*, 210–218.

(30) Deen, P. P.; Bakke, I. M. B.; Hansen, T.; Haubro, M.; Lefmann, K.; Ørduk Sandberg, L. Oxygen defects in spin ice. *ILL* **2019**,

(31) Rodriguez-Carvajal, J. FULLPROF: A Program for Rietveld Refinement and Pattern Matching Analysis. **1990**, 127.

(32) Baroudi, K.; Gaulin, B. D.; Lapidus, S. H.; Gaudet, J.; Cava, R. J. Symmetry and light stuffing of $Ho_2Ti_2O_7, Er_2Ti_2O_7$, and $Yb_2Ti_2O_7$ characterized by synchrotron x-ray diffraction. *Phys. Rev. B* **2015**, *92*, 024110.

TOC Graphic

Some journals require a graphical entry for the Table of Contents. This should be laid out "print ready" so that the sizing of the text is correct.

Inside the `tocentry` environment, the font used is Helvetica 8 pt, as required by *Journal of the American Chemical Society*.

The surrounding frame is 9 cm by 3.5 cm, which is the maximum permitted for *Journal of the American Chemical Society* graphical table of content entries. The box will not resize if the content is too big: instead it will overflow the edge of the box.

This box and the associated title will always be printed on a separate page at the end of the document.

Appendix B

Morten Haubro Report on Pressure Cell B .

Design and Calibration of Uniaxial Pressure Cell for Neutron Scattering

Project Outside the Course Scope
Written by *Morten Lunn Haubro*
February 19, 2020

Supervised by
Kim Lefmann

University of Copenhagen

UNIVERSITY OF
COPENHAGEN

Name of Institute:	Niels Bohr Institutet
Name of Department:	Science
Author(s):	Morten Lunn Haubro
Email:	flr522@alumni.ku.dk
Title and subtitle:	Design and Calibration of Uniaxial Pressure Cell for Neutron Scattering -
Supervisor(s):	Kim Lefmann
Handed in:	-
Defended:	-

Name ______________________

Signature ______________________

Date ______________________

Contents

1 Introduction

High pressure experiments in condensed matter physics have historically been a source of significant discoveries [1]. In neutron scattering these experiments prove extremely challenging as large samples are needed in order to secure a descent signal, this in turn means that larger forces are needed to achieve high pressures. Larger cells are then needed which in turn increases the background signal significantly. This coupled with the considerable risk of the sample breaking and the cost and difficulty of sample preparation is enough to make high pressure experiments a fairly small branch of the neutron community. All of these issues are only exacerbated in a uniaxial pressure experiment. Uniaxial pressure allows for an asymmetric distortion of the lattice, offering a unique possibility to force the sample into novel structural as well as magnetic phases. This distortion however makes it exceedingly likely that the sample might break.

In this project i describe a method for calibrating a load gauge that enables in situ measurement of the pressure during neutron experiments. Since the pressure cell will contract during cooling, the pressure will also change and an accurate measurement of the pressure is crucial.
The particular pressure cell discussed in this project is developed as a collaboration between the ESS and ILL and is to be used on neutron beamlines at both facilities in the future. At the moment however, it is meant to be used to explore the pressure dependency of the spin ice system $Ho_2Ti_2O_7$ (HTO) as well as the similar compound $Dy_2Ti_2O_7$ (DTO). These materials are interesting because of the very unique dynamics that arise due to the geometrically frustrated lattice [2]. Applying uniaxial pressure lifts the magnetic frustration a little bit and forces the system into a novel, ordered phase. The phase diagram for DTO and HTO can be seen in Fig. 1.1, it is this phase diagram that we wish to explore using uniaxial pressure. Measurements have already been performed, these and theoretical simulations can be found in [3].

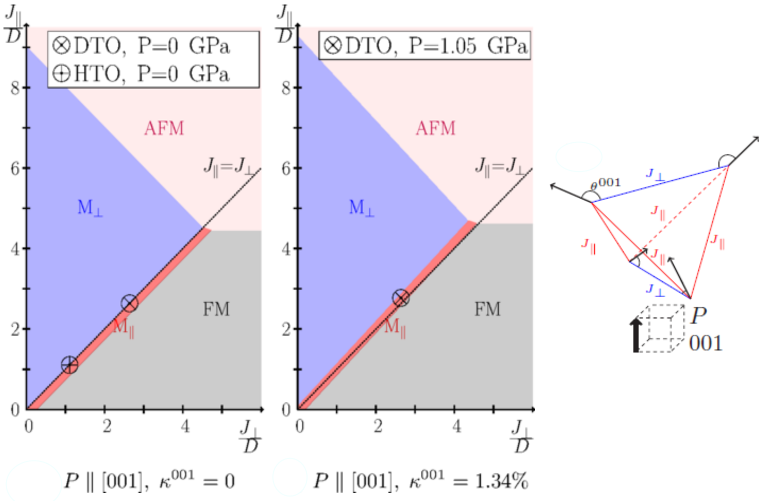

$P \parallel [001]$, $\kappa^{001} = 0$ $P \parallel [001]$, $\kappa^{001} = 1.34\%$

Figure 1.1: Left: Phase diagram for pyrochlore materials as a function of different coupling constants, DTO are placed for no and 1.05 GPa applied pressure. **Right:** A tetrahedron as the ones in pyrochlore materials, the coupling constants are drawn in. Figure from [3]

In the following i will discuss the cell design and attempts at calibrating the load gauge to low temperatures.

2 Pressure cell

The pressure cell is constructed according to the schematic shown in Fig. 2.1. The body and piston is constructed from copper berylium (alloy 25 CW-101C [4]) and the anvils are made of steel. The cell is designed specifically to contain a load gauge, which allows a continuous measurement of the pressure on the sample during the experiment.

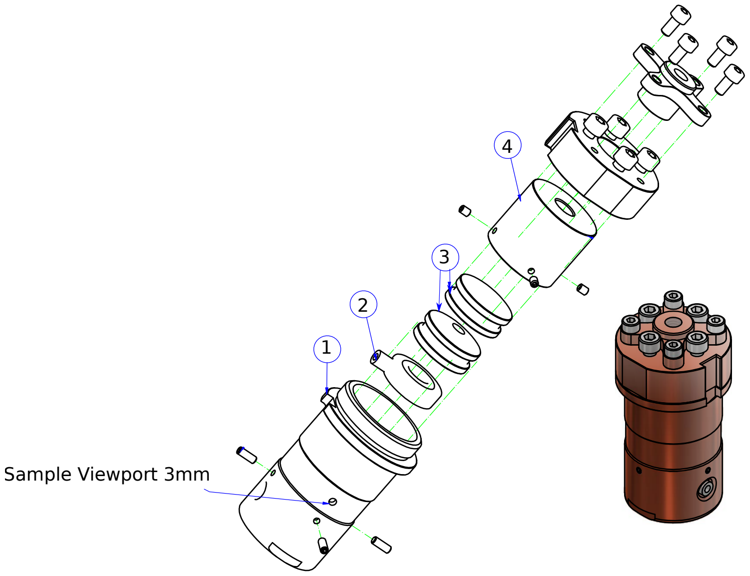

Figure 2.1: A schematic of the cell design. The cell body (1) contains a space in the bottom for the force washer (2) which is located underneath the anvils (3). The sample is placed between the anvils and is located at the same height as the viewports. Pressure is applied to the piston (4) and the pressure is held constant by screws.

The cell walls are solid except for two "viewports" that are 3 mm in diameter, these are used to ensure that the sample is upright and aligned. The thickness of the cell wall is 4.5 mm except at the sample position where it has been reduced to 2.5 mm to increase the signal-to-noise ratio. The steel anvils are a temporary solution as they are not at all hard enough to withstand the pressures needed during an experiment. Furthermore steel can be magnetized and this is a problem as this will be enough to potentially ruin a measurement with polarized neutrons.
During the calibration of the force washer, a different cell design was used. The deign is essentially the same except that this cell is larger and has two windows at the sample position. This load gauge also has the option to be mounted with a gas membrane. The membrane can be connected to a container of pressurized Nitrogen which is then used to vary the pressure. This allows for a constant exertion of force, largely independent of changes in the cell due to thermal contraction or expansion. A picture of this cell and the gas membrane can be seen in Fig. 2.2.

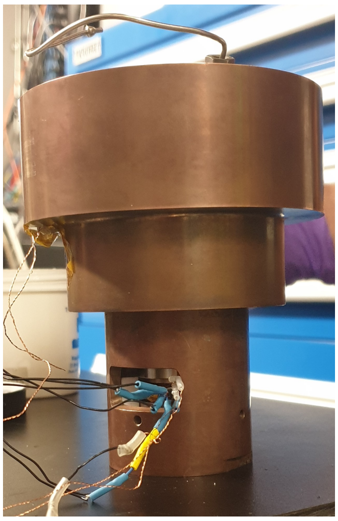

Figure 2.2: Pressure cell used for calibration. As with the other cell, Fig. 2.1, this one has a BeCu body and steel anvils. The main differences being the windows at the sample position as well as the option to use with a gas membrane. Nitrogen gas is connected to the tube on the top.

3 Load Gauge

The pressure sensor chosen for this project is a commercially available 40 kN load gauge from HBM [5]. Initially a 100 kN gauge was chosen but it was changed to the 40 kN model due to its higher sensitivity in the pressure range of interest. The gauge employs a strain gauge based setup in order to measure the applied load. The exact design is unknown as these gauges are commercially available and thus that information is proprietary. The design however is some version of a wheatstone bridge [6] as the one shown in Fig. 3.1. The strain gauges are resistors mounted with glue inside an outer shell. They are constructed such that they sensitive to strain in

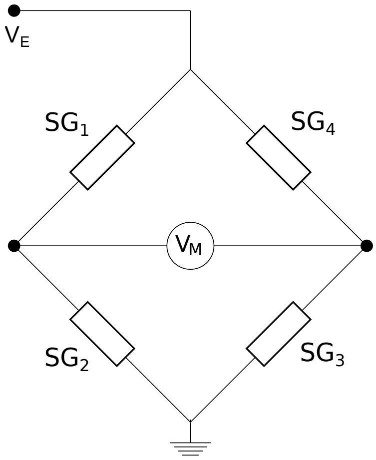

Figure 3.1: A Wheatstone bridge setup as the one used in the Load gauges. When no load is applied the bridge is balanced and $V_{SG} = 0$. The specific bridges in the force washers are most likely more complicated and given the size of the cell more strain gauges are needed to ensure accurate measurements.

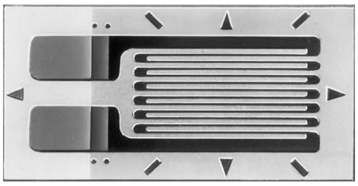

Figure 3.2: An example of a strain gauge, the dark wire is the conducting part. Picture from [7]

one direction, a picture of a strain gauge is presented in Fig. 3.2. The idea is to place SG_1 and SG_3 at a position where the material contracts and SG_2 and SG_4 at a position where it expands when a force is applied to the outer shell. The signal from the load gauge can then be shown to be,

$$R_{LG} = \frac{V_M}{V_E} = \frac{SG_2}{SG_1 + SG_2} - \frac{SG_4}{SG_3 + SG_4}. \tag{3.1}$$

The idea is that this value should be zero for a balanced bridge, when no load is applied. When a load is applied, the resistance in the odd numbered strain gauges will decrease whereas it will increase in the even numbered strain gauges. This particular setup wheatstone setup is called a full bridge because it utilizes all 4 active elements in the wheatstone bridge, contrary to the simpler quarter or half bridge setups where 3 and 2 of the strain gauges are exchanged for normal resistors. The option to use a piezoelectric Load gauge was considered, but since we will be cooling to ~ 2 K there is a risk that a phase transition will cause the piezoelectric effects to disappear. Most likely the strain gauges are attached with glue and there is a risk that the glue will become brittle and break as it is cooled. The risk of some material in the circuit becoming superconducting is of course present, but no super conducting phase transition were observed. If the glue does not break and nothing becomes superconducting, the resistance in the circuit might still change dramatically with temperature and thus the load gauge still has to be calibrated down to ~ 2 K in order to accurately determine the pressure during experiments.

4 Data

Before the temperature dependence of the load gauge can be determined, a room temperature calibration is needed in order to convert between membrane pressure and applied force. Naively, this should not be necessary as the membrane area is known and thus it should be straight forward to calculate the relationship between the membrane pressure and the applied force

$$F = PA_{memb}. \tag{4.1}$$

This is however not correct as the membrane bulges quite a lot causing the contact area between the membrane and the piston to be somewhat smaller than the membrane area. In order to get such a calibration curve the load gauge response is measured as a function of applied force with a press at room temperature, the corresponding curve can be seen in Fig. 4.1a. Then the load gauge response as a function of membrane pressure is measured at room temperature, these two measurements are then combined yielding the curve in Fig. 4.1b. Luckily this relationship is linear meaning that the contact area is constant in the pressure range of interest.

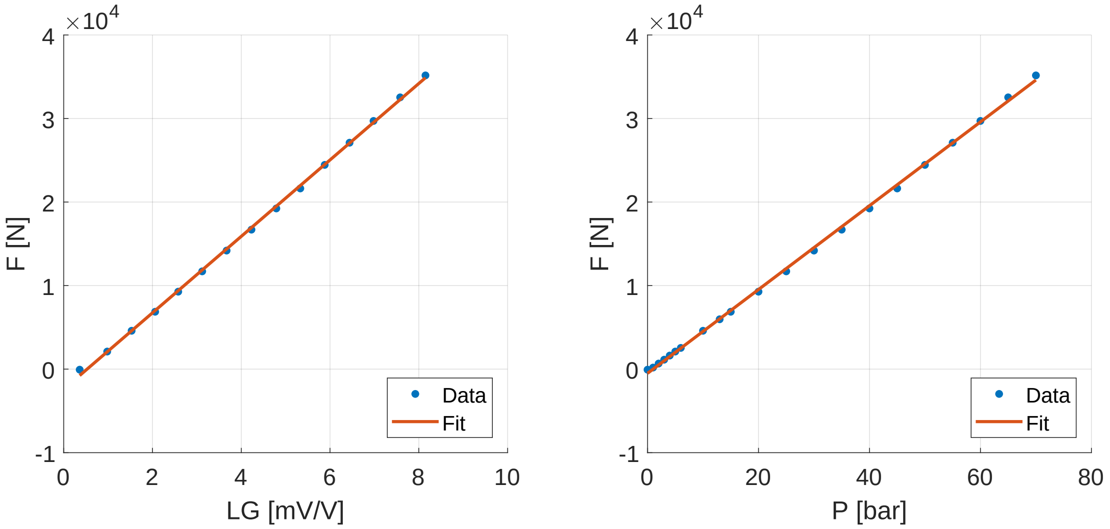

(a) Measurement of the force from a press as a function of the load gauge response (LG), the fit yields the relationship: $F = 5.6\cdot10^4$ NV/mV$\cdot$ $R_{LG} - 0.07\cdot10^4$ N

(b) Measurement of LG as a function of the membrane pressure, LG is translated into a force using the result from Fig. 4.1a, the fit yields: $F = 501.52$ N/bar $\cdot P - 501.47$ N.

Figure 4.1

4.1 Oak Ridge Measurements

The following measurements were done at SNS at Oak Ridge National Laboratories, TN, USA. The pressure cell containing the load gauge was cooled in a cryostat, membrane pressure was then increased to 30 bar in steps of 5 bar. The cell was then cooled further and the process was repeated. Around 75 K, clear signs of the piston jamming was observed and after heating the cell back to 100 K the process was changed. The pressure was then kept constant during cooling to prevent the piston jamming. The lowest temperature achieved was around 40 K which is a lot higher than base temperature of the cryostat used, but a heat leak prevented further cooling. The first thing to notice is the two lowest membrane pressures, 0 and 5 bar behave very differently from the rest of the pressures. These two curves are only separate above $\sim$ 240 K and around 170 K they merge with the 10 Bar signal as well. This is a sign of the piston jamming. As the temperature is lowered, the piston and cell body contracts at slightly different rates causing increased friction. Essentially this means that a higher pressure is needed to move the piston. This is not much of a problem since the pressure range of interest is higher $\sim$ 20-30 Bar.
Each of the curves have been fitted with a third order polynomial, the parameters can be seen in Tab. The gauge response changes quite drastically all the way down to the lowest achieved temperatures, this is somewhat surprising as the thermal contraction of both copper and steel stops around LN temperatures at 77 K [8]. This indicates that the change below 80 K is mostly due to the electrical properties of the gauge changing.
The Load gauge response as a function of the membrane pressure is plotted in Fig. 4.3. According to the manufacturer this relationship should be linear and, disregarding the 0 and 5 Bar data, it does however seem that the error might be slightly overestimated.

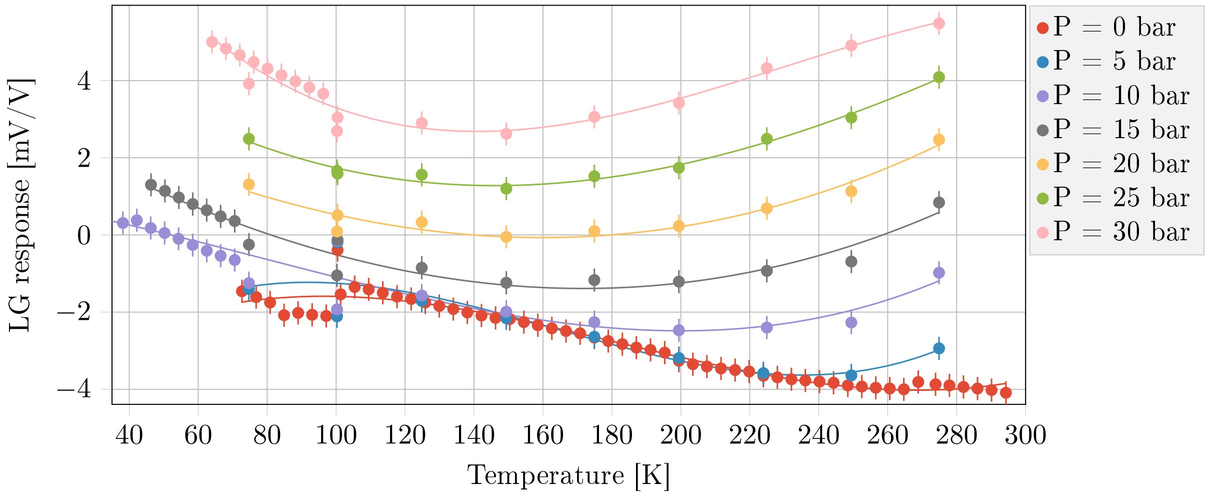

Figure 4.2: Load gauge response as a function of temperature for 7 different pressures. Each of which have been fitted to a third order polynomial $R_{LG} = aT^3 + bT^2 + cT + d$. The error on each point is estimated to be 0.3 mV/V.

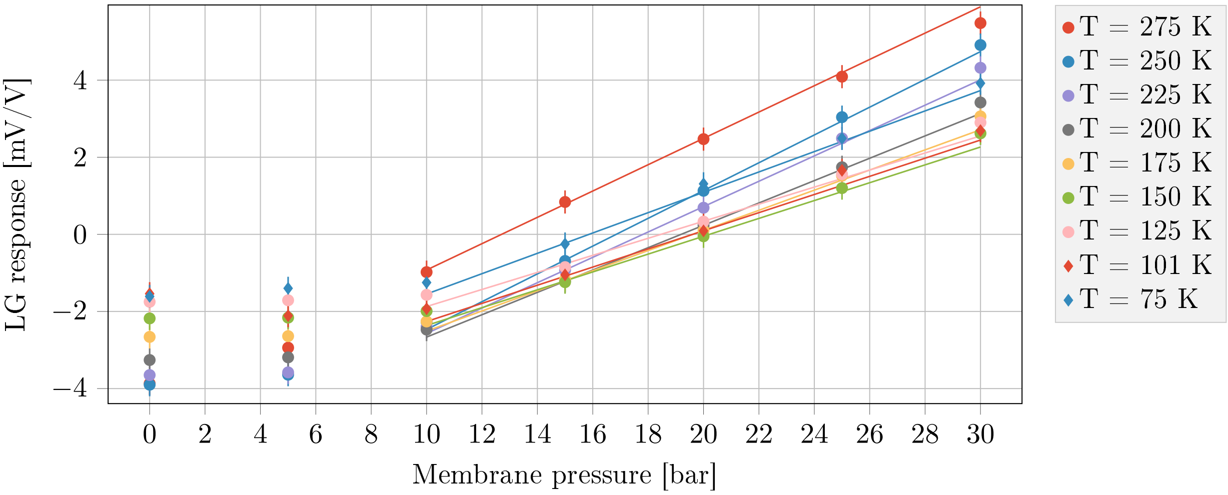

Figure 4.3: Load gauge response as a function of pressure for 9 different temperatures. The response for the 5 highest pressures are fitted to a linear model.

The fact that the load gauge response is linear is key in order to produce a simple relationship between the applied force and the measured response as a function of temperature. It could also be done with a more complicated function but data at more pressures would be needed to accurately map the dependency. An alternative could be to determine the material composition and theoretically predict the temperature dependency of the response.

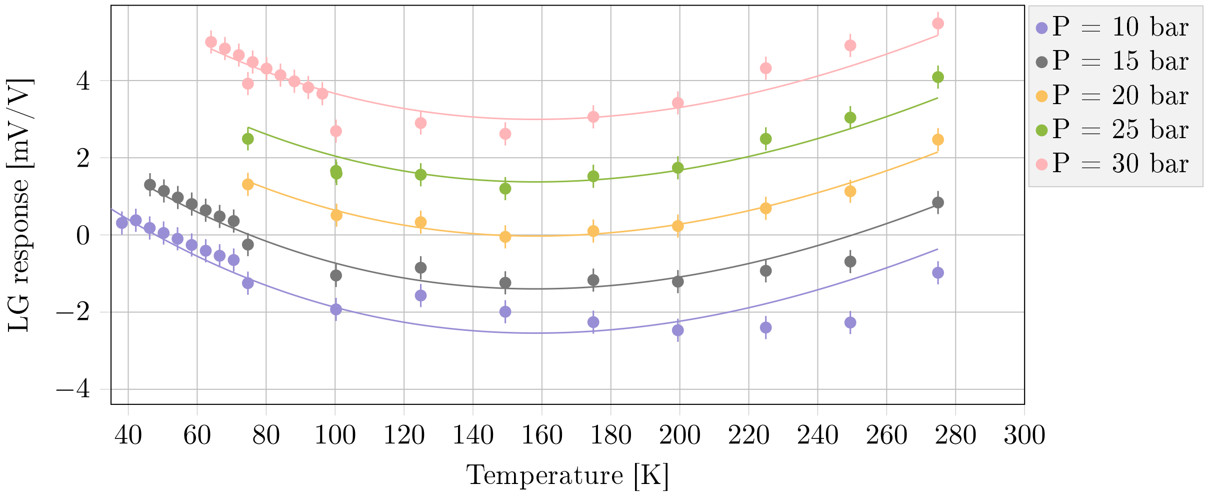

Figure 5.1: Load gauge response as a function of temperature for 5 different pressures. Each of which have been fitted to a third order polynomial. $R_{LG} = aT^3 + bT^2 + cT + d(F)$ with the same a, b and c parameters found as the weighted average of the a,b and c parameters found in Fig. 4.2. They can be found in Tab.1

5 Analyzing the data

The objective is to obtain an expression that allows ud to measure a temperature and a response from the load gauge and calculate the corresponding force applied to the sample. It seems like all the curves in Fig. 4.2, except for the two lowest pressures, have the same temperature dependency except of an offset. This means that for a given applied force F The load gauge response can be described by a 3rd order polynomial

$$R_{LG} = aT^3 + bT^2 + cT + d(F). \tag{5.1}$$

As the constant a, b and c are should be the same for different pressure, they are found as the weighted average of the fit parameters of the 10 bar - 30 bar fits from Fig. 4.2. The data is then refitted with 3rd order polynomials with d(F) being the only free parameter, as i assume that the other parameters are independent of the applied force. The resulting fits can be seen in Fig. 5.1. The 0 bar and 5 bar measurements are discounted due to the apparent jamming of the piston. These fits describe the data to an acceptable degree. The offset parameter $d(F)$ can then be plotted as a function of the force and fitted to a linear model. The fit is rather poor $\chi_{red} = 4.2$ this seems to be due to the errors being slightly underestimated. The parameters with errors are shown in Tab.1. Combining the results from Fig. 5.1 and Fig. 5.2 yields an expression that given a measurement of the temperature and load gauge response gives the force applied to the gauge.

$$F = \frac{R_{LG} - aT^3 - bT^2 - cT - f}{e}, \tag{5.2}$$

with simple error propagation [9] the error is given as

$$\sigma_F^2 = \left(\frac{\sigma_a T^3}{e}\right)^2 + \left(\frac{\sigma_b T^2}{e}\right)^2 + \left(\frac{\sigma_c T}{e}\right)^2 + \left(\frac{\sigma_f}{e}\right)^2 + \left(\frac{\sigma_e F}{e}\right)^2. \tag{5.3}$$

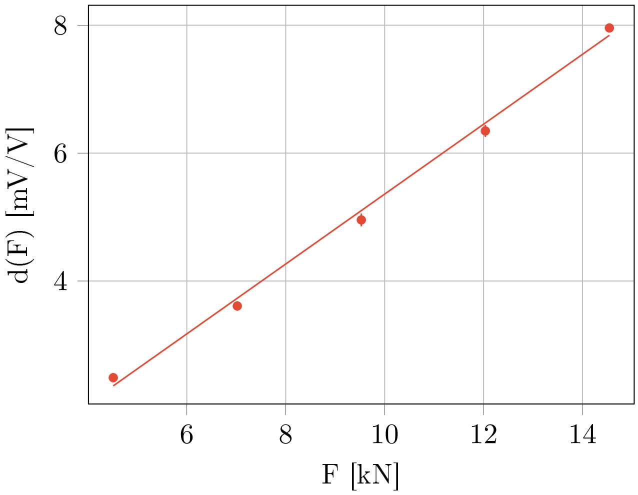

Figure 5.2: The offset parameter ($d(F)$) from Eq. 5.1 plotted as a function of the force applied to the load gauge. Fitted to a linear model ($d(F) = eF + f$) with parameters shown in Tab. 1.

The error on the load gauge response and the temperature is left out, it is assumed that the temperature measurement is so precise that it will contribute negligibly. We simply have no good estimate for the error on the load gauge response, more measurements to get actual statiscs are needed. Looking at Eq. 5.3 it is clear that the error will depend quite heavily on temperature, and indeed calculating the force for T = 100 K and $R_{LG} = 0$ mV/V gives $F = 31 \pm 9$ kN where as for 4 K and the same measured signal it gives $F = 16 \pm 2$ kN. This is obviously still a massive error, solutions to this will be considered in the discussion.

$\mathbf{R_{LG} = aT^3 + bT^2 + cT + d(F)}$		
a	b	c
$(-1.6 \pm 1.5) \cdot 10^{-7}\ \frac{\text{mV}}{\text{V K}^3}$	$(2.4 \pm 0.7) \cdot 10^{-4}\ \frac{\text{mV}}{\text{V K}^2}$	$(-0.06 \pm 0.01)\ \frac{\text{mV}}{\text{V K}}$

$\mathbf{d(F) = eF + f}$	
e	f
$(0.5543 \pm 0.0007)\ \frac{\text{mV}}{\text{V kN}}$	$(0.350 \pm 0.006)\ \frac{\text{mV}}{\text{V}}$

Table 1: Fit parameters for the polynomial fits in Fig. 5.1 and Fig. 5.2

6 Additional measurements

Upon returning from Oak Ridge the 40 kN load gauge turned out to be broken, whether this is was a consequence of the cooling or rough handling during preparation or travel is unknown. In fig. 6.1 a measurement of the load gauge response as a function of time during cooling is shown, where multiple sharp drops and jumps are observed. This is a measurement of the load gauge without the cell at ambient pressure so any change observed is purely due to changes happening in the load gauge.

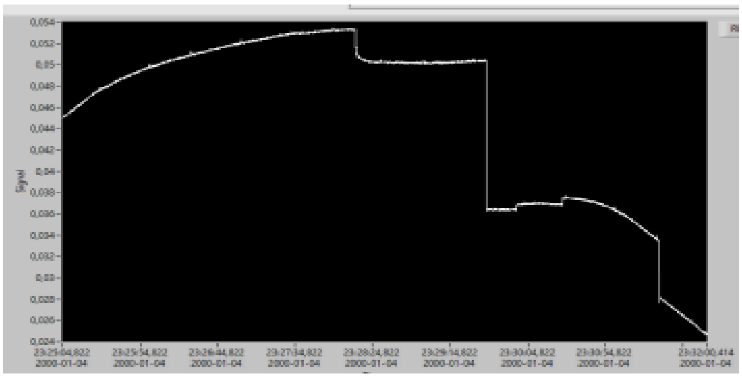

Figure 6.1: The load gauge at ambient pressure signal in units of mV/V as a function of time during cooling.

These changes could be due to either the gauge itself contracting or it could be due to electrical changes in the gauge circuit. It is most likely the latter, as the former would result in slower continuous changes instead of the steep discontinuous jumps observed.

7 Discussion and Conclusion

Obtaining an expression to calculate the force from the load gauge response is a very important step in order to be able to measure the force during a neutron experiment. The large error associated with the result is however troubling. The best solution to this problem would be to perform additional measurements at constant membrane pressure and measure the response during cooling. Getting better statistics would also allow an estimate on the actual error of the measurement instead of the estimate used here. As the magnitude error is very uncertain it is not possible to estimate how well the 3rd order polynomial fits the data compared to other models. However, the important thing is that it offers a consistent estimate of the applied force and then the underlying physical relationship is of no actual interest.

The behavior observed in Fig. 6.1 might indicate that air trapped inside the gauge is messing with the signal as it is condensing during cooling. This could be alleviated by drilling a hole in the outer shell of the load gauge or by introducing space for the air to pass through in the wire. Both of these approaches are however risky with the commercial gauges as we have no way of knowing exactly how they are constructed and thus we risk breaking the wires or in the worst case the strain gauges mounted on the inside.

Before this particular gauge can be used as a reliable sensor at cryogenic temperatures it is necessary to establish whether or not the components are able to withstand multiple cooling cycles. Two seperate gauges broke during the measurements presented here, we cannot be sure that it was because of the cooling, but at this point it seems highly likely. Since the design is proprietary it is impossible to know what we might need to change in order to make them work. For these reasons the approach presented in this project has been abandoned for a simpler gauge design.

8 Acknowledgements

I would like to thank Malcolm Guthrie and Alexander Holmes for their help and assistance during this project. This project would not have become reality without their expertise. I would also like to thank Jamie Molaison at the SNS, Oak Ridge National Laboratory for letting me use their setup to perform the measurements.

References

[1] A. P. Drozdov, M. I. Eremets, I. A. Troyan, V. Ksenofontov, and S. I. Shylin, “Conventional superconductivity at 203 kelvin at high pressures in the sulfur hydride system,” *Nature News*, Aug 2015. [Online]. Available: https://www.nature.com/articles/nature14964

[2] T. Fennell, P. P. Deen, A. R. Wildes, K. Schmalzl, D. Prabhakaran, A. T. Boothroyd, R. J. Aldus, D. F. McMorrow, and S. T. Bramwell, “Magnetic coulomb phase in the spin ice ho2ti2o7,” *Science*, Oct 2009. [Online]. Available: https://science.sciencemag.org/content/326/5951/415.full

[3] R. Edberg, L. r. Sandberg, I. M. B. Bakke, M. L. Haubro, L. C. Folkers, L. Mangin-Thro, A. Wildes, O. Zaharko, M. Guthrie, A. T. Holmes, M. H. Sørby, K. Lefmann, P. P. Denn, and P. Henelius, “Dipolar spin ice under uniaxial pressure,” *Physical Review B*, vol. 100, no. 14, 2019. [Online]. Available: https://journals.aps.org/prb/abstract/10.1103/PhysRevB.100.144436

[4] L. Matthey, “Precision cold rolled strip and foil.” [Online]. Available: https://www.matthey.ch/index.php?id=45&L=1

[5] “Kmr strain gauge-based force washer for monitoring tasks,” Jan 2020. [Online]. Available: https://www.hbm.com/en/2423/kmr-force-washer-for-force-monitoring-tasks/

[6] (2018, Oct) Wheatstone bridge circuit and theory of operation. [Online]. Available: https://www.electronics-tutorials.ws/blog/wheatstone-bridge.html

[7] “Strain gage selection: Criteria, procedures, recommendations,” May 2018. [Online]. Available: http://www.vishaypg.com/docs/11055/tn505.pdf

[8] F. Pobell, *Matter and methods at low temperatures.* Springer-Verlag, 2007.

[9] R. J. Barlow, *Statistics: a guide to the use of statistical methods in the physical sciences R. J. Barlow.* J. Wiley, 1989.

Appendix C

Data Sheets

C.1 Copper Beryllium C17200 (CuBe)

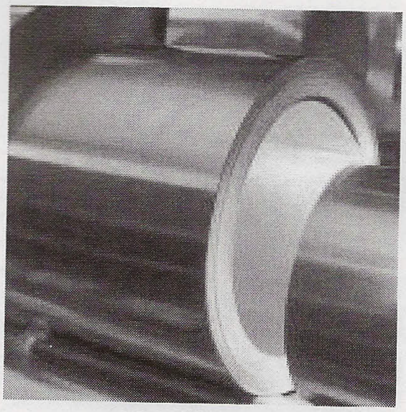

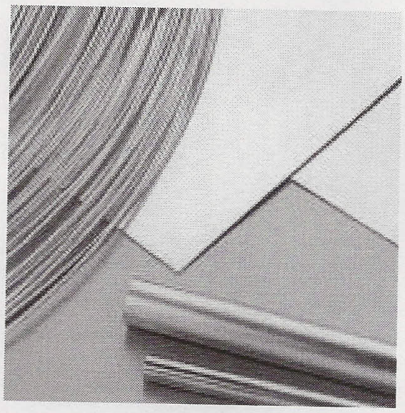

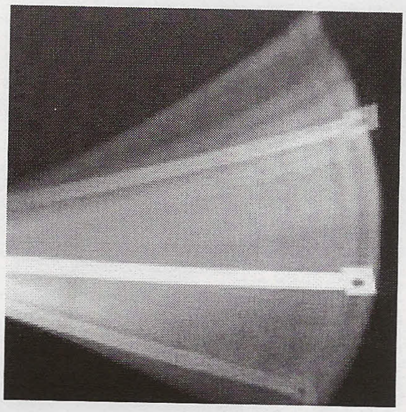

KUPFER-BERYLLIUM

Technisches Datenblatt

Wertetabelle - Bänder

Zustand	Werkstoffnummer EN	Werkstoffnummer DIN	Wärmebehandlung bei [h]/[°C]	Zugfestigkeit Rm [N/mm^2]	Dehngrenze Rp 0,2 [N/mm^2]	Federbiegegrenze σ FB min. N/mm^2 für Dicken (mm)* 0,10-0,25 / 0,25-1,0	% Dehnung A ML=50 mm	Vickers Härte (HV)	Elektrische Leitfähigkeit $\left(\frac{m}{\Omega \cdot mm}\right) \geq$	Verformbarkeit R/S Verhältnis 90° Quer/Parallel[1]
Brush Legierung 25 CuBe 2, W.Nr.2.1247.CW 101 C										
vor dem Aushärten										
A	R 410	2.1247.40	-	410 - 540	190 - 380	- / -	35 - 60	90 - 150	9	0,0 / 0,0
1/4 H	R 510	2.1247.54	-	510 - 610	420 - 560	- / -	10 - 35	130 - 190	9	0,0 / 0,0
1/2 H	R 580	2.1247.55	-	580 - 690	530 - 660	- / -	8 - 25	180 - 220	8	0,8 / 1,5
H	R 680	2.1247.56	-	680 - 830	650 - 800	- / -	2 - 8	215 - 270	8	2,5 / 5,0
nach dem Aushärten (vom Kunden)										
AT	R 1130	2.1247.60	3 h / 315	1130 - 1350	960 - 1210	780 / 830	3 - 10	350 - 410	13	- / -
1/4 HT	R 1190	2.1247.74	2 h / 315	1190 - 1420	1050 - 1300	820 / 910	3 - 6	360 - 430	13	- / -
1/2 HT	R 1270	2.1247.75	2 h / 315	1270 - 1490	1100 - 1350	880 / 980	1 - 5	370 - 440	12	- / -
HT	R 1310	2.1247.76	2 h / 315	1310 - 1520	1150 - 1420	920 / 1020	1 - 3	380 - 450	12	- / -
Brush Legierung 190 CuBe 2, W.Nr.2.1247. CW 101 C										
werksvergütet										
AM	R 690	-	-	690 - 760	480 - 660	400 / 410	16 - 23	210 - 250	11	0,0 / 0,0
1/4 HM	R 750	-	-	750 - 830	550 - 760	480 / 500	15 - 20	240 - 280	11	1,3 / 1,8
1/2 HM	R 820	2.1247.69	-	830 - 930	690 - 870	530 / 580	12 - 18	260 - 310	11	1,5 / 2,0
HM	R 930	-	-	930 - 1040	750 - 950	600 / 660	9 - 15	290 - 350	11	2,5 / 3,0
SHM	-	-	-	1030 - 1100	860 - 970	670 / 730	9 - 14	310 - 360	11	2,8 / 3,5
XHM	-	2.1247.79	-	1100 - 1250	970 - 1150	760 / 840	4 - 10	350 - 390	11	3,5 / 5,5
XHMS	R 1200	-	-	1200 - 1320	1030 - 1250	780 / 870	3 - 9	360 - 420	11	4,5 / 8,0
Brushform 290 CuBe 2										
werksvergütet										
TM 00	-	-	-	690	510 - 670	- / -	19 - 28	225 - 310	9	0,0 / 0,0
TM 02	-	-	-	830	660 - 800	- / -	14 - 25	255 - 340	9	0,0 / 0,0
TM 04	-	-	-	960	790 - 940	- / -	9 - 20	285 - 370	9	1,0 / 1,0
TM 06	-	-	-	1070	930 - 1070	- / -	6 - 13	315 - 400	9	2,5 / 2,5
TM 08	-	-	-	1210	1070 - 1210	- / -	3 - 10	345 - 430	9	3,5 / 3,5
Brush Legierung 165 CuBe 1,7, W.Nr. 2.1245. CW 100 C										
vor dem Aushärten										
A	R 410	2.1245.40	-	410 - 530	190 - 380	- / -	35 - 60	80 - 150	9	0,0 / 0,0
1/4 H	R 510	2.1245.54	-	510 - 610	410 - 560	- / -	15 - 35	120 - 190	9	0,0 / 0,5
1/2 H	R 580	2.1245.55	-	580 - 690	510 - 660	- / -	8 - 25	180 - 220	8	1,0 / 1,8
H	R 680	2.1245.56	-	680 - 830	620 - 800	- / -	2 - 8	210 - 270	8	3,0 / 5,5
nach dem Aushärten (vom Kunden)										
AT	R 1030	2.1245.60	3 h / 315	1030 - 1250	900 - 1140	700 / 780	3 - 12	330 - 380	13	- / -
1/4 HT	R 1100	2.1245.74	2 h / 315	1100 - 1330	930 - 1210	740 / 820	3 - 8	340 - 390	13	- / -
1/2 HT	R 1170	2.1245.75	2 h / 315	1170 - 1380	1030 - 1250	800 / 890	1 - 5	360 - 410	12	- / -
HT	R 1240	2.1245.76	2 h / 315	1240 - 1450	1060 - 1300	890 / 980	1 - 3	370 - 440	12	- / -
werksvergütet										
AM	-	-	-	680 - 760	480 - 660	390 / 400	18 - 23	220 - 250	11	1,3 / 1,8
1/4 HM	-	-	-	750 - 830	550 - 760	460 / 480	15 - 20	240 - 280	11	1,5 / 1,8
1/2 HM	-	-	-	830 - 940	650 - 870	520 / 560	12 - 18	260 - 300	11	2,0 / 2,5
HM	-	-	-	930 - 1040	750 - 950	580 / 640	9 - 15	285 - 345	11	3,8 / 5,5
SHM	-	-	-	1030 - 1100	860 - 970	630 / 700	9 - 14	310 - 360	11	5,0 / 8,5
XHM	-	-	-	1100 - 1210	930 - 1140	720 / 790	3 - 9	330 - 380	11	6,5 / 11,0
Brush Legierung 10 CuCo 2 Be, W.Nr. 2.1285. CW 104 C **Brush Legierung 3 CuNi 2 Be, W.Nr. 2.0850. CW 110 C**										
vor dem Aushärten										
A	R 240	2.1285.40	-	240 - 380	140 - 320	- / -	20 - 35	60 - 130	11	0,0 / 0,0
H	-	2.1285.56	-	480 - 590	370 - 560	- / -	2 - 10	140 - 180	14	0,5 / 0,6
HR	-	2.1285.59	-	550 - 700	450 - 650	- / -	2 - 8	160 - 200	14	- / -
nach dem Aushärten										
AT	R 680	2.1285.60	3 h / 480	680 - 900	550 - 690	370 / 370	10 - 20	195 - 250	25	1,0 / 1,8
1/2HT/HT	R 750	2.1285.75/76	2 h / 480	750 - 940	650 - 870	500 / 530	5 - 15	215 - 270	27	2,0 / 2,5
HTR	R 820	2.1285.79	werksvergütet	820 - 1040	750 - 970	- / -	1 - 8	240 - 290	27	3,0 / 6,0
HTC	-	-	werksvergütet	520 - 620	340 - 520	- / -	5 - 15	150 - 200	34	1,0 / 1,5

*DIN EN 12384

[1] Richtwert (eigener Verformungstest empfohlen)

Wertetabelle - Bänder

Zustand	Zugfestigkeit Rm [N/mm^2]	Dehngrenze Rp 0,2 [N/mm^2]	Federbiegegrenze σ FB min. N/mm^2 für Dicken (mm)* 0,10-0,25 / 0,25-1,0	% Dehnung A ML=50 mm	Vickers Härte (HV)	Elektrische Leitfähigkeit $(\frac{m}{\Omega \cdot mm^2}) \geq$	% Relaxation	E-Modul [kN/mm^2]	Biegewechselfestigkeit (10^8 Lastwechsel) [N/mm^2]	Verformbarkeit R/S Verhältnis 90° Quer/Parallel[1]
Brush Legierung 174 CuCo 0.5 Be										
werksvergütet										
HT	760 - 895	690 - 825	580/680	7 - 17	230 - 280	26	15	138	275 - 310	1,2/5,0
1/2 HT	665 - 790	550 - 690	530/630	10 - 20	180 - 230	29	20	138	275 - 310	0,5/0,5
Brush Legierung 60										
werksvergütet										
3/4 HT	790 - 930	655 - 790	600/700	≥ 11 %	210 - 270	29	–	138	275 - 310	0,7/0,7
HT	825 - 965	720 - 860	610/730	≥ 10 %	230 - 290	29	–	138	275 - 310	1,5/1,5

Zustand	Wärmebehandlung [h]/[°C]	Zugfestigkeit Rm [N/mm^2]	Dehngrenze Rp 0,2 [N/mm^2]	Biegewechselfestigkeit bei n ≧ 10^7 [N/mm^2]	% Dehnung A ML=50 mm	Vickers Härte (HV)	Elektrische Leitfähigkeit $(\frac{m}{\Omega \cdot mm^2}) \geq$	Verformbarkeit R/S Verhältnis 90° Quer/Parallel[1]
Brush Legierung 360 NiBe 2								
vor dem Aushärten								
A	-	650 - 890	270 - 480	-	30	105 - 200	2	0,0 / 0,0
1/4 H	-	750 - 1030	440 - 860	-	15	150 - 295	2	0,0 / 0,0
1/2 H	-	890 - 1170	790 - 1100	-	8	160 - 385	2	0,7 / 1,2
H	-	1060 - 1340	1030 - 1310	-	1	180 - 495	2	1,2 / 2,0
nach dem Aushärten (vom Kunden)								
AT	2,5 h / 510	min. 1480	1000 - 1200	+/- 586	12	340 - 530	4	- / -
1/4 HT	2,5 h / 510	min. 1580	1050 - 1300	+/- 586	10	380 - 600	4	- / -
1/2 HT	1,5 h / 510	min. 1680	1100 - 1350	+/- 586	9	395 - 695	4	- / -
HT	1,5 h / 510	min. 1860	1150 - 1400	+/- 586	8	445 - 695	4	- / -
Brush Legierung 360 NiBe 2								
werksvergütet								
MH 2	-	1060 - 1240	680 - 860	-	14	auf Anfrage	3	0,0 / 0,0
MH 4	-	1240 - 1410	820 - 1060	-	12	auf Anfrage	3	0,5 / 0,5
MH 6	-	1370 - 1550	1030 - 1200	-	10	auf Anfrage	3	1,0 / 1,2
MH 8	-	1510 - 1670	1170 - 1410	-	9	auf Anfrage	3	1,2 / 1,6
MH 10	-	1650 - 1860	1370 - 1550	-	8	auf Anfrage	3	1,5 / 2,2
MH 12	-	1790 - 2000	1510 - 1860	-	8	-	3	2,0 / 3,0

*DIN EN 12384

[1] Richtwert (eigener Verformungstest empfohlen)

Liste gültiger Normen

Produktform	Deutsche und Europäische Normen:
Band	DIN 17670, DIN 1777, DIN 17666, DIN EN 1654, DIN EN 1652, DIN EN 1758
Stangen, Rohre	DIN 17672, DIN 1791, DIN 17671, DIN 1756, DIN 17666, DIN EN 12163, DIN EN 12164, DIN EN 1652, DIN EN 1758
Draht	DIN 17682, DIN 17666, DIN 2076, DIN EN 12166
	Ausländische Normen:
ASTM	B-194, B-196, B-197, B-441, B-534, B-570, B-564
U. S. Federal	QQ-C-530, QQ-C-533
U. S. MIL	MIL-C-46087, MIL-C-81021
AMS	4530, 4532, 4650, 4651, 4725
CDA	C-17000, C-17200, C-17300, C-17500, C-17400, C-17510, C-17460
B. S.	BSS-2870, BSS-2873
SAE	J461, J463
RWMA	RWMA Class 3, RWMA Class 4

Physikalische Eigenschaften von CuBe Legierungen

Brush Legierung	Kupfer-Nr.	Dichte kg/dm^3	Elastizitätsmodul kN/mm^2	Mittlerer thermischer Ausdehnungskoeffizient ($x10^{-6}/°C$, 20 °C bis 200 °C)	Thermische Leitfähigkeit W/m °k	Schmelzbeginn (Solidustemperatur) °C	Biegewechselfestigkeit $n = 10^8$ +/- N/mm^2 (nach Aushärtung)
25/190/290	C 17 200	8,3	125 - 135	17	110	870	270
M 25	C 17 300	8,3	125 - 135	17	110	870	270
165	C 17 000	8,4	125 - 135	17	110	890	260
10	C 17 500	8,8	131 - 138	18	210	1000	210 - 240
3	C 17 510	8,8	131 - 138	18	230	1000	210 - 240
17410	C 17 410	8,8	138	18	239	1020	280 - 310
60	C 17 460	8,8	138	18	225	1030	-
360	N 03 360	8,75	200	14	49	1380	-

Chemische Zusammensetzung

Brush Legierung	Kupfer-Nr.	Beryllium %	Kobalt %	Nickel %	Blei %	Kobalt+Nickel %	Kobalt+Nickel+ Eisen %	Zinn %	Titan %	Kupfer %
25/190/290	C 17 200	1.80 - 2.00	-	-	-	0.20 Min.	0.60 Max.	-	-	Rest
M 25	C 17 300	1.80 - 2.00	-	-	0.20 - 0.60	0.20 Min.	0.60 Max.	-	-	Rest
165	C 17 000	1.60 - 1.80	-	-	-	0.20 Min.	0.60 Max.	-	-	Rest
10	C 17 500	0.40 - 0.70	2.40 - 2.70	-	-	-	-	-	-	Rest
3	C 17 510	0.20 - 0.60	-	1.40 - 2.20	-	-	-	-	-	Rest
17 410	C 17 410	0.15 - 0.50	0.35 - 0.60	-	-	-	-	-	-	Rest
60	C 17 460	0.15 - 0.50	-	1.00 - 1.40	-	-	-	0,25 Max.	-	Rest
360	N 03 360	1.80 - 2.00	-	Rest	-	-	-	-	0,4 - 1,0	-

Verformbarkeit

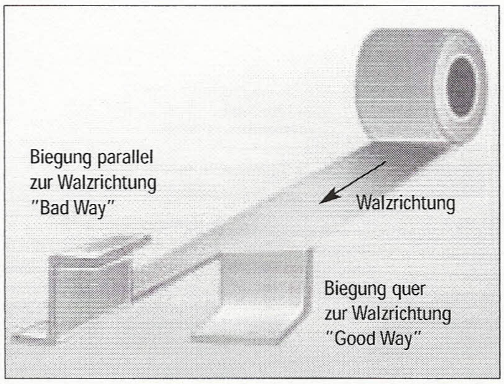

Aushärtung

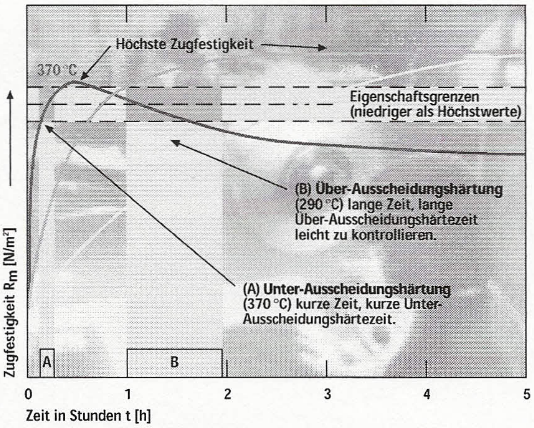

Ansprechen von Brush Legierung 25 auf eine Ausscheidungshärtung bei drei verschiedenen Auslagerungstemperaturen.

Wertetabelle - Stangen, Drähte, Platten, Rohre

Zustand	Werkstoffnummer EN	Werkstoffnummer DIN	Wärmebehandlung bei [h]/[°C]	Zugfestigkeit Rm [N/mm²]	Dehngrenze Rp 0,2 [N/mm²]	% Dehnung A ML=50 mm	Härte Rockwell	Vickers Härte (HV)	Elektrische Leitfähigkeit $(\frac{m}{\Omega \cdot mm^2}) \geq$
Brush Legierung 25 CuBe 2									
vor dem Aushärten									
A	R 420	2.1247.40	-	420 - 600	140 - 250	35	B 45 - 80	90 - 150	9
<25mm H	R 650	2.1247.55	-	650 - 900	500 - 750	10	B 88 - 103	200 - 250	8
>25mm H	R 650	2.1247.55	-	600 - 800	500 - 750	10	B 88 - 103	180 - 240	8
nach dem Aushärten (vom Kunden)									
AT	-	2.1247.60	3 h / 325	1150 - 1350	1000 - 1250	3	C 36 - 41	360 - 390	13
<25mm HT	-	2.1247.75	2 h / 325	1300 - 1500	1150 - 1400	2	C 39 - 44	390 - 430	12
>25mm HT	-	2.1247.75	2 h / 325	1200 - 1500	1050 - 1400	2	C 38 - 43	380 - 420	12
Brush Legierung M25 Automatenqualität CuBe 2Pb W.Nr.2.1248. CW 102 C nur für Stangen									
vor dem Aushärten									
A	R 410	2.1248.40	-	410 - 600	140 - 250	35	B 45 - 80	90 - 150	9
<25mm H	R 620	2.1248.56	-	650 - 900	520 - 750	10	B 88 - 103	200 - 250	8
>25mm H	R 620	2.1248.56	-	620 - 870	500 - 750	10	B 88 - 103	180 - 240	8
nach dem Aushärten (vom Kunden)									
AT	-	2.1248.60	3 h / 325	1150 - 1350	1000 - 1250	3	C 36 - 41	360 - 390	13
<25mm HT	-	2.1248.75	2 h / 325	1300 - 1500	1150 - 1400	2	C 39 - 44	390 - 430	12
>25mm HT	-	2.1248.75	2 h / 325	1200 - 1500	1050 - 1400	2	C 38 - 43	380 - 420	12
Brush Legierung 25, CuBe 2 und M25 Automatenqualität CuBe 2 Pb W.Nr.2.1248. CW 101 C/CW 102 C nur für Drähte									
vor dem Aushärten				min.	min.				
A	-	2.1247.40	-	420	140	35	-	-	9
1/2 H	-	2.1247.55	-	650	580	5	-	-	9
H	-	2.1247.56	-	900	730	2	-	-	8
nach dem Aushärten (vom Kunden)									
AT	-	2.1247.60	3 h / 325	1140	1000	3	-	-	13
1/2 HT	-	2.1247.75	2 h / 325	1250	1140	1	-	-	13
HT	-	2.1247.76	2 h / 325	1300	1240	1	-	-	12
Brush Legierung 10 CuCo 2 Be, W.Nr. 2.1285. CW 104 C **Brush Legierung 3 CuNi 2 Be, W.Nr. 2.0850. CW 103 C**									
vor dem Aushärten									
A	R 250	2.1285.40	-	250 - 370	140 - 210	20	B 25 - 45	70 - 100	11
H	R 450	2.1285.56	-	450 - 550	380 - 530	10	B 60 - 80	130 - 180	11
nach dem Aushärten									
AT	R 650	2.1285.60	3 h / 480	650 - 800	500 - 650	10	B 92 - 100	195 - 235	25
HT	R 750	2.1285.76	2 h / 480	750 - 900	680 - 830	8	B 95 - 102	210 - 260	27

Empfohlene Schnitt- und Vorschubgeschwindigkeiten

Bearbeitung	Schnittgeschwindigkeit m/min.	Vorschub mm/U	Schnitttiefe	Werkzeugmaterial[3]
Legierungen 25, M 25 und 165				
Drehen				
angelassen	450	0,25 - 0,5	0,2 - 3	C-2
gezogen, hart	360	0,25 - 0,5	0,2 - 3	C-2
wärmebehandelt	270	0,25 - 0,5	0,2 - 3	C-2
Bohren				
angelassen	60 - 100	0,05 - 0,23	-	H.S.S.
gezogen, hart	45 - 90	0,05 - 0,23	-	H.S.S.
wärmebehandelt	30 - 90	0,05 - 0,23	-	H.S.S.
Gewindebohren				
angelassen	15 - 30	-	-	H.S.S.
gezogen, hart	9 - 18	-	-	H.S.S.
wärmebehandelt	4 - 8	-	-	H.S.S.
Legierungen 10 und 3[4]				
Drehen	450 - 540	0,25 - 0,64	1,3 - 3,2	C-2
Bohren	38 - 180	0,05 - 0,12	-	H.S.S.
Gewindebohren	5 - 45	-	-	H.S.S.

[3] H.S.S. = Schnellstahl

[4] Beim Gewindebohren von Brush Legierung 3 und Brush Legierung 10 ist die Schnittgeschwindigkeit sehr kritisch. Je kleiner der Gewindebohrer ist, desto kleiner sollte die Schnittgeschwindigkeit sein.
C-2 = Hartmetall

C.2 Stainless Steel 316

1.4436 AISI 316

Standards

Material No.	EN Designation	AISI/SAE	UNS
1.4436	X3CrNiMo17-13-3	316	S31600

Description

1.4436 / AISI 316 is an austenitic chromium-nickel-molybdenum stainless steel.

Special properties

1.4436 is a higher alloyed version of 1.4401 an is specified when the corrosion resistance of 1.4401 is no longer considered to be sufficient.

Chemical Composition

C %	Si ≤ %	Mn ≤ %	P ≤ %	S ≤ %
≤ 0.05	1.00	2.00	0.045	0.015
Cr %	Mo %	Ni %	N %	
16.5-18.5	2.50-3.00	10.5-13.0	≤ 0.11	

Mechanical Properties 20°C

Hardness HB 30 ≤ HB	0.2% Yield strength R_p ≥ N/mm²	Tensile strength R_m N/mm²	Elongation A_5 ≥ %	Modulus of elasticity kN/mm²
215	200	500-700	40/30	200

Physical Properties 20°C

Density g/cm³	Specific heat capacity J/kg K	Thermal conductivity W/m K	Electrical resistivity Ω mm²/m
8	500	15	0.75

Suitable welding filler materials

1.4403; 1.4430; 1.4576

Application

Cellulose industry, textile industry

Available forms for 1.4436 / AISI 316

Sheets/Plates	Bars	Wire	Tubes/Pipes	Fittings	Forged / cast parts	Finished part (drawing)
						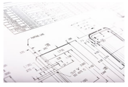

C.3 Cemented Tungsten Carbide MT10MG (WC10)

Datasheet – MT10MG

Product	**MT10MG**
Chemical Composition (%)	
WC	90 %
Co	10 %
Microstructure Grain Size (µm)	0,70
Density	14,45
Hardness (HV30)	1 610
K_{1C}	11,0
Transverse Rupture Strength (N/mm²)	4 000
Porosity	A <02 B 00 C 00